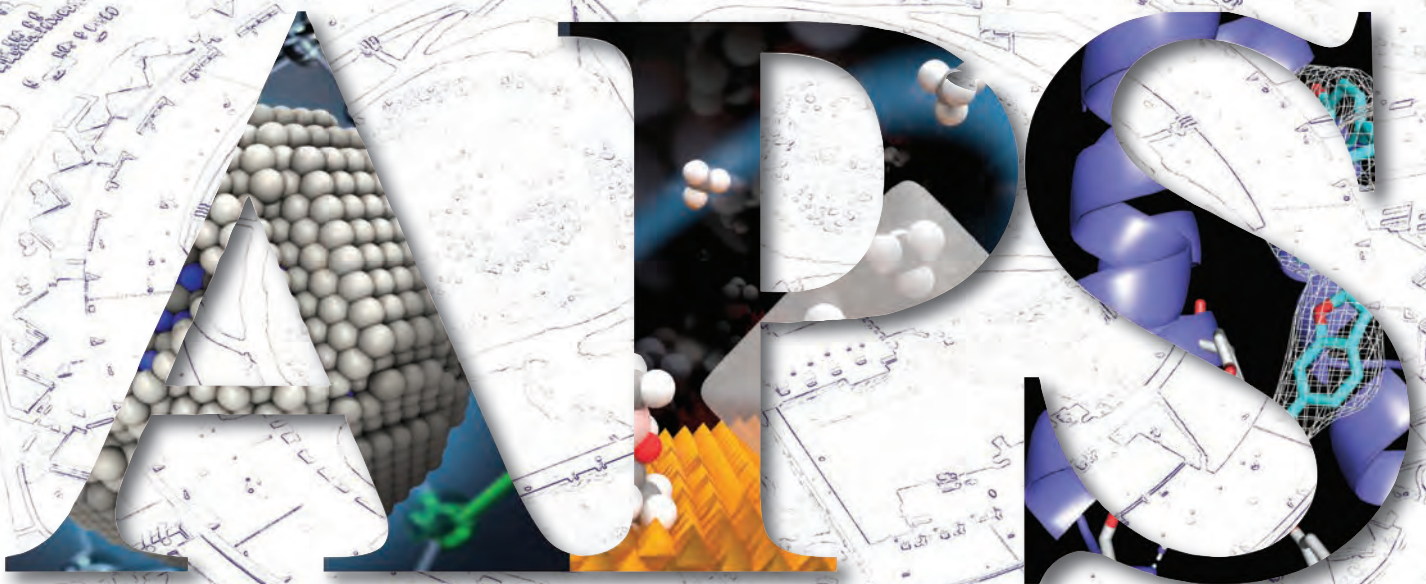


APS Science 2018 Vol. 2



RESEARCH AND ENGINEERING HIGHLIGHTS FROM THE
ADVANCED PHOTON SOURCE AT
ARGONNE NATIONAL LABORATORY

About Argonne National Laboratory

Argonne is a U.S. Department of Energy laboratory managed by UChicago Argonne, LLC under contract DE-AC02-06CH11357. The Laboratory's main facility is outside Chicago, at 9700 South Cass Avenue, Argonne, Illinois 60439. For information about Argonne and its pioneering science and technology programs, see www.anl.gov.

DOCUMENT AVAILABILITY

Online Access: U.S. Department of Energy (DOE) reports produced after 1991 and a growing number of pre-1991 documents are available free at OSTI.GOV (<http://www.osti.gov/>), a service of the US Dept. of Energy's Office of Scientific and Technical Information.

Reports not in digital format may be purchased by the public from the National Technical Information Service (NTIS): U.S. Department of Commerce National Technical Information Service
5301 Shawnee Rd
Alexandria, VA 22312
www.ntis.gov
Phone: (800) 553-NTIS (6847) or (703) 605-6000
Fax: (703) 605-6900
Email: orders@ntis.gov

Reports not in digital format are available to DOE and DOE contractors from the Office of Scientific and Technical Information (OSTI):
U.S. Department of Energy
Office of Scientific and Technical Information
P.O. Box 62
Oak Ridge, TN 37831-0062
www.osti.gov
Phone: (865) 576-8401
Fax: (865) 576-5728
Email: reports@osti.gov

Disclaimer

This report was prepared as an account of work sponsored by an agency of the United States Government. Neither the United States Government nor any agency thereof, nor UChicago Argonne, LLC, nor any of their employees or officers, makes any warranty, express or implied, or assumes any legal liability or responsibility for the accuracy, completeness, or usefulness of any information, apparatus, product, or process disclosed, or represents that its use would not infringe privately owned rights. Reference herein to any specific commercial product, process, or service by trade name, trademark, manufacturer, or otherwise, does not necessarily constitute or imply its endorsement, recommendation, or favoring by the United States Government or any agency thereof. The views and opinions of document authors expressed herein do not necessarily state or reflect those of the United States Government or any agency thereof, Argonne National Laboratory, or UChicago Argonne, LLC.

APS Science 2018 Vol. 2

RESEARCH AND ENGINEERING HIGHLIGHTS FROM THE
ADVANCED PHOTON SOURCE AT
ARGONNE NATIONAL LABORATORY

Argonne is a U.S. Department of Energy (DOE) laboratory managed by UChicago Argonne, LLC.
The Advanced Photon Source is a DOE Office of Science user facility
operated for the DOE Office of Science by Argonne National Laboratory under Contract No. DE-AC02-06CH11357.

TABLE OF CONTENTS

Access to Beam Time at the Advanced Photon Source	iii
The Advanced Photon Source Facility at Argonne National Laboratory — Contact Us	iv
APS Planview	v
APS Beamlines	vi-vii
Upgrade Update	viii
Electronic & Magnetic Materials	1
Pressuring Jarosite to Reveal Its Magnetostructural Mechanism	2
The First Observation of Near-Room-Temperature Superconductivity	4
Finding Non-trivial Quantum Criticality in an Antiferromagnetic Pyrochlore	6
Mapping the Electrons in Multi-Metal Clusters	8
A Switch in Time	10
Sun Block: Protecting Electronics from Cosmic Rays	12
Engineering Materials & Applications	15
Formation of Dislocations Damages Lithium-Rich Cathode Performance	16
A Better Look Inside a Promising Battery Material	18
Understanding Why Nanoporous Silicon-Battery Anodes Fail	20
Distortions Present New Directions for Quantum Devices	22
Harnessing DNA to Improve Optical Technologies	24
Understanding Deformation Mechanisms in an AM-Fabricated Superalloy	26
Adding It Up: Three Routes to Better 3-D Printing	28
Casting Light on Some New Benefits of Perovskite Solar Cells	32
Spinning Out a High-Temperature Magnetic Insulator	34
Illuminating a Key Industrial Process	36
Soft Materials & Liquids	37
Melting and Recrystallization Established Unambiguously in Shock-Compressed Silicon	38
Photo-switching the Network Topology of Polymer Gels	40
Chemical Science	43
MOFs for Methane Manipulation	44
Converting Shale Gas Ethane to Valuable Ethylene	46
The Stresses and Strains of a New Type of Chemistry	48
Pulling Back the Mechanistic Curtain on Iron Zeolite Catalysts	50
A Highly Efficient Fuel Cell Catalyst with an Ultralow Amount of Platinum	52
Mixing Metals to Make Better Catalysts	54
Life Science	57
Lead Levels in the Franklin Expedition: A Closer Look	58
Freeze! Revealing Mechanistic Details for Insulin-Related Diseases	60
Watching Oxygen Bond Formation in Real Time	62
Structural Biology	65
A New Molecule Could Help Put the STING on Cancer	66
A Target Mutation that Renders a Cancer Drug Ineffective	68
A Compound that Exploits a Novel Binding Site on a Diabetes Target	70
The First-Ever Binding Trajectory of a Cancer Drug to its Target	72
A Small Molecule Plays a Big Role in HIV Infectivity	74
Toward a Universal Therapy against Ebola Virus	76
The Power of Entropy: Solving the Allosteric Mystery of a Disordered Tail	78
Structuring Hearing and Deafness	80
Peering Inside a Pathogen	82
Control Yourself!	84
Innovation Accelerates Our Understanding of Lysine Methylation Signaling	86
How to Select a Selective Antagonist	88
Protecting Cells against Reactive Oxygen Species	90
Small Molecules Show Therapeutic Potential for Alzheimer's Disease	92

Environmental, Geological & Planetary Science	93
Amorphous Boron Oxide at Megabar Pressures	94
Cell Envelope Sulfhydryl Sites Play a Key Role in Se(IV) Interactions With Microbes	96
Shock-Compressed Forsterite Overturns Prior “Mixed Phase” Theories	98
Constraining Partial Melt Fractions in Upper Mantle Low-Velocity Zones	100
Nanoscience	103
Unexpected Nanoclusters in Lithium-Ion Battery Electrolytes	104
Transforming Hydrogels May Improve Sustained Drug Delivery	106
Novel Molecular Rotors that Meet Theoretical Requirements for Nano-Electronics	108
How Surface Ligands Influence the Lattice Dynamics of Cadmium Selenide Quantum Dot Nanoparticles	110
Revealing the Hole Story for ZnO Nanoparticles	112
X-ray Availability and Reliability — Typical APS Machine Parameters	114
Novel Accelerator & X-ray Techniques & Instrumentation	115
Production of Vacuum Chambers for the Linac Coherent Light Source II	116
EPICS @ 30: EPICS 7 Advances the Capabilities of the APS Controls Network	118
Making Fine Pictures from Coarse Data	120
How Convolutional Neural Networks Greatly Enhance Low-Dose X-ray Tomography	122
The APS Data Management System	124
Variable X-ray Focal Spot Sizes for Kirkpatrick-Baez Mirrors Using Compound Refractive Lenses	126
Development of a Kappa Diffractometer for Intermediate X-ray Energies at APS Beamline 29-ID	128
The Mechanism of Hemoglobin-ligand Allostery is Not a Closed Case	130
Bringing Hybrid MBE Thin-Film Growth and Characterization to the APS	132
Extending Multispeckle X-Ray Photon Correlation Spectroscopy to Sub-Microsecond Timescales	134
Around the APS	136
APS Organization Chart	137
APS Source Parameters	138-139
Acknowledgments	140
Data	14, 42, 56, 64, 102

Access to Beam Time at the Advanced Photon Source

Five types of beam-time proposals are available at the Advanced Photon Source (APS): general user, partner or project user, collaborative access team (CAT) member, CAT staff, and APS staff. All beam time at the APS must be requested each cycle through the web-based Beam Time Request System. Each beam-time request (BTR) must be associated with one of the proposals mentioned above.

GENERAL-USER PROPOSALS AND BTRS Proposals are peer reviewed and scored by a General User Proposal Review Panel, and time is allocated on the basis of scores and feasibility. A new BTR must be submitted each cycle; each cycle, allocation is competitive. Proposals expire in two years or when the number of shifts recommended in the peer review has been utilized, whichever comes first.

PARTNER- OR PROJECT-USER PROPOSALS AND BTRS Proposals are peer reviewed by a General User Proposal Review Panel and reviewed further by a subcommittee of the APS Scientific Advisory Committee and by APS senior management. Although a new BTR must be submitted each cycle, a specific amount of beam time is guaranteed for up to three years.

CAT-MEMBER PROPOSALS Proposals from CAT members are typically much shorter and are reviewed by processes developed by individual CATs. Allocation/scheduling is determined by the CAT management.

CAT- AND APS STAFF-MEMBER PROPOSALS AND BTRS These proposals are also very short and are reviewed through processes developed by either the CAT or the APS. Each CAT/beamline determines how beam time is allocated/scheduled. Collaborative access team and/or APS staff may submit general user proposals, in which case the rules for general user proposals and BTRs are followed.

In addition to the above, the APS has developed an industrial measurement access mode (MAM) program to provide a way for industrial users to gain rapid access for one-time measurements to investigate specific problems. A MAM proposal expires after one visit. The APS User Information page (www.aps.anl.gov/Users-Information) provides access to comprehensive information for prospective and current APS users.



The Advanced Photon Source Facility at Argonne National Laboratory

The APS, a national synchrotron radiation research facility operated by UChicago Argonne, LLC, and Argonne National Laboratory for the U.S. Department of Energy (DOE) Office of Science-Basic Energy Sciences, Scientific User Facilities Division provides this nation's brightest high-energy x-ray beams for science. Research by APS users extends from the center of the Earth to outer space, from new information on batteries, combustion engines and microcircuits, new and improved pharmaceuticals, and nanotechnologies whose scale is measured in billionths of a meter. The APS helps researchers illuminate answers to the challenges of our high-tech world, from developing new forms of energy to sustaining our nation's technological and economic competitiveness to pushing back against the ravages of disease. Research at the APS promises to have far-reaching impact on our technology, our economy, our health, and fundamental knowledge of the materials that make up our world.

The APS occupies an 80-acre site on the Argonne campus, about 25 miles from downtown Chicago, Illinois. It shares the site with the Center for Nanoscale Materials and the Advanced Protein Characterization Facility.

For directions to Argonne, see anl.gov/directions-and-visitor-information.

CONTACT US

For more information about the APS send an email to apsinfo@aps.anl.gov or write to APS Info, Bldg. 401, Rm. A4115, Argonne National Laboratory, 9700 S. Cass Ave., Argonne, IL 60439.

To order additional copies of this, or previous, issues of *APS Science* send email to apsinfo@aps.anl.gov.

To download PDF versions of APS Science back issues go to www.aps.anl.gov/Science/APS-Science

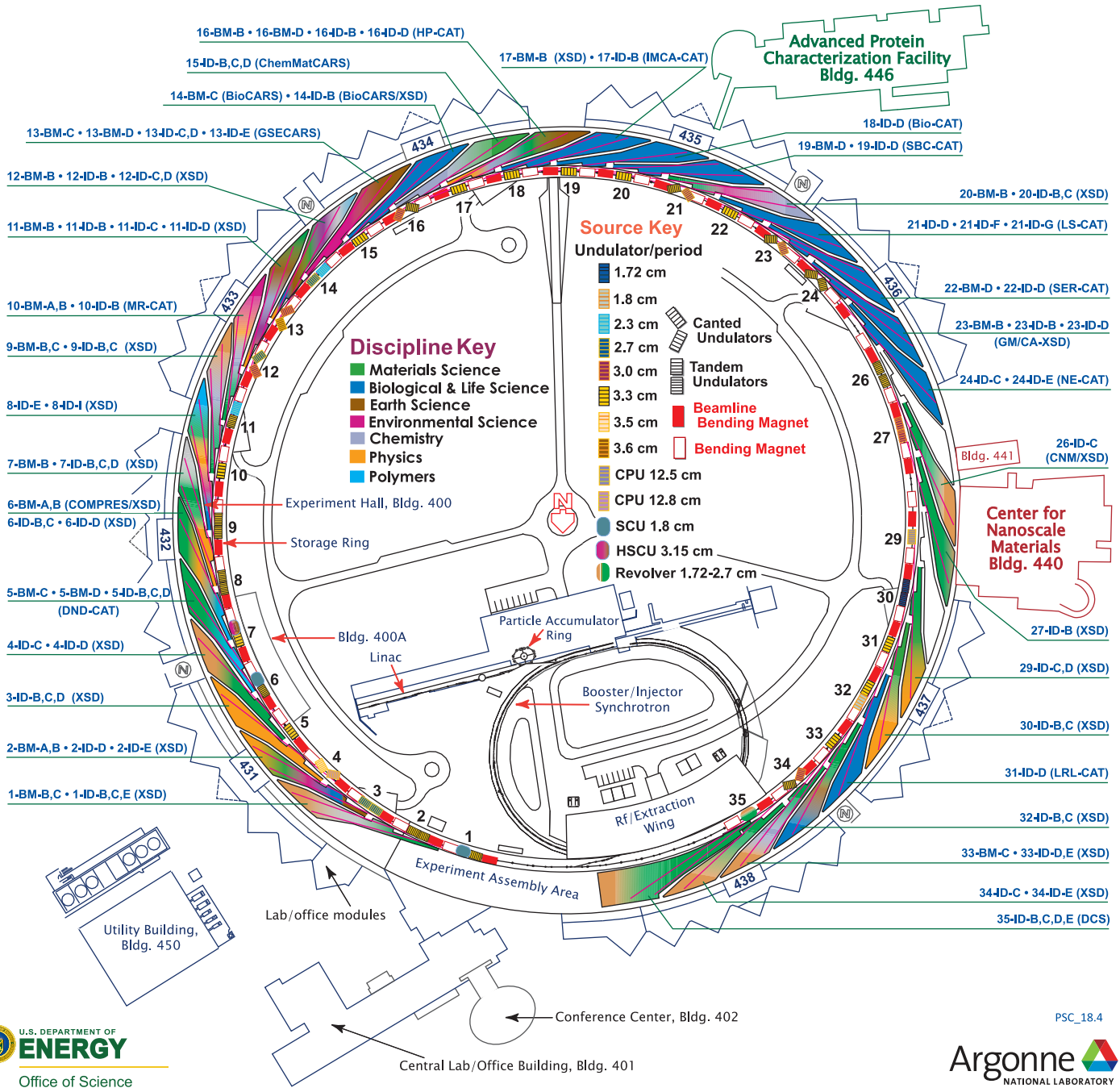
Visit the APS on the Web at www.aps.anl.gov

ARGONNE NATIONAL LABORATORY 400-AREA FACILITIES

ADVANCED PHOTON SOURCE (Beamlines, Disciplines, and Source Configuration)

ADVANCED PROTEIN CHARACTERIZATION FACILITY

CENTER FOR NANOSCALE MATERIALS



APS Sectors: At the APS, a “sector” comprises the radiation sources (one bending magnet and nominally one insertion device, although the number of insertion devices in the straight sections of the storage ring can vary) and the beamlines, enclosures, and instrumentation that are associated with a particular storage ring sector. The APS has 35 sectors dedicated to user science and experimental apparatus. X-ray Science Division sectors comprise those beamlines operated by the APS. Collaborative access team sectors comprise beamlines operated by independent groups made up of scientists from universities, industry, and/or research laboratories both federal and private.

APS Beamlines

Key: Beamline designation • Sector operator • Disciplines • Techniques • Radiation source energy • User access mode(s) • General-user status

1-BM-B,C • X-ray Science Division (XSD) • Materials science, physics, optics testing, detector testing, topography • Energy dispersive x-ray diffraction, white Laue single-crystal diffraction • 6-30 keV, 50-120 keV • On-site • Accepting general users

1-ID-B,C,E • XSD • Materials science, physics, chemistry • High-energy x-ray diffraction, tomography, small-angle x-ray scattering, fluorescence spectroscopy, pair distribution function, phase contrast imaging • 41-136 keV, 45-116 keV • On-site • Accepting general users

2-BM-A,B • XSD • Physics, life sciences, geoscience, materials science • Tomography, phase contrast imaging • 10-170 keV, 11-35 keV • On-site • Accepting general users

2-ID-D • XSD • Life sciences, materials science, environmental science • Microfluorescence (hard x-ray), micro x-ray absorption fine structure, nanoimaging, ptychography • 5-30 keV • On-site • Accepting general users

2-ID-E • XSD • Life sciences, environmental science, materials science • microfluorescence (hard x-ray), tomography • 7-10.5 keV, 11-17 keV • On-site • Accepting general users

3-ID-B,C,D • XSD • Physics, geoscience, life sciences, chemistry, materials science • Nuclear resonant scattering, inelastic x-ray scattering, high-pressure diamond anvil cell • 7-27 keV, 14.41-14.42 keV • On-site • Accepting general users

4-ID-C • XSD • Physics, materials science • Magnetic circular dichroism (soft x-ray), x-ray magnetic linear dichroism, x-ray photoemission spectroscopy, x-ray photoemission electron microscopy, anomalous and resonant scattering (soft x-ray) • 500-2800 eV • On-site • Accepting general users

4-ID-D • XSD • Physics, materials science • Anomalous and resonant scattering (hard x-ray), magnetic x-ray scattering, magnetic circular dichroism (hard x-ray) • 2.7-40 keV • On-site • Accepting general users

4-ID-E • XSD • Materials science, physics • Synchrotron x-ray scanning tunneling microscopy • 500-1800 eV • On-site • Accepting general users

5-BM-C • DND-CAT • Materials science, polymer science • Powder diffraction, tomography, wide-angle x-ray scattering • 10-42 keV • On-site • Accepting general users

5-BM-D • DND-CAT • Materials science, polymer science, chemistry • X-ray absorption fine structure, high-energy x-ray diffraction, general diffraction • 4.5-25 keV, 4.5-80 keV • On-site • Accepting general users

5-ID-B,C,D • DuPont-Northwestern-Dow Collaborative Access Team (DND-CAT) • Materials science, polymer science, chemistry • Powder diffraction, x-ray standing waves, x-ray optics development/ techniques, small-angle x-ray scattering, surface diffraction, x-ray reflectivity, wide-angle x-ray scattering • 6-17.5 keV • On-site • Accepting general users

6-BM-A,B • COMPRES/XSD • Materials science, geoscience • Energy dispersive x-ray diffraction, high-pressure multi-anvil press • 20-200 keV • On-site • Accepting general users

6-ID-B,C • XSD • Physics, materials science • Magnetic x-ray scattering, anomalous and resonant scattering (hard x-ray), general diffraction, grazing incidence diffraction • 3.2-38 keV • On-site • Accepting general users

6-ID-D • XSD • Physics, materials science • Magnetic x-ray scattering, high-energy x-ray diffraction, powder diffraction, pair distribution function • 50-100 keV, 70-130 keV • On-site • Accepting general users

7-BM-B • XSD • Physics • Radiography, tomography, microfluorescence (hard x-ray) • 5-150 keV, 6-15 keV, 25-55 keV • On-site • Accepting general users

7-ID-B,C,D • XSD • Materials science, atomic physics, chemistry • Time-resolved x-ray scattering, time-resolved x-ray absorption fine structure, phase contrast imaging • 6-21 keV • On-site • Accepting general users

8-BM-B • XSD • Chemistry, life sciences, environmental science, materials science • Microfluorescence (hard x-ray) • 5.5-20 keV, 9-18 keV • On-site • Accepting general users

8-ID-E • XSD • Materials science, polymer science, physics • Grazing incidence small-angle scattering, x-ray photon correlation spectroscopy • 7.35-7.35 keV, 11-11 keV • On-site • Accepting general users

8-ID-I • XSD • Polymer science, materials science, physics • X-ray photon correlation spectroscopy, intensity fluctuation spectroscopy, small-angle x-ray scattering • 6-12.5 keV, 10.9-10.9 keV • On-site • Accepting general users

9-BM-B,C • XSD • Materials science, chemistry, environmental science • X-ray absorption fine structure, x-ray absorption near-edge structure • 2.1-25.2 keV • On-site • Accepting general users

9-ID-B,C • XSD • Chemistry, materials science, life sciences • Nano-imaging, microfluorescence (hard x-ray), coherent x-ray scattering (hard x-ray), ultra-small-angle x-ray scattering • 4.5-30 keV • On-site • Accepting general users

10-BM-A,B • Materials Research (MR)-CAT • Materials science, chemistry, environmental science, physics • X-ray absorption fine structure • 4-32 keV • On-site • Accepting general users

10-ID-B • MR-CAT • Materials science, environmental science, chemistry • X-ray absorption fine structure, time-resolved x-ray absorption fine structure, microfluorescence (hard x-ray) • 4.3-27 keV, 4.8-32 keV, 15-65 keV • On-site • Accepting general users

11-BM-B • XSD • Chemistry, materials science, physics • Powder diffraction • 22-33 keV • On-site, mail-in • Accepting general users

11-ID-B • XSD • Chemistry, environmental science, materials science • Pair distribution function, high-energy x-ray diffraction • 58.66 keV, 86.7 keV • On-site • Accepting general users

11-ID-C • XSD • Materials science, chemistry, physics • High-energy x-ray diffraction, diffuse x-ray scattering, pair distribution function • 105.6 keV • On-site • Accepting general users

11-ID-D • XSD • Chemistry, environmental science, materials science • Time-resolved x-ray absorption fine structure, time-resolved x-ray scattering • 6-25 keV • On-site • Accepting general users

12-BM-B • XSD • Materials science, polymer science, chemistry, physics, environmental science • X-ray absorption fine structure, small-angle x-ray scattering, wide-angle x-ray scattering • 4.5-30 keV, 10-40 keV • On-site • Accepting general users

12-ID-B • XSD • Chemistry, materials science, life sciences, polymer science, physics • Small-angle x-ray scattering, grazing incidence small-angle scattering, wide-angle x-ray scattering, grazing incidence diffraction • 7.9-14 keV • On-site • Accepting general users

12-ID-C,D • XSD • Chemistry, physics, materials science • Small-angle x-ray scattering, grazing incidence small-angle scattering, wide-angle x-ray scattering, surface diffraction • 4.5-40 keV • On-site • Accepting general users

13-BM-C • GeoSoilEnviroCARS (GSECARS) • Geoscience • Environmental science • Surface diffraction, high-pressure diamond anvil cell, single-crystal diffraction • 15-15 keV, 28.6-28.6 keV • On-site • Accepting general users

13-BM-D • GSECARS • Geoscience, environmental science • Tomography, high-pressure diamond anvil cell, high-pressure multi-anvil press • 4.5-80 keV • On-site • Accepting general users

13-ID-C,D • GSECARS • Geoscience, environmental science • Microdiffraction, x-ray standing waves, x-ray absorption fine structure, resonant inelastic x-ray scattering, x-ray emission spectroscopy, high-pressure diamond anvil cell, high-pressure multi-anvil press • 4.9-45 keV, 10-75 keV • On-site • Accepting general users

13-ID-E • GSECARS • Geoscience, environmental science • Microfluorescence (hard x-ray), micro x-ray absorption fine structure, microdiffraction, fluorescence spectroscopy • 2.4-28 keV, 5.4-28 keV • On-site • Accepting general users

- 14-BM-C • BioCARS** • Life sciences • Macromolecular crystallography, fiber diffraction, biohazards at the BSL2/3 level, subatomic (<0.85 Å) resolution, large unit cell crystallography • 8-14.9 keV • On-site • Accepting general users
- 14-ID-B • BioCARS** • Life sciences, materials science, physics, chemistry • Time-resolved crystallography, time-resolved x-ray scattering, Laue crystallography, wide-angle x-ray scattering, biohazards at the BSL2/3 level, macromolecular crystallography • 7-19 keV • On site • Accepting general users
- 15-ID-B,C,D • ChemMatCARS** • Materials science, chemistry • Anomalous and resonant scattering (hard x-ray), microdiffraction, high-pressure diamond anvil cell, single-crystal diffraction, liquid surface diffraction, x-ray reflectivity • 6-32 keV, 10-70 keV • On-site • Accepting general users
- 16-BM-B • High Pressure (HP)-CAT** • Materials science, geoscience, chemistry, physics • White Laue single-crystal diffraction, energy dispersive x-ray diffraction, phase contrast imaging, radiography, pair distribution function • 10-120 keV • On-site • Accepting general users
- 16-BM-D • HP-CAT** • Materials science, geoscience, chemistry, physics • Powder angular dispersive x-ray diffraction, single-crystal diffraction, x-ray absorption near-edge structure, x-ray absorption fine structure, tomography • 6-45 keV • On-site • Accepting general users
- 16-ID-B • HP-CAT** • Materials science, geoscience, chemistry, physics • Microdiffraction, single-crystal diffraction, high-pressure diamond anvil cell • 18-60 keV • On-site • Accepting general users
- 16-ID-D • HP-CAT** • Materials science, geo science, chemistry, physics • Nuclear resonant scattering, inelastic x-ray scattering (1-eV resolution), x-ray emission spectroscopy, high-pressure diamond anvil cell • 5-37 keV, 14.41-14.42 keV • On-site • Accepting general users
- 17-BM-B • XSD** • Chemistry, materials science • Powder diffraction, pair distribution function • 27-51 keV • On-site • Accepting general users
- 17-ID-B • Industrial Macromolecular Crystallography Association (IMCA)-CAT** • Life sciences • Macromolecular crystallography, multi-wavelength anomalous dispersion, microbeam, single-wavelength anomalous dispersion, large unit cell crystallography • Subatomic (<0.85 Å) resolution • 6-20 keV • On-site, remote • Accepting general users
- 18-ID-D • Biophysics (Bio)-CAT** • Life sciences • Fiber diffraction, microdiffraction, small-angle x-ray scattering, time-resolved x-ray scattering • 3.5-35 keV • On-site • Accepting general users
- 19-BM-D • Structural Biology Center (SBC)-CAT** • Life sciences • Multi-wavelength anomalous dispersion, macromolecular crystallography, single-wavelength anomalous dispersion • 6-13.5 keV • Remote, on-site, mail-in • Accepting general users
- 19-ID-D • SBC-CAT** • Life sciences • Macromolecular crystallography, multi-wavelength anomalous dispersion, subatomic (<0.85 Å) resolution, large unit cell crystallography, single-wavelength anomalous dispersion • 6.5-19.5 keV • On-site, remote, mail-in • Accepting general users
- 20-BM-B • XSD** • Materials science, environmental science, chemistry • X-ray absorption fine structure, microfluorescence (hard x-ray) • 2.7-32 keV, 2.7-35 keV • On-site • Accepting general users
- 20-ID-B,C • XSD** • Materials science, environmental science, chemistry • X-ray absorption fine structure, x-ray Raman scattering, micro x-ray absorption fine structure, microfluorescence (hard x-ray), x-ray emission spectroscopy • 4.3-27 keV, 7-52 keV • On-site • Accepting general users
- 21-ID-D • Life Sciences (LS)-CAT** • Life sciences • Macromolecular crystallography • 6.5-20 keV • On-site, remote, mail-in • Accepting general users
- 21-ID-F • LS-CAT** • Life sciences • Macromolecular crystallography • 12.7 keV • Remote, on-site, mail-in • Accepting general users
- 21-ID-G • LS-CAT** • Life sciences • Macromolecular crystallography • 12.7 keV • Remote, on-site, mail-in • Accepting general users
- 22-BM-D • Southeast Regional (SER)-CAT** • Life sciences • Macromol-
- ecular crystallography, single-wavelength anomalous dispersion, multi-wavelength anomalous dispersion • 8-20 keV • On-site, remote • Accepting general users
- 22-ID-D • SER-CAT** • Life sciences • Macromolecular crystallography, multi-wavelength anomalous dispersion, single-wavelength anomalous dispersion, microbeam • 6-20 keV • On-site, remote • Accepting general users
- 23-BM-B • National Institute of General Medical Sciences and National Cancer Institute (GM/CA-XSD)** • Life Sciences • Macromolecular crystallography • 12.5-12.75 keV • On-site • Accepting general users
- 23-ID-B • GM/CA-XSD** • Life sciences • Macromolecular crystallography, microbeam, large unit cell crystallography, subatomic (<0.85 Å) resolution, multi-wavelength anomalous dispersion, single-wavelength anomalous dispersion • 3.5-20 keV • On-site, remote • Accepting general users
- 23-ID-D • GM/CA-XSD** • Life sciences • Macromolecular crystallography, microbeam, large unit cell crystallography, subatomic (<0.85 Å) resolution, multi-wavelength anomalous dispersion, single-wavelength anomalous dispersion • 5-20 keV • On-site, remote • Accepting general users
- 24-ID-C • Northeastern (NE)-CAT** • Life sciences • Macromolecular crystallography, microdiffraction, single-wavelength anomalous dispersion, single-crystal diffraction, microbeam, multi-wavelength anomalous dispersion, subatomic (<0.85 Å) resolution • 6.5-20 keV • On-site, remote • Accepting general users
- 24-ID-E • NE-CAT** • Life sciences • Macromolecular crystallography, microbeam, microdiffraction, single-wavelength anomalous dispersion, single-crystal diffraction • 12.68 keV • On-site, remote • Accepting general users
- 26-ID-C • Center for Nanoscale Materials (CNM)/XSD** • Physics, materials science • Nanodiffraction, nano-imaging, coherent x-ray scattering • 6-12 keV • On-site • Accepting general users
- 27-ID-B • XSD** • Physics • Resonant inelastic x-ray scattering • 5-14 keV, 5-30 keV • On-site • Accepting general users
- 29-ID-C,D • XSD** • Physics, materials science • Resonant soft x-ray scattering, angle-resolved photoemission spectroscopy • 250-2200 eV, 2200-3000 eV • On-site • Accepting general users
- 30-ID-B,C • XSD** • Physics, materials science • Inelastic x-ray scattering • 23.7-23.9 keV • On-site • Accepting general users
- 31-ID-D • Lily Research Laboratories (LRL)-CAT** • Life sciences • Macromolecular crystallography, single-wavelength anomalous dispersion • 9-13.5 keV • Mail-in • Accepting general users
- 32-ID-B,C • XSD** • Materials science, life sciences, geoscience • Phase contrast imaging, radiography, transmission x-ray microscopy, tomography • 7-40 keV • On-site • Accepting general users
- 33-BM-C • XSD** • Materials science, physics, chemistry • Diffuse x-ray scattering, general diffraction, powder diffraction, x-ray reflectivity, grazing incidence diffraction, anomalous and resonant scattering (hard x-ray) • 5-35 keV • On-site • Accepting general users
- 33-ID-D,E • XSD** • Materials science, physics, chemistry, environmental science • Anomalous and resonant scattering (hard x-ray), diffuse x-ray scattering, general diffraction, surface diffraction, surface diffraction (UHV), x-ray reflectivity • 4-40 keV, 6-25 keV • On-site • Accepting general users
- 34-ID-C • XSD** • Materials science, physics • Coherent x-ray scattering • 5-15 keV • On-site • Accepting general users
- 34-ID-E • XSD** • Materials science, physics, environmental science, geo science • Microdiffraction, Laue crystallography, microbeam, microfluorescence (hard x-ray) • 7-30 keV • On-site • Accepting general users
- 35-ID-B,C,D,E • Dynamic Compression Sector (DCS)** • Physics, materials science, geoscience • Time-resolved x-ray scattering, phase contrast imaging, radiography • 7-35 keV, 7-100 keV, 24-24 keV • On-site • Accepting general users

Upgrade Update

During the week of June 17, 2019, the Advanced Photon Source (APS-U) Project team had a positive DOE Critical Decision-3 (CD-3) review. With the full spending authority that will be granted with CD-3 approval, the APS can look forward to an expeditious and successful completion of this exciting project. For an in-depth look at the APS-U science program, see <https://bit.ly/2x4Vb2i>.

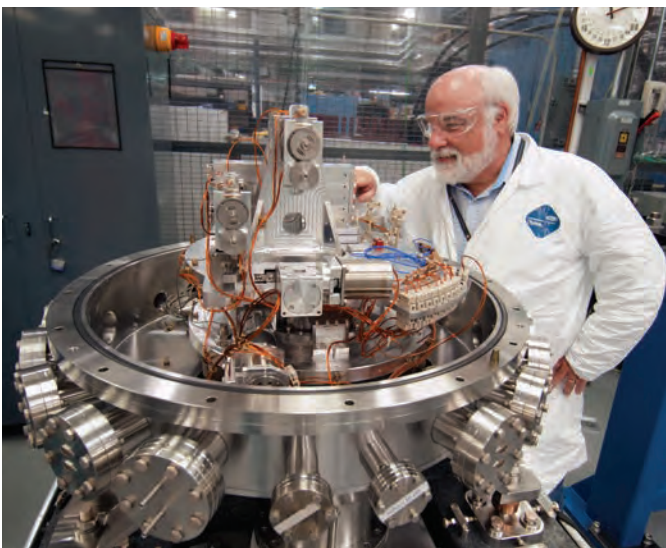


Above: A computer-aided rendering of a typical APS-U storage ring sector showing the MBA-lattice configuration of red, blue, and purple electromagnets and associated components. Rendering by the AES Design and Drafting Group.



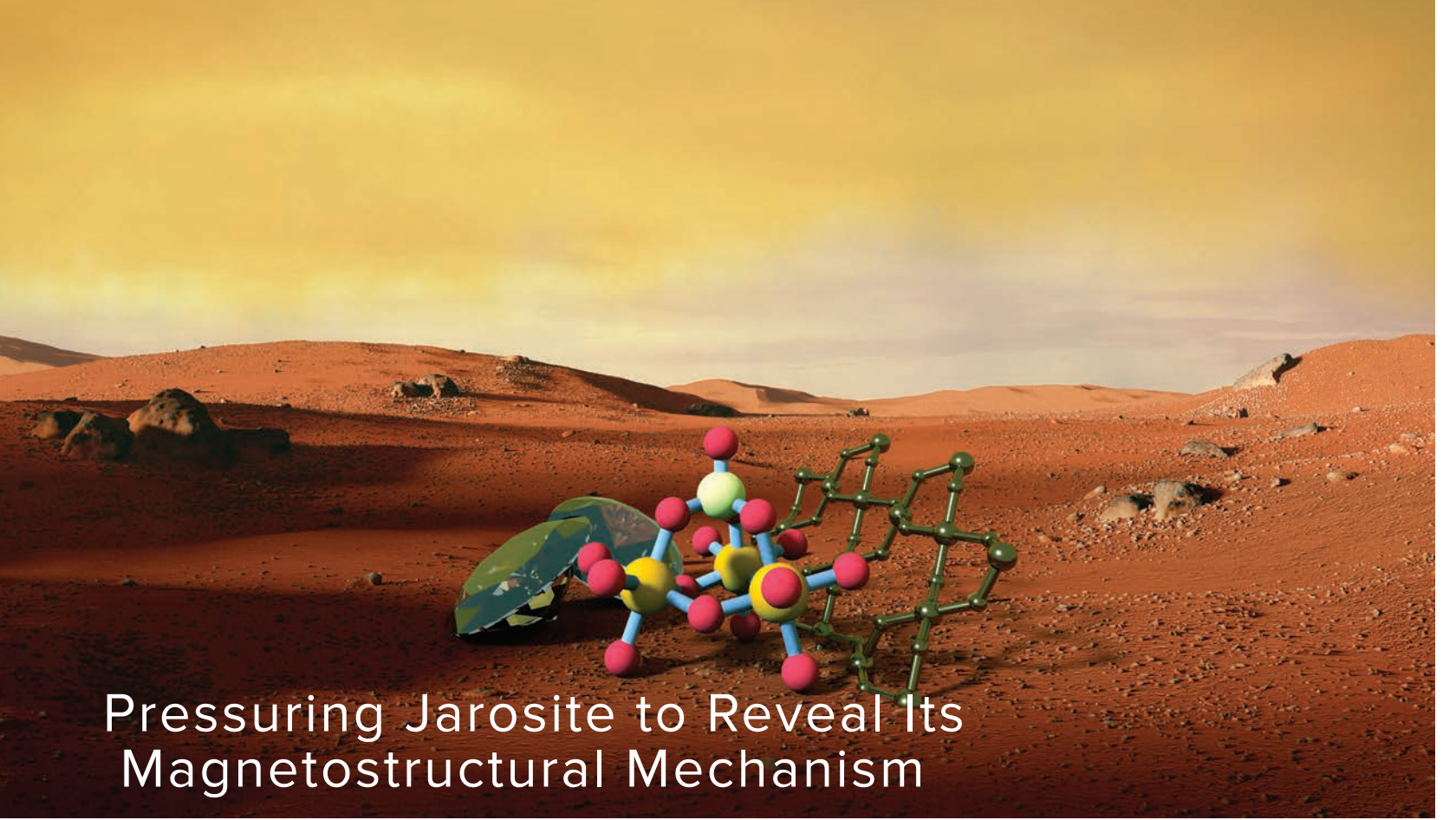
Left: APS-U technicians prepare an assortment of APS-U storage ring magnets for tests in the new, state-of-the-art APS-U Magnet Measurement Lab at Argonne.

Below: A monochromator from Instrument Design Technologies, Inc., designed for use with the upgraded APS, undergoes acceptance testing by an APS-U physicist following delivery to the APS. The monochromator is now installed and operating at the 2-ID beamline.



Above: Technicians from the APS Accelerator Systems Division Magnetic Devices Group and the APS Engineering Support Division Survey and Alignment Group working on a helical superconducting undulator insertion device. Super-conducting undulators are now in operation in the APS storage ring and are a key component of the APS-U. They produce stronger magnetic fields and thus higher-energy x-rays than conventional permanent magnetic undulators having the same period lengths.

ELECTRONIC & MAGNETIC MATERIALS



Pressuring Jarosite to Reveal Its Magnetostructural Mechanism

Jarosite, a hydrous sulfate mineral exhibiting unusual magnetic behavior, has intrigued scientists in a range of fields from planetary science to inorganic chemistry. Interactions between iron ions in the material's lattice structure cause instances of magnetic frustration, which should lead the material to be magnetically disordered. So then, why does jarosite display overall magnetic order under certain conditions? Previous attempts to unravel the mystery of jarosite's magnetism resulted in contradictory data. Researchers now understand that past studies lacked the technology necessary to account for the material's myriad magnetic interactions. In this study, researchers working at the APS subjected samples of jarosite to extreme pressures in order to systematically vary local coordination environments throughout the material, then observed how these changes affected the material's magnetic ordering behavior. These findings ultimately unveiled the mechanism for jarosite's three-dimensional (3-D) magnetic ordering and revealed a great deal about the nature of geometric magnetic frustration. Moreover, this study serves as a blueprint for how chemists can use pressure to conduct chemically pure magnetostructural correlation studies. By bringing high-pressure techniques to the attention of the chemistry community, even the most perplexing magnetostructural mechanisms can be unraveled.

Fig. 1. Artist's rendering of the structure of jarosite, "relocated" to the surface of Mars.

How does a material's geometric structure impact its magnetic behavior? And how can we find out? These are a few of the questions occupying the minds of scientists studying magnetic and superconducting materials. One material in particular has confounded researchers across a wide range of scientific disciplines.

Jarosite, $\text{KFe}_3(\text{OH})_6(\text{SO}_4)_2$, is a mineral that can be found not only in ore deposits on Earth but has also been detected by rovers on the surface of Mars. The structure of jarosite (Fig. 1) consists of two-dimensional lattice sheets with triangular coupling. Interactions between iron atoms on these kagomé lattices cause the iron ions to exhibit spin-frustrated, antiferromagnetic behavior. But although this antiferromagnetic coupling should cause the material to be magnetically frustrated, the material displays overall magnetic order below 65 K. This counterintuitive magnetic behavior, which has puzzled researchers for decades, has recently been explained.

Understanding jarosite's magnetic behavior requires that scientists be able to systematically control all of the variables contributing to the material's overall magnetism. To do this requires sophisticated experimental techniques. In this study, researchers from Northwestern University, Argonne National Laboratory, the University of Illinois at Urbana-Champaign, and the Carnegie Institu-

tion for Science employed diamond anvil cells to apply extreme pressure to samples of jarosite. Under high pressure, the local coordination environments around the iron ions were able to be manipulated without affecting the material's chemical composition. Then, to observe the resulting changes in magnetic ordering behavior, the researchers combined various cutting-edge synchrotron x-ray research methods at the APS to study the material's crystallographic, magnetic, and electronic properties under pressure.

To determine a structure-function correlation, *in situ* synchrotron powder x-ray diffraction experiments were conducted using the HP-CAT beamline 16-ID-B at the APS. Single-crystal x-ray diffraction data were collected using the 6-circle diffractometer at the GSECARS beamline 13-BM-C, also at the APS. With these techniques, researchers were able to vary the interlayer spacing and metal-ligand bond distances. Then, using data from SQUID-based magnetometry and synchrotron Mössbauer spectroscopy experiments, which were collected at the HP-CAT 16-ID-D beamline, as well as data from x-ray magnetic circular dichroism experiments, which were collected using the XSD 4-ID-D beamline at the APS, the researchers constructed a pressure-dependent magnetic phase diagram and determined jarosite's magnetic and electronic structures at high pressure. These data, seen in Fig. 2, revealed a comprehensive map of jarosite's magnetic coupling interactions.

This study represents a first-of-its kind simultaneous structural-electronic-magnetic study of jarosite. By conducting an innovative combination of experimental techniques at the APS, these researchers were able to achieve a pressure-induced phase transition without breaking the kagomé lattice symmetry or altering the iron ion spin state. The researchers ultimately discovered that jarosite's unique magnetic ordering temperature was — surprisingly — not due to interlayer magnetic coupling as previously thought, but instead due to an increase in the Fe-O-Fe magnetic coupling, which is directly proportional to the Fe-O metal ligand covalency.

The impacts of this research stretch beyond the study of jarosite. This research demonstrates that high-pressure techniques are highly effective at elucidating structural, electronic, and magnetic mechanisms while maintaining a material's chemical integrity. Chemistry conducted at extreme pressures can induce new phases and unlock ex-

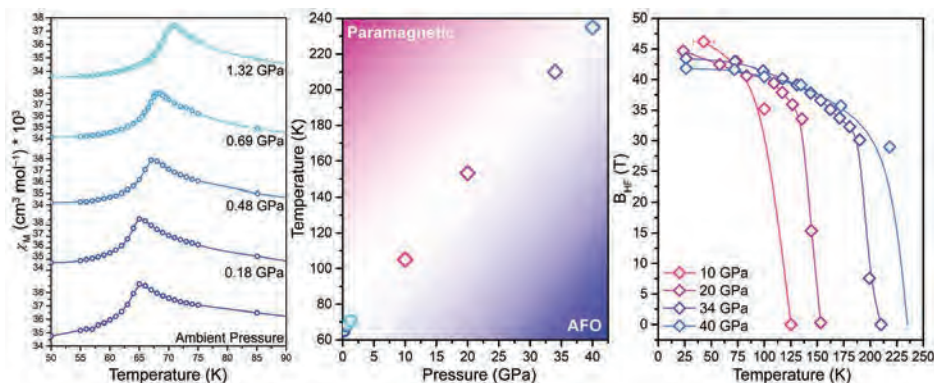


Fig. 2. Researchers determined magnetic susceptibility (left), magnetic phase diagram (center), and magnetic ordering (right) of jarosite as a function of pressure. From R.A. Klein et al., *J. Am. Chem. Soc.* **140**, 12001 (2018). Copyright © 2018 American Chemical Society

traordinary material properties. The researchers believe that these techniques may eventually play a part in illuminating complicated superconducting mechanisms, such as the puzzling doped cuprate systems. — Alicia Surrao

See: Ryan A. Klein¹, James P.S. Walsh¹, Samantha M. Clarke¹, Yinsheng Guo¹, Wenli Bi^{1,3}, Gilberto Fabbris², Yue Meng^{2,4}, Daniel Haskel², E. Ercan Alp², Richard P. Van Duyne¹, Steven D. Jacobsen¹, and Danna E. Freedman^{1*}, "Impact of Pressure on Magnetic Order in Jarosite," *J. Am. Chem. Soc.* **140**, 12001 (2018). DOI: 10.1021/jacs.8b05601

Author affiliations: ¹Northwestern University, ²Argonne National Laboratory, ³University of Illinois at Urbana-Champaign, ⁴Carnegie Institution for Science

Correspondence: * danna.freedman@northwestern.edu

This experimental work on creating materials is supported by the Air Force Office of Scientific Research (FA9550-17-1-0247). Research on kagomé lattices is supported by the Army Research Office (W911NF1810006). The collaborative project between D.E.F. and S.D.J. is supported by Northwestern University through the Innovative Initiatives Incubator and supports J.P.S.W. S.M.C. acknowledges support from the U.S. National Science Foundation (NSF) GRFP (DGE-1324585). S.D.J. acknowledges support from the Carnegie/U.S. Department of Energy (DOE) Alliance Center, the NSF (EAR-1452344), and the David and Lucile Packard Foundation. W.B. is partially supported by the Consortium for Materials Properties Research in Earth Sciences (COMPRES). The UV-vis spectroscopy work was supported by NSF Grant CHE1506683. HP-CAT operations are supported by the DOE-National Nuclear Security Administration Office of Experimental Sciences. GSECARS is supported by the NSF-Earth Sciences (EAR - 1634415) and DOE-GeoSciences (DE-FG02-94ER14466). Use of the COMPRES-GSECARS gas loading system was supported by COMPRES under NSF Cooperative Agreement EAR - 1606856 and by GSECARS through NSF grant EAR-1634415 and DOE grant DE-FG02-94ER14466. Experiments at 13-BM-C were conducted under the Partnership for Extreme Crystallography (PXΛ2), also supported by COMPRES. This work made use of the IMSERC facility at NU, supported by NSF NNCI-1542205; the Keck Foundation; the State of Illinois; and the IIN. This research used resources of the Advanced Photon Source, a U.S. DOE Office of Science User Facility operated for the DOE Office of Science by Argonne National Laboratory under Contract No. DE-AC02-06CH11357.

The First Observation of Near-Room-Temperature Superconductivity

For decades, room-temperature superconductivity has been one of physics' ultimate goals, a Holy Grail-like objective that seems to keep drifting within realization yet always stubbornly out of reach. Various materials, theories, and techniques have been proposed and explored in search of this objective, but its realization has remained elusive. Yet recent experimental work on hydrogen-rich materials at high pressures is finally opening the pathway to practical superconductivity and its vast potential. Russell Hemley, a materials chemist at George Washington University in Washington, D.C., first announced evidence of superconductivity at 260 K in May, 2018, and then hints of an even higher 280 K transition in August of that year. Now Hemley, along with a team of researchers from The George Washington University and the Carnegie Institution for Science, synthesized several lanthanum superhydride materials that demonstrated the first experimental evidence of superconductivity at near room temperature, and with colleagues from Argonne, characterized them at the APS.

One of the major experimental challenges in the study of these materials under high pressures is the extreme difficulty of creating and properly characterizing them in the laboratory. The research team in this study have developed new techniques to deal with these problems, using *in situ* four-probe measurements and x-ray diffraction to measure electrical conductivity in diamond anvil cells.

Modulated, pulsed laser heating was utilized to react lanthanum metal with hydrogen at megabar pressures (nearly 2 million ATM) to synthesize the samples. These synthesis and characterization x-ray diffraction studies were performed at the HP-CAT 16-ID-B of beamline of the APS. The authors note that these new experiments bring to focus the synergy of laboratory techniques with on-line, *in situ* synchrotron x-ray techniques that provided the necessary confirmation of the phase responsible for the near room temperature superconductivity in this system.

The team created several types of superhydride materials with pulsed laser heating, using both ammonia borane and pure hydrogen as a source of hydrogen. Cubic $\text{LaH}_{10\pm x}$ was synthesized at pressures above 180 GPa. Along with the x-ray diffraction studies, electrical conductivity measurements were performed *in situ* at pressures

up to 200 GPa, with resistance being measured as a function of temperature.

The researchers observed a sharp drop in electrical resistance of the first sample occurring around 275 K, then remaining near-zero below 255 K. In subsequent experiments, resistivity transitions starting as high as 280 K were observed. The current-voltage characteristics and the effect of applied current on the transition temperature were also measured. This showed the material has a large critical current in the superconducting phase. X-ray diffraction measurements as a function of temperature through the region of the transition showed no evidence for major structural changes associated with the transition, in agreement with their predictions for LaH_{10} .

In addition to the important observations of superconductivity at temperatures above 260 K, the work highlights the importance of synchrotron x-ray diffraction as a critical tool for these experiments and for extreme conditions materials science in general, and the crucial role played by the APS in this effort. For example, in the most recent set of experiments, electrical transport as a function of temperature was measured "*in situ*" in a cryostat on the HP-CAT beamline. The experiments also made use of the high-pressure support labs managed by the EFree Energy Frontier Research Center located at the

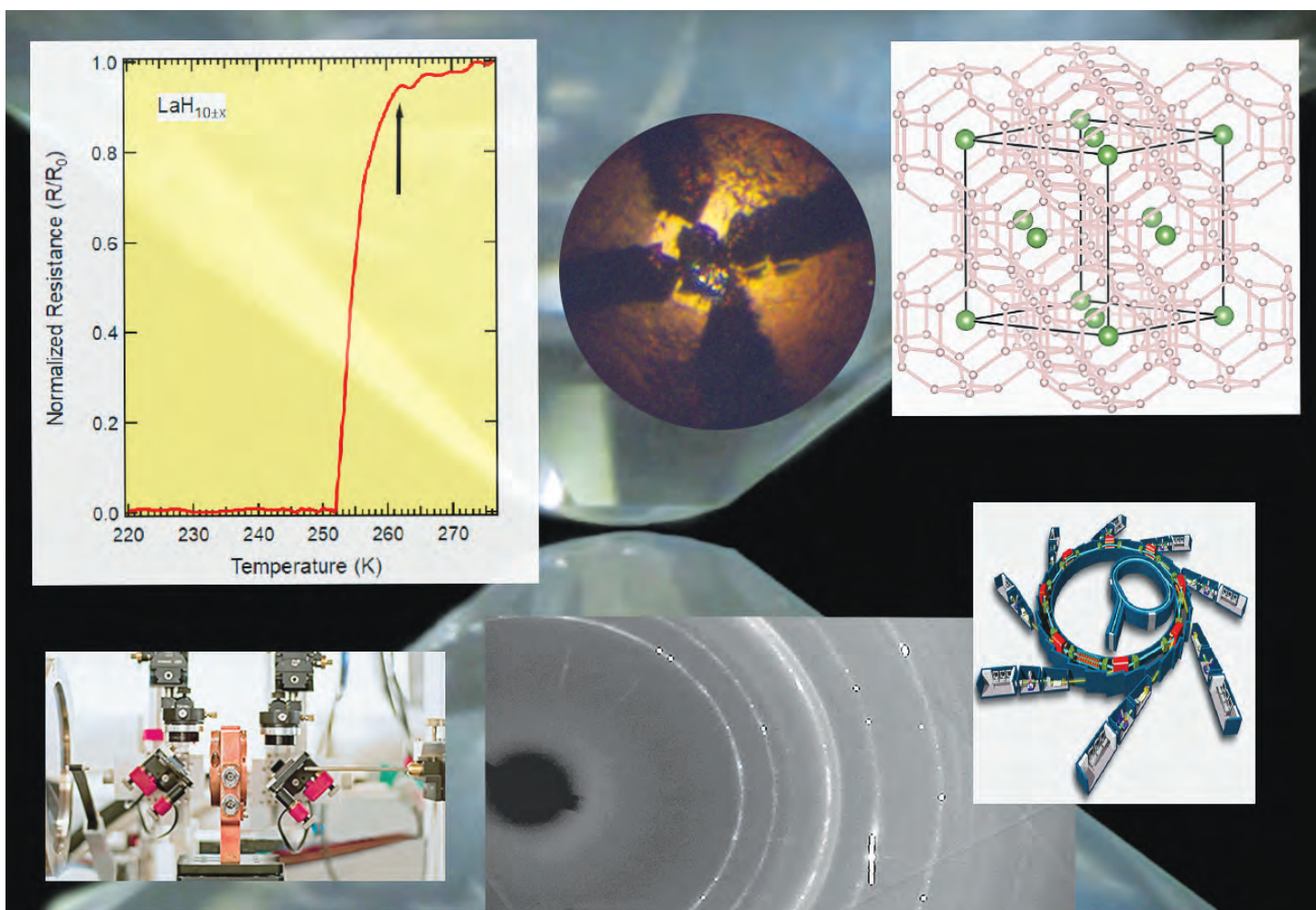


Fig. 1. The structure of LaH_{10} with the sample and the four platinum leads at 180 GPa. The confirmation with *in situ* x-ray diffraction after laser heating shows the drop in resistivity starting at around 265 K in one of the samples synthesized. The confirmation of the structure was determined from the powder diffraction pattern shown in the lower panel. The data was obtained at HP-CAT beamline 16-ID-B at the APS.

APS. The authors note that it is crucial to have x-ray (e.g., synchrotron) characterization of the very sample exhibiting the superconductivity. Thus, down the road they see the need for multiple complementary probes to be brought to bear on the same, well-characterized samples. Such multifaceted characterization will be essential for understanding its precise mechanisms.

Others are confirming these results with additional reports of diamagnetic signatures of superconductivity. Hand in hand with advancing extreme conditions experimental techniques is the increasing accuracy of theoretical and simulation methods that guide these experiments.

These methods, in concert with the critical role of large-scale advanced synchrotron x-ray sources such as the APS, will ultimately lead to the structural control needed to synthesize these materials for practical applications, and to the revolutionary technologies that will follow. — Mark Wolverton

See: Maddury Somayazulu^{1*}, Muhtar Ahart¹, Ajay K Mishra², Zachary M. Geballe², Maria Baldini², Yue Meng³, Viktor V. Struzhkin², and Russell J. Hemley^{1**}, “Evidence for superconduc-

tivity above 260 K in lanthanum superhydride at megabar pressures,” *Phys. Rev. Lett.* **122**, 027001 (14 January 2019). DOI: <https://doi.org/10.1103/PhysRevLett.122.027001>
 Author affiliations: ¹The George Washington University, ²Carnegie Institution for Science, ³Argonne National Laboratory
 Correspondence: * zulu58@gwu.edu, ** rhemley@gwu.edu

This research was supported by EFree, an Energy Frontier Research Center funded by the U.S. Department of Energy (DOE) Office of Science-Basic Energy Sciences (BES), under Award No. DE-SC0001057. The instrumentation and facilities used were supported by DOE-BES (DE-FG02-99ER45775, VVS), the U.S. DOE/National Nuclear Security Administration (DE-NA-0002006, CDAC; and DE-NA0001974, HP-CAT), and the National Science Foundation (DMR-1809783). This research used resources of the Advanced Photon Source, a U.S. DOE Office of Science User Facility operated for the DOE Office of Science by Argonne National Laboratory under Contract No. DE-AC02-06CH11357.

Finding Non-trivial Quantum Criticality in an Antiferromagnetic Pyrochlore

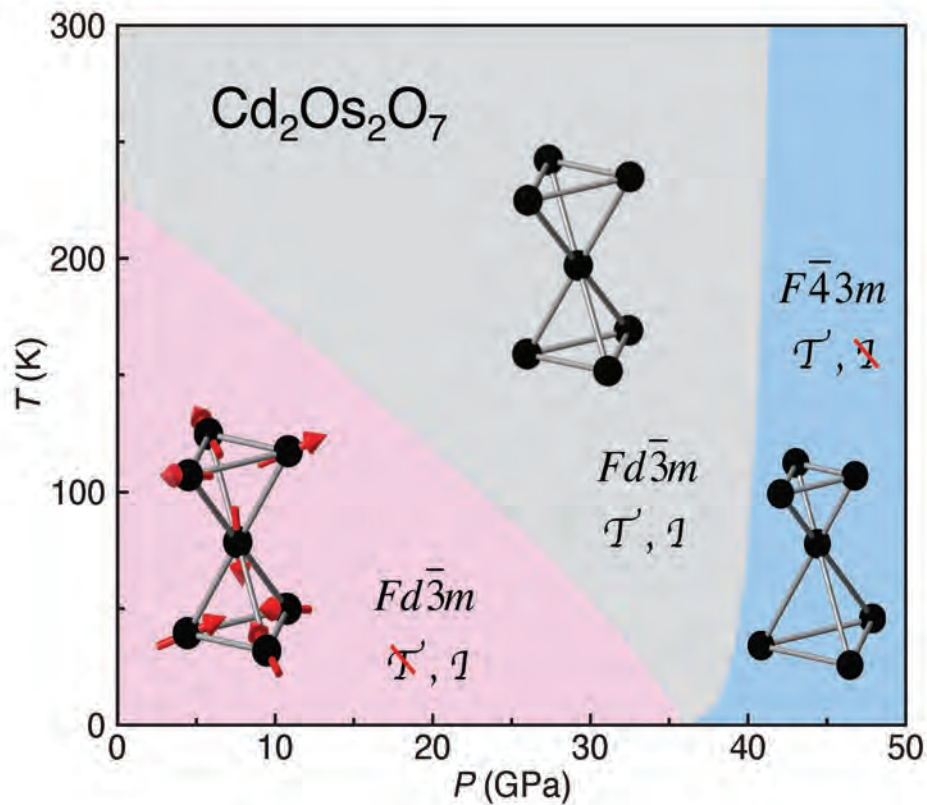


Fig. 1. Schematics of the phase diagram of $\text{Cd}_2\text{Os}_2\text{O}_7$, manifesting three contrasting states of matter under high pressure. The low-pressure phase on the left has an all-in-all-out type of antiferromagnetic spin arrangement, located on two identical-sized adjacent tetrahedra, which breaks the time reversal symmetry but preserves the inversion symmetry for both spins and lattice ions. The high-pressure state on the right represents a disordered spin state with preserved time reversal symmetry, in a lattice that breaks the spatial inversion symmetry with a breathing lattice made of different sized tetrahedra. The disordered state in the middle represents the quantum critical region with coexisting spin, lattice, and charge fluctuation modes. From Y. Wang et al., Nat. Commun. **9**, 2953 (2018). © 2019 Springer Nature Publishing AG

A quantum critical point (QCP) anchors a type of phase transition at absolute zero that is continuous and driven not by temperature but by the quantum fluctuations. Many quantum critical phenomena are well-described by mean-field theory where fluctuation effects are not critical, largely due to dimensionality reasons. However, when competing ground states converge at one QCP, expected only in a few systems, exotic critical behavior emerges from the coupled quantum fluctuations. These systems are often termed as the “strongly-coupled” type and help to illustrate the origin of collective phenomena that are responsible for technically important functional materials featuring piezoelectricity, magnetism, and superconductivity. Researchers carrying out studies at the APS discovered an intriguing QCP in $\text{Cd}_2\text{Os}_2\text{O}_7$, a pyrochlore lattice with all-in-all-out (AIAO) antiferromagnetic order, showing strongly-coupled quantum critical phenomena under extreme pressure even in a three-dimensional space prone to mean-field critical behavior. (Pyrochlore is a complex oxide mineral composed of niobium, sodium, and calcium that forms brown to black, glassy octahedral crystals and irregular masses.) This work could lead to the development of better and more complete models of these phenomena, including interactions between breathing mode phonons, AIAO spin fluctuations, and charge quasiparticles. Such knowledge might enable more precise control of such quantum critical phase states in these pyrochlore materials.

Because cubic lattice symmetry remains preserved in compounds with AIAO spin order, the researchers from the California Institute of Technology, The University of Chicago, Argonne, the University of Tennessee, Knoxville, Oak Ridge National Laboratory, and the Okinawa Institute of Science and Technology Graduate University (Japan) identified several AIAO spin systems as promising candidates in which to explore strongly-coupled quantum criticality. They chose $\text{Cd}_2\text{Os}_2\text{O}_7$, because it exhibits both the least disorder and the strongest correlation effects, judging by the transition temperature. Under cryogenic temperatures and diamond anvil cell pressures beyond 40 GPa, the experiment team explored the spin, orbit, and charge degrees of freedom under resonant x-ray magnetic and charge diffraction techniques at the XSD 4-ID-D beamline of the APS.

Although the $\text{Cd}_2\text{Os}_2\text{O}_7$ compound displays a $Fd-3m$ space group structure at ambient pressures, it changes

continuously to a $F-43m$ space group beyond the quantum phase transition. At the quantum critical point of 35.8 ± 0.7 GPa, the AIAO order disappears and lattice inversion symmetry is simultaneously broken. The coincidence of both the structural and magnetic phase transitions at around 35.8 GPa would suggest the existence of a single critical point between the insulating AIAO order and a more metallic phase with spin disorder. Such a confluent change of several symmetry conditions, from time reversal to space inversion in addition to charge localization to itinerancy, provides the experimental evidence to support physics of strong coupling type in the region of quantum criticality in this compound.

These quantum phase transitions of structure, charge, and antiferromagnetism, concurrent and all continuous, can serve as a foundation for a general approach to describe and understand three-dimensional, strongly-coupled, non-mean-field quantum criticality. Brilliant x-ray beams from the future APS Upgrade will allow extending this type of measurement to significantly higher pressures for exploration of quantum critical phenomena in systems with stronger correlation effects. — Mark Wolverton

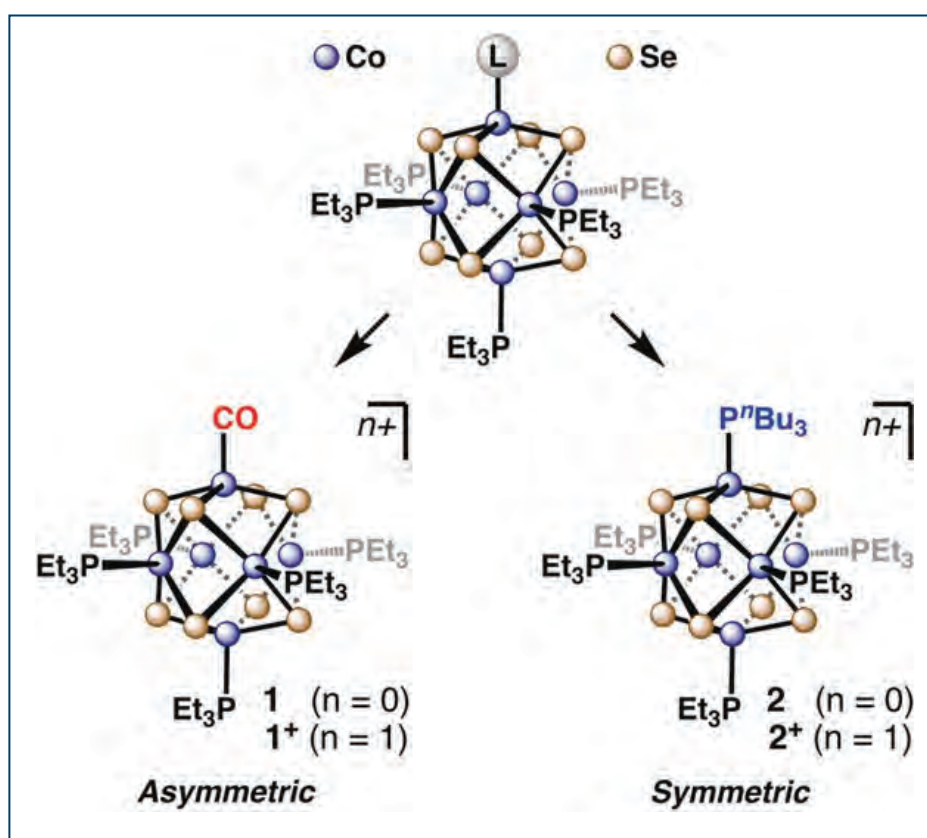
See: Yishu Wang¹, T.F. Rosenbaum^{1*}, A. Palmer², Y. Ren³, J.-W. Kim³, D. Mandrus^{4,5}, and Yejun Feng^{1,6**}, “Strongly-coupled quantum critical point in an all-in-all-out antiferromagnet,” *Nat. Commun.* **9**, 2953 (2018). DOI: 10.1038/s41467-018-05435-7

Author affiliations: ¹California Institute of Technology, ²The University of Chicago, ³Argonne National Laboratory, ⁴University of Tennessee, Knoxville, ⁵Oak Ridge National Laboratory, ⁶Okinawa Institute of Science and Technology Graduate University
Correspondence: * tfr@caltech.edu,
** yejun@oist.jp

The use of shared facilities of the University of Chicago Materials Research Science and Engineering Center (MRSEC) was supported by National Science Foundation (NSF) Grant No. DMR-1420709. Use of the COMPRES-GSECARS gas loading system was supported by COMPRES under National Science Foundation (NSF) Cooperative Agreement EAR-606856 and by GSECARS through NSF grant EAR-1634415 and U.S. Department of Energy (DOE) grant DE-FG02-94ER14466. The work at Caltech was supported by NSF Grant No. DMR-1606858. D.M. acknowledges support from the U.S. DOE Office of Science-Basic Energy Sciences, Materials Sciences and Engineering Division. This research used resources of the Advanced Photon Source, a U.S. DOE Office of Science User Facility operated for the DOE Office of Science by Argonne National Laboratory under Contract No. DE-AC02-06CH11357.

Mapping the Electrons in Multi-Metal Clusters

Metals are essential for human life. In addition to their many important roles acting as free ions, metals also integrate themselves into biological molecules, acting as catalytic centers in enzymes. The reason metals are a catalytic workhorse is their electronic tunability; metal ions can exist in multiple electronic states depending on their environment, facilitating electron transfer reactions, so scientists are eager to understand how proteins tune their metal centers. Using multiwavelength x-ray anomalous diffraction data collected at the APS, researchers mapped out the electronic structure around individual atoms within a series of compounds with a $[\text{Co}_6\text{Se}_8]$ core and varying peripheral moieties. Beyond biological systems, the results have implications in understanding and developing magnetic and superconducting materials, and better synthetic catalysts.



The rules of how an electron-donating or electron-withdrawing substituent affects the properties of purely organic molecules are well-understood. These are absent in metal-containing compounds, especially when several metal centers interact with each other and their surroundings. Scientists have been making progress in understanding how these ligands surrounding metal centers tune the metal's properties. However, most of the headway in reactivity prediction has been in systems with a single metal center, while biological and synthetic polynuclear systems are rarely so simple. Clusters containing several metals are of significant interest, but are harder to predict.

In this study, the team of researchers from Columbia University and The University of Chicago tackled a challenging polynuclear system: well-defined $[\text{Co}_6\text{Se}_8]$ cluster compounds. The metal cluster forms an octahedral shape, with ligands protruding from the top, sides, and bottom. The researchers studied four different cluster compounds, each with the same $[\text{Co}_6\text{Se}_8]$ core and sharing the same ligands (Et_3P) in 5 out of 6 positions. They created two different types of clusters by varying the ligand at the sixth position (L); thus, an asymmetric ligand sphere was created when $\text{L}=\text{CO}$, while in contrast, $\text{L}=\text{P}^n\text{Bu}_3$ formed a symmetric environment around the cluster core. They also studied each of these cluster types before and after oxidation, when neutral and when positively charged, respectively. The researchers wanted to get a better sense of how electron density at specific locations within the molecule differed depending on a ligand's symmetry, and how the density reconfigures upon oxidation.

To answer these questions, the researchers turned to the multiwavelength anomalous diffraction (MAD) synchrotron x-ray science technique at the ChemMatCARS 15-ID x-ray beamline at the APS. This method solves the phase problem by collecting x-ray diffraction data at dif-

< Fig. 1. Synthetic strategy to modify the cluster's external ligand field environment. Ligand substitution of L in the cluster type $[\text{Co}_6\text{Se}_8(\text{L})-(\text{PEt}_3)_5]^n$ for CO or P^nBu_3 produces an asymmetric or symmetric environment around the cluster core $[\text{Co}_6\text{Se}_8]$, respectively. From Sánchez et al., *Angew. Chem. Int. Ed.* **57**, 13815 (2018). Copyright © 1999-2018 John Wiley & Sons, Inc. All rights reserved

ferent wavelengths around the absorption K-edge of cobalt and selenium, and can report on the electron density at the individual atom-level within the cluster.

The data revealed that in the neutral, asymmetric cluster ($\text{L}=\text{CO}$), the cobalt that is attached to the CO moiety is more highly oxidized (less electron dense) than the other five cobalt atoms in the cluster. Upon oxidation, the selenium atoms get involved, collectively giving up electron density. The situation for the symmetric cluster ($\text{L}=\text{P}^n\text{Bu}_3$) looks different; in the neutral state, half the cobalt atoms have one electron distribution, while the other half have another. Upon oxidation, the electron hole is shared among the cobalt atoms (Fig. 1).

These results underscore the importance of ligand-dependent tuning of the electron distribution in compounds with metal centers. These findings can help to inform quantum mechanical calculations used to predict the reactivity of metal centers, perhaps improving prediction capabilities for complex metal centers. Future work will explore the effect of ligands and oxidation state in metal centers in a larger context: biological molecules.

— Erika Gebel Berg

See: Raúl Hernández Sánchez^{1*}, Anouck M.Champsaur¹, Bonnie Choi¹, Suyin Grass Wang², Wei Bu², Xavier Roy¹, Yu-Sheng Chen², Michael L. Steigerwald^{1**}, Colin Nuckolls^{1***}, and Daniel W. Paley^{1****}, "Electron Cartography in Clusters," *Angew. Chem. Int. Ed.* **57**, 13815 (2018). DOI: 10.1002/anie.201806426

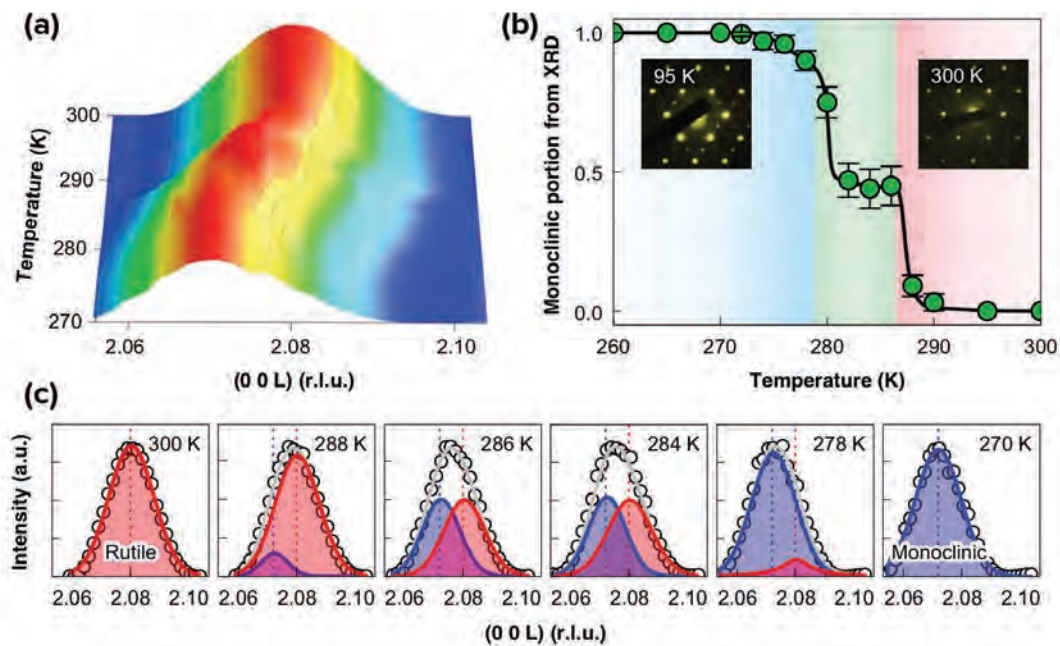
Author affiliations: ¹Columbia University, ²The University of Chicago

Correspondence: * raulha@pitt.edu, ** mls2064@columbia.edu, *** cn37@columbia.edu, **** dwp2111@columbia.edu

R.H.S. acknowledges the support from the Columbia Nano Initiative Postdoctoral Fellowship. B.C. acknowledges support by the National Science Foundation (NSF) Graduate Research Fellowship under Grant DGE 11-44155. C.N. thanks Sheldon and Dorothea Buckler for their generous support. ChemMatCARS is supported by the NSF under grant number NSF/CHE-1346572. Support for this research was provided by the Center for Precision Assembly of Superstratic and Superatomic Solids, a NSF MRSEC (award number DMR-1420634), and the Air Force Office of Scientific Research (award number FA9550-18-1-0020). The Columbia University Shared Materials Characterization Laboratory was used extensively for this research. We are grateful to Columbia University for support of this facility. This research used resources of the Advanced Photon Source, a U.S. Department of Energy (DOE) Office of Science User Facility operated for the DOE Office of Science by Argonne National Laboratory under Contract No. DE-AC02-06CH11357.

A Switch in Time

Electronic switches change an electrical circuit from one route to another. They are a key component of computerized devices, and the faster an electronic switch can change states from open to closed, the faster the computer. One possibility that could dramatically increase computing speeds is if a switch could be constructed from a single material that could open or close by quickly changing from an insulator, which blocks the flow of electricity, to a conductor that allows it. There are several materials known to do this, including vanadium oxide. But all of them must physically shift their atomic structure to do so. Waiting for the atoms to move takes time and slows the switching action. Researchers wondered if they could create a material that didn't have that lag time, i.e., a material that could switch from insulator to conductor instantaneously. Using a double layer of vanadium oxide and the powerful x-rays of the APS, they showed this was possible, and found hints of how they might engineer other types of materials to switch the same way.



Vanadium oxide, a compound of vanadium and oxygen, is a correlated insulator at room temperature but changes to a metal when heated. When it's a metal, the atoms are arranged in a regular pattern that lets electrons, and thus electric current, flow freely. When it's an insulator, the atoms are in a monoclinic structure, an arrangement of atoms that looks like rectangles but with a parallelogram at the base. No naturally occurring materials are known to conduct electricity when their atoms are in a monoclinic arrangement.

But sometimes materials behave differently when they are interfaced with a neighboring layer. Researchers from the University of Wisconsin-Madison, Sungkyunkwan University (Korea), Pennsylvania State University, the Korea Institute of Materials Science, Argonne, Dublin City University (Ireland), the University of Nebraska-Lincoln, and Boise State University suspected that if they created a double layer of vanadium oxide, with one layer monoclinic and the other metallic, one layer might become conductive while remaining monoclinic.

They could do this because the temperature at which vanadium oxide changes to a metal varies depending on the amount of oxygen in the material. The two layers had different amounts of oxygen and thus different transition temperatures. The researchers heated them until one layer transformed structurally to a metal, while the other stayed monoclinic. The team then performed x-ray diffraction on XSD beamline 6-ID-B at the APS. The APS high flux of x-rays allowed for very-high-resolution x-ray diffraction (XRD) images that precisely delineated the atomic structure of both layers of vanadium oxide (Fig. 1). This x-ray beamline could also go below room temperature to get even higher resolution data.

The x-ray diffraction confirmed what the researchers had suspected: the monoclinic layer of vanadium oxide remained monoclinic even as it conducted electricity.

Other groups have managed to drive insulating mate-

rials into a conductive state, but those materials lost their properties almost instantly. The vanadium oxide material, on the other hand, is stable. The key to the approach is the suppression of electronic correlation in the ultrathin dual-layer stack interacting with each other, the researchers say. The two layers are thin enough that the interface between them dominated their behavior.

This interface behavior might be a clue to designing other materials with unusual structures and functions. The next step in this research is to study the crystal's electronic properties independent of the underlying lattice structure of its atoms. The charge, spin, and orbital degrees of freedom of the lattice are strongly coupled in materials like vanadium oxide, and in the past it has been difficult to analyze them and their effects on material properties separately from one another. But the bilayer structural advance illustrated by this research done at the APS has made this possible. Understanding this new, purely electronic transition will likely lead to similar advances in other materials systems. — Kim Krieger

See: D. Lee¹, B. Chung², Y. Shi³, G.-Y. Kim^{4*}, N. Campbell¹, F. Xue³, K. Song⁴, S.-Y. Choi^{4†}, J.P. Podkaminer¹, T.H. Kim¹, P.J. Ryan^{5,6}, J.-W. Kim⁵, T.R. Paudel⁷, J.-H. Kang¹, J.W. Spinuzzi⁸, D.A. Tenne⁸, E.Y. Tsybal⁷, M.S. Rzchowski⁵, L.Q. Chen³, J. Lee^{2**}, and C.B. Eom^{1*}, "Isostructural metal-insulator transition in VO₂," *Science* **362**, 1037 (30 November 2018). DOI: 10.1126/science.aam9189

Author affiliations: ¹University of Wisconsin-Madison, ²Sungkyunkwan University, ³Pennsylvania State University, ⁴Korea Institute of Materials Science, ⁵Argonne National Laboratory, ⁶Dublin City University, ⁷University of Nebraska-Lincoln, ⁸Boise State University †Present address: POSTECH
Correspondence: * eom@engr.wisc.edu, ** jclee@skku.edu

Supported by the National Science Foundation (NSF) under DMREF grant DMR-1629270, AFOSR grant FA9550-15-1-0334, and Office of Naval Research N00014-13-1-0183. Transport measurement at the University of Wisconsin-Madison was supported by the U.S. Department of Energy (DOE) Office of Science-Basic Energy Sciences under award DE-FG02-06ER46327. The work at Sungkyunkwan University was supported by National Research Foundation of Korea through the Basic Research Program (2009-0092809) and KISTI supercomputing center (KSC-2015-C3-067). The work at Penn State is also partially supported by the NSF MRSEC under grant DMR-1420620 (Y.S.). S.Y.C. and G.Y.K. acknowledge the support by the Global Frontier Hybrid Interface Materials of the NRF funded by the Korea Government (2013M3A6B1078872). K.S. acknowledges the Fundamental Research Program of the Korean Institute of Materials Science (PNK5570). The research at the University of Nebraska-Lincoln is supported by NSF through the Nebraska Materials Science and Engineering Center (MRSEC grant DMR-1420645). This research used resources of the Advanced Photon Source, a U.S. DOE Office of Science User Facility operated for the DOE Office of Science by Argonne National Laboratory under Contract DE-AC02-06CH11357.

< Fig. 1. (a) X-ray diffraction scans of the vanadium oxide bilayer, measured on cooling. (b) Relative monoclinic portion as a function of temperature, estimated from XRD peak analysis shown at upper right. Insets show the measured electron diffraction patterns of the bilayer at low and high temperatures. (c) Representative XRD peaks at several temperatures. Experimental data (open circles) are fitted using Gaussian curves (solid lines). Adapted from D. Lee et al., *Science* **362**, 1037 (30 November 2018). © 2018 American Association for the Advancement of Science. All rights reserved.

Sun Block: Protecting Electronics from Cosmic Rays

Solar and galactic cosmic rays pose a constant threat to electronic devices in space. A high-energy particle streaking through a device can ionize the transistors inside, causing transient or permanent malfunctions. Earth's atmosphere blocks most of these rays, but satellites and airplanes are always vulnerable. Occasionally a ray gets through the upper atmosphere, strikes another atom and causes a shower of rays that can damage electronics even at ground level. To better understand which parts of a device are most vulnerable and how to best defend them, international teams of researchers used the APS to expose defined sections of electronic devices to exact doses of high-energy x-rays. By identifying which parts of the circuits were affected – and how – researchers will be able to engineer satellite and airplane electronics to render them less vulnerable to damage from high-energy radiation.

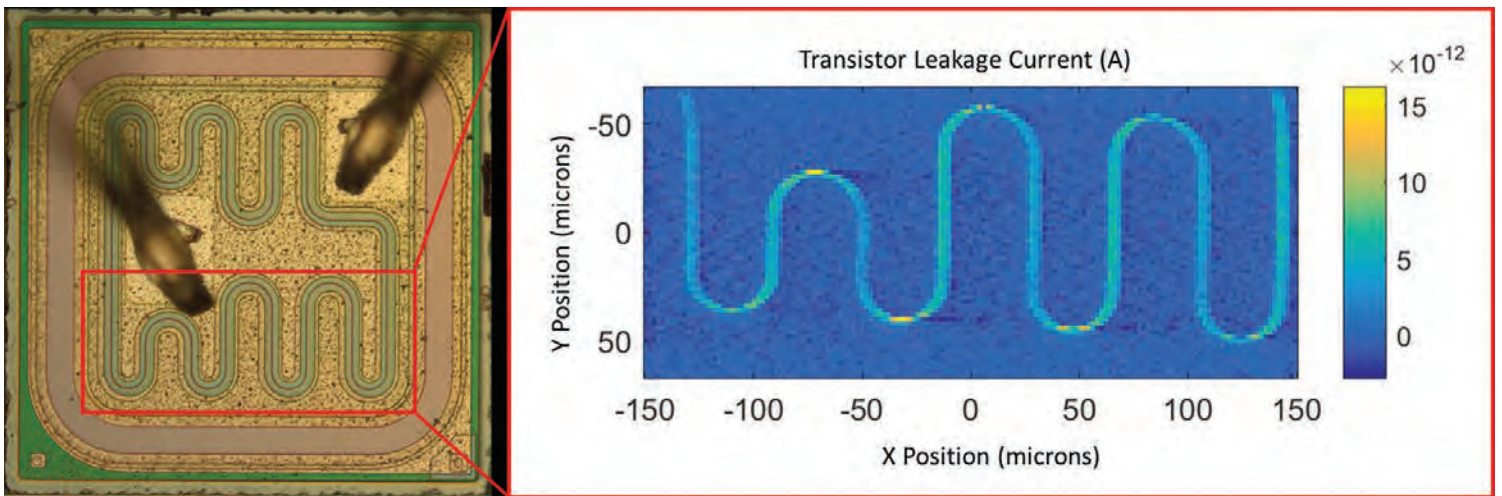


Fig. 1. The change in transistor leakage current as a function of where the total dose occurs. The region most sensitive to the total ionizing dose is the base-emitter junction. The transistor was scanned with a 1.5- μm -diameter x-ray spot at 10 keV and the raster scan was performed with 1.5- μm steps. The total dose was approximately 200 krad(Si) per point.

Conventional testing to evaluate electronics' vulnerability to cosmic rays puts a whole device into a broad radiation beam and irradiates it. This gives good information on how a device could malfunction or fail overall when exposed, but it does not reveal precisely which individual elements are vulnerable, nor how they malfunction when hit by a cosmic ray. When an energetic particle such as a heavy ion passes through an integrated circuit, it generates a dense track of charge. If that charge is near a sensitive node in a circuit, it can generally have several effects. Since transistors interact, a single effect can propagate throughout a circuit board and cause all sorts of errors: a satellite could suddenly turn to point in the wrong direction, or a circuit might malfunction so severely that it must be turned off and restarted. Using broad beams of energetic particles from a cyclotron (the gold-standard used to test for these effects) it is often impossible to isolate exactly where a failure occurred.

To get more precise information about how electronic components are susceptible to cosmic ray effects, two teams of researchers used the XSD 20-ID-B x-ray beamline at the APS to irradiate specific regions inside devices to look for these failures and observe exactly what happened (Fig. 1.)

First, one team proved they could track localized effects in semiconductor electronic components [1]. Then, a second team investigated the origins of single-event effects in random-access memory (RAM) devices [2]. (Single-event effects are what happen when a single cosmic ray hits an electronic device.)

The teams chose the 20-ID-B beamline because the high flux of the APS can approximate the interactions of high-energy cosmic rays, and the staff scientists at this beamline are highly skilled and were able to help design the experiments and focus the APS x-ray beam down to a tiny 1- μm spot size, which is very useful when performing precise irradiations of specific regions of an integrated circuit.

Different regions of an FRAM component were scanned with the tiny, tightly-focused, high-flux beam from 20-ID-B. The results showed that when the beam passed only through the FRAM cells, no errors were observed; the rays could not affect the polarization of the cells' ferroelectric capacitors, which store the data.

But in addition to ferroelectric capacitors, which are used to store the data, FRAMs also rely on conventional semiconductor circuits to implement the read-write func-

tions. When these circuits were hit by radiation, the results were potentially serious, corrupting entire lines and sections of memory in the FRAM.

To effectively protect a device against cosmic rays, engineers need to know exactly which circuits were hit, and how they reacted. So the next step is to generate physical maps of where the x-ray single-event effects occur, locate the specific vulnerable transistors, nodes, and circuits, and then develop ways to harden them against these effects.

Because this work is so unconventional, and the scientists at APS were so helpful, these researchers and the APS are exploring ways of deepening this collaboration.

— Kim Krieger

[1] See: Stephen D. LaLumondiere^{1*}, Erik C. Dillingham¹, Adam C. Scofield¹, Jeremy P. Bonsall¹, Petras Karuza¹, Dale L. Brewé², Ronald D. Schrimpf³, Andrew L. Sternberg³, Nathan P. Wells¹, David M. Cardoza¹, William T. Lotshaw¹, and Steven C. Moss¹, "Application of a Focused, Pulsed X-ray Beam for Total Ionizing Dose Testing of Bipolar Linear Integrated Circuits," IEEE Trans. Nucl. Sci. **65**(1), 478 (January 2018).

DOI: 10.1109/TNS.2017.2780827

Author affiliations: ¹The Aerospace Corporation, ²Argonne National Laboratory, ³Vanderbilt University

Correspondence: * stephen.lalumondiere@aero.org

This research used resources of the Advanced Photon Source, a U.S. Department of Energy (DOE) Office of Science User Facility operated for the DOE Office of Science by Argonne National Laboratory under Contract No. DE-AC02-06CH11357. This work was performed as part of The Aerospace Corporation's Independent Research and Development Program.

[2] See: A.L. Bosser^{1,2,*}, V. Gupta^{2,3,##}, A. Javanainen^{1,4}, G. Tsiligianis⁵, S. D. LaLumondiere⁶, D. Brewé⁷, V. Ferlet-Cavrois⁸, H. Puchner⁹, H. Kettunen¹, T. Gil², F. Wrobel¹⁰, F. Saigné¹⁰, A. Virtanen¹, and L. Dilillo², "Single-Event Effects in the Peripheral Circuitry of a Commercial Ferroelectric Random Access Memory," IEEE Trans. Nucl. Sci. **65**(80), 1708 (August 2018).

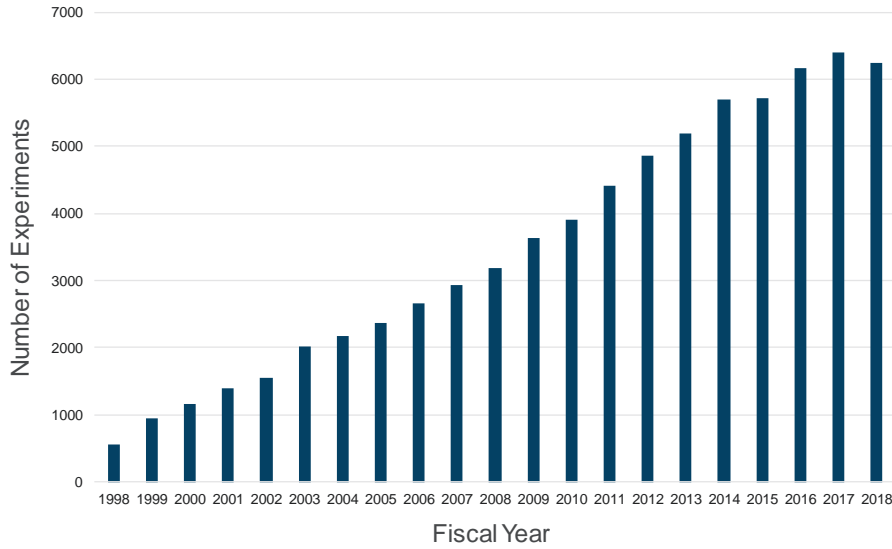
DOI: 10.1109/TNS.2018.2797543

Author affiliations: ¹University of Jyväskylä, ²LIRMM, University of Montpellier/CNRS, ³Jet Propulsion Laboratory, ⁴Vanderbilt University, ⁵CERN, ⁶The Aerospace Corporation, ⁷Argonne National Laboratory, ⁸ESA/ESTEC, ⁹Cypress Semiconductor, ¹⁰Institut d'Électronique du Sud Present addresses: [†]Aalto University, ^{##}Redu Space Services

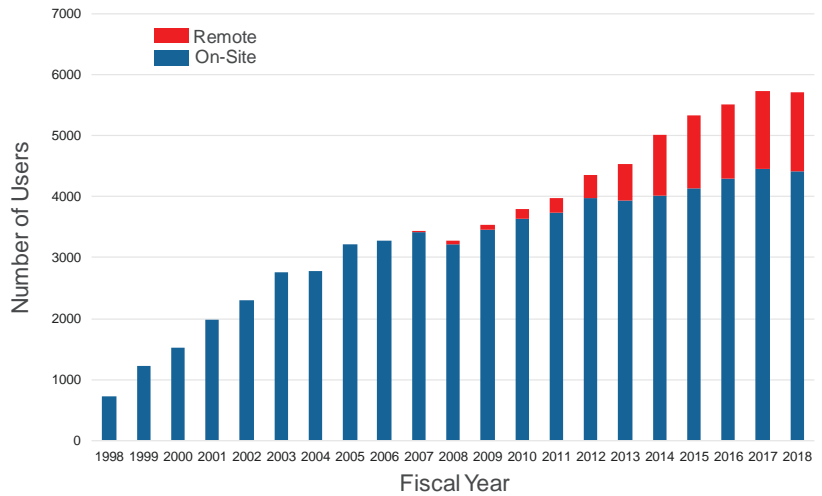
Correspondence: * alexandre.bosser@aalto.fi

This research used resources of the Advanced Photon Source, a U.S. DOE Office of Science User Facility operated for the DOE Office of Science by Argonne National Laboratory under Contract No. DE-AC02-06CH11357. This work was performed as part of The Aerospace Corporation's Independent Research and Development Program.

NUMBER OF APS EXPERIMENTS (FY1998-2018)

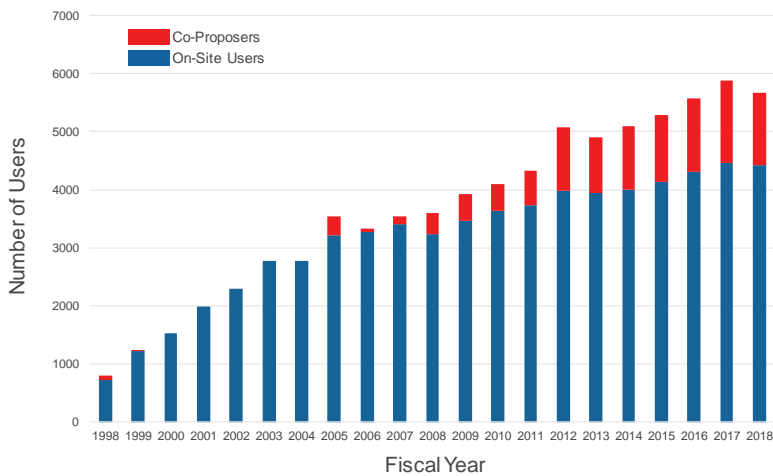


APS ON-SITE AND REMOTE USERS (FY 1998-2018)



Note: Prior to FY14, mail-in users were not included in the Remote category

ON-SITE APS USERS & CO-PROPOSERS (FY 1998-2018)

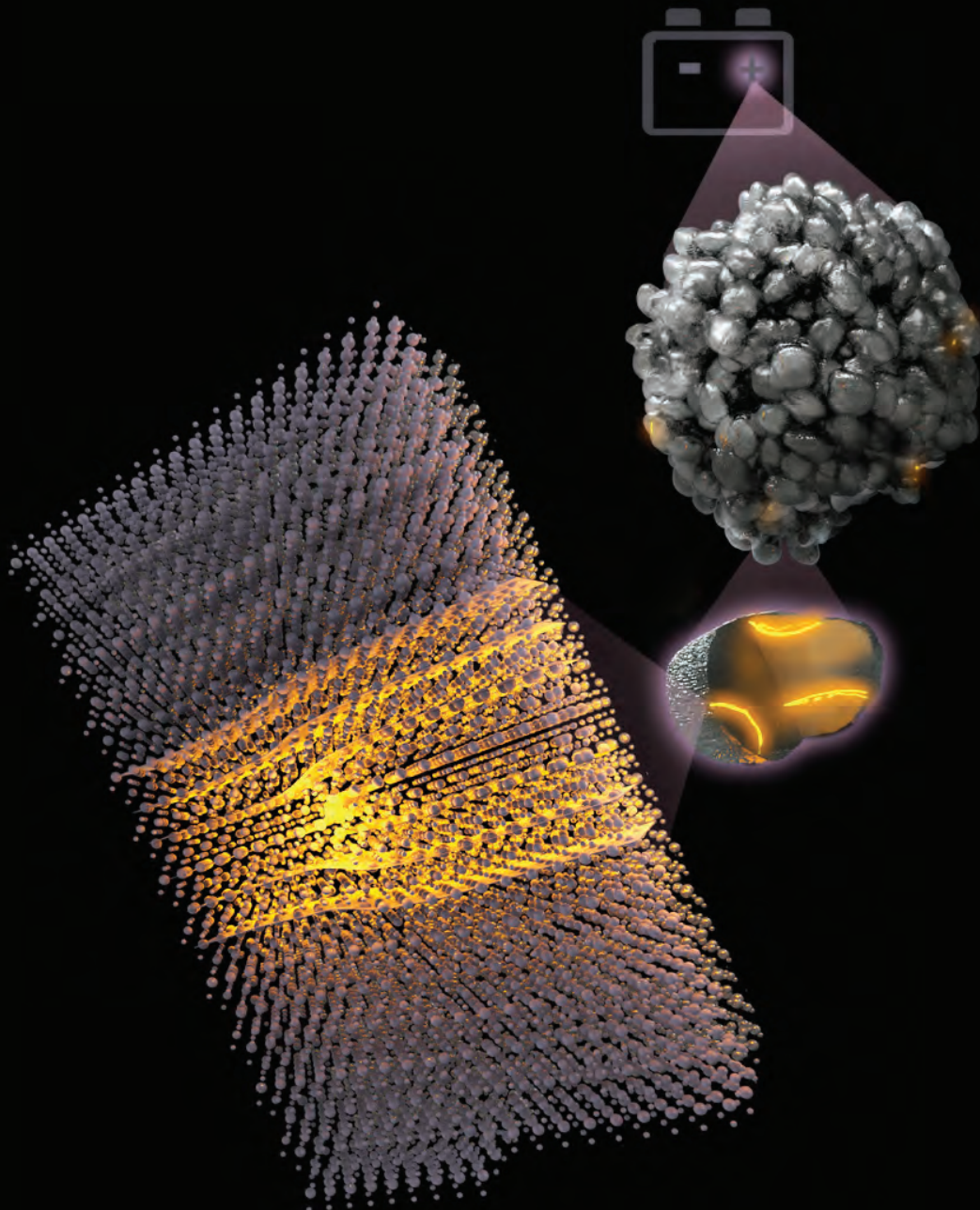




ENGINEERING MATERIALS & APPLICATIONS

Formation of Dislocations Damages Lithium-Rich Cathode Performance

In the search for better rechargeable batteries, a new class of lithium-rich layered oxides (LRLOs) shows great promise. Batteries with cathodes made of this material can store 50% more energy per unit weight than conventional lithium-based storage systems, an enormous advantage for cars and portable electronics. In practice, however, these novel batteries suffer from voltage fade: after repeated charge-discharge cycles, the voltage they can sustain and the energy they can store fall dramatically. Working at the APS, researchers performed x-ray diffraction studies of a lithium-rich layered oxide nanoparticle while it was charging, and found that numerous dislocations disrupted the crystal structure. The researchers demonstrated that they could reverse this damage and restore the material's electrical performance, but their method is not practical for realistic battery uses, and it is likely that modification of the crystal structure will be required to realize the full advantages of these materials.



The LRLOs consist of LiMO₂ layers, where M is nickel, manganese, or cobalt, interleaved with Li₂MO₃ layers. The charging process removes lithium ions from the structure, while discharging restores them. The high storage capacity of LRLO cathodes — better than 300 milliampere-hours per gram — has been attributed to the ease with which lithium ions can come and go from the open crystal structure. However, this openness goes hand-in-hand with a lack of robustness, suggesting that the charge-discharge cycle damages the material in ways that inhibit lithium mobility.

A typical battery cathode consists of particles 300 to 400 nm across pressed together to make a packed powder. The research team from the University of California, San Diego, the Chinese Academy of Sciences, Argonne, and the Deutsches Elektronen-Synchrotron (DESY, Germany) first performed three charge-discharge cycles to 4.1 V in order to stabilize the material and improve its electrochemical response. Cycling to this voltage is fully reversible. They then took a single grain of the material and used Bragg coherent diffraction imaging at XSD x-ray beamline 34-ID-C at the APS to discern changes to its structure as it was being charged.

The team observed that as the charged voltage rose to 4.2 V, the x-ray imaging revealed little change, but above 4.3 V, dislocations in the structure began to appear, becoming more abundant as the voltage rose further and eventually, at 4.4 V, forming a complex dislocation network (Fig. 1). The dislocations had the effect of breaking the structure in the plane of the layers in such a way that a half-layer interposed itself. At the same time, the lithium diffusion length fell dramatically, to 1/10 or less of the nanoparticle size.

The diffraction studies also allowed the researchers to infer the strain field from the distortion of the LRLO structure. They found that the strain was greatest in regions of the grain where lithium loss was most dramatic. This suggests that the dislocations result from the lattice trying to accommodate the change in lattice volume accompanying the departure of lithium ions.

For comparison, the researchers made a similar analysis of a particle of a conventional lithium-containing cathode at the PETRA III light source at DESY. One sample showed a dislocation appearing at 4.2 V, but no more

< Fig. 1. The lithium-rich layered oxide cathode of a rechargeable battery (top right) consists of packed nanoparticles. X-ray diffraction study of a single particle in the process of charging reveals that its structure is altered by dislocations, leading to voltage fade and loss of capacity on repeated cycling.

at higher voltages, and another sample was taken up to 4.8 V with not a single dislocation evident.

Although the exact mechanism by which the dislocation network causes the degradation of electrical performance in LRLO is hard to pin down, the research team found that annealing the grain at a temperature of about 150° C healed the lattice and also restored its pristine cathode properties.

The study suggests that modifications to LRLO materials to give them a more robust lattice might solve the voltage fade problem, but the researchers say that this approach has its pitfalls. It is the openness and, to some extent, fragility of the LRLO lattice that makes it unusually easy for lithium ions to move in and out. A more rigid lattice might fare better in the charge/discharge cycle, but might also have poorer electrical performance for the same reason. Even so, the study points the way to turning LRLO into a cathode material that surpasses current devices. — David Lindley

See: A. Singer^{1‡}, M. Zhang¹, S. Hu¹, D. Cela¹, C. Fang¹, T.A. Wynn¹, B. Qiu², Y. Xia², Z. Liu², A. Ulvestad³, N. Hua¹, J. Wingert¹, H. Liu¹, M. Sprung⁴, A.V. Zozulya^{4‡‡}, E. Moxey³, R. Harder³, Y.S. Meng^{1*}, and O.G. Shpyrko^{1**}, “Nucleation of dislocations and their dynamics in layered oxide cathode materials during battery charging,” *Nat. Energy* **3**, 641 (August 2018).

DOI: 10.1038/s41560-018-0184-2

Author affiliations: ¹University of California, San Diego, ²Chinese Academy of Sciences, ³Argonne National Laboratory, ⁴Deutsches Elektronen-Synchrotron (DESY) Present addresses: [‡]Cornell University, ^{‡‡}European XFEL GmbH

Correspondence: * shirleymeng@ucsd.edu,

** oshpyrko@physics.ucsd.edu

We acknowledge K. Wiaderek for providing the potentiostat during the measurements at the APS and H. Liu and K. Chapman for collecting the *ex situ* powder diffraction data on the NCA material. The x-ray imaging was supported by the U.S. Department of Energy (DOE) Office of Science-Basic Energy Sciences, under contract DE-SC0001805 (A.S., D.C., J.W., N.H., and O.G.S.). S.H., C.F., M.Z., H.L., and Y.S.M. acknowledge support on the materials synthesis, electrochemical, and materials characterization from the NorthEast Center for Chemical Energy Storage, an Energy Frontier Research Center funded by the U.S. DOE Office of Science-Basic Energy Sciences under Award no. DE-SC0012583. The sample exchanges and collaborations between UCSD and NIMTE are made possible with the support from Office of Vehicle Technology of the U.S. DOE under the Advanced Battery Materials Research Program. We thank the staff at Argonne National Laboratory and the Advanced Photon Source for their support. Parts of this research were carried out at the light source PETRA III at DESY, a member of the Helmholtz Association. This research used resources of the Advanced Photon Source, a U.S. DOE Office of Science User Facility operated for the DOE Office of Science by Argonne National Laboratory under contract no. DE-AC02-06CH11357.

A Better Look Inside a Promising Battery Material

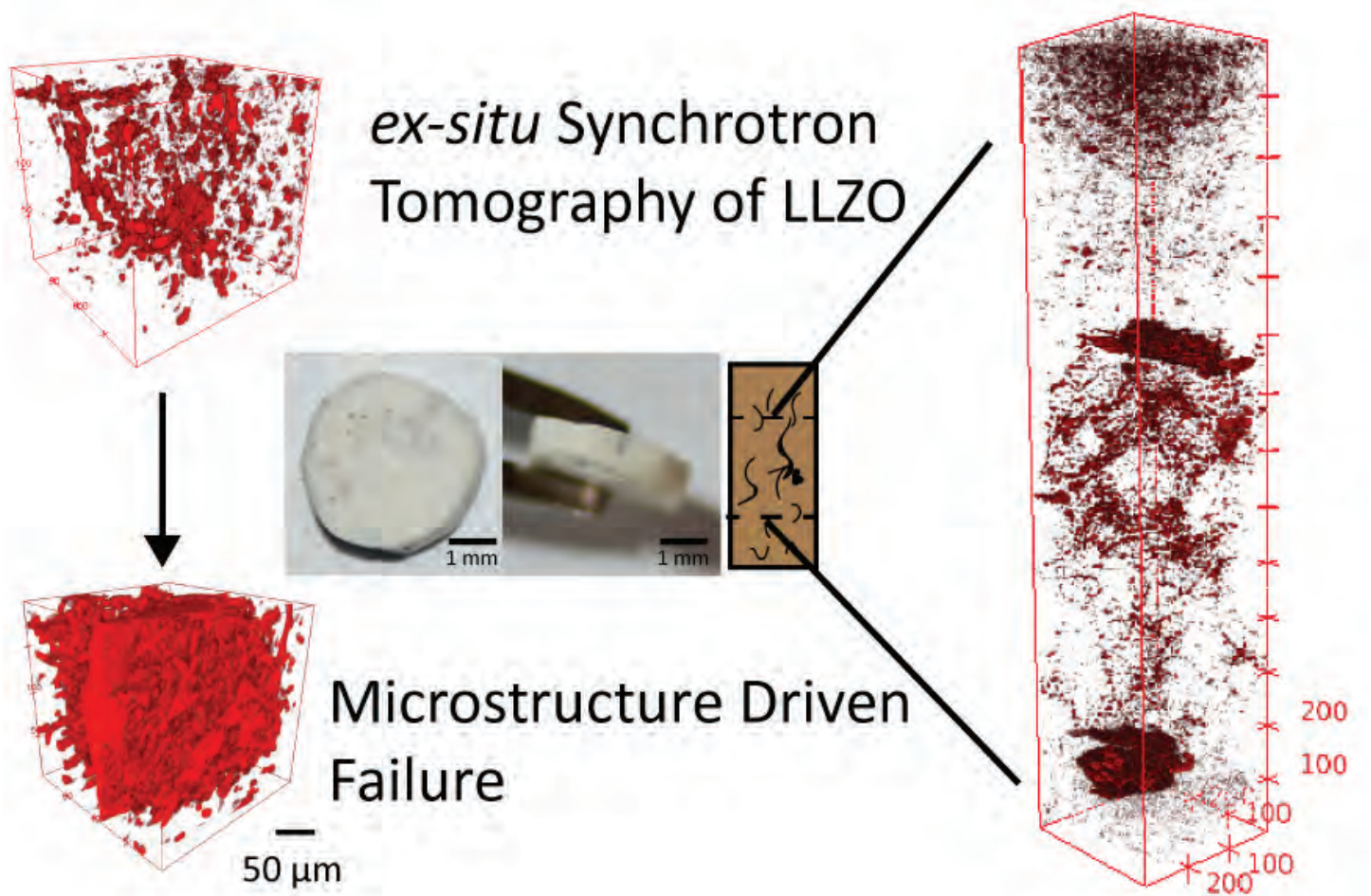


Fig. 1. Left: the dark red regions show areas transparent to x-ray radiation; cracks and lithium deposition. The top shows the pristine LLZO, the bottom the LLZO after cycling until battery failure. Right: a cross section of the LLZO cycled to failure. The large blots indicate areas of lithium plating. From F. Shen et al., ACS Energy Lett. **3**, 1056 (2018). ©2018 American Chemical Society

Solid-state batteries are safer, potentially less explosive, and can have greater energy storage capacity and longer lifetimes than batteries with liquid electrolytes. Lithium lanthanum zirconate (LLZO) is a particularly promising material for solid-state batteries due to its high lithium ion conductivity, but it has a serious drawback: it tends to short circuit at low current densities. What's worse, the short circuiting escalates as the material ages and experiences multiple discharge-recharge cycles. Researchers suspect that lithium dendrites are to blame. These treelike branches of metal grow through pores in the ceramic material and could be damaging the electrolyte and prematurely ending its usable life. But there has been no established way to see inside solid-state batteries while they operate. To investigate, a team of researchers used the high energy x-rays at the APS, where the unique characteristics of the APS x-rays showed that the apparent “open spaces” in the material – either pores and cracks, or lithium dendrites – grew as the batteries cycled.

LLZO is a ceramic material compatible with lithium metal that has potential as an electrolyte, the substance that produces carriers of electric charge in a battery. Researchers from Vanderbilt University wanted to understand how the microstructure of LLZO (the size and shape of the grains, the pore sizes between the grains, and the atomic arrangement) affected the material's tendency to fail. They also wanted to understand whether and how lithium dendrites grew through the material.

They took a LLZO battery and cycled it over and over, charging and discharging it until it failed. While they did that, they and a colleague from Argonne took three-dimensional tomographic images of the microstructure inside the battery using the XSD 2-BM x-ray beamline at the APS. This beamline is tuned for microtomography, meaning it can map out interior structures on the scale of 0.5 μm to 1 mm in size. That resolution was perfect for this application, allowing the researchers to capture the interior structure and changes throughout entire LLZO sample. Another reason the researchers chose the APS was because the x-rays are high-energy, around 40 keV. LLZO contains zirconium, a heavy element that would just block the lower-energy x-ray beams available at many other synchrotron facilities. The high-energy x-rays at the APS allowed the researchers to see the position of the zirconium atoms. The x-rays were so high energy they tended not to interact with the lithium ions and metal in the sample, so pores, cracks, and dendrites all appeared as open space in the images.

Indeed, the researchers were able to image the entire sample and characterize the entire pore structure of the dense ceramic. This is one of the first times this has ever been done for this type of material. They used the technique to similarly characterize a pristine sample of LLZO and compared the two.

They found that they could indirectly track lithium plating in the electrolyte after failure (Fig. 1). One of the unexpected features they saw were clues suggesting that lithium may plate in an isolated manner in the solid electrolyte. That plating could only happen if there was electrical conduction in the LLZO — but it's not supposed to be electrically conducting; the ceramic is supposed to be electrically insulating. Another possibility is that strain in the material could induce strong localized electric fields at the boundaries between grains, and these localized fields could also cause local lithium deposition.

If there really is electrical conductivity in the interior of LLZO batteries, that should play a significant role in the battery performance. The researchers hope to better characterize the apparent lithium plating and electrical conductivity, learn what causes it, and whether it can be tuned or eliminated.

The next steps in this research will explore techniques to understand more specifically how the shape of the pores and grain interfaces affect battery operation, and how to improve the contact between the battery electrodes and the LLZO electrolyte. — Kim Krieger

See: Fengyu Shen¹, Marm B. Dixit¹, Xianghui Xiao², and Kelsey B. Hatzell^{1*}, “Effect of Pore Connectivity on Li Dendrite Propagation within LLZO Electrolytes Observed with Synchrotron X-ray Tomography,” *ACS Energy Lett.* **3**, 1056 (2018). DOI: 10.1021/acsenerylett.8b00249

Author affiliations: ¹Vanderbilt University, ²Argonne National Laboratory

Correspondence: * Kelsey.B.Hatzell@vanderbilt.edu

K.B.H and M.D. were supported by the National Science Foundation under Grant No. 1727863. F.S. acknowledges support from Vanderbilt School of Engineering Start-Up Grants. The authors acknowledge the Vanderbilt Institute of Nanoscience and Engineering (VINSE) for access to their shared characterization facilities. This research used resources of the Advanced Photon Source, a U.S. Department of Energy (DOE) Office of Science User Facility operated for the DOE Office of Science by Argonne National Laboratory under Contract No. DE-AC02-06CH11357.

Understanding Why Nanoporous Silicon-Battery Anodes Fail

One way researchers are trying to improve lithium-ion batteries is by coming up with better materials for the anodes, and silicon is one of the candidates. Silicon has a theoretical capacity almost 10 times that of carbon, a commonly used anode material, and so could be utilized to create batteries that last much longer between charges. Unfortunately, silicon anodes degrade quickly during cycling. Now, researchers using the APS have uncovered the cause of the failure.

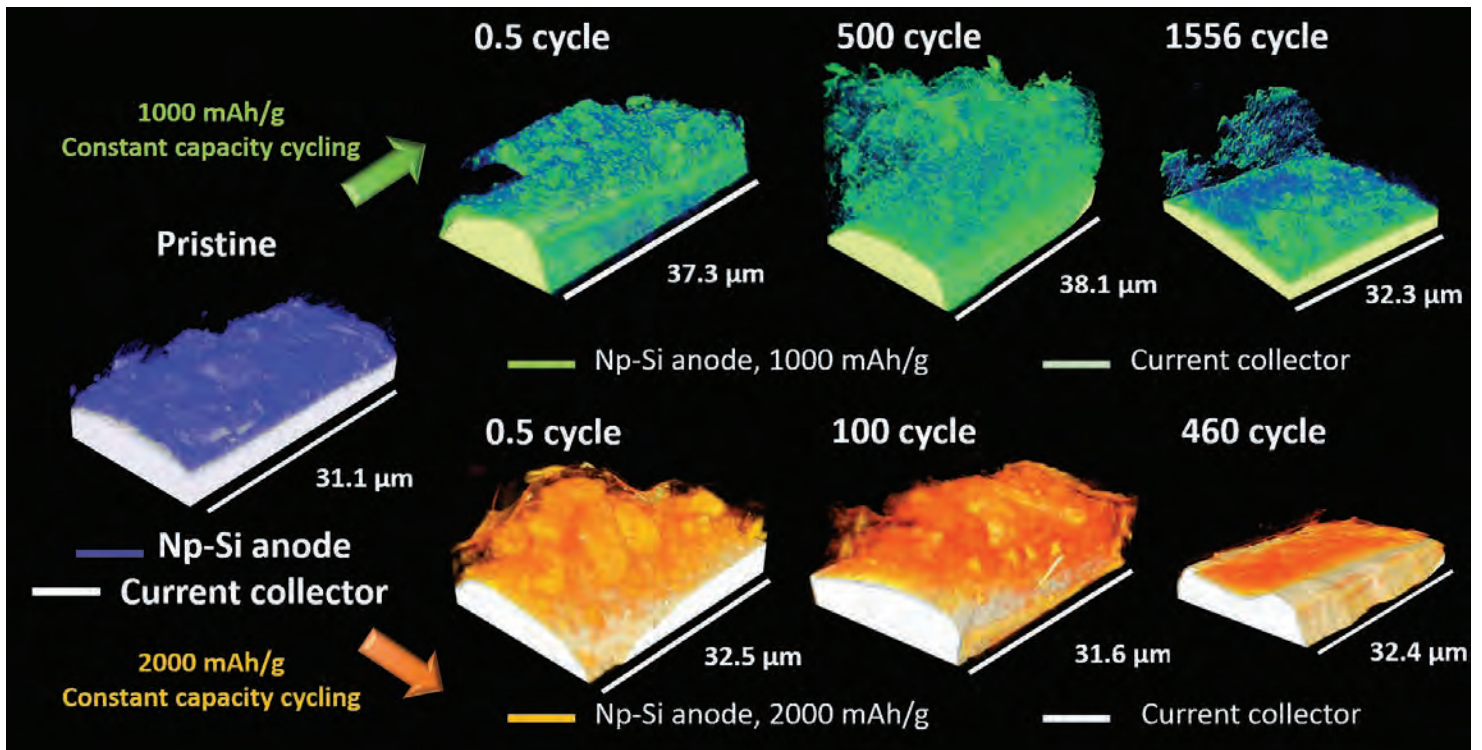


Fig. 1. An x-ray tomography reconstruction of a nanoporous silicon anode shows how its structure changes from the pristine state (blue) with more discharge-recharge cycles. At 1000 mAh/g (green), the anode expands, then loses material, over 1500 cycles. At 2000 mAh/g (orange), it loses most of its material by 460 cycles. From C. Zhao et al., *Nano Energy* **52**, 381 (2018). © 2018 Published by Elsevier Ltd.

As a battery discharges, lithium enters the silicon anode, causing it to swell up to four times its original size, then shrink again as the lithium departs during recharging. Eventually, the stress from swelling and shrinkage causes the anodes to crack. Researchers hoped that silicon full of nanoscopic pores would have enough empty space to accommodate the volume expansion, but the result was less than expected. During cycling at a rate of 1000 mAh/g, the anode was able to handle more than 1500 cycles without losing performance. But at 2000 mAh/g, performance started to degrade after roughly 460 discharge-charge cycles.

To build their anodes, the researchers in this study, from Stony Brook University, Tohoku University (Japan), Argonne, Northwestern University, and Brookhaven National Laboratory, started with an alloy of silicon and magnesium, which they immersed in molten bismuth. The bismuth dissolved the magnesium selectively, which separated from the silicon. Nitric acid was then used to etch away the bismuth and magnesium phase together, leaving behind silicon particles studded with nanopores. The researchers used the nanoporous silicon to make coin cell batteries, which they cycled different numbers of times at different capacity levels to see how the anodes would look under different conditions.

They then took their cycled battery electrodes — encapsulated in polymer tubes to protect them from air and humidity — to the XSD transmission x-ray microscopy beamline 32-ID-C at APS, where they performed x-ray nanotomography, which allowed them to reconstruct the shape of the anodes in three dimensions. In addition to the beamline itself, the APS provided software and expertise to help with the reconstruction and analysis of the data.

For the 1000-mAh/g cycling, the thickness of the anode increased after the second lithiation — the movement of lithium into the anode. At 500 cycles, the electrode expanded by more than eight times but performance did not degrade. After 1556 cycles, the thickness dropped significantly and some, but not all, of the silicon had separated from the current-collector underneath. In the 2000-mAh/g cycling, the anode changed much more after the first lithiation than the other had after the second lithiation. By 460 cycles, the battery lost most of its active material,

with only a thin electrode remaining on the current collector (Fig. 1).

It turned out that at the higher cycling capacity, some of the nanoporous silicon particles started to merge together into larger clumps, blocking the movement of lithium ions and reducing the battery capacity. Additionally, other materials in the battery — polymer binders that hold components in place and carbon that increases the conductivity — could also swell along with the silicon, actively involved in the structural evolution of electrode during battery cycling.

This work shows that it is important to pay attention not just to the design of the nanoscale materials in a new battery electrode, but also to the design of its interface with other components in the battery, the researchers say. They plan to explore batteries and other applications with nanoporous structures made from different elements, including metals. — Neil Savage

See: Chonghang Zhao¹, Takeshi Wada², Vincent De Andrade³, Doğa Gürsoy^{3,4}, Hidemi Kato², and Yu-chen Karen Chen-Wiegart^{1,5*}, “Imaging of 3D morphological evolution of nanoporous silicon anode in lithium ion battery by X-ray nano-tomography,” *Nano Energy* **52**, 381 (2018). DOI: 10.1016/j.nanoen.2018.08.009
Author affiliations: ¹Stony Brook University, ²Tohoku University, ³Argonne National Laboratory, ⁴Northwestern University, ⁵Brookhaven National Laboratory
Correspondence: * Karen.Chen-Wiegart@stonybrook.edu

K. Chen-Wiegart and C. Zhao acknowledge the support of J. Thieme and G. Williams at NSLS-II, and the financial support by the Department of Materials Science and Chemical Engineering, the College of Engineering and Applied Sciences, and the Stony Brook University, as well as by the Brookhaven National Laboratory under Contract No. DE-SC0012704. H.K and T.W. acknowledge the financial support by Creation of Life Innovation Materials for Interdisciplinary and International Researcher Development, Tohoku University. Portions of this work — the use of the Ar-filled glovebox at APS — were performed at the laboratory of HP-CAT. HP-CAT operations are supported by the U.S. Department of Energy (DOE)-National Nuclear Security Administration under Award No. DE-NA0001974, with partial instrumentation funding by the National Science Foundation. The authors also would like to acknowledge the great support and efforts provided by the HP-CAT staff scientists - Curtis Kenney-Benson and Jesse Smith. This research used resources of the National Synchrotron Light Source II, a U.S. DOE Office of Science User Facility operated for the DOE Office of Science by Brookhaven National Laboratory under Contract No. DE-SC0012704. This research used resources of the Advanced Photon Source, a U.S. DOE Office of Science User Facility operated for the DOE Office of Science by Argonne National Laboratory under Contract DE-AC02-06CH11357.

Distortions Present New Directions for Quantum Devices

Devices that harness quantum electronic phenomena are at the forefront in the development of new information technologies. One approach to realizing these devices involves multilayered semiconductor crystals featuring quantum dots, which are thin nanoscale regions within crystals where quantum-mechanical phenomena can be used to control the behavior of individual electrons. Synthesizing such multilayered devices invariably involves the introduction of mechanical stress, which can adversely affect the structure and location of quantum dots. These stress effects can be quite complex and present a major challenge to successful development of robust quantum semiconductor devices. To address these issues, researchers carried out x-ray nano-diffraction experiments at the APS to reveal the variety of stresses that arise within semiconductor quantum dots. The resulting x-ray data were interpreted by developing a modeling technique using the dynamical theory of x-ray diffraction. The results of these methods will help materials scientists achieve greater control over quantum dots in multilayered semiconductors. It is anticipated that this improved control will significantly aid the emergent field of quantum electronics, which encompasses a variety of devices for quantum computing and other emerging information technologies.

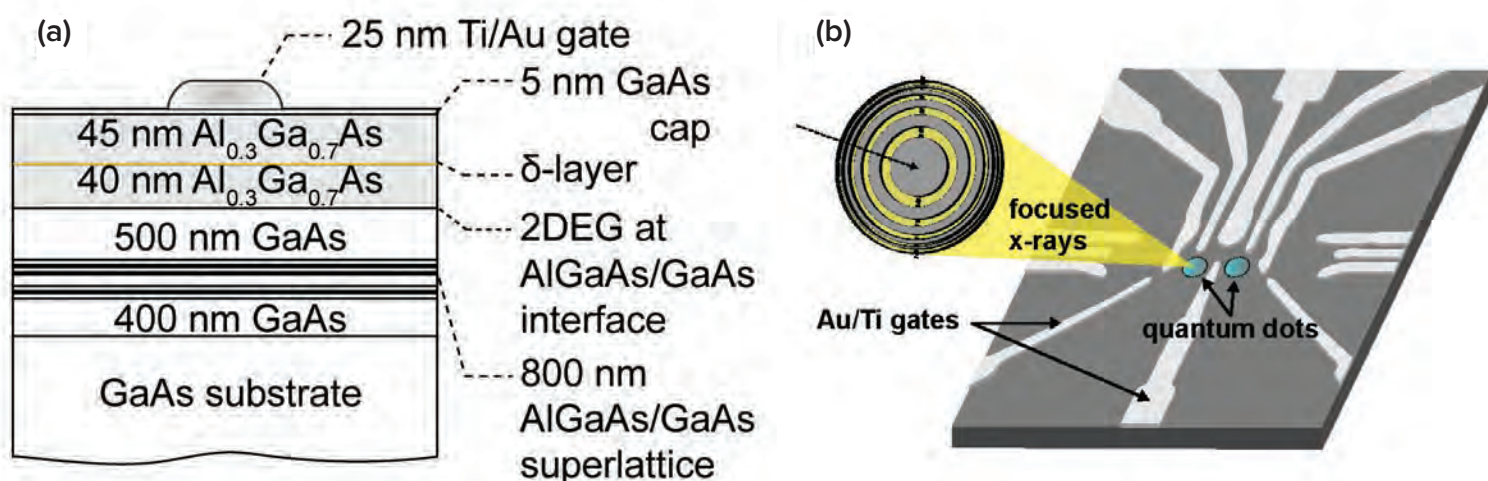


Fig. 1. Left-hand side (a) depicts the multilayered semiconductor, commonly referred to as a heterostructure. Thicknesses of the crystalline gallium arsenide (GaAs) and aluminum gallium arsenide (AlGaAs) layers appear in nanometers (nm). The depth beneath the surface where the two-dimensional electron gas (2DEG) is located is also indicated. A metallic gold/titanium (Au/Ti) electrode is situated on top. Panel (b) indicates the basic experimental setup. An x-ray beam is used to probe the quantum dots present within the heterostructure. Voltages supplied by the electrodes/gates (assorted white lines) produce and control the quantum dots. Figures from A. Pateras et al., *Nano Lett.* **18**, 2780 (2018). © 2018 American Chemical Society

The quantum device examined for this research by a team from the University of Wisconsin-Madison, Argonne, ETH Zürich (Switzerland), and Delft University of Technology (The Netherlands) consisted of multiple thin layers of single-crystalline gallium arsenide (GaAs) and aluminum gallium arsenide (AlGaAs). A two-dimensional electron gas (2DEG) forms at the interface where the two different semiconductor materials meet. Practical devices normally exploit 2DEG interfaces for transport and manipulation of electrons under conditions in which the electrons can propagate for long distances without scattering from other electrons or impurities. These conditions also allow electrons to persist in a precisely prepared quantum state for times sufficiently long to control them with electrical signals. The schematic in Fig. 1(a) shows the distinct layers of GaAs and AlGaAs that formed the multilayered semiconductor (heterostructure) and the location of the 2DEG interface.

External voltages can be used to manipulate the quantum behavior of electrons at a 2DEG interface. In operating devices, quantum dots are formed by selecting the voltages applied to the fine metal electrodes on the surface. The electronic properties of the quantum dots were influenced by the stresses and strains within the heterostructure. Characterizing these internal forces, and how they affected the quantum dots, was the overriding aim of this research.

Strain can occur unintentionally, stemming from dislocations or imperfections inside a heterostructure. It can also be caused during fabrication, as demonstrated in this work, where it was induced by the metallic electrodes deposited atop the heterostructure [Fig. 2(c)] illustrates the electrodes). The complex pattern of metallic electrodes and the intricate crystallographic microstructure within them created stresses that are very difficult to predict and model. Moreover, stresses in the metallic gates induced a pattern of tilting of the lattice within the crystal, which in turn produced a distortion affecting the electron

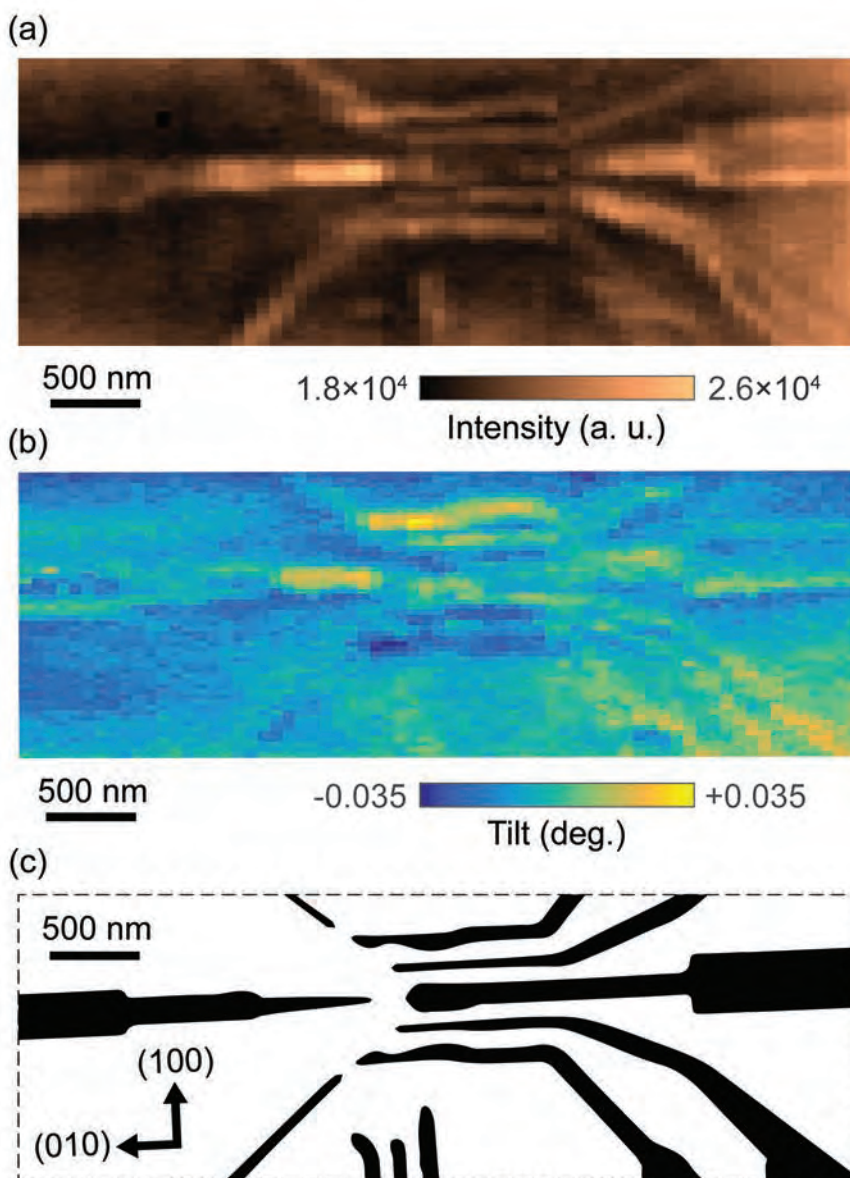


Fig. 2. Top panel (a) indicates x-ray diffraction intensity in the vicinity of the quantum dots. The electrodes are clearly visible in this close-up view. Scale provided in nanometers (nm). Middle panel (b) shows angular tilts of the crystalline lattices within the heterostructure in the same region. Drawing in bottom panel (c) displays the actual pattern of electrodes in this area.

gas and its quantum dots. An additional electric potential due to the piezoelectric effect modified the applied (gate) voltage used to operate the device and shifted the positions and energies of the quantum dots.

A nanobeam diffraction study conducted at the APS revealed the primary sources of the internal stresses and quantified their effects. The x-ray nanodiffraction measurements at the Hard X-ray Nanoprobe facility at the CNM/XSD 26-ID-C beamline probed regions in and around the semiconductor's quantum dots. Figure 1(b) shows the key features of this nanobeam experiment.

“Quantum” cont'd. on page 25

Harnessing DNA to Improve Optical Technologies

A crystal with different crystallographic symmetries is said to be anisotropic. Because optical modes are highly dependent on crystal shape, the ability to produce colloidal crystals with specific shapes is important for next-generation, innovative optoelectronic devices. As such, the use of shape anisotropy in colloidal crystals composed of inorganic nanoparticles has been suggested as a promising path to design and control optical responses in metamaterials being investigated for such devices. Nano- and microstructures with hexagonal cross-sections are particularly interesting because they support properties such as whispering gallery modes that exhibit low power loss and high quality factors. These properties make such crystals promising candidates for nonlinear optics and photocatalytic applications. However, there has not been any method that could control the crystal shape of these structures to incorporate them into such applications. In this study, researchers investigated DNA-mediated single-crystal engineering as a way to achieve this goal. In particular, they demonstrate for the first time that colloidal crystal engineering with DNA can be applied to generate highly anisotropic hexagonal prismatic single crystals, which were characterized at the APS and at Northwestern University. Furthermore, this study highlights a mechanism for preparing non-equilibrium crystal shapes. Overall, the results shown in this study have important implications for scientists involved in developing novel optical devices.

One technique used to generate highly selective interactions between colloidal particles involves using DNA strands on nanoparticle surfaces to direct nanoparticle assembly, taking advantage of binding specificity afforded by DNA. This allows the use of colloidal spheres functionalized with DNA to engineer colloidal crystallization. With this in mind, researchers conducted a study to investigate the use of DNA to engineer non-equilibrium anisotropic colloidal single crystals with uniform shapes.

To examine the internal ordering of the crystal structures, the researchers from Northwestern University em-

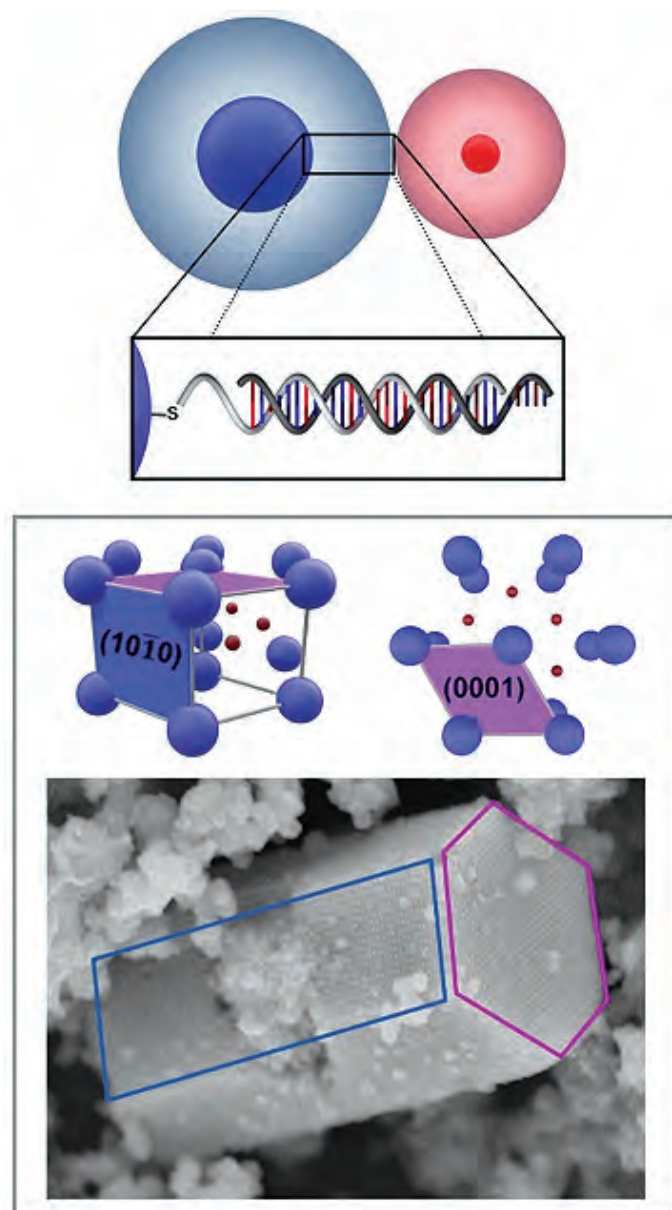


Fig. 1. Top: Scheme of a set of DNA-functionalized gold nanoparticles used to produce superlattices with AB₂ crystallographic symmetry. Bottom: SEM image of a representative hexagonal prism microcrystal enclosed by the highest surface energy facets.

ployed small-angle x-ray scattering at the DND-CAT x-ray beamline 5-ID-B,C,D at the APS. Mesoscale crystal shape and surface morphology of colloidal crystals were characterized using scanning electron microscopy at Northwestern University.

To synthesize colloidal crystals with anisotropic shapes, the researchers used a combination of two different sizes of nanoparticles that form lattices with noncubic crystallographic symmetry. As a proof of concept, they chose AB_2 -type superlattices with crystallographic symmetry identical to that of aluminum diboride, which has a hexagonal unit cell. By slowly cooling a solution of DNA-nanoparticles with complementary DNA strands, the researchers were able to generate single crystals with uniform shapes (Fig. 1, top). These crystals comprised hexagonal prisms enclosed by the highest surface energy facets [$(AB_2)(10\bar{1}0)$ and $(AB_2)(0001)$] (Fig. 1, bottom). This phenomenon contrasts with usual Wulff construction, which is used to explain crystal shape formation where the equilibrium shape is enclosed by the facet with minimal surface energy.

Molecular dynamics and simulations reveal that this behavior is a result of the large energy barrier between different layers of the $(AB_2)(10\bar{1}0)$ facet, which results in a significant deceleration of the facet growth rate, despite its high surface energy.

This work reports for the first time how colloidal crystal engineering with DNA can be used to produce highly anisotropic hexagonal prism microcrystals. Additionally, it introduces a mechanism that can be used to design crystals with non-equilibrium Wulff shapes, a capability important in many areas, including optics and photocatalysis.

— Nicola Parry

See: Soyoung E. Seo, Martin Girard, Monica Olvera de la Cruz, and Chad A. Mirkin, “Non-equilibrium anisotropic colloidal single crystal growth with DNA,” *Nat. Commun.* **9**, 4558 (2018). DOI: 10.1038/s41467-018-06982-9

Author affiliation: Northwestern University

Correspondence: * chadnano@northwestern.edu

This work supported by the Center for Bio-Inspired Energy Science, an Energy Frontier Research Center funded by the U.S. Department of Energy (DOE) Office of Science-Basic Energy Sciences Award DE-SC0000989 (oligonucleotide syntheses and purification, simulations and theory); the Air Force Office of Scientific Research Award FA9550-17-1-0348 (DNA-functionalization of gold nanoparticles, superlattice assembly); and the National Science Foundation’s Materials Research Science and Engineering Center program (DMR-1121262) and made use of its Shared Facilities at the Materials Research Center of Northwestern University (SEM characterization). DND-CAT is supported through Northwestern University, The Dow Chemical Co., and E. I. duPont de Nemours & Co. (the latter two are both part of DowDuPont). Additional support has been provided by the State of Illinois through the Department of Commerce and the Board of Education, the U.S. DOE Office of Energy Research, and the U.S. National Science Foundation Division of Materials Research. S.E.S. acknowledges partial support from the Center for Computation and Theory of Soft Materials Fellowship. This research used resources of the Advanced Photon Source, a U.S. DOE Office of Science User Facility operated for the DOE Office of Science by Argonne National Laboratory under Contract No. DE-AC02-06CH11357.

“Quantum” cont’d. from page 23

Applying dynamical x-ray diffraction modeling to the x-ray data allowed the researchers to characterize nanoscale-sized distortions within the heterostructure. A close-up view of the x-ray diffraction intensity appears in Fig. 2(a), clearly showing the outlines of multiple electrodes. This region encompasses the quantum dots, which reside in the 2DEG layer beneath the electrodes. Figure 2(b) shows the lattice tilts caused by the convoluted electrode pattern.

The x-ray measurements also allowed the calculation of spurious voltages and electron energy changes caused by the electrodes and lattice misalignments. For example, the piezoelectric effect introduced a 5-mV potential between the electrodes and the quantum dots.

This study demonstrates techniques that can decipher the complex set of induced stresses and voltages within heterostructures. Besides using these techniques to reduce the negative effects of internal stresses, scientists and engineers designing quantum devices could also use them to strategically place metal electrodes to control and enhance quantum dots. The researchers also anticipate applying their x-ray method to the study of other electronic systems. — Philip Koth

See: Anastasios Pateras¹, Joonkyu Park¹, Youngjun Ahn¹, Jack A. Tilka¹, Martin V. Holt², Christian Reichl³, Werner Wegscheider³, Timothy A. Baart⁴, Juan Pablo Dehollain⁴, Uditendu Mukhopadhyay⁴, Lieven M.K. Vandersypen⁴, and Paul G. Evans^{1*}, “Mesoscopic Elastic Distortions in GaAs Quantum Dot Heterostructures,” *Nano Lett.* **18**, 2780 (2018). DOI: 10.1021/acs.nanolett.7b04603

Author affiliations: ¹University of Wisconsin-Madison, ²Argonne National Laboratory, ³ETH Zürich, ⁴Delft University of Technology

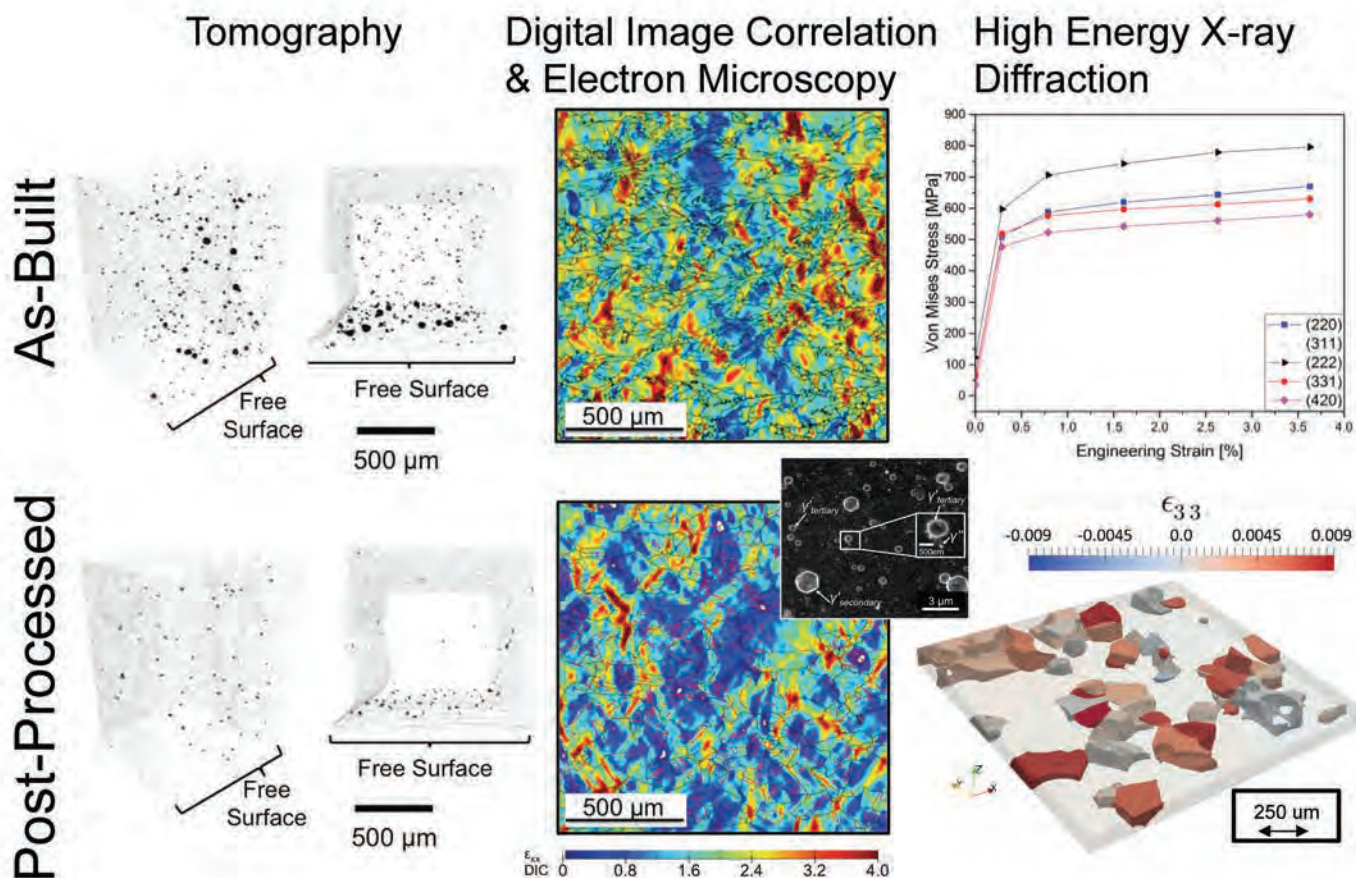
Correspondence: * pgevans@wisc.edu

Correspondence: * pgevans@wisc.edu

A.P., J.P., Y.A., and P.G.E. were supported by the U.S. Department of Energy (DOE) Office of Science-Basic Energy Sciences, Materials Sciences and Engineering, under contract no. DE-FG02-04ER46147 for the x-ray scattering studies and analysis. J.A.T. acknowledges support from the National Science Foundation Graduate Research Fellowship Program under grant no. DGE-1256259. Work at TU Delft was supported by The Netherlands Organization of Scientific Research (NWO). The Center for Nanoscale Materials, a U.S. DOE Office of Science user facility, was supported by the U.S. DOE Office of Science-Basic Energy Sciences, under Contract No. DE-AC02-06CH11357. This research uses resources of the Advanced Photon Source, a U.S. DOE Office of Science User Facility operated for the DOE Office of Science by Argonne National Laboratory under Contract No. DE-AC02-06CH11357.

Understanding Deformation Mechanisms in an AM-Fabricated Superalloy

Nickel-based superalloys have become indispensable for applications involving very high temperatures and pressures, including the aerospace and nuclear power industries. As additive manufacturing (AM) technologies mature and become more versatile and affordable, the prospect of using AM in the fabrication of superalloy parts is increasingly attractive, but requires more information about the deformation mechanisms of AM-built superalloy parts. Researchers used the APS in their study of the microstructural deformation and strain mechanisms of the popular nickel (Ni)-based superalloy Inconel 718 (IN718). They employed a range of advanced techniques to achieve a deeper understanding of the structure to property relationships in IN718 made with the AM method of selective laser melting.



The research team, from Purdue University, fabricated sample IN718 parts in several different configurations to facilitate a suite of various advanced characterization studies, including (Fig. 1) scanning electron microscopy (SEM), electron backscatter diffraction (EBSD) with digital image correlation (DIC), synchrotron-based x-ray micro-tomography (micro-SCT), and high-energy x-ray diffraction (HEXD), with the latter two techniques performed along with Argonne colleagues at the XSD 2-BM-A,B and 1-ID-E x-ray beamlines, respectively. These methods were used to investigate the role of build direction and the resulting anisotropy contributing to deformation behavior, as well as the effects of heat treatment and its contribution to strengthening the material.

The sample parts were divided into two groups, one with a stress-relief treatment performed on the build plate (designated “as-built” specimens) and the second with a post-processing treatment of homogenizing, solution treating, and aging (designated “post-processed” specimens). As might be expected, SEM images of the as-built specimens showed no γ' or γ'' precipitate structures, which are usually a result of the post-processing treatment in IN718 to strengthen the material. The post-processed samples did display the precipitates in the microstructure.

Other marked differences between the microstructures of both sample groups were evident. While both the as-built and post-processed specimens showed random grain orientation, the as-built samples showed greater anisotropy, with a higher percentage of low-angle grain boundaries (LAGBs) and remnants of laser melt tracks from the SLM process. The post-processed specimens demonstrated that the post-processing heat treatment removes many of these defects, reducing LAGBs and forming coherent annealing twins, thus reducing the general anisotropy of the microstructure.

The micro-CT studies at the APS provided data on porosity, showing that the as-built IN718 tended to contain greater numbers of pores, with the largest-sized pores generally seen in the vicinity of a free surface. In-

< Fig. 1. Characterization of the AM-produced IN718 for the “as built” and “post processed” conditions, via synchrotron-based micro-CT, DIC coupled with EBSD, and HEXD.

terior bulk samples were less porous, but the as-built samples still showed more porosity in these regions than did the post-processed samples. The experimenters note that the heat treatment used on these specimens did not include the hot isostatic pressing that is usually associated with reduction in porosity.

Strain analysis of the specimens with DIC mapping demonstrated greater anisotropy and lesser strength in the build direction in the as-built samples. This was noted to still be present after heat treatment in the post-processed specimens, but at a far lesser degree. The HEXD studies of both sample sets under *in situ* loading showed a greater dislocation density content in the as-built specimens, producing a powder pattern that is not seen in the post-processed samples. The heat treatment helped to regularize the alloy microstructure and removed any traces of the laser path remaining from the build (although the researchers note that the laser melt paths remaining in the as-built specimens did not appreciably influence the strain patterning).

The detailed, advanced characterization presented in this work fills in major gaps in our knowledge of the microstructure and behavior of AM-made IN718. Such knowledge will ultimately allow the industries that rely upon this and other similarly important nickel-based superalloy materials to reap the benefits that additive manufacturing strategies can provide. — Mark Wolverton

See: Michael D. Sangid^{1*}, Todd A. Book¹, Diwakar Naragani¹, John Rotella¹, Priya Ravi¹, Alexander Finch¹, Peter Kenesei², Jun-Sang Park², Hemant Sharma², Jonathan Almer², and Xianghui Xiao², “Role of heat treatment and build orientation in the microstructure sensitive deformation characteristics of IN718 produced via SLM additive manufacturing,” *Additive Manu.* **22**, 479 (2018). DOI: 10.1016/j.addma.2018.04.032

Author affiliations: ¹Purdue University, ²Argonne National Laboratory ³Present affiliation: United States Military Academy
Correspondence: * msangid@purdue.edu

This work was financially supported by DARPA (N66001-14-1-4041) under program managers M. Maher and J. Vanderbrande and team: D. Schesser, J. Margiotta, D. Cheng, W. Roy, J. Williams, and B. Cowles. This research used resources of the Advanced Photon Source, a U.S. Department of Energy (DOE) Office of Science User Facility operated for the DOE Office of Science by Argonne National Laboratory under Contract No. DE-AC02-06CH11357.

Adding It Up: Three Routes to Better 3-D Printing

Additive manufacturing (AM), more commonly known as three-dimensional (3-D) printing, is transforming the industrial world in myriad ways, making the journey from initial concept to finished design to physical reality much faster, cheaper, and more efficient. Various AM techniques have been developed, including laser powder bed fusion (LPBF), binder jetting, material extrusion, direct energy deposition, and others, each with its own characteristics and applicability to different materials, objects, and purposes. Yet our understanding of the basic dynamics and physical processes controlling these techniques remains incomplete and imprecise, leading to a lack of precision control during fabrication and the creation of defect-laden parts that may fail to meet desired standards. In some cases, models of AM processes are based on indirect measurements and visualizations and on analogies with other industrial techniques such as welding, not all of which are fully comparable to AM. Researchers have been working to change this situation through the development of ul-

1. Finding the Keys to Keyhole Formation in 3-D Printing

In their latest work [1], they investigated the phenomenon of vapor depressions (known as “keyholes”) in the laser melting of metals, commonly involved in the AM technique of LPBF (Fig. 1). Working at the XSD beamline 32-ID-B at the APS, they found that contrary to the gradual transition from a “conduction mode” (a shallow, semi-circular melt pool) to a “keyhole mode” (deep and narrow melt pool) as traditionally believed, there is a well-defined threshold for the transition, keyholes are present throughout the LPBF process, and they vary in a predictable manner.

The ability to directly visualize the evolution of the vapor depression dynamics through ultrafast x-ray imaging allowed the research team to precisely characterize the development of the melt pool and formation of the vapor depression, and the quantitative relationship between power density, drilling rate, and front wall angle of the keyhole, with both a stationary and moving laser beam.

Under a stationary x-ray beam, the research team observed five distinct regimes. After initial melting of the metal powder under the laser, a vapor depression formed and began to grow, followed by the formation of instabilities in the vapor depression. This led to formation of a keyhole and finally a marked change in the shape of the melt pool, from a semicircular shape to bimodal, with a bowl-shaped area on top and a deep spike on the bot-

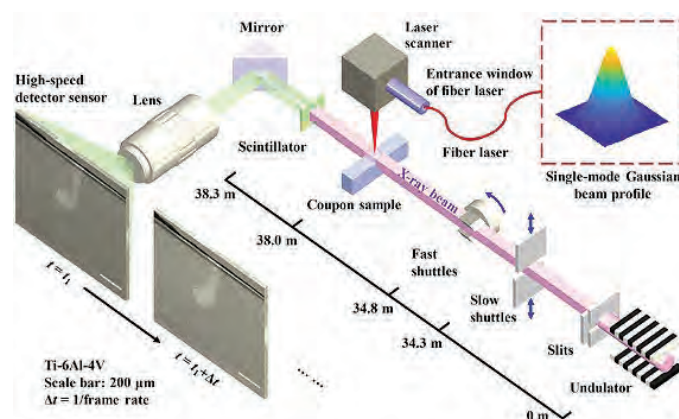


Fig. 1. Top right: Schematic of high-speed x-ray imaging experiment. Bottom left: Tableau of representative x-ray images in laser power-velocity parameter space of Ti-6Al-4V plate samples, showing the variation in vapor depression size and morphology.

tom. More power translated into deeper penetration.

The main parameters for both laser welding and AM are laser power and velocity, defined as P-V space. In the scanning beam experiments, the research team found that unlike in the stationary beam measurements, vapor depression morphologies changed markedly in P-V space, with almost all combinations of power and velocity resulting in the formation of a substantial vapor depression. Measuring vapor depression depths as a function of laser velocity and power for spot sizes of 95 μm and 140 μm showed a very linear depth vs. power relationship for most beam-scanning velocities.

Although models to predict vapor depression dynam-

ics are available, they tend to require large computational resources and are not easily scalable. The current experiment team adopted a less complex prediction model based on these experiments, which uses the unique capabilities of the ultrafast x-ray imaging method and the high brightness of APS x-rays. By calculating the front-wall angle of the keyhole as a function of beam velocity and power density, it is possible to estimate the keyhole depth. With some minor corrections, this model proved to fit the present data sets quite well. Further experiments using powder-bed samples and different materials introduced some variations — but similar overall trends — with the relationship between front-wall angle and keyhole depth shown to be unaffected by the type of material used.

These imaging studies and modeling of keyhole formation and morphology under laser heating in LPBF additive manufacturing are an important advance that will allow LPBF users to better predict the behavior of their equipment and avoid the problems of deep keyholing that result in porosity defects and instability in AM-made parts. — *Mark Wolverton*

2. Penetrating the Depths of the Binder Printing Process

Binder jetting is one of the most versatile and powerful methods of 3-D printing. After a part is created, it can be used as a mold, sintered to make a final part, or combined with another material to create a composite object. Binder jetting can be performed with both metallic and ceramic materials, does not require support structures for the fabrication of parts, and has the added advantage of mitigating thermal stresses and microstructural defects because the printing and densification processes are performed separately.

But as with every other AM process, certain phenomena can affect the quality and durability of objects created through binder jetting. Variations in the characteristics of the powder and binder material used, the design of the individual part, and the choice of post-fabrication procedures can all introduce defects in the finished part. One obstacle is a limited understanding of the basic mechanisms that control the binder jetting process. Previous studies using visible light were unable to completely visualize the fundamental mechanisms, and also employed continuous-jetting inkjet print-heads rather than the droplet-on-demand (DoD) heads used in most commercial printers.

Now, the team of Argonne and Carnegie Mellon Uni-

versity researchers, with colleagues from The Barnes Group Advisors, utilized high-speed synchrotron x-ray imaging at the APS to open a more revealing window into the processes of binder jetting AM (Fig. 2). [2]

The research team adapted an experimental set-up they previously used to study other AM mechanisms at the XSD beamline 32-ID-B to investigate binder jetting with a variety of materials with high spatial and temporal resolution. Because the process begins with the generation and subsequent behavior of the binder droplets, the team first examined droplet geometry and dynamics in DoD-type print heads, which are more commonly used because of their high resolution and reliability.

Repeated experiments revealed that the droplet initially displayed a chiefly cylindrical head, which changed to spherical as it fell, followed by a long, thin tail. Three to five main satellite droplets were seen at the end of the tail, with some smaller droplets at the very end. The droplet velocity and separation were measured to be essentially consistent with the printer settings.

As the droplet changed shape, a neck region formed between the head and tail, which can pinch off; although in the present experiments, the head was seen to impact the powder bed before this occurred. Satellite droplets fell more slowly than the head droplet, indicating that they were formed by the instability of the tail. No splashing of the binder was observed, but the horizontal movement of the print head resulted in drift of the satellite droplets. This drift can be expected to increase with greater print-head velocity, which may account for the decreased dimensional accuracy previously seen in binder jetting printed parts as print-head speed increases.

Unlike other imaging modalities, the high-speed, hard x-rays from the APS allowed visualization of the subsurface activity in the powder bed after the binder droplets fell. Upon droplet impact, the powder particles underneath were ejected from the bed. Defining the depth of disturbance as the “interaction depth,” the experimenters observed that the interaction depth depended on particle size and morphology, decreasing with larger particles and increasing with more irregularly-shaped particles. The particle substance also affected ejection behavior because of different flow-ability and mass characteristics. These phenomena are important factors in the possible formation of defects: Deep interaction depths can create subsurface pores, particle ejections can result in depletion zones and pores, and

“3-D” cont’d. on page 30

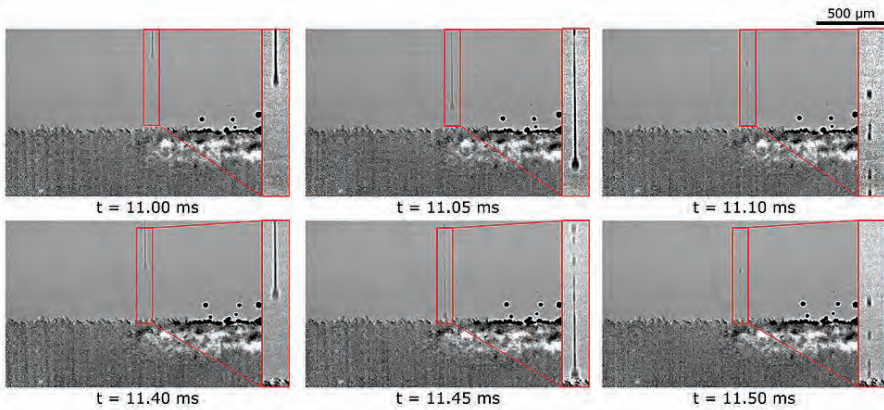


Fig. 2. High-speed x-ray imaging of the binder jetting additive manufacturing process. A closer look at the binder droplet is also displayed on the side of each image. The frame rate is 20,000 frames per second. [2]

“3-D” cont’d. from page 29

ejected particles can affect the formation of subsequent powder layers, causing roughness and dimensional inaccuracies. Smaller particle sizes also displayed significant agglomeration, with binder droplets coalescing to form larger spherical agglomerates that could disrupt spreading of subsequent layers and form defects.

These experiments provide a vital insight into the fundamental mechanisms at work in binder jetting. With this more complete and detailed knowledge now available, it will be possible to better tailor the fabrication of binder jetting-produced parts using various materials and conditions with fewer defects, and develop new binder-jetting printers with enhanced capabilities. – *Mark Wolverton*

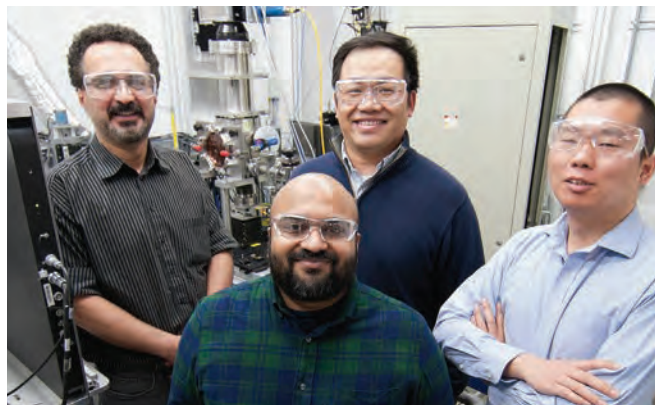
3. An Ultrafast Look Inside Laser Powder Bed Fusion

In the continually expanding realm of AM, laser powder bed fusion (LPBF) has become the most popular method for the fabrication of metal parts. In LPBF, a laser scans an extremely thin powder layer atop a substrate layer, creating a new metal layer by melting powder particles along with some of the substrate. Because the processes involved are highly dynamic, including high temperatures and rates of melting and cooling, LPBF is a complex technique involving powder ejection, melting and vaporization, molten metal flow and solidification, nonequilibrium phase transitions, and other various phenomena, all of which can have crucial implications for the

quality and characteristics of the finished part and the presence or absence of structural defects. Thus, the ability to observe and study the LPBF process *in situ* is vitally important in order to achieve a better understanding and control of this 3-D printing technique. But because of the extremely localized and very fast nature of these phenomena, they are quite difficult to visualize adequately. Most previous attempts to do so have used high-speed visible light or thermal imaging techniques, but these are limited by their inability to image sub-surface features and the behavior of scat-

tered particles. The experimenters from Argonne, Carnegie Mellon University, the Missouri University of Science and Technology, and the DOE National Security Campus used ultra-high-speed x-ray synchrotron imaging techniques at the APS to observe the fundamental physical processes involved in the LPBF method. [3]

Again using the XSD 32-ID-B beam-



XSD researchers involved in the experiments: Left to right, back row: Kamel Fezzaa, beamline scientist; Tao Sun, beamline scientist; Cang Zhao, postdoc; (foreground) Niranjana Parab, postdoc. Behind them is the home-built laser system that can simulate the laser powder-bed fusion process in a commercial 3-D printer. This laser system, together with the high-speed x-ray imaging capability at the APS, enables the study presented in the *Science* paper [1].

line, the research team used a custom experimental setup they had previously employed to study other AM methods, adding an ultrafast-imaging camera capable of extremely high temporal resolution and recording speeds, and also a laser scanner so that the actual LPBF process could be reproduced with a moving laser beam instead of the stationary beam of previous experiments. Powder bed samples of three different metallic alloys commonly used in LPBF manufacturing were studied: aluminum alloy (Al-10Si-Mg, Fig. 3), titanium alloy (Ti-6Al-4V), and nickel alloy (Inconel 718). Both absorption and phase contrast x-ray images were obtained at various frame rates and exposure times to capture different phenomena at various time scales.

A variety of exposure times and speeds allowed the visualization of a wide range of phenomena. For example, denser samples such as the Inconel alloy required

greater exposure times in order to image details of the melt pool formation, while the behavior of other materials could be adequately seen at lesser exposures. The multi-frame, high-speed camera was used to image the entire length of the laser scan with each sample, providing a full record and imaging of the important phenomena governing the LPBF process.

Ultrafast imaging was used at rates of 1.08 million and 10 million frames s^{-1} to examine some of the extremely fast and dynamic events that occur during LPBF fabrication. The latter speed is the fastest rate possible with currently available cameras. This allowed visualization of the formation of vapor depressions in the aluminum samples and changes in their sizes and shapes. Other experiments showed the behavior of particles ejected from the powder bed, including tracking of their velocities and trajectories with better accuracy than previously possible, even those with irregular shapes.

This work has produced a wealth of new information on the intricacies of the LPBF process, from the formation and dynamics of melt pools to the formation of porosity in materials, the behavior of vapor depressions, and the ejection of powder particles. The experiments also helped to identify phenomena that particularly lend themselves to study under ultrafast recording speeds, and quantified for the first time the oscillations of vapor depressions and high-velocity rotating particles.

Unlike previous imaging methods, which could only provide incomplete and less detailed data, this ultrahigh-speed synchrotron x-ray technique provides new insights into the basic processes at the heart of the LPBF method of additive manufacturing. Such knowledge will not only facilitate the development of better control of LPBF fabrication methods and the consequent creation of stronger and more robust parts with fewer defects, but also help to devise improved numerical models as LPBF and other AM techniques continue to expand in their versatility and popularity. – *Mark Wolverton*

[1] See: Ross Cunningham¹, Cang Zhao², Niranjan Parab², Christopher Kantzos¹, Joseph Pauza¹, Kamel Fezzaa², Tao Sun², and Anthony D. Rollett^{1*}, “Keyhole Threshold and Morphology in Laser Melting Revealed by Ultrahigh-Speed X-ray Imaging,” *Science* **363**, 849 (22 February 2019). DOI: 10.1126/science.aav4687

Author affiliations: ¹Carnegie Mellon University, ²Argonne National Laboratory

Correspondence: * rollett@andrew.cmu.edu

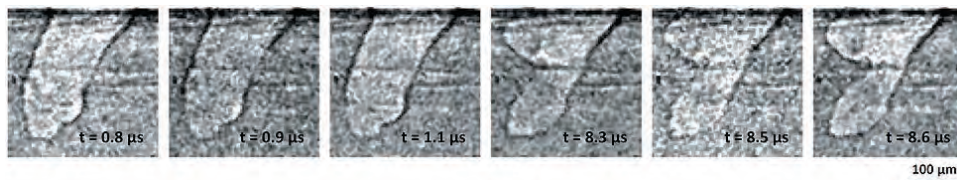


Fig. 3. High-speed x-ray imaging of the binder jetting additive manufacturing process. A closer look at the binder droplet is also displayed on the side of each image. The frame rate is 20,000 frames per second. [3]

The work was supported by the Department of Defense, Office of Economic Adjustment, under grant number ST1605-17-02, Michael Gilroy, CTO & Program Director. The work was also supported by Laboratory Directed Research and Development funding from Argonne National Laboratory, provided by the Director, Office of Science, of the U.S. Department of Energy (DOE) under Contract No. DE-AC02-06CH11357.

[2] See: Niranjan D. Parab¹, John E. Barnes^{2*}, Cang Zhao¹, Ross W. Cunningham³, Kamel Fezzaa¹, Anthony D. Rollett^{3**}, and Tao Sun^{1***}, “Real time observation of binder jetting printing process using high-speed X-ray imaging,” *Sci. Rep.* **9**, 2499 (2019). DOI:10.1038/s41598-019-38862-7

Author affiliations: ¹Argonne National Laboratory, ²The Barnes Group Advisors, ³Carnegie Mellon University

Correspondence: *John@thebarnes.group,

rollett@andrew.cmu.edu, * taosun@aps.anl.gov

We thank Alex Deriy from the APS for technical and safety support for beamline experiments, and Sean Wang from Northwestern University for the assistance in data analysis. A.D.R. and R.W.C. are grateful for the support of the ADAPT Mountain West Manufacturing Network. This research used resources of the Advanced Photon Source, a U.S. DOE Office of Science User Facility operated for the DOE Office of Science by Argonne National Laboratory under Contract No. DE-AC02-06CH11357.

[3] See: Niranjan D. Parab¹, Cang Zhao¹, Ross Cunningham², Luis I. Escano³, Kamel Fezzaa¹, Wes Everhart⁴, Anthony D. Rollett², Lianyi Chen³, and Tao Sun^{1*}, “Ultrafast X-ray imaging of laser-metal additive manufacturing processes,” *J. Synchrotron Rad.* **25**, 1467 (2018). DOI: 10.1107/S1600577518009554

Author affiliations: ¹Argonne National Laboratory, ²Carnegie Mellon University, ³Missouri University of Science and Technology, ⁴Department of Energy’s Kansas City National Security Campus

Correspondence: * taosun@aps.anl.gov

This work was financially supported by Laboratory Directed Research and Development funding from Argonne National Laboratory, provided by the Director, Office of Science, of the U.S. DOE under Contract No. DE-AC02-06CH11357. N.D. Parab, L.I. Escano, L. Chen, and T. Sun are grateful for the support of Honeywell Federal Manufacturing and Technologies. A.D. Rollett and R. Cunningham are grateful for support from the University of Utah under grant No. U000095690. L. Chen acknowledges funding from the University of Missouri Research Board. This research used resources of the Advanced Photon Source, a U.S. DOE Office of Science User Facility operated for the DOE Office of Science by Argonne National Laboratory under Contract No. DE-AC02-06CH11357.

Casting Light on Some New Benefits of Perovskite Solar Cells

One of the most vital areas of research in the quest for better and cheaper photovoltaic devices centers on hybrid materials based on a perovskite structure. But while many promising compounds have been identified, the realization of truly efficient and commercially viable perovskite-based solar cells continues to be hampered by several factors, including material stability and fragility problems in varying environmental conditions. A university-national laboratory team of researchers has found a promising solution to those problems in a perovskite compound that actually expands under illumination, smoothing out defects in its crystal lattice and allowing more efficient charge transport across the interface, with improved power conversion efficiency (PCE) to over 20%. Their work is based in part on studies carried out at the APS.

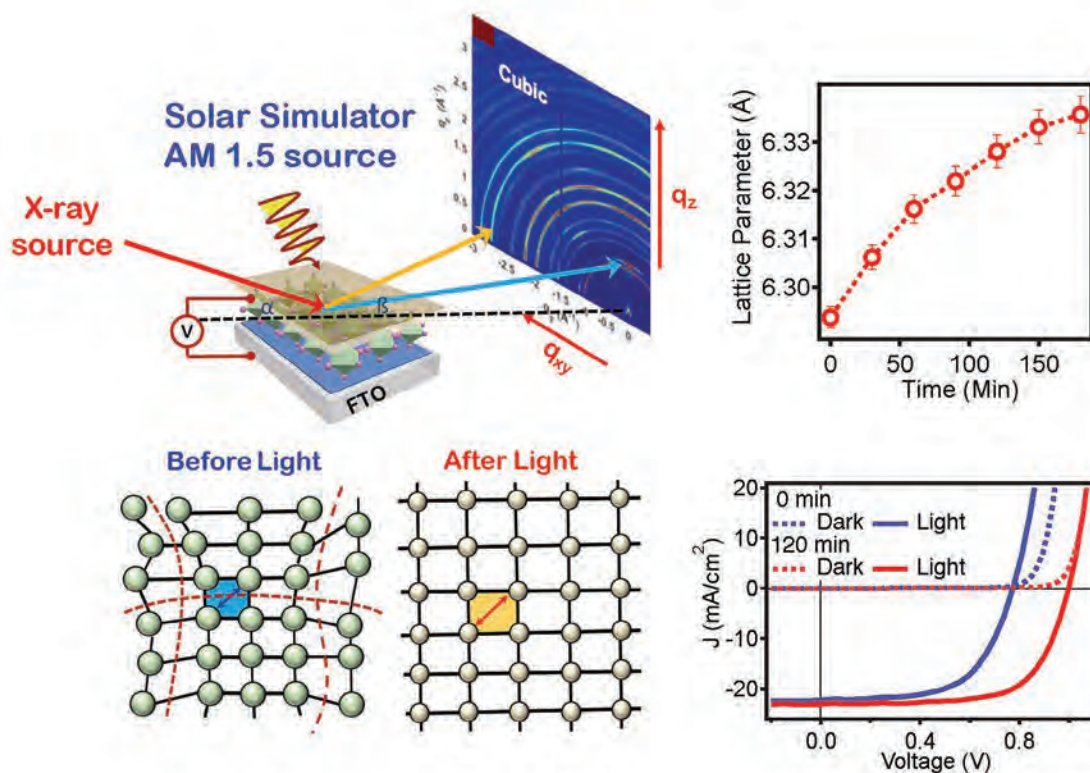


Fig. 1. The experimental setup (top left) and the corresponding light-induced lattice expansion effect (top right: lattice constant vs. illumination time), which leads to curing defects and relieving of lattice strain (bottom left) and as a result, an increase in the open circuit voltage of a solar cell.

Much of the work on perovskite materials has followed a somewhat trial-and-error approach, combining different materials into a perovskite ABX₃ structure and testing the characteristics of the resulting compound. Prior studies have demonstrated that light soaking of certain materials could induce structural changes that improve photovoltaic efficiency, but detailed in situ information that could help researchers better understand — and perhaps tailor — the phenomenon has been lacking.

In the present work, the team from Los Alamos National Laboratory, Rice University, Purdue University, Northwestern University, Institut FOTON CNRS UMR 6082 (France), and Argonne fashioned a number of hybrid perovskite solar cells with a FA_{0.7}MA_{0.25}Cs_{0.05}PbI₃ composition and measured them using a variety of techniques including grazing-incidence wide-angle x-ray scattering (GIWAXS) maps at the XSD 8-ID-E x-ray beamline of the APS.

In most of the cells, the researchers noted a substantial improvement in PCE from 18.5% to 20.5% under continuous light soaking with a 1-sun (100-mW/cm²) source as the lattice structure of the hybrid cells uniformly expanded (Fig. 1). This relieved local strains in the bulk material and better aligned the crystal planes, as evidenced by narrowing and uniform shifting of the Bragg peaks toward lower scattering values as seen by GIWAXS. The researchers explain that constant illumination generates electron-hole pairs in the perovskite material, decreasing the distortions of some bonds while elongating others, resulting in a generalized lattice expansion and relaxation. A similar phenomenon was seen with pure MAPbI₃ thin films, suggesting that such lattice expansion under light is common for hybrid perovskite materials.

The effects of this light-induced lattice expansion improve the photovoltaic characteristics of the perovskite material in several significant ways. Using various techniques, the team observed that the open-circuit voltage and fill factor, both crucial parameters of PV performance, are significantly increased upon lattice expansion. Another factor contributing to substantially increased efficiency is considerable suppression and lowering of the energetic barrier at the perovskite-contact interfaces. In an operational solar cell, this would allow easier current flow from the absorber to the electrodes.

Previous experiments with MAPbI₃ films demonstrated

some changes in contact interfaces following light soaking, which were attributed to ion migration from the perovskite material to the contact. To rule out such effects in the current work, the experimenters performed x-ray photoelectron spectroscopy before and after illumination, and also monitored open-circuit voltage and fill factor values in darkness while applying a constant bias current. Neither technique showed any evidence of ion migration as seen in the MAPbI₃ film experiments.

The lattice expansion persists for at least 30 min in the perovskite materials even when the films are rested in complete darkness after illumination. To exclude any possibility that the lattice expansion might be heat-induced, the experimenters maintained the perovskite films at constant temperature during illumination and in darkness. When exposed to greater illuminations of 10-sun intensity, the films maintained their PV efficiency for considerable time, degrading only to 80% after 600 minutes. The investigators also noted that the light-induced lattice expansion had no noticeable effects on the photovoltaic stability of their devices, even after more than 1500 hours of continuous operation under 1-sun illumination.

These findings not only represent a highly significant step forward in the search for stable and practical perovskite-based photovoltaic devices, but also point the way toward new research possibilities in the fundamental understanding of perovskite-based materials and their behaviors. — [Mark Wolverton](#)

See: Hsinhan Tsai^{1,2}, Reza Asadpour³, Jean-Christophe Blancon¹, Constantinos C. Stoumpos⁴, Olivier Durand⁵, Joseph W. Strzalka⁶, Bo Chen², Rafael Verduzco², Pulickel M. Ajayan², Sergei Tretiak¹, Jacky Even⁵, Muhammad Ashraf Alam³, Mercouri G. Kanatzidis⁴, Wanyi Nie^{1*}, and Aditya D. Mohite^{1,2**}, “Light-induced lattice expansion leads to high-efficiency perovskite solar cells,” *Science* **360**, 67 (6 April 2018). DOI: 10.1126/science.aap8671
Author affiliations: ¹Los Alamos National Laboratory, ²Rice University, ³Purdue University, ⁴Northwestern University, ⁵Institut FOTON CNRS UMR 6082, ⁶Argonne National Laboratory
Correspondence: * wanyi@lanl.gov, ** adm4@rice.edu

Work at Northwestern was supported by the U.S. Department of Energy (DOE) Office of Science (grant SC0012541, structure characterization). A.D.M. acknowledges support by U.S. DOE Office of Energy Efficiency and Renewable Energy grant DE-FOA-0001647-1544 for this work. This research used resources of the Advanced Photon Source, a U.S. DOE Office of Science User Facility operated for the DOE Office of Science by Argonne National Laboratory under Contract No. DE-AC02-06CH11357.

Spinning Out a High-Temperature Magnetic Insulator

Scientists would like to use the quantum property called “spin,” which is the basis of magnetism, to make equipment such as ultra-compact computer memories and new types of logic circuits. Building such spintronic devices often requires the use of ferromagnetic insulators, which can keep spin from leaking from one part of a device to another while simultaneously picking out specific spins. Such insulators have been hard to make, but now an international team of scientists, performing studies at the APS and the Advanced Light Source at Lawrence Berkeley National Laboratory, has found a promising material.

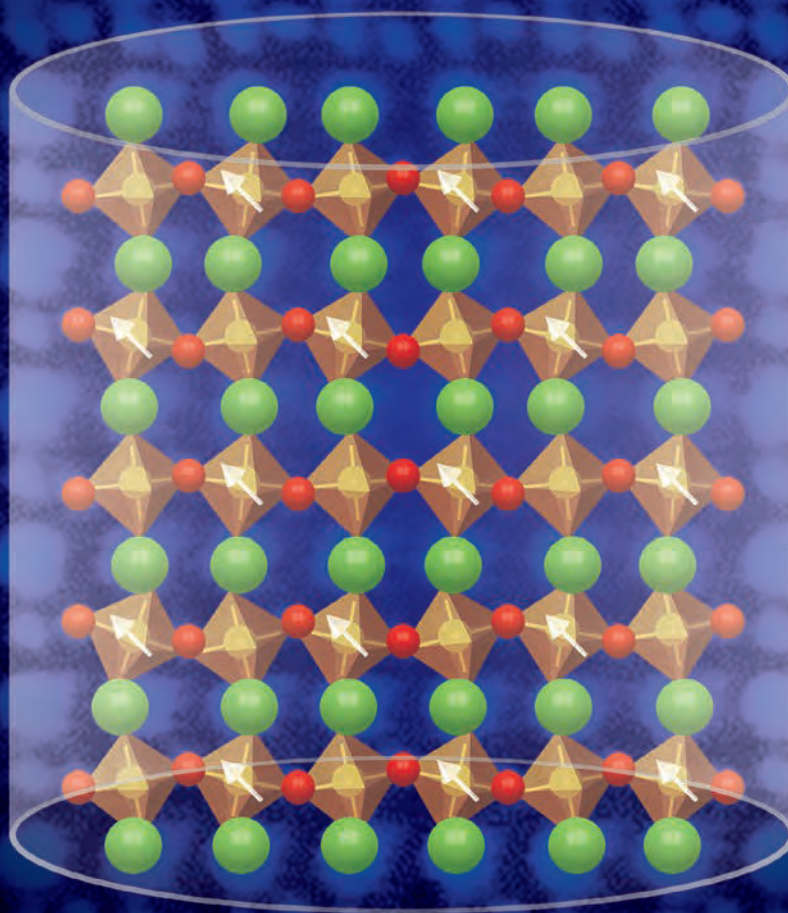


Fig. 1. In a strain-induced, high-temperature perovskite ferromagnetic insulator, the lanthanum, oxygen, and cobalt atoms are arranged symmetrically and electron spins (white arrows) are aligned.

Ferromagnetic insulators with all the right properties are rare. With some materials, insulators can be created in thin films by controlling the placement of magnetic ions at an atomic level. But those materials tend to have low crystalline symmetry. The substrates they're attached to, however, usually are highly symmetrical crystals. Placing low-symmetry films on high-symmetry substrates is difficult and often introduces unwanted strain that changes the properties of the device.

On the other hand, materials that are highly symmetrical usually require the addition of chemicals to make them ferromagnetic, and those chemicals can introduce unwanted effects such as added conductivity. There are a few candidate materials that have high symmetry and require no chemical doping, but they only become magnetic at extremely low temperatures, close to absolute 0. For instance, europium sulfide has a magnetic transition temperature, known as a "Curie temperature," of 16 K, and strained europium titanium oxide's is even lower, at 4 K.

These researchers found, however, that they could make a ferromagnetic insulator at a much higher temperature by using a thin film of lanthanum cobaltite (LaCoO_3). The material, a type of crystal known as a perovskite, has high symmetry and needs no doping with another element. When they subjected it to tensile strain, they found it had a Curie temperature of almost 90 K, still well below room temperature, but higher than liquid nitrogen temperature, and therefore easier and less expensive to reach.

By adjusting the oxygen pressure under which they deposited the thin films and changing the thickness of the films, the researchers found they could alter the concentration of cobalt defects in the structure. When the concentration reached about 10%, the ferromagnetism of the material disappeared. Reducing the film's thickness also allowed them to more finely tune the Curie temperature of the LaCoO_3 .

To measure the lattice structure of the thin films, and to confirm their thickness, the researchers used the XSD 33-BM-C beamline at the APS, as well as beamlines at the Shanghai Synchrotron X-ray Facility and the Beijing Synchrotron X-ray Facility. They also characterized the material using x-ray absorption spectroscopy at the Ad-

vanced Light Source at Lawrence Berkeley National Laboratory, and the National Synchrotron Radiation Laboratory of the University of Science and Technology of China. They performed x-ray absorption near-edge structure spectroscopy to characterize the state of the cobalt at the Shanghai and Beijing facilities.

The researchers do not yet know why the Curie temperature of the LaCoO_3 is so surprisingly higher than that of other un-doped, high-symmetry, ferromagnetic insulators. Theory suggests it may have to do with the large overlap between the electron orbitals in cobalt and oxygen atoms, because overlapping orbitals in europium and sulfur are what is thought to give europium sulfide its magnetism. In any case, they say strained LaCoO_3 is a much better candidate for ferromagnetic insulators than those previously known because of its relatively high Curie temperature, its high symmetry (Fig. 1), and the ease with which high-quality films of the material can be grown over large areas of commonly used substrates.

— Neil Savage

See: Dechao Meng¹, Hongli Guo¹, Zhangzhang Cui^{1,2}, Chao Ma¹, Jin Zhao¹, Jiangbo Lu², Hui Xu¹, Zhicheng Wang¹, Xiang Hu¹, Zhengping Fu¹, Ranran Peng¹, Jinghua Guo^{2,4}, Xiaofang Zhai^{1*}, Gail J. Brown⁵, Randy Knize⁶, and Yalin Lu^{1,5,6**}, "Strain-induced high-temperature perovskite ferromagnetic insulator," *Proc. Natl. Acad. Sci. U.S.A.* **115**(12), 2873 (March 20, 2018).

DOI: 10.1073/pnas.1707817115

Author affiliations: ¹University of Science and Technology of China, ²Lawrence Berkeley National Laboratory, ³Shaanxi Normal University, ⁴University of California, Santa Cruz, ⁵Air Force Research Laboratory, ⁶US.. Air Force Academy

Correspondence: * xfzhai@ustc.edu.cn, ** yllu@ustc.edu.cn

This work was supported by the National Natural Science Foundation of China (Grants 51627901, 11574287, 21373190, 11620101003, and 11574281), the National Key Research and Development Program of China (Grant 2016YFA0401004), Open Programs for the Key Science & Technology Infrastructures of Chinese Academy of Sciences, Youth Innovation Promotion Association Chinese Academy of Sciences (Grant 2016389), and the Fundamental Research Funds for the Central Universities (Grant WK234000065). This research used resources of the Advanced Light Source, which is a U.S. Department of Energy (DOE) Office of Science User Facility under Contract DE-AC02-05CH11231; and of the Advanced Photon Source, a U.S. DOE Office of Science User Facility operated for the DOE Office of Science by Argonne National Laboratory under Contract No. DE-AC02-06CH11357.

Illuminating a Key Industrial Process

Rare earths such as lanthanides, which are elements in the range of atomic number 57 to 71, are not actually rare. They exist in large quantities in the world, but are only found in the form of trace amounts in rocks. Since rare earths are important for a variety of applications (e.g., electronics) their extraction is a major mining-related industry. Results of research carried out at the APS may pave the way to improvements in industrial processes based on solvent extraction, which is used in the mining and refinement of technologically important rare earths.

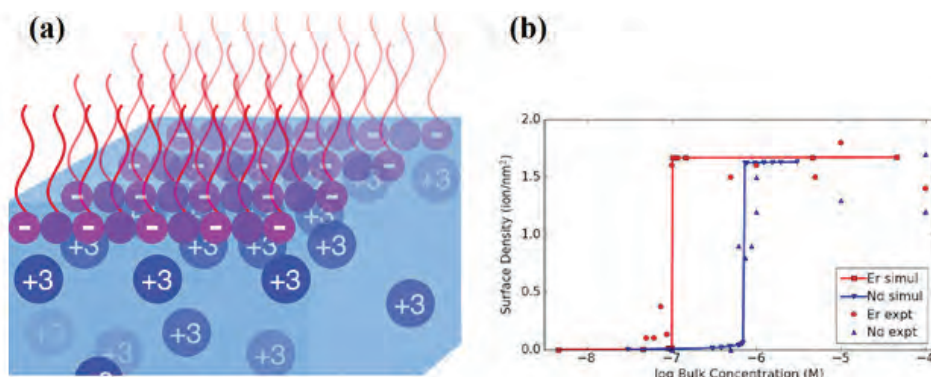


Fig. 1. (a) Schematic diagram of the system studied — the positively charged lanthanide ions (blue circles) are dissolved in the water, while the negatively charged surfactant molecules (purple) float on the water surface. (b) Data showing how the density of ions at the surfactant surface jumps suddenly as the concentration of ions in the bulk water increases (Er = erbium, a heavier lanthanide, Nd = neodymium, a lighter lanthanide). The lines through the data are predictions from computer simulations. Adapted from M. Miller et al., *Phys. Rev. Lett.* **122**, 058001 (2019). © 2019 American Physical Society All rights reserved

A common process by which rare earths are extracted involves dissolving rocks in acids, then shaking up the solution with an organic solvent and a surfactant. Under the right conditions, the desired ions move out of the aqueous phase and into the organic solvent. This is known as “liquid-liquid extraction” or “solvent extraction,” and is conducted on a large scale by the mining industry. This process also separates heavier lanthanides from lighter lanthanides present in the same solution, because the heavier lanthanides separate more easily. While this fact is known and exploited in industrial separation processes, the nanoscale mechanisms of the separation process are not well understood.

New light has been shined on these mechanisms thanks to x-ray diffraction experiments carried out at the ChemMatCARS 15-ID-B,C,D x-ray beamline at the APS. Employing synchrotron x-ray fluorescence measurements, researchers from Northwestern University and The University of Chicago revealed that a heavier lanthanide segregates to a surfactant-laden interface at much lower

concentrations compared to a lighter lanthanide.

Furthermore, the concentration-dependent onset of surface segregation happens quite suddenly at a specific solution concentration (reminiscent of a phase transition, such as that between ice and water). The authors explain this unexpected behavior using computer simulations based on electrostatic interactions. In solutions that contain two lanthanides at the same time, the heavier lanthanide dominates at the interface, displacing the lighter lanthanide (Fig. 1).

Together, these results imply that ionic selectivity during separation happens at the interface rather than in the bulk or during dynamic processes such as stirring or mixing. By revealing the nanoscale processes responsible, such studies may pave the way to improvements in industrial extraction processes.

See: Mitchell Miller¹, Yihao Liang¹, Honghao Li¹, Miaoqi Chu¹, Sangjun Yoo¹, Wei Bu², Monica Olvera de la Cruz¹, and Pulak Dutta^{1*}, “Electrostatic Origin of Element Selectivity during Rare Earth Adsorption,” *Phys. Rev. Lett.* **122**, 058001 (2019). DOI: 10.1103/PhysRevLett.122.058001

Author affiliations: ¹Northwestern University, ²The University of Chicago

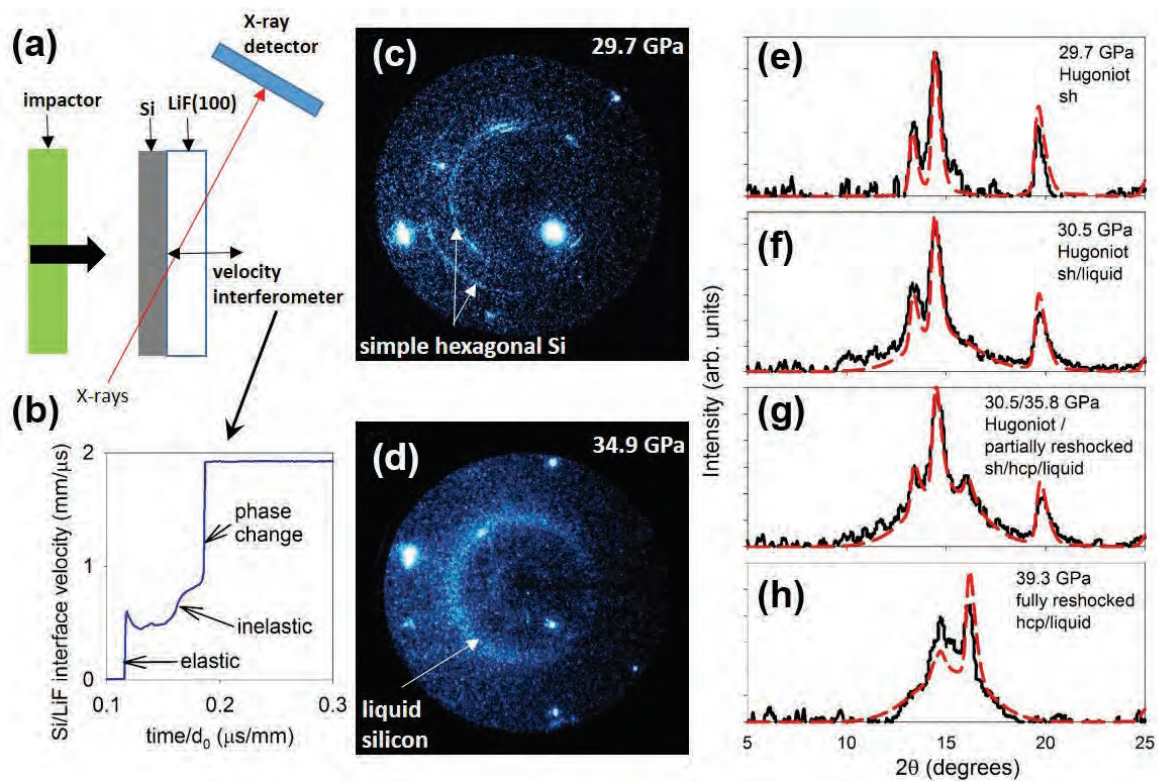
Correspondence: * p.dutta@northwestern.edu

M.M., M. C., S.Y., and P.D. were supported by National Science Foundation (NSF) Grant No. DMR- 362 1612876. Y.L., H.L., and M.O. were supported by NSF Grant No. DMR-1611076. ChemMatCARS is supported by the U.S. National Science Foundation, Grant No. CHE- 367 1346572. This research used resources of the Advanced Photon Source, a U.S. Department of Energy (DOE) Office of Science User Facility operated for the DOE Office of Science by Argonne National Laboratory under Contract No. DE-AC02-06CH11357.

SOFT MATERIALS & LIQUIDS

Melting and Recrystallization Established Unambiguously in Shock-Compressed Silicon

In situ x-ray diffraction (XRD) measurements have played a crucial role in identifying high-pressure structures in shock-induced, solid-solid phase transformations. However, solid-liquid phase transformations have proved to be more challenging, in part because volume changes associated with melting and freezing are often small and XRD patterns from liquids are not easily distinguished from those of amorphous solids. For such reasons, the direct and unequivocal demonstration of shock melting and recrystallization remained important unrealized objectives until researchers used high-brightness x-rays from the APS to perform *in situ* time-resolved XRD and simultaneous velocity interferometry measurements to examine structural changes in silicon (Si) shock-compressed to 54 GPa.



The shock-compression experiments were performed by researchers from Washington State University at the DCS 35-ID-E beamline at the APS using the 24-bunch synchrotron mode, which consists of ~100-ps-duration x-ray pulses appearing every 153.4 ns. This arrangement allowed each plate-impact experiment to consist of four powder XRD measurements 153.4-ns apart to resolve the Si structures upon initial shock compression and after re-shock from the shocked state. Simultaneous laser interferometry measurements recorded the elastic, inelastic, and phase-transformation waves propagating through the shock-compressed Si disks. Shock melting was unambiguously established above ~31–33 GPa shock stress as all sharp crystalline diffraction peaks vanished and were replaced by a single broad diffraction ring corresponding to the melted state. The experimental setup and major findings are depicted in Fig. 1.

For an impact stress of 29.7 GPa, the diffraction line profile was well matched by an XRD simulation assuming a simple hexagonal (sh) Si structure. The diffraction profile for Si shocked to a stress of 30.5 GPa matched a combination of simulated sh Si diffraction and a Gaussian hump due to liquid Si. For Si shocked to 32.7 GPa, the diffraction pattern was primarily a broad hump with weak superposed sh Si peaks, indicating that melting was nearly complete. Only a broad diffraction hump was observed for impact stresses of 34.7 GPa and higher, indicating complete melting during shock compression.

The re-shocked states provided further insight into the Si phase diagram near the melt boundary. After re-shock from states on the sh Si-liquid phase boundary, a new sharp hexagonal close-packed (hcp) peak emerged, in addition to a broad liquid Si hump, showing that the re-shocked Si passed the sh-hcp-liquid triple point but remained on the melt boundary. For complete re-shock from 32.7 to 39.3 GPa, the sh peaks were no longer present and the observed line profile matched simulated hcp diffraction peaks and a Gaussian representing liquid Si.

< Fig. 1. (a) Schematic of plate-impact experiments to examine melting and recrystallization in shock-compressed silicon. (b) Continuum velocity interferometry results showing shock waves in Si. (c), (d) Representative XRD patterns showing high-pressure simple hexagonal Si and liquid Si, respectively. (E-H) XRD line profiles showing evolution of shocked and re-shocked Si structures; black lines depict representative background-subtracted measured XRD line profiles, while red lines show simulated XRD line profiles. Adapted from S.J. Turneaure et al., Phys. Rev. Lett. **121**, 135701 (2018). © 2018 American Physical Society All rights reserved

Crystalline diffraction peaks were not observed for Si re-shocked from shock-compression stresses of 36.7 GPa or higher, indicating that the liquid-solid phase boundary was not crossed during re-shock of pure liquid Si.

In principle, the broad diffraction peaks observed from shock-melted Si could also be due to amorphization during shock compression. However, the observations of recrystallization during stress release from non-crystalline shocked states and during re-shock from a primarily non-crystalline state (from a shock stress of 32.7 GPa) suggest that the non-crystalline state in shocked Si was liquid rather than a metastable amorphous solid, since large temperature increases are typically required to initiate crystallization of an amorphous solid.

In summary, the *in situ*, time-resolved XRD measurements of shock-compressed Si showed that all crystalline diffraction peaks vanished above ~33 GPa, providing unambiguous proof of shock melting. The research was unique in that shock-compressed and re-shocked states were both examined with *in situ* XRD in the same experiment, allowing Si phase boundaries to be examined during re-shock from the high-pressure shocked state. Recrystallization of liquid Si was observed on nanosecond timescales during both re-shock and during stress release.

Such measurements provide a new approach for distinguishing between shock-induced melting and amorphization. The results also provided new insight into the high-temperature, high-pressure Si phase diagram by constraining the sh-hcp-liquid triple point, by demonstrating that the derivative $dP/dT < 0$ for the sh-hcp phase boundary, and by constraining the hcp-liquid melt line.

— Vic Comello

See: Stefan J. Turneaure, Surinder M. Sharma, and Y. M. Gupta*, “Nanosecond Melting and Recrystallization in Shock-Compressed Silicon,” Phys. Rev. Lett. **121**, 135701 (2018).

DOI: 10.1103/PhysRevLett.121.135701

Author affiliation: Washington State University

Correspondence: * ymgupta@wsu.edu

Yoshi Toyoda, Paulo Rigg, Adam Schuman, Nicholas Sinclair, and the Dynamic Compression Sector staff are thanked for their assistance with the plate-impact experiments. The research was supported by the U.S. Department of Energy (DOE) National Nuclear Security Administration (NNSA) under Award No. DE-NA0002007. The work performed at the Dynamic Compression Sector was also supported by the DOE/NNSA under Award No. DE-NA0002442. The sector is operated by Washington State University. This research used resources of the Advanced Photon Source, a DOE Office of Science User Facility operated for the DOE Office of Science by Argonne National Laboratory under Contract No. DE-AC02-06CH11357.

Photo-switching the Network Topology of Polymer Gels

A polymer network is a material composed of interconnecting polymer strands and scientists have been able to produce polymer networks with a wide range of useful properties. Researchers have now designed a polymer network that exhibits one set of properties after exposure to green light, and a second set after exposure to ultraviolet (UV) light. This two-state polymer network is based on a polymer gel incorporating numerous metal-organic cage (MOC) molecules, referred to as “polymer metal-organic cage,” or polyMOC. The researchers investigated their innovative polyMOC material using computer simulations and laboratory experiments. The latter included small-angle x-ray scattering (SAXS) experiments carried out at the APS. These studies were used to confirm the mechanism responsible for the polyMOC’s light-induced property changes. The researchers posit that the kind of switchable polyMOC they have developed could prove useful in many applications, including as a photo-actuator and in the field of soft robotics.

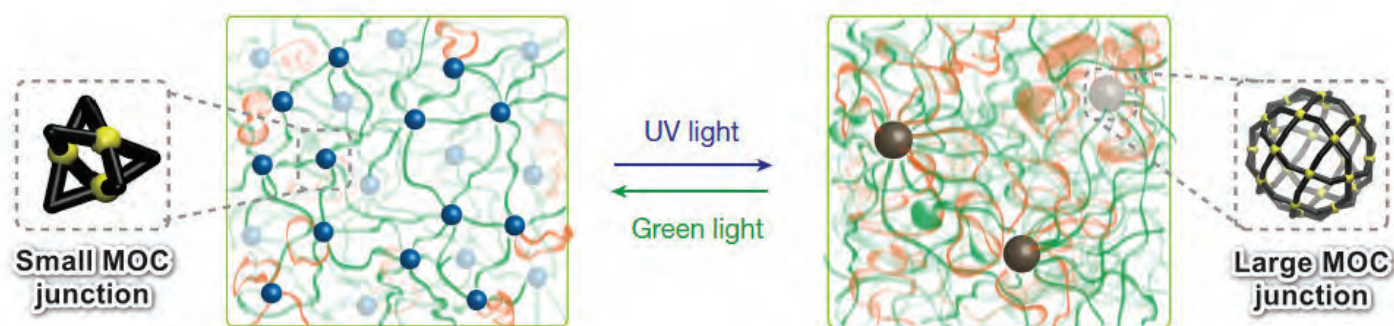


Fig. 1. The two distinct forms of the polyMOC polymer network. The left-hand box depicts the open (o-PL) form, which has many more small MOCs. Each MOC consists of palladium atoms (yellow spheres) connected to ligands (dark segments), depicted at far left and far right of the figure. The closed (c-PL) form appears in the right-hand box with fewer and larger MOCs. Changing the size and quantity of MOCs dramatically alters the distribution of the polymer strands (red and green squiggly lines). Red lines indicate primary loops, meaning both ends connect to the same MOC junction. Arrows indicate switching between the two polyMOC forms in response to light.

Polymers are long, chain-like molecules made of linked molecular monomers. Some polymer-based materials, like nylon, consist of polymer strands running more-or-less parallel to one another. In a cross-linked polymer material, such as rubber, the long polymer strands are joined together by short polymer segments to form a three-dimensional structure. The polymer strands of polymer networks twist and turn throughout the material, with their ends meeting up at common junctions. Epoxy is an example of a polymer network.

PolyMOC polymer networks have drawn considerable attention in recent years. A polyMOC is mostly composed of polymer gel, which contains polymer strands dispersed within a solvent such as water or acetonitrile; the amount of solvent helps determine the gel's pliability. A third ingredient is some type of MOC, which, in contrast to pliable polymer gels, are rigid. Chemists and materials scientists can vary the properties of polyMOCs by adjusting the material's solvent, polymer strands, and MOCs.

The goal in this study was to create a "photoswitchable" polyMOC that could reliably change between two sets of properties in response to light. The key was to select the right metal-organic cages, because the structure and bulk properties of a polyMOC depend largely upon the MOCs that form the junctions linking its polymer strands. These junctions dictate the network's topology, or structure. Palladium (Pd) was chosen for the MOC's metal component, while a photosensitive polymer ligand was selected for its organic, or carbon-based, segment. The resulting palladium/ligand (PdL) cages were linked to poly(ethylene-glycol)-based polymer chains and formed a photosensitive polyMOC network. Formation of the polyMOC was a self-directed process.

The researchers, from the Massachusetts Institute of Technology and the University of South Florida, employed light to switch their custom-designed polyMOC between two states. These two states were associated with the orientation of the ligands in PdL cages: a more open ligand structure was dubbed open-form polymer ligand (o-PL), while the more closed structure was dubbed closed-form polymer ligand (c-PL). Exposure to UV light switched the polyMOC from its o-PL to c-PL form. Applying green light reversed the process, converting it from c-PL to o-PL. Switching the polyMOC from one form to an-

other simultaneously changed its internal properties, such as its active strand density and junction connections.

Computer simulations provided insight into the photo-switching process. The o-PL ligand structure meant smaller MOC cages, while the c-PL structure yielded larger cages. The simulations indicated that differences in the size and shape of the MOC cages significantly altered the polyMOC's structure and properties. For instance, the simulations revealed that in the c-PL form, more of the polyMOC's polymer strands formed so-called "primary loops," which are elastically inactive. A primary loop occurs when both ends of a polymer strand connects to the same MOC. Figure 1 highlights differences between the o-PL and c-PL forms.

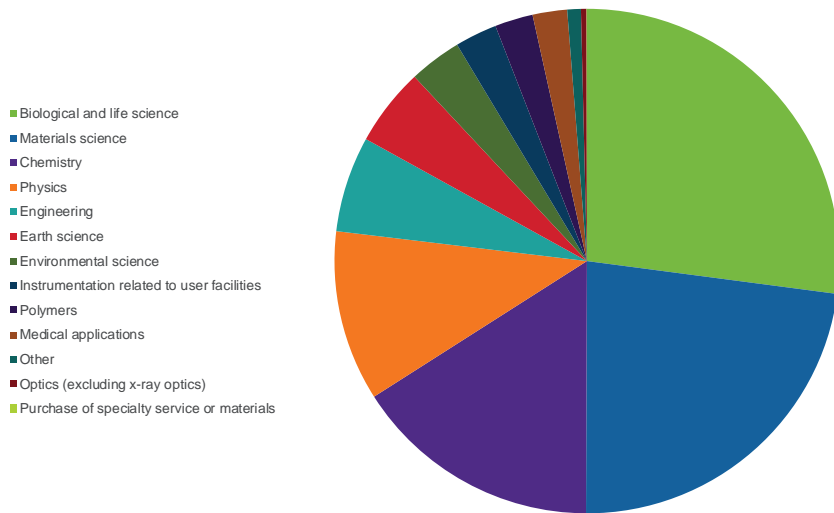
Small-angle x-ray scattering experiments to definitively measure MOC cage size were carried out at the XSD 12-ID-B x-ray beamline at the APS. The results confirmed that the polyMOC's cages were much smaller in the o-PL form than in the c-PL form, indicating that changes in the polyMOC's properties were directly tied to changes in cage size.

The researchers note other interesting properties of their custom-designed polyMOC that invite further development. For instance, its o-PL form can self-repair damage, while the c-PL form cannot. The ability to switch between the two states could promote the polyMOC's use as a self-healing material. The polyMOC might also prove useful as a model system for conducting basic polymer science research. — Philip Koth

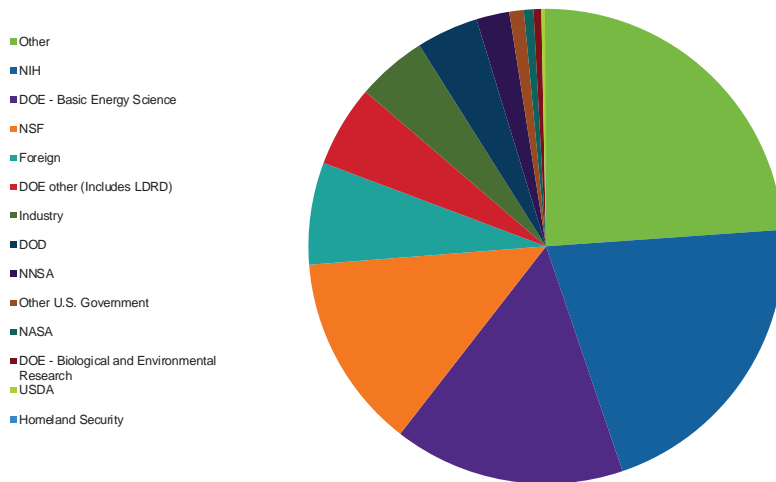
See: Yuwei Gu¹, Eric A. Alt¹, Heng Wang², Xiaopeng Li², Adam P. Willard¹, and Jeremiah A. Johnson^{1*}, "Photoswitching topology in polymer networks with metal-organic cages as crosslinks," *Nature* **560**, 65 (2 August 2018). DOI: 10.1038/s41586-018-0339-0
Author affiliations: ¹Massachusetts Institute of Technology, ²University of South Florida
Correspondence: * jaj2109@mit.edu

We thank the National Science Foundation (NSF) — CHE-1629358 for J.A.J. and CHE-1506722 for X.L. — for support of this work. This work was supported in part by the MRSEC Program of the NSF under award number DMR-1419807. Y.G. thanks ExxonMobil for an ExxonMobil-MIT Energy Fellowship. A.P.W. and E.A.A. acknowledge funding from the Research Corporation for Scientific Advancement through a Cottrell Scholars Award. This research used resources of the Advanced Photon Source, a U.S. Department of Energy (DOE) Office of Science User Facility operated for the DOE Office of Science by Argonne National Laboratory under Contract No. DE-AC02-06CH11357.

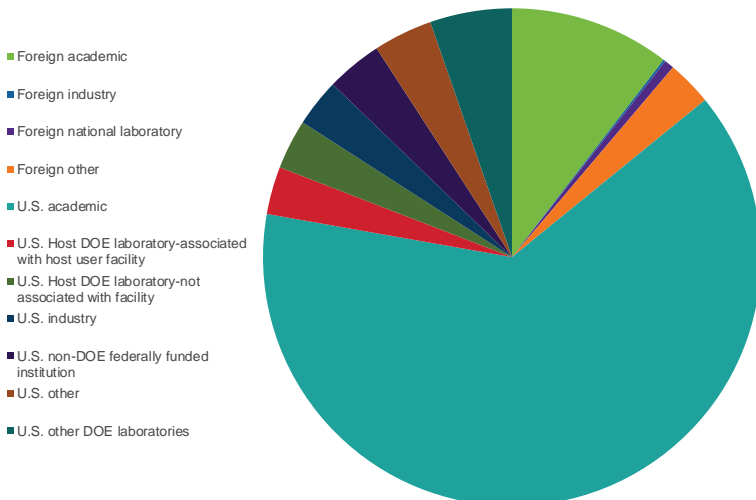
APS USERS BY EXPERIMENT SUBJECT (FY 2018)



APS USERS BY SOURCE OF SUPPORT (FY 2018)



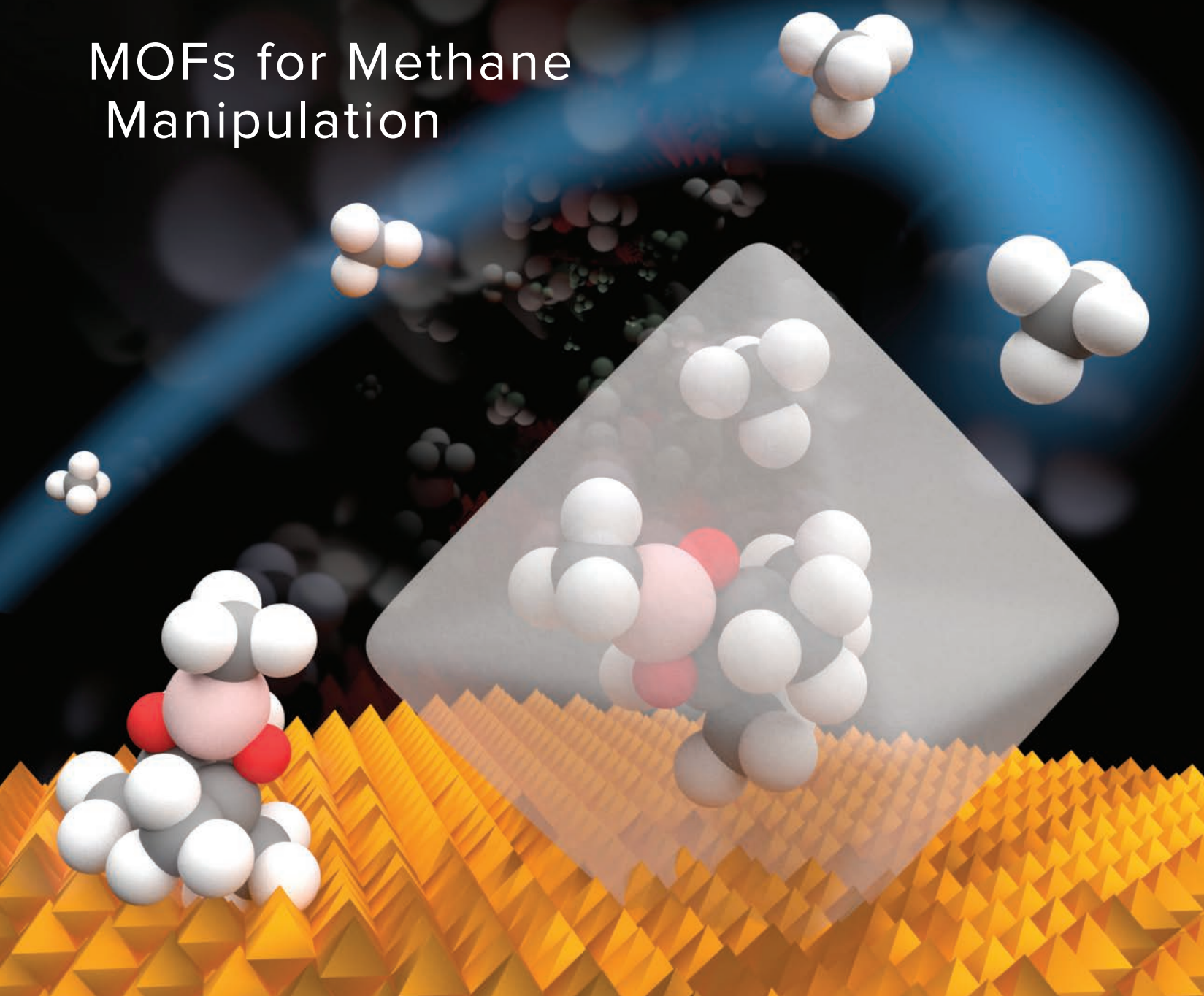
APS USERS BY EMPLOYER (FY 2018)





CHEMICAL SCIENCE

MOFs for Methane Manipulation



Methane is the main component of natural gas and there are vast quantities of this fossil fuel in reserves around the world. However, rather than just burning it for heating, this organic compound can be converted into other useful products: liquid fuels, agrochemicals, pharmaceuticals, polymers, and much more. But methane is not particularly reactive, chemically speaking. A research project from scientists using the APS has found a way to "activate" methane by using a catalyst supported in a porous, synthetic material known as a metal-organic framework (MOF). The catalyst is more than 99% selective, so it generates very little byproduct.

Fig. 1. Methane molecules are transformed in a highly selective manner within the nanopores of a MOF catalyst.

Shale gas and hydraulic fracturing technologies have opened underground and submarine reserves of natural gas, and specifically methane, to petrochemical companies. In the face of climate change and limited supplies of petrochemical feed stocks, there is pressure to exploit fossil reserves in novel ways.

The methane molecule might be thought of as a tiny tetrahedron, with a single carbon atom at its heart and a hydrogen atom at each apex of the polyhedron. Such a sturdy chemical structure cannot react with other chemi-

cals in a synthesis aimed and generating more complicated and so more useful compounds. But, there are hopes that a particular reaction known as “selective functionalization” could be used to build more sophisticated molecules from methane for conversion into useful products. The barrier to exploiting this reaction is finding a catalyst that can make the reaction occur quickly without the need of harsh conditions, such as untenable reaction temperatures and pressures or the use of strong acids. The search for an efficient and effective methane-converting catalyst is considered to be one of the grand challenges facing chemists today.

There are many different types of catalysts used industrially in a wide range of chemical reactions. By definition, a catalyst lowers the so-called activation energy of a chemical reaction and so allows the reaction to get over this metaphorical hill in a much, much shorter time than is possible without the catalyst being present. At the end of the reaction, the ideal catalyst is left wholly unchanged by the process and can be used again.

Reaction conditions are never ideal, of course, and catalysts inevitably become damaged, poisoned, and otherwise lose some of the activity with each repeated use. Finding catalysts that are powerful enough to accelerate methane activation and tough enough to be reused might be possible with a particular class of designer compounds: the MOFs. These materials are akin to a synthetic version of porous minerals known as zeolites. The unique advantage of using MOF catalysts combines the qualities of a metal catalyst and a porous support with organic chemical components, which can, in some cases, be tailored to have pores with specific shapes and sizes.

The pores within a MOF provide a vast internal surface area, which can mop up molecules of methane gas and, once attached within those pores, facilitate the interaction of the methane molecules with another chemical reagent that can convert the methane to a more sophisticated molecule. The use of a compound containing the element boron as the other reagent — specifically bis(pinacolborane) — in methane conversion has been shown to work to add a boryl group to the methane molecule. This activates it and allows attachment of other chemical groups by displacing the reactive boryl group.

One particular MOF — Universitetet i Oslo-67, or UiO-67 — is very stable and contains a hexazirconium cluster in each unit with an organic molecular group, 4,4'-biphenyl dicarboxylate linking the metal clusters together. The openings in this porous material are 0.8 nm in diameter and the octahedral cavities have a volume of 1.1

nm³. This allows methane and bis(pinacolborane) inside and once held within, they can react to generate a new borylated methane molecule with just a single boryl group (Fig. 1). A second form of the molecule, which has two boryl groups, would normally be more likely to form in solution, but within the precise confines of UiO-67 it is too big to fit and so does not form in the MOF.

The team of researchers from Argonne and Northwestern University acquired x-ray absorption measurements on the insertion device beamline 10-ID-B of MR-CAT at the APS. Critically, this work, in combination with inductively coupled plasma atomic emission spectroscopy, showed that the iridium metal atoms in UiO-67-Mix-Ir were present with two atoms per zirconium node in the porous structure. Additionally, the energy-dispersive x-ray analysis showed that the iridium was uniformly present throughout the MOF crystallites.

Such chemical details about the catalyst is essential to proving that the catalyst is working in the way the team predicted it would. Moreover, understanding the details of the catalyst's structure and how it facilitates the chemoselective borylation of methane will allow researchers to fine tune the catalyst and potentially develop related MOFs that could be used to modify methane in other ways. It might also help in the design of MOFs that could be used for entirely different chemical transformations of other small organic molecules.

— David Bradley

See: Xuan Zhang¹, Zhiyuan Huang², Magali Ferrandon², Dali Yang², Lee Robison¹, Peng Li¹, Timothy C. Wang¹, Massimiliano Delferro^{2*}, and Omar K. Farha^{1**}, “Catalytic chemoselective functionalization of methane in a metal–organic framework,” *Nat. Catal.* **1**, 356 (May 2018). DOI: 10.1038/s41929-018-0069-6
Author affiliations: ¹Northwestern University, ²Argonne National Laboratory

Correspondence: * delferro@anl.gov,

** o-farha@northwestern.edu

This work was supported as part of the Inorganometallic Catalyst Design Center, an Energy Frontier Research Center funded by the U.S. Department of Energy (DOE) Office of Science-Basic Energy Sciences, under award DESC0012702. MR-CAT operations are supported by the U.S. DOE and the MR-CAT member institutions. This work made use of the IMSERC, Jerome B. Cohen X-Ray Diffraction, EPIC, and KECK II facilities of Northwestern University's NUANCE Center, which has received support from the Soft and Hybrid Nanotechnology Experimental Resource (National Science Foundation ECCS-1542205), the MRSEC programme (NSF DMR-1121262) at the Materials Research Center, the International Institute for Nanotechnology, the Keck Foundation, and the State of Illinois, through the International Institute for Nanotechnology. This research used resources of the Advanced Photon Source, a U.S. DOE Office of Science User Facility operated for the DOE Office of Science by Argonne National Laboratory under Contract No. DE-AC02-06CH11357.

Converting Shale Gas Ethane to Valuable Ethylene

We are in the midst of a “Shale Gas Revolution” that has dramatically altered the domestic energy and petrochemical landscape. Petrochemical companies that had situated themselves in the Middle East for decades are flocking to the Gulf Coast and Appalachia to take advantage of the abundance of cheap ethane feed stocks and the advancements in cracking technology to produce ethylene for plastics. With plastics firmly integrated into every aspect of modern life, scientists are continuing to push the boundaries of what is possible in the conversion of ethane to ethylene by improving atom economy, reducing hazardous gas emissions, and even utilizing other undesirable byproducts like carbon dioxide. Toward this goal, a team of researchers recently evaluated a new class of multi-functional catalysts capable of reducing carbon dioxide and dehydrogenating ethane in tandem. In order to increase ethane-to-ethylene selectivity, the researchers sought to identify the catalytic active sites. Using *in situ* characterization experiments, some of which were performed at the APS and the Stanford Synchrotron Radiation Lightsource, combined with density-functional theory calculations, the researchers identified two types of metal-oxide active sites responsible for the CO₂-assisted ethane dehydrogenation reaction. These findings present a pathway for tuning the catalytic activity and selectivity, which allows ethane from shale gas to be more efficiently converted to ethylene and, eventually, valuable end-products. Additionally, making use of shale gas byproducts, which would otherwise be emitted, helps to mitigate man-made CO₂ emissions.

Ethylene is one of the most important intermediates in the chemical industry and is used to make everyday products like textiles, pharmaceuticals, plastic packaging, agricultural products, diapers, electronics, and so much more. Since many of the traditional routes for producing ethylene from ethane are energy-intensive and riddled with inefficiencies, alternative routes for producing ethylene from ethane are piquing the interest of those in the petrochemical industry. One such alternative route uses a bifunctional catalyst to facilitate the dehydrogenation of ethane using carbon dioxide (CO₂). Specifically, the researchers propose that atomic oxygen produced from the reduction of CO₂ on a supported metal-oxide catalyst will assist the dehydrogenation of ethane to ethylene.

Although a variety of supported metal oxide catalysts have been used for the activation of CO₂ and ethane, little is known about the nature of the catalyst active sites. This lack of knowledge presents a problem because the structure of the catalytic active sites largely determines catalyst activity and selectivity. Now, a team of re-

searchers has presented their findings on the catalytic active sites of a series of NiFe-CeO₂ catalysts.

Using a set of *in/ex situ* diffraction experiments available at the APS and the Stanford Linear Accelerator Center coupled with density functional theory, the team of researchers from Brookhaven National Laboratory, Tsinghua University (China), Stony Brook University, and Columbia University was able to show that the two most likely active sites of the catalyst are the Ni-FeO_x and the Ni-CeO_x interfaces. More interestingly, the researchers successfully applied x-ray diffraction at XSD beamline 17-BM and x-ray absorption spectroscopy at XSD beamline 9-BM, both at the APS, and x-ray absorption near-edge spectroscopy at the 2-2 beamline at the Stanford Synchrotron Radiation Lightsource to show that these two sites exhibited very distinct catalytic behavior. Specifically, the Ni-FeO_x interfacial sites can selectively break the C-H bonds and preserve the C-C bond of ethane to produce ethylene, whereas the Ni-CeO_x interfacial sites efficiently cleave all of the C-H and C-C

Active Sites and Reaction Mechanisms

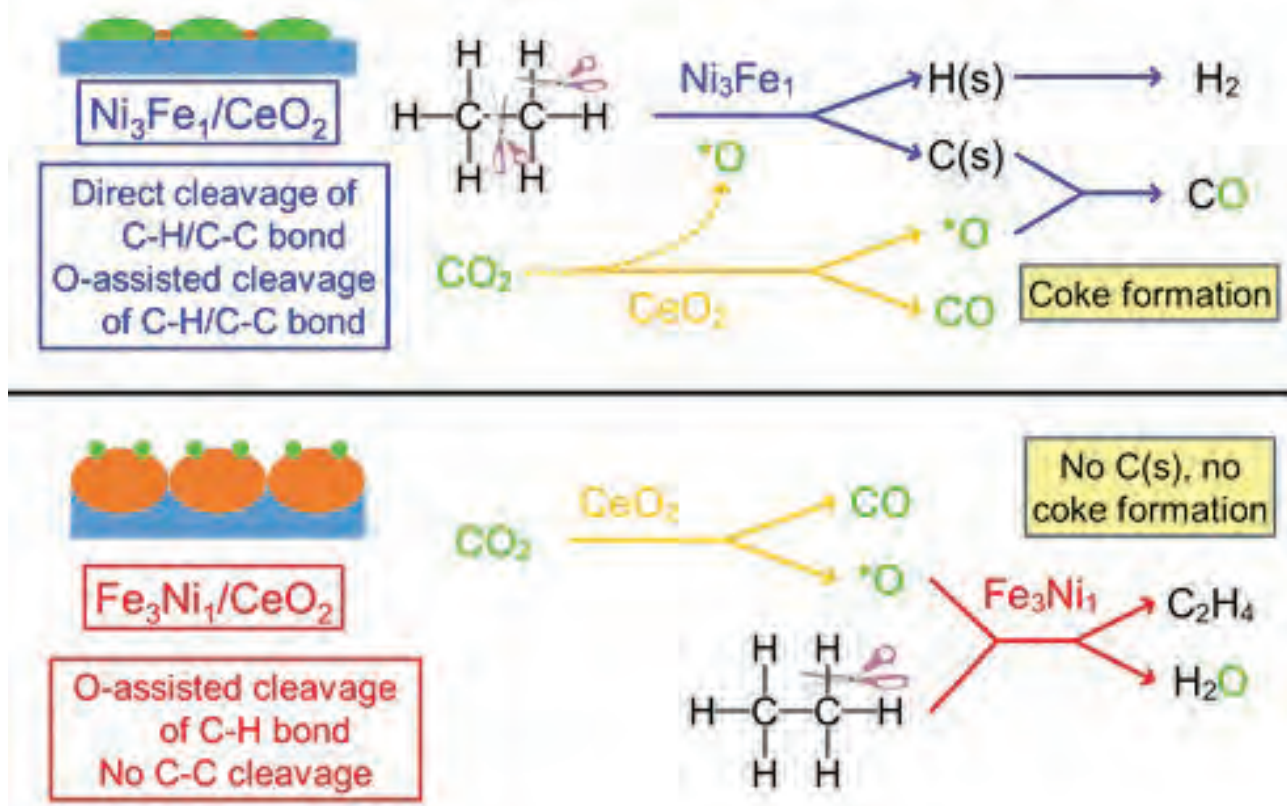


Fig. 1. Reaction mechanisms for the CO_2 -assisted dehydrogenation of ethane to ethylene using $\text{Ni}_3\text{Fe}_1/\text{CeO}_2$ (above) and $\text{Fe}_3\text{Ni}_1/\text{CeO}_2$ (below). The $\text{Ni}-\text{CeO}_x$ interfacial sites cleaves all of the C-H and C-C bonds to produce synthesis gas, while the $\text{Ni}-\text{FeO}_x$ interfacial sites selectively break the C-H bonds and preserve the C-C bond of ethane to produce ethylene.

bonds to produce synthesis gas. By varying the amount of iron in the catalyst, the researchers were able to tune the selectivity of the catalyst by controlling the quantity of $\text{Ni}-\text{CeO}_x$ sites on the catalyst.

Favoring the formation of dispersed $\text{Ni}-\text{FeO}_x$ active sites, the researchers were able to rationally design a catalyst with high ethylene selectivity through the CO_2 -assisted dehydrogenation of ethane. A visual representation of the reaction mechanisms and active sites are illustrated in Fig. 1.

By gaining a better understanding of the structure-function relationships between catalytic active sites and performance, the researchers showed the ability to rationally tune the selectivity of a bi-functional catalyst aimed at utilizing CO_2 to assist in the dehydrogenation of ethane.

This research is one part of the overall need to improve our ability to convert shale gas into value-added

products. By rationally designing catalysts aimed at lowering the overall energy requirements and improving atom economy for industrially relevant systems like ethane dehydrogenation, the chemical industry will continue to be positioned to capitalize on our abundant natural resources in the U.S. while also minimizing the environmental footprint. — Alicia Surrao

See: Binhang Yan^{1,2}, Siyu Yao¹, Shyam Kattel¹, Qiyan Wu³, Zhenhua Xie⁴, Elaine Gomez⁴, Ping Liu¹, Dong Su¹, and Jingguang G. Chen^{1,4*}, "Active sites for tandem reactions of CO_2 reduction and ethane dehydrogenation," Proc. Natl. Acad. Sci. U.S.A. **115**(33), 8278 (August 14, 2018). DOI: 10.1073/pnas.1806950115

Author affiliations: ¹Brookhaven National Laboratory, ²Tsinghua University, ³Stony Brook University, ⁴Columbia University
Correspondence: * jgchen@columbia.edu

The work that was partly carried out at Brookhaven National Laboratory (BNL) was supported by the U.S. Department of Energy (DOE) Office of Science-Basic Energy Sciences, under Contract DE-SC0012704. The DFT calculations were performed using computational resources at the Center for Functional Nanomaterials at BNL, a DOE Office of Science User Facility, and at the National Energy Research Scientific Computing Center, a DOE Office of Science User Facility, supported by the Office of Science of the DOE under Contract DE-AC02-05CH11231. This research used resources of the Advanced Photon Source, a U.S. DOE Office of Science User Facility operated for the DOE Office of Science by Argonne National Laboratory under Contract No. DE-AC02-06CH11357.

The Stresses and Strains of a New Type of Chemistry

Chemical reactions usually proceed when we heat reagents or when we shine light on them. Others happen when an acid or an alkali is added. Rare is the reaction that occurs when we squeeze or stretch the ingredients, but such mechanochemical reactions could be useful in making novel compounds that are wholly inaccessible to conventional chemistry. One approach to mechanochemistry that is yet to come to the fore is the idea of compression leading to chemical changes. Now, just such reactions have been followed using high-pressure x-ray absorption spectroscopy (XAS) and x-ray diffraction (XRD) experiments performed at the APS and Advanced Light Source (ALS), respectively. This research reveals the secrets of what might be referred to as a molecular anvil in action.

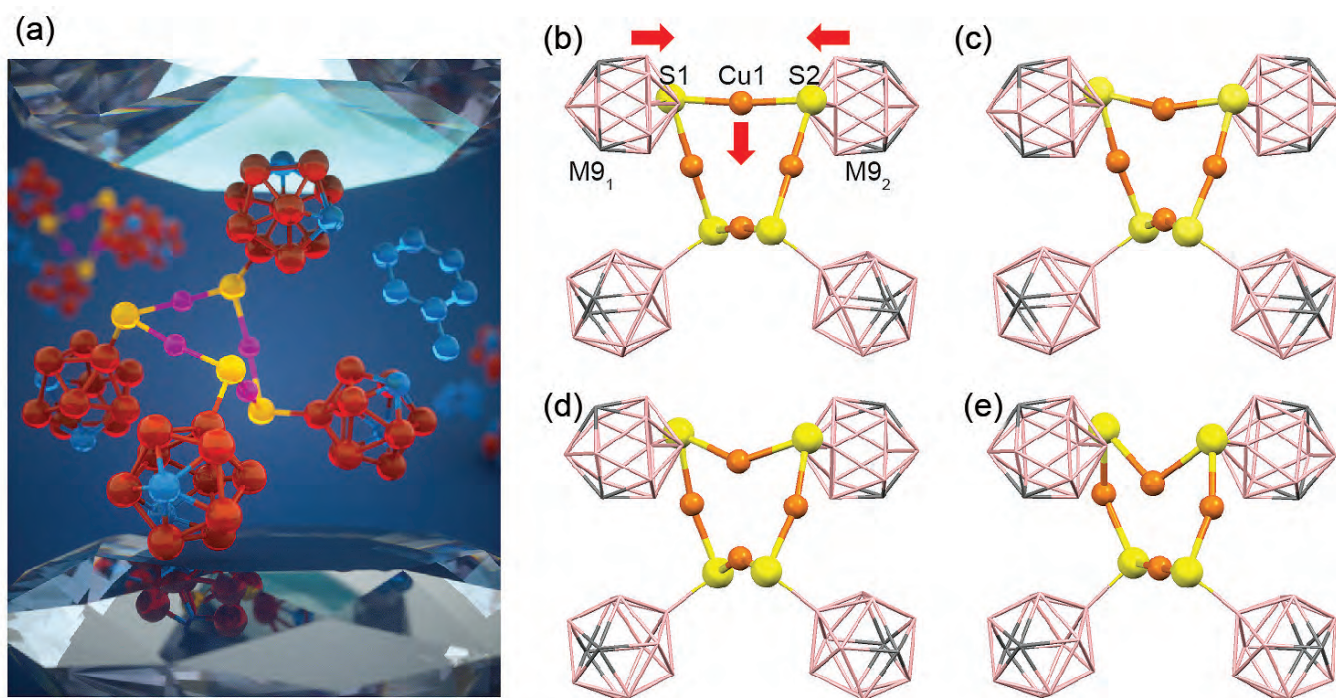


Fig. 1. “Molecular anvils” squeezed to react. (a) Artist’s rendition of compression-driven reactions in a diamond anvil cell. (Image courtesy of P. Allen, UC Santa Barbara.) (b)-(e), Structures of the Cu-S-M9 molecule from a pressure of 2 to 12 GPa showing the bending of S-Cu-S bond angle, which leads to the redox reaction.

Chemists have tested some of the possibilities of mechanochemistry. By tugging on polymer strands they have deformed and even managed to break bonds within the molecules that make up the chain-like strands. With these long molecules under tensile stress, they have seen reorganization of the atoms within the chains, unzipping the polymers. They have even seen so-called “ring-opening” reactions, where groups of carbon atoms joined in a circle, and those circles hooked into the polymer chain have been pulled open. They have also observed disulfide reduction reactions taking place because of mechanical forces. All of these reactions offer a model for what might be possible when mechanical stresses and strains are applied to molecules.

The present research by a multi-institute, multi-nation collaboration demonstrates how a molecular-level stress can be converted into a strain in a material that comprises a compressible, soft component (the mechano-phore), and incompressible, hard ligands (Fig. 1).

Ligands are simply chemical groups, while the term mechano-phore refers to the part of the system that responds to mechanical stress just as a chromophore in a molecule responds to color. In parallel with this, the researchers in this study also discuss the converse wherein rigid ligands that are touching each other impede relative motion and so block any reaction that might otherwise be induced by compression.

Experiments with crystals of copper(I) m-carborane-9-thiolate (Cu-S-M9) demonstrated the molecular anvil concept. In this reaction system, pressure drives the redox reactions in materials known generally as metal–organic chalcogenides of which Cu-S-M9 is an example. These materials incorporate molecular elements that have different degrees of compressibility depending on how they are compressed; they are heterogeneous.

The m-carborane-9-thiolate (M9) ligands are structurally rigid because of their cage-like nature. As such, bending of bond angles or shearing of adjacent chains of atoms in the material activates the metal–chalcogen bonds and this actually releases the metal as its elemental form. This is a very different reaction route to that which would otherwise be taken by the same chemicals if they were simply heated rather than being exposed to mechanical stress. Heating the material produces cop-

per(I) sulfide rather than metallic copper. The XAS data obtained at the HP-CAT beamline 16-BM-D at the APS and the XRD data from the Lawrence Berkeley National Laboratory ALS help explain this difference in terms of the positions of the atoms within the material and how mechanochemistry, rather than heat, leads them to rearrange in two very different ways.

The important outcome from this current approach to mechanochemistry is that, whereas polymer mechanochemistry requires long chain-like molecules that are difficult to handle, the new anvil approach involves different types of chemical ligands that have been well studied in conventional chemistry and might be adapted easily to expand their repertoire as agents for this kind of chemistry under pressure. — David Bradley

See: Hao Yan^{1,2*}, Fan Yang^{1,2*}, Ding Pan^{3,4*}, Yu Lin¹, J. Nathan Hohman⁵, Diego Solis-Ibarra⁶, Fei Hua Li^{1,2}, Jeremy E.P. Dahl¹, Robert M.K. Carlson¹, Boryslav A. Tkachenko⁷, Andrey A. Fokin^{7,8}, Peter R. Schreiner⁷, Giulia Galli⁹, Wendy L. Mao^{1,2}, Zhi-Xun Shen^{1,2}, and Nicholas A. Melosh^{1,2*}, “Sterically controlled mechanochemistry under hydrostatic pressure,” *Nature* **554**, 505 (22 February 2018). DOI: 10.1038/nature25765

Author affiliations: ¹SLAC National Accelerator Laboratory, ²Stanford University, ³Hong Kong University of Science and Technology, ⁴HKUST Fok Ying Tung Research Institute, ⁵Lawrence Berkeley National Laboratory, ⁶Universidad Nacional Autónoma de México, ⁷Justus-Liebig University, ⁸Igor Sikorsky Kiev Polytechnic Institute, ⁹The University of Chicago
Correspondence: * nmelosh@stanford.edu

We thank C. Park and D. Popov from the APS for XAS measurements, and C. Beavers, J. Yan, and S. Teat from the Advanced Light Source for help with XRD measurements. This work was supported by the U.S. Department of Energy (DOE) Office of Science-Basic Energy Sciences, Division of Materials Science and Engineering, under contracts DE-AC02-76SF00515 and DE-FG02-06ER46262. D.P. acknowledges support from Hong Kong Research Grants Council (project number ECS-26305017), the National Natural Science Foundation of China (project number 11774072), and the Alfred P. Sloan Foundation through the Deep Carbon Observatory. D.S.-l. acknowledges support from PAPIIT IA203116/27 and CONACYT FC-2015-2/829. This research used resources of the Advanced Light Source, which is a U.S. DOE Office of Science User Facility under contract DE-AC02-05CH11231. Portions of this work were performed at the Stanford Nano Shared Facilities, supported by the National Science Foundation under award ECCS-1542152. This research also used resources of the Advanced Photon Source, a U.S. DOE Office of Science User Facility operated for the DOE Office of Science by Argonne National Laboratory under contract DE-AC02-06CH11357.

Pulling Back the Mechanistic Curtain on Iron Zeolite Catalysts

An economical and selective process for converting inert hydrocarbons like alkanes and aromatics into alcohols remains a fundamental challenge in the area of catalysis and could bring with it significant economic benefits. In particular, selective production of phenol from benzene remains an elusive target and the traditional Hock process used to make phenol has very poor atom economy, resulting in the production of unwanted byproducts like acetone. With the global phenol market expected to reach ~14.5 million tons by 2022, improved catalytic processes are needed to ensure that market demand can be reached, preferably without flooding the market with unwanted byproducts. In comparison to the Hock process, a processing route was discovered that used iron zeolites for the partial oxidation of benzene to phenol. These catalysts achieved outstanding selectivity and impressive conversion rates. However, the mechanism for this reaction and the catalyst deactivation has remained something of a mystery. That is, until a team of researchers working at the APS and the Stanford Synchrotron Radiation Lightsource (SSRL) employed advanced spectroscopic techniques to successfully define the catalytic mechanism and deactivation pathway for these important industrial catalysts. This research has shifted the field closer to understanding the relationship between active site structure and catalytic activity and selectivity. This knowledge brings with it a more realistic possibility of achieving synthetic control over catalytic function in the selective oxidation of hydrocarbons.

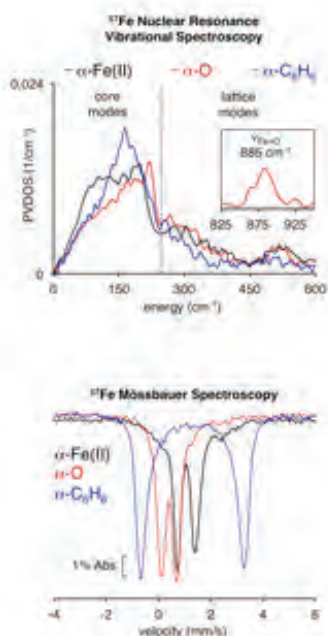
Zeolite catalysts are microporous, aluminosilicate materials that are used to synthesize a variety of products we encounter in our everyday lives. They catalyze reactions from pharmaceutical to petrochemical, where they're used in catalytic crackers to break down large hydrocarbon molecules into gasoline, diesel, kerosene, waxes, and more. Fe-containing zeolites are known for their potential as catalysts in the selective partial oxidation of methane to methanol at room temperature, and the direct conversion of benzene to phenol. However, the mechanism governing selective benzene hydroxylation with Fe zeolite catalysts has been an enigma until recently, when researchers from Stanford University, the Katholieke Universiteit Leuven (Belgium), Argonne, and the SLAC National Accelerator Laboratory used advanced spectroscopic techniques to identify the catalytic active site and reveal mechanistic details.

The active site, known as α -Fe(II), was identified by the same researchers from Stanford University and the Katholieke Universiteit Leuven in previous studies as a mononuclear square planar Fe(II) center. α -Fe(II) is activated by nitrous oxide to form a mononuclear square pyramidal Fe(IV)=O reactive intermediate. The constrained coordination geometry of the Fe(IV)=O species enables

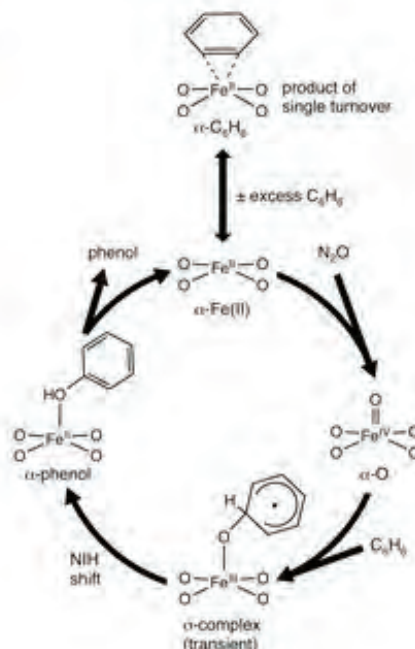
H-atom abstraction from methane at room temperature. However, direct experimental tracking of the reaction between the Fe(IV)=O species and benzene had been lacking. In this work, the teams of researchers conducted x-ray absorption spectroscopy experiments at the SSRL beamlines 7-3 and 9-3, and ^{57}Fe nuclear resonance vibrational spectroscopy (NRVS) at XSD beamline 3-ID-D at the APS to characterize the ligation of benzene to the active site. This combination of techniques allowed the researchers to selectively probe the vibration of the iron active sites. And more importantly, the techniques proved to be highly sensitive to the S=2 Fe(II) centers, which are notoriously difficult to resolve using traditional laboratory spectroscopic techniques.

From data collected in this study (Fig. 1), the researchers determined that the conversion of benzene to phenol results from a room temperature reaction between benzene and the Fe(IV)=O active species, with the release of the phenol product, regenerating the reduced α -Fe(II) site. In fact, efficient regeneration of the α -Fe(II) active site explains why this Fe-zeolite system is such an effective catalyst, compared to systems involving other mononuclear Fe(IV)=O intermediates. Specifically, the catalytic system studied here achieves high levels of se-

spectroscopy of catalytic intermediates



catalytic mechanism



assignment of single turnover product

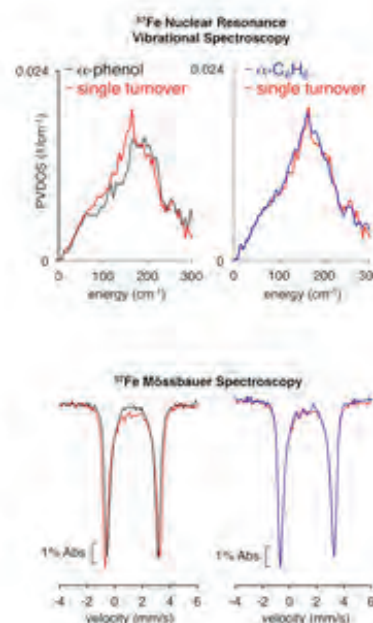


Fig 1. Spectroscopic studies, including ^{57}Fe NRVS experiments performed at APS (left), enabled structural characterization of key intermediates in the catalytic mechanism of benzene hydroxylation (center). For example, NRVS data proved crucial in determining the product of single turnover for this reaction (right), as structural candidates could not be distinguished

lectivity (95+%) at high levels of conversion (40+%), while other Fe(IV) = O intermediates attain lower levels of selectivity (0–70%) at lower levels of conversion (<10%). However, the regeneration of the α -Fe(II) species is not 100% efficient. Instead, using a combination of resonance Raman spectroscopy, ^{57}Fe Mössbauer spectroscopy, and variable-temperature variable-field magnetic circular dichroism, the authors showed that between 0.2% and 5% of the iron sites deactivate during a single catalytic turnover, producing an inactive Fe(III) phenolate species.

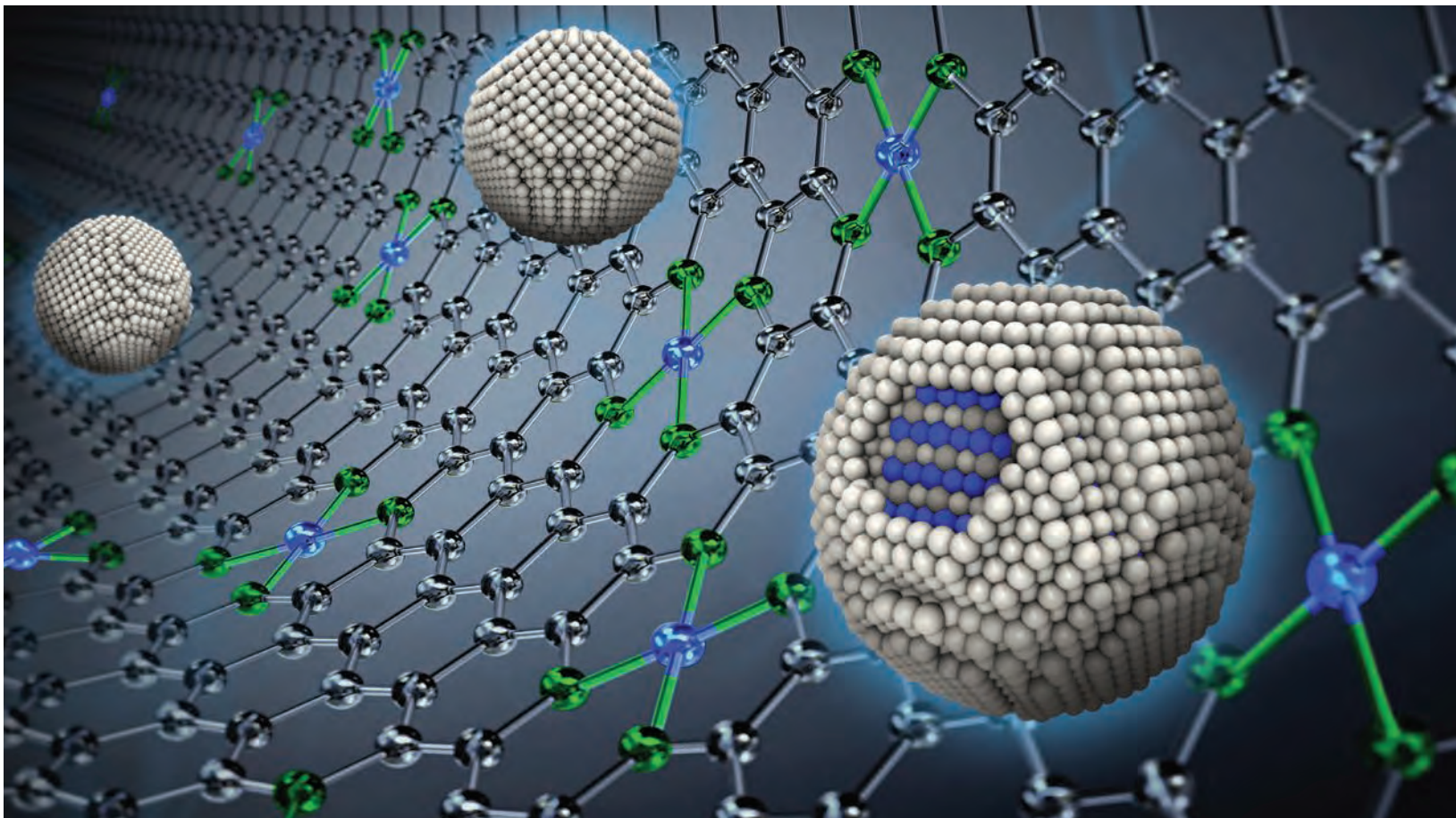
The focus of this research was to define the mechanism for benzene hydroxylation by an unusually reactive Fe(IV) = O active site stabilized in a zeolite lattice. This was achieved with the help of sophisticated spectroscopic techniques from the APS and the SSRL. The researchers also employed a set of techniques to elucidate the deactivation mechanism through the formation of inactive Fe(III)-phenolate species. The knowledge from this paper extends beyond the hydroxylation of benzene. Mechanistic insights developed through this work could potentially be applied used for enhancing the catalytic hydroxylation of inert hydrocarbons in microporous materials. — Alicia Surrao

See: Benjamin E. R. Snyder¹, Max L. Bols², Hannah M. Rhoda¹, Pieter Vanelderden^{1,2}, Lars H. Böttger¹, Augustin Braun¹, James J.

Yan¹, Ryan G. Hadt¹ⁱⁱ, Jeffrey T. Bobicz, Jr.¹, Michael Y. Hu³, Jiyong Zhao³, E. Ercan Alp³, Britt Hedman⁴, Keith O. Hodgson^{1,4}, Robert A. Schoonheydt^{2*}, Bert F. Sels^{2**}, and Edward I. Solomon^{1,4***}, “Mechanism of selective benzene hydroxylation catalyzed by iron-containing zeolites,” *Proc. Natl. Acad. Sci. U.S.A.* **115**(48), 12124 (November 27, 2018). DOI: 10.1073/pnas.1813849115
 Author affiliations: ¹Stanford University, ²Katholieke Universiteit Leuven, ³Argonne National Laboratory, ⁴SLAC National Accelerator Laboratory Present addresses: ¹University of California, Berkeley, ⁱⁱCalifornia Institute of Technology
 Correspondence: *robert.schoonheydt@biw.kuleuven.be, **bert.sels@biw.kuleuven.be, *** edward.solomon@stanford.edu

B.E.R.S. acknowledges support from National Science Foundation (NSF) Graduate Research Fellowship Program Grant DGE-11474 and from the Munger, Pollock, Reynolds, Robinson, Smith & Yoedicke Stanford Graduate Fellowship. M.L.B. acknowledges the Research Foundation–Flanders for funding of his stay at Stanford University (Grant V417018N). R.G.H. acknowledges a Gerhard Casper Stanford Graduate Fellowship. P.V. acknowledges Research Foundation–Flanders (Grant 12L0715N) and Katholieke Universiteit Leuven for his postdoctoral fellowships and travel grants during his stay at Stanford University. Funding for this work was provided by NSF Grant CHE-1660611 (to E.I.S.) and Research Foundation–Flanders Grant G0A2216N (to B.F.S.). Use of the SSRL, SLAC National Accelerator Laboratory, is supported by the U.S. Department of Energy (DOE) Office of Science-Basic Energy Sciences under Contract DE-AC02-76SF00515. The SSRL Structural Molecular Biology Program is supported by the DOE Office of Biological and Environmental Research and by the National Institutes of Health, National Institute of General Medical Sciences Grant P41GM103393 (to K.O.H.). This research used resources of the Advanced Photon Source, a U.S. DOE Office of Science User Facility operated for the DOE Office of Science by Argonne National Laboratory under Contract DE-AC02-06CH11357.

A Highly Efficient Fuel Cell Catalyst with an Ultralow Amount of Platinum



Fuel cells generate much of the back-up electrical power for both urban and rural residences thanks to their reliability and efficiency. Proton exchange membrane fuel cells are considered to be the next-generation power train for midsize and heavy-duty vehicles. The electrochemical reactions inside of fuel cell electrodes need to be promoted by catalysts. Typically, these catalysts are made of platinum, a scarce and expensive material. A recent study carried out at the APS demonstrated a new catalyst that contains an ultra-low quantity of platinum, yet maintains a high degree of efficiency. This catalyst has already exceeded a number of performance targets set by the U.S. Department of Energy's Fuel Cell Technologies Office for the year 2025.

Fuel cells convert the chemical energy of a fuel into electricity through oxidation and reduction reactions. They differ from batteries because they are open systems and require a constant supply of fuel and reactant. They have less volume and weight than batteries because they do not have to store the energy inside themselves. The parts of all fuel cells are similar: an anode (for oxidizing fuel) and a cathode (for reducing oxygen), separated by an electrolyte such as a proton-exchange membrane, which allows ions to move between the two electrodes while keeping fuel and oxygen apart. A proton-exchange membrane fuel cell commonly uses platinum or platinum-group metals (PGMs) as the catalysts to facilitate the chemical reactions at both electrodes. One of the biggest challenges in fuel cell catalyst research is how to reduce or even eliminate the heavy use of costly platinum without compromising the fuel-to-electricity conversion efficiency. Using PGM-free catalysts made of abundant natural materials represents an attractive choice, but they are not, at present, as effective as platinum.

A team comprising members from Argonne, Purdue University, and Shanghai Jiao Tong University (China) set about overcoming the problems of high platinum usage and a low-performance PGM-free catalyst by leveraging the synergistic interaction between the two through an innovative design. The team first used a cobalt metal-organic framework to prepare a catalytic substrate densely populated with PGM-free active sites and cobalt nanoparticles through thermal activation. They then added a very low amount of platinum over the cobalt nanoparticles to form an alloy with a platinum-cobalt core and a platinum shell. The synergistic catalysis between the platinum-cobalt core-shell catalytic centers and PGM-free active sites greatly improved catalytic efficiency even with an ultralow amount of platinum in the fuel cell.

The catalysts developed by this approach were analyzed via x-ray absorption near edge structure and extended x-ray absorption fine structure spectroscopy at XSD beamline 12-BM at the APS. Both types of x-ray data confirmed the formation of the alloys and PGM-free catalytic site by revealing the platinum and cobalt electronic and coordination structures.

< [An artistic rendition of Pt-Co shell nanoparticles supported on Co-N-C catalytic substrate.](#) Image: Christopher E. Galvin

To test the catalytic performance, the team added the catalysts to the cathode of a membrane electrode assembly within a single-cell proton-exchange membrane fuel cell. They tested the catalysts using both oxygen and air at different feed rates and pressures. They measured the mass activities and current densities and found that both exceeded the DOE target values, indicating that the catalysts have strong commercial potential.

In addition, they compared other characteristics of their catalysts to the commercial platinum catalysts and found that their catalysts can generate higher fuel cell performance even at 3-to-5 times lower platinum loading than the commercial cells.

The team also studied the durability of their ultra-low platinum catalysts by putting them through a 30,000-voltage-cycle accelerated stress test. The catalyst further demonstrated an excellent stability by exceeding several DOE durability targets, paving the way for its application in fuel cell for transportation. — [Mary Alexandra Agner](#)

See: Lina Chong¹, Jianguo Wen¹, Joseph Kubal^{1,2}, Fatih G. Sen¹, Jianxin Zou³, Jeffery Greeley², Maria Chan¹, Heather Barkholtz¹, Wenjiang Ding³, and Di-Jia Liu^{*}, “Ultralow-loading platinum-cobalt fuel cell catalysts derived from imidazolate frameworks,” *Science* **362**, 1276 (2018). DOI: 10.1126/science.aau0630

Author affiliations: ¹Argonne National Laboratory, ²Purdue University, ³Shanghai Jiao Tong University

Correspondence: * djliu@anl.gov

This work was supported by the U.S. Department of Energy (DOE) Fuel Cell Technologies Office through the Office of Energy Efficiency and Renewable Energy. J.Z. and W.D. wish to thank the National Key Research and Development Program of China (2016YFB0701200) and Chinese National Nature Science Foundation (51771112) for support. L.C. wishes to thank Argonne National Laboratory for the Maria Goeppert Mayer Fellowship. J.K. and J.G. acknowledge funding through the U.S. DOE Office of Science-Basic Energy Sciences, Chemical, Biological, and Geosciences Division under DE-SC0010379. J.K. wishes to thank the U.S. DOE Office of Science, Office of Workforce Development for Teachers and Scientists, Office of Science Graduate Student Research (SCGSR) program. The SCGSR program is administered by the Oak Ridge Institute for Science and Education for the DOE under contract number DE-SC0014664. This research used resources of the National Energy Research Scientific Computing Center (NERSC), a U.S. DOE Office of Science User Facility supported under contract no. DE-AC02-05CH11231. Use of the Center for Nanoscale Materials, an Office of Science user facility, was supported by the U.S. DOE Office of Science-Basic Energy Sciences, under Contract No. DE-AC02-06CH11357. This research used resources of the Advanced Photon Source, a US Department of Energy (DOE) Office of Science User Facility operated for the DOE Office of Science by the Argonne National Laboratory under Contract DE-AC02-06CH11357.

Mixing Metals to Make Better Catalysts

Energy companies that extract natural gas from shale formations in the ground want to convert that gas into transportation fuel. To do that, they need a new generation of catalysts with long lifetimes, high selectivity, and the ability to survive high-temperature, high-pressure processes. Scientists using the APS are examining the structures of nanoparticles to see which have potential for the next-generation catalyst. The aim is to convert the ethane in shale gas into hydrogen and ethylene, which can then be processed further into fuel.

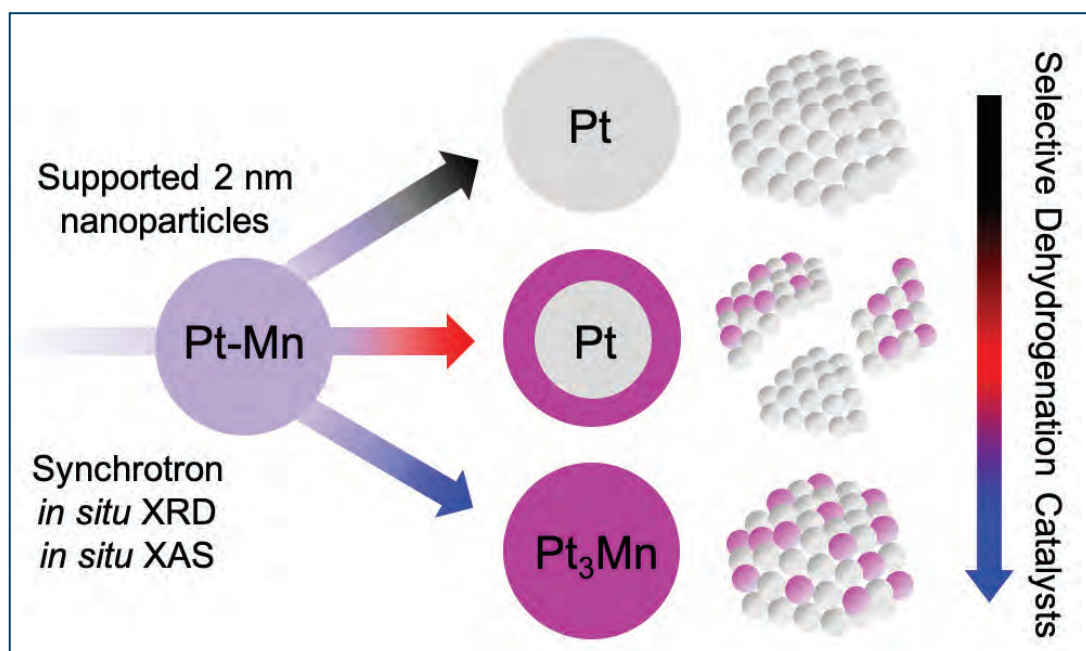


Fig. 1. Platinum and manganese can make different types of supported nanoparticles with different characteristics. Synchrotron x-ray diffraction and x-ray absorption spectroscopy analyses show that pure platinum nanoparticles have lower selectivity for the desired product, ethylene. Nanoparticles with a platinum core and alloy shell have higher selectivity, and those that are entirely alloys have the highest.

It's also important not to produce methane or deposit carbon too quickly on the catalyst, reducing its effectiveness and requiring it to be regenerated. Platinum, a widely used catalyst, can help speed up the conversion, but works better when combined with a so-called promoter metal. In this case, the researchers from Purdue University, Iowa State University, Ames Laboratory, and Argonne selected manganese as the second metal and created bimetallic nanoparticles. The nanoparticles are about 2 nm in diameter and are supported on a high-surface-area scaffold of silicon or aluminum oxide. They provide a surface on which the reactions can take place, and the researchers thought the manganese would give a stable, alloy nanoparticle structure.

It's possible for the nanoparticles to form in different ways. The surface could be an alloy of platinum and manganese and the core of the particle could be pure platinum. Or the particle could be an alloy throughout, with manganese atoms not only on the surface but beneath it. The question was whether that would make a difference in the quality of the catalyst.

As it turned out, the full-alloy nanoparticle outperformed the core-shell version. The nanoparticle with manganese atoms beneath the surface showed 98% selectivity for olefin production, whereas the platinum core version had 82% selectivity. The alloy also had a longer useful lifetime.

The researchers believe that neighboring manganese atoms change the chemistry of the platinum atoms because of how they bond, making the platinum a more effective catalyst. Platinum atoms in the surface layer had a certain number of manganese neighbors, and the more manganese atoms, the better the effect. Having manganese atoms in the subsurface layer increased the number of promoter atoms that were available, and so improved the platinum's chemistry even more.

The researchers were able to determine the arrangement of atoms close to the surface of the nanoparticles using x-ray absorption spectroscopy at the MR-CAT 10-BM bending magnet x-ray beamline at the APS. That allowed them to look at individual platinum atoms and see

whether their neighbors were platinum or manganese.

But they also wanted to see the arrangement of atoms over the longer range, which required high-energy x-ray diffraction, so they turned to the XSD 11-ID-C insertion device beamline, also at the APS. The particles in question were so small that they produced very little signal, but the high flux and high energy of the APS x-rays allowed the researchers to detect the signals and determine subtle differences in structure. In both studies, the experiments were also performed under catalytic reactions by using reaction cells, thus enabling gas to flow over the heated nanoparticles, which gave insights about the changes in the nanoparticles under working conditions

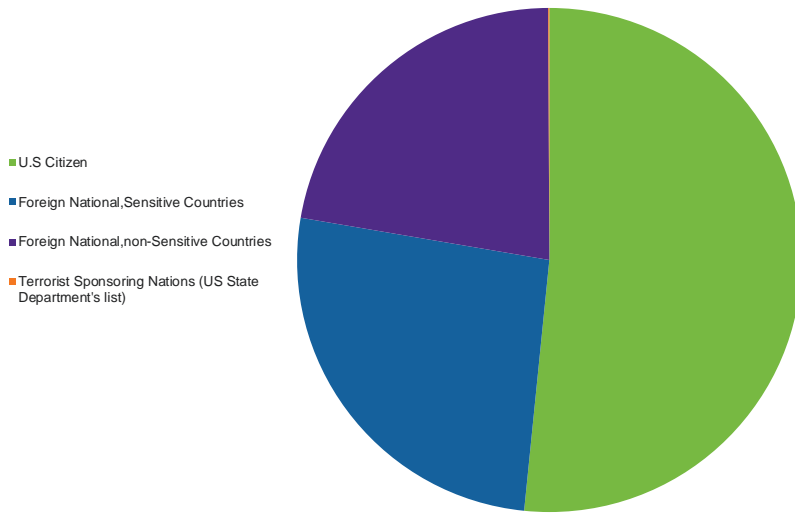
While manganese turns out to work very well as a promoter metal, the team is also testing other bimetallic platinum compounds. The research not only scouts out different candidates, but also leads to an understanding of what factors go into improving a catalyst's performance. Ultimately it will take long-term testing in commercial-type reactors to determine whether a particular catalysts meets the needs of the gas refining industry.

— Neil Savage

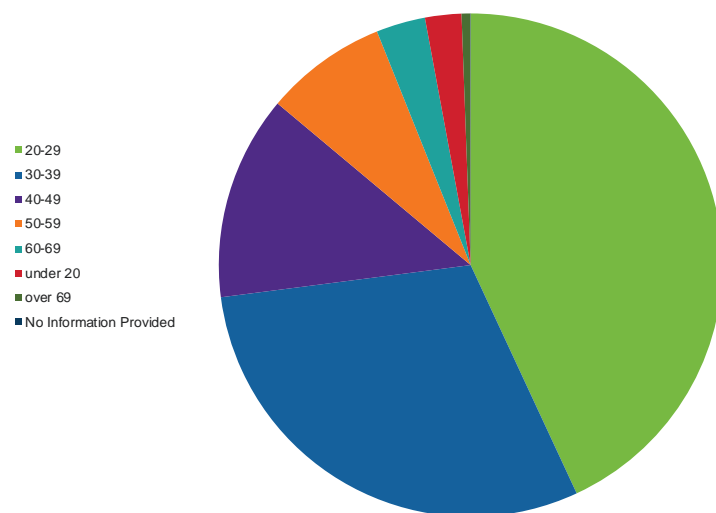
See: Zhenwei Wu¹, Brandon C. Bukowski¹, Zhe Li², Cory Milligan¹, Lin Zhou³, Tao Ma³, Yue Wu², Yang Ren⁴, Fabio H. Ribeiro¹, W. Nicholas Delgass¹, Jeffrey Greeley¹, Guanghui Zhang^{1*}, and Jeffrey T. Miller^{1**}, "Changes in Catalytic and Adsorptive Properties of 2 nm Pt₃Mn Nanoparticles by Subsurface Atoms," *J. Am. Chem. Soc.* **140**, 14870 (2018). DOI: 10.1021/jacs.8b08162
Author affiliations: ¹Purdue University, ²Iowa State University, ³Ames Laboratory, ⁴Argonne National Laboratory
Correspondence: * gzhang@dlut.edu.cn, ** mill1194@purdue.edu

This work is supported in part by the National Science Foundation under Cooperative Agreement No. EEC-1647722. Z.W. and J.T.M. gratefully acknowledge the financial support provided by the Davidson School of Chemical Engineering, Purdue University, and use of the Electron Microscopy Facility at Birk Nanotechnology Center, Purdue University. MR-CAT operations are supported by the U.S. Department of Energy (DOE) and the MR-CAT member institutions. This research used resources of the Advanced Photon Source, a U.S. DOE Office of Science User Facility operated for the DOE Office of Science by Argonne National Laboratory under Contract DE-AC02-06CH11357.

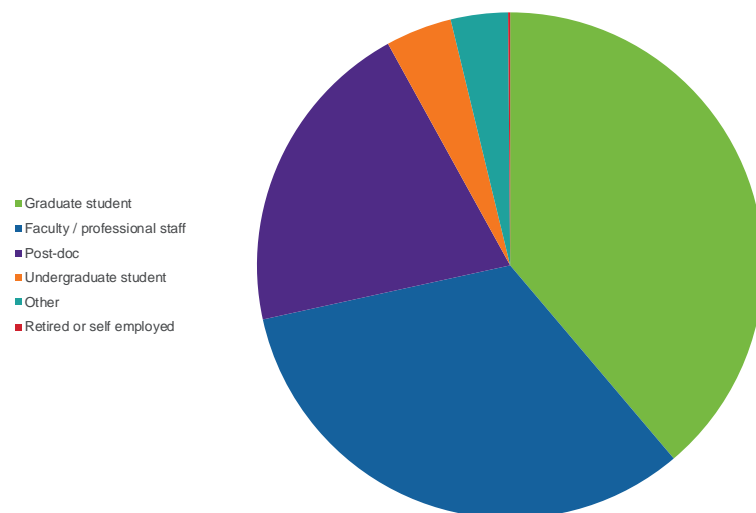
APS USERS BY CITIZENSHIP (FY 2018)



APS USERS BY AGE (FY 2018)



APS USERS BY EMPLOYMENT LEVEL (FY 2018)





LIFE SCIENCE

Lead Levels in the Franklin Expedition: A Closer Look

In the summer of 1845, 129 sailors aboard two British Royal Navy ships sailed into Lancaster Sound, in the Nunavut territory of Canada, on an Arctic exploration mission. Led by Captain Sir John Franklin, they were hoping to complete the discovery of a Northwest Passage by navigating the uncharted area between the Barrow Strait and the Simpson Strait. However, the mission encountered extreme hardships that resulted in three early fatalities and killed the remainder of the officers and crew over the next few years. The recent discovery of their wrecked ships, the HMS Erebus and the HMS Terror, has reignited interest in the Franklin Expedition, including what led to the deaths of the entire crew. Although the extreme conditions they encountered included cold and hunger that probably played overarching roles in their demise, some early analyses of bone, hair, and soft tissue from crew members' graves have suggested that lead poisoning may also have contributed to their deaths. However, questions regarding timing and degree of exposure have introduced doubt into the true impact of lead on the crew members. To better understand lead exposure in the Franklin Expedition, researchers came to the APS to analyze samples of bone and teeth from crew members who died both early and later in the mission, as well as contemporary sailors engaged in different missions who were buried elsewhere. The data suggest that sailors who died earlier in the expedition had just as much lead exposure as those who died later; that there was more lead in structures that formed close the time of death compared to at earlier points; and that lead exposure was about the same between those on the Franklin Expedition and contemporaries buried elsewhere. Although the data is mixed, the authors say, taken together it suggests that lead did not play a central role in the loss of the Franklin sailors.

For more information on the doomed Franklin Expedition see “How the Discovery of Two Lost Ships Solved an Arctic Mystery,” National Geographic, <https://news.nationalgeographic.com/2017/04/franklin-expedition-ship-watson-ice-ghosts/>

The researchers from six Canadian Universities and the Canadian Light Source started by isolating 14 bone samples from 13 individuals. Two samples were from sailors who died early in the Franklin Expedition, 10 were from sailors who died later on the same expedition, and two were from contemporary sailors buried at the Antigua Royal Naval Hospital Cemetery. The researchers also collected samples of dental cementum, the external tissue of the tooth root.

Using information on elemental content derived from data collected using the confocal x-ray fluorescence technique at XSD beamline 20-ID-B at the APS, the researchers determined overall lead levels as well as which tissues were older and which were younger based on their mineralization (Fig.1).

The study authors hypothesized that if Franklin's crew members experienced elevated lead exposure during the expedition, those sailors who survived longer should have more extensive uptake of lead in the microstructure of their bones, and vice versa. However, the data didn't reflect this — lead levels were approximately the same in the sailors who died early and later in the expedition.

Secondly, the researchers hypothesized that lead concentration would be markedly elevated in bone and dental microstructural features that formed at or near the time of death. The x-ray fluorescence data showed this to be true in some samples; however, consistent evidence of a marked elevation in lead levels was lacking.

Finally, the researchers hypothesized that if lead levels truly played a key role in the Franklin Expedition sailors' deaths, then bone and dental samples should hold evidence of higher and more sustained uptake of lead than their naval contemporaries. However, comparing samples from these two populations showed similar lead levels.

Together, the researchers suggest, the lead distribution data don't support the conclusion that lead played a pivotal part in the loss of the Franklin Expedition sailors.

— Christen Brownlee

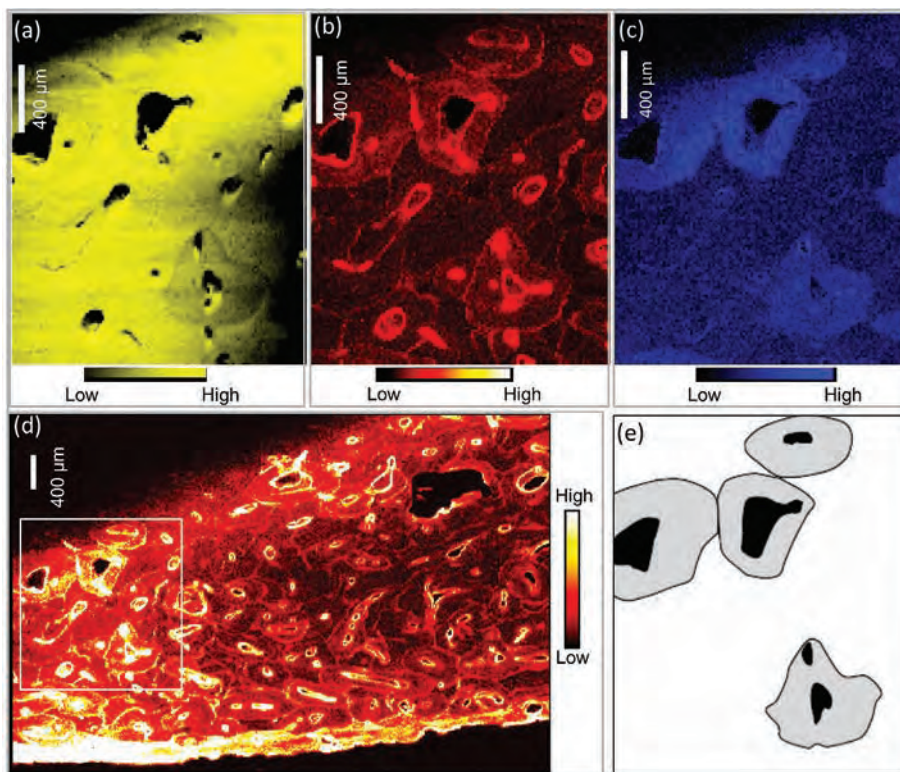


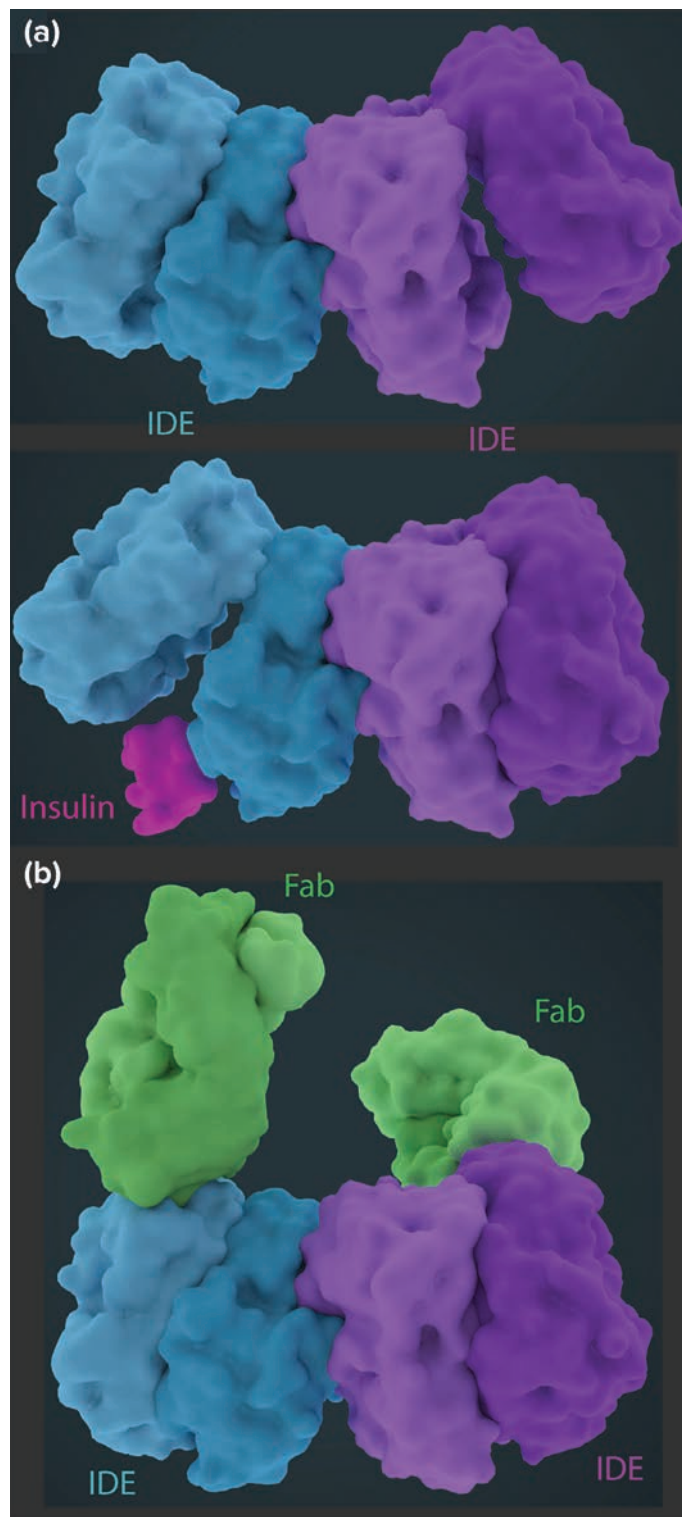
Fig. 1. X-ray fluorescence images from King William Island sample KWI-51-NgJ-2. Zoomed-in maps of calcium in yellow (a), lead in red (b), strontium in blue (c) from the full lead scan (d). The relatively low-density (calcium) osteons schematically highlighted (e) reflect younger osteons relative to the surrounding bone and those in the upper portion of the zoomed images have large canals surrounded by lower density bone which supports the interpretation that these osteons were forming at the time of death. These newer structures are elevated in Sr and also show lead deposition. From T. Swanton et al., PLoS One **13**(8), e0202983 (2018).

See: Treena Swanston^{1*}, Tamara L. Varney², Madalena Kozachuk³, Sanjukta Choudhury⁴, Brian Bewer⁵, Ian Coulthard⁵, Anne Keenleyside⁶, Andrew Nelson³, Ronald R. Martin³, Douglas R. Stenton⁷, David M. L. Cooper⁴, “Franklin expedition lead exposure: New insights from high resolution confocal x-ray fluorescence imaging of skeletal microstructure,” PLoS One **13**(8), e0202983 (2018). DOI: 10.1371/journal.pone.0202983
 Author affiliations: ¹MacEwan University, ²Lakehead University, ³Western University, ⁴University of Saskatchewan, ⁵Canadian Light Source, ⁶Trent University, ⁷University of Waterloo
 Correspondence: * swanstont@macewan.ca

This research used resources of the Advanced Photon Source, an Office of Science User Facility operated for the U.S. Department of Energy (DOE) Office of Science by Argonne National Laboratory, and was supported by the U.S. DOE under Contract No. DE-AC02-06CH11357, and the Canadian Light Source and its funding partners.
 Franklin Expedition graphic: wikimediacommons, https://commons.wikimedia.org/wiki/File:John_Franklin-Expedition-_1845-_auf_der_Suche_nach_der_Nordwestpassage_14.5.2010.jpg

Freeze! Revealing Mechanistic Details for Insulin-Related Diseases

According to the World Health Organization (WHO), non-communicable diseases like diabetes and dementia make up more than half of the top 10 leading causes of human death and are expected to rise over the next decade. To illustrate the scale of the problem, the WHO estimated in 2014 that 347 million people live with diabetes and predicted that diabetes would be the seventh leading cause of death in the world by 2030. Unfortunately, this happened much sooner, with diabetes reaching number 7 by 2016. Similarly, the prevalence of dementia-related deaths more than doubled between the years 2000 and 2016, making dementia the world's fifth leading cause of death. Despite the rapidly increasing prevalence of these diseases, we still don't fully understand how the diseases work. What we do know is that insulin-degrading enzymes (IDE) are responsible for breaking down peptides that are implicated in the pathogenesis of diseases like diabetes and dementia. But how? To answer this question, a multinational, multi-institutional team of scientists set out to reveal structural and mechanistic details about the process by which IDE selectively breaks down these peptides. As part of an advanced, integrative structural analysis, the researchers conducted small-angle x-ray scattering (SAXS) and macromolecular x-ray crystallography experiments at the APS, and cryogenic electron microscopy (cryoEM) experiments at the National Resource for Automated Macromolecule Microscopy (NRAMM). Through this research, the authors have uncovered the molecular changes IDE goes through as it captures, unfolds, and degrades insulin and peptides. This information will help advance the development of therapeutic agents for IDE-related diseases and limit their impact on human life.



IDE is a major enzyme responsible for degradation of insulin, glucagon, atrial natriuretic peptides, and beta-amyloid peptides. Previously, crystallographic and biochemical studies had provided a framework for the IDE substrate recognition. However, until this work, the structures of open and insulin-bound IDE, two key conformations involved in the catalytic degradation process, have remained unsolved. Part of the reason is that determination of the three-dimensional structures of these conformations were not possible via crystallography due to their heterogeneity. Using a combination of cryoEM, hydrogen-deuterium exchange coupled with mass spectrometry (HDX-MS), small-angle x-ray scattering (SAXS), and macromolecular x-ray crystallography, the team of scientists were able to integrate data collected through all four techniques to identify how IDE captures, unfolds, and degrades its substrates.

First, the researchers conducted cryoEM experiments at NRAMM to characterize a series of IDE structures. Displayed in Fig. 1 are the cryoEM structures of human IDE. From these data, the researchers concluded that only the fully open-state IDE was capable of capturing insulin and releasing the degraded products. Crystallography data, captured using x-ray diffraction on the SBC-CAT 19-ID x-ray beamline at the APS, showed the IDE dimer existing only in the closed state, likely due to crystal lattice constraints.

In order to assess the distribution of the open- and closed-state IDE dimer both in the presence and absence of insulin, the researchers coupled size exclusion chromatography with SAXS using the Bio-CAT 18-ID beamline at the APS. Data collected from SAXS experiments suggested that IDE exists in equilibrium with the open and partially open states and that insulin constrains IDE into the partially closed and closed states. Results from time-resolved SAXS, also carried out at the Bio-CAT beamline, showed that the insulin-induced open-closed transition is likely a key step for insulin degradation, and when coupled with HDX-MS data, insulin-IDE binding stabilizes the

< Fig 1. CryoEM structures of human insulin degrading enzyme (IDE): (a) Dimeric IDE has the combination of open and closed states, allowing capture, unfolding, and degradation of insulin. (b) The synthetic antibody increases the size of IDE particles and serves as the fiducial, allowing the structural determination of IDE by cryoEM. The high affinity IDE-binding synthetic antibody was rapidly identified from screening the “restricted chemical diversity” library without the need of immunization. Visit cryoem101.org for more details.

IDE catalytic site leading to catalytic insulin degradation. This research demonstrated that IDE can only degrade peptides that can fit into the IDE catalytic chamber, which tends to be those that are less than 80 amino acids long. However, IDE is also capable of non-catalytically modulating the kinetics of fibril formation of larger substrates like α -synuclein. Previous work by the authors showed that IDE plays a role in proteostasis by both catalytically and non-catalytically reducing monomer levels of amyloidogenic peptides.

This research reveals a road-map for conducting similar integrative studies using advanced characterization techniques like cryoEM, SAXS, and HDX-MS to study difficult biological systems. This study presents insights that will help researchers develop insulin-selective inhibitors or amyloid beta selective enhancers to treat diseases like diabetes and dementia. Perhaps as important as the research findings themselves is the expansive collaborative network involved in the work. In total, 21 researchers from 11 institutions and 2 continents pulled together their collective research and expertise to shed light on molecular structures and mechanistic details about IDE that had previously only been hypothesized. — Alicia Surrao

See: Zhening Zhang¹, Wenguang G. Liang², Lucas J. Bailey², Yong Zi Tan^{1,3}, Hui Wei¹, Andrew Wang², Mara Farcasanu², Virgil A. Woods⁴, Lauren A. McCord², David Lee⁴, Weifeng Shang⁵, Rebecca Deprez-Poulain⁶, Benoit Deprez⁶, David R. Liu⁷, Akiko Koide⁸, Shohei Koide⁸, Anthony A. Kossiakoff², Sheng Li^{4*}, Bridget Carragher^{1,3**}, Clinton S. Potter^{1,3***}, and Wei-Jen Tang^{2****}, “Ensemble cryoEM elucidates the mechanism of insulin capture and degradation by human insulin degrading enzyme,” *eLife* **7**, e33572 (2018). DOI: 10.7554/eLife.33572

Author affiliations: ¹New York Structural Biology Center, ²The University of Chicago, ³Columbia University, ⁴University of California, San Diego, ⁵Bio-CAT, ⁶Université de lille, ⁷Harvard University, ⁸New York University School of Medicine

Correspondence: * s4li@ucsd.edu, ** bcarr@nysbc.org, *** cpotter@nysbc.org, **** wtang@bsd.uchicago.edu

This work was supported by the National Institutes of Health (NIH) grants GM81539 and GM121964 to Wei-Jen Tang, GM103310 to Bridget Carragher and Clinton S. Potter; Agency for Science, Technology and Research Singapore to Yong Zi Tan, and DARPA Fold Fx program (N66001-14-2-4053), NIH R35 GM118062, and the Howard Hughes Medical Institute to David Liu. This project was supported by grant 9 P41 GM103622 from the National Institute of General Medical Sciences of the National Institutes of Health. This research used resources of the Advanced Photon Source, a U.S. Department of Energy (DOE) Office of Science User Facility operated for the DOE Office of Science by Argonne National Laboratory under Contract No. DE-AC02-06CH11357.

Watching Oxygen Bond Formation in Real Time

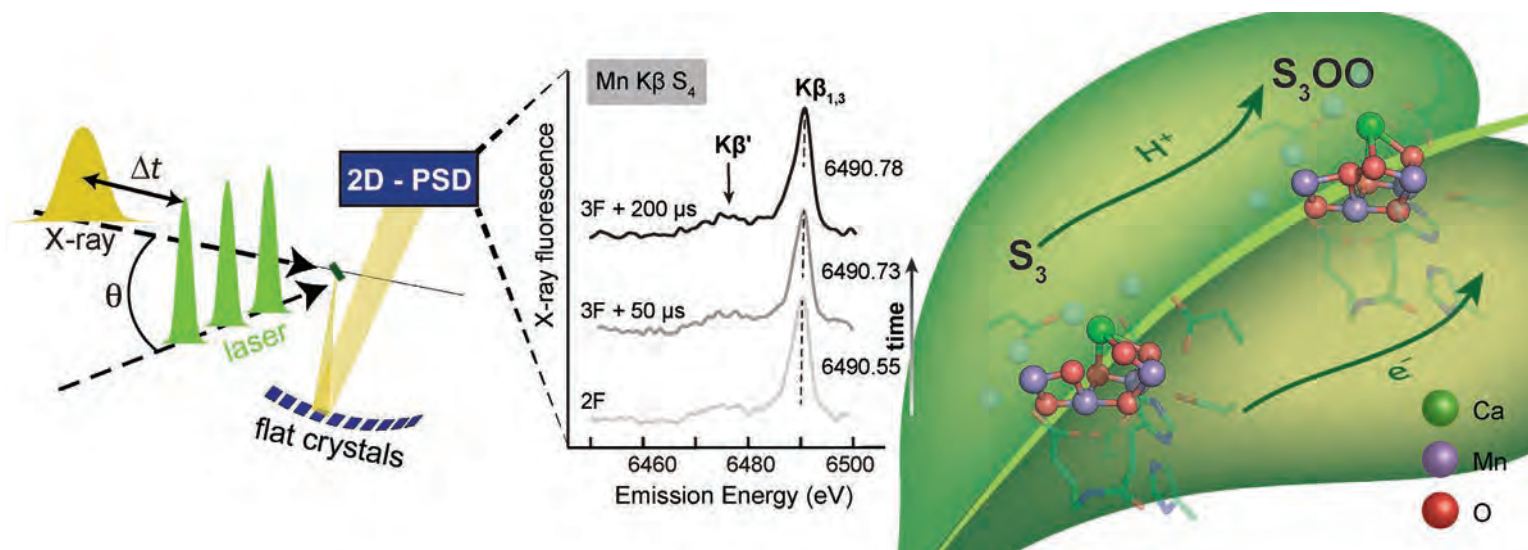


Fig. 1. X-ray fluorescence signals reflected onto a two-dimensional position-sensitive detector (2D-PSD) revealed that during the oxygen evolution step, the first moment of the Mn $K\beta_{1,3}$ peak increases $\sim 50 \mu$ s and $\sim 200 \mu$ s after the last laser flash, indicating that the OEC undergoes a significant transformation at short timescales during the S_3 -to- S_0 transition.

In photosynthesis, green plants, algae, and cyanobacteria convert light energy into chemical energy, which they use to produce their own food while releasing oxygen (O₂) into the atmosphere and removing carbon dioxide (CO₂) from it. Oxygen forms at a membrane-bound pigment-protein cluster called photosystem II (PSII), which contains an oxygen-evolving complex (OEC) that catalyzes water splitting. The OEC binds environmental water and oxidizes it during four consecutive photon-induced electron extractions. While it is known that the OEC's catalytic center contains a Mn₄Ca cluster, and that the electron extractions correspond to oxidation states of manganese as the OEC cycles through five so-called S-states (S₀–S₄), the critical step during which the O–O bonds form remains poorly understood. Recently, a group of researchers used time-resolved x-ray emission spectroscopy (TR XES) at the APS to observe the process of oxygen formation in real time.

These researchers' previous investigation into photosynthetic oxygen formation using dispersive TR-XES data led them to propose a new mechanistic model in which the O–O bonds form prior to the transfer of the fourth electron from the Mn₄Ca cluster; that is, during the S₃-to-S₀ transition. In the experiment carried out at the BioCARS 14-ID x-ray beamline at the APS, the team from Purdue University and the University of Washington, with colleagues from The University of Chicago, examined the earliest dynamic in this transition, accumulating almost a half-million repetitive interrogations of the OEC electronic structure. The researchers then performed an extensive statistical analysis of both datasets, which totaled more than two million x-ray measurements of different S-states. To avoid uncertainties, the researchers conducted the first-ever analysis of primary photosystem II emission data, meaning that the datasets were subjected to no manipulation beyond extraction of the spectra. The statistical significance of the observed spectral changes was determined using a one-way analysis of variance, with the 95% confidence interval being taken to indicate statistical significance.

Mn Kβ spectral emission lines reflect the number of unpaired 3d electrons, which provide information about the oxidation and/or spin states of manganese (Mn) ions, with an exchange interaction causing multiplet splitting that results in separate Kβ_{1,3} and Kβ' peaks. The electronic state of Mn is directly linked to this coupling such that an increase in the oxidation state results in decreased splitting between the Kβ spectral lines, an effect that is most apparent in the Kβ_{1,3} peak's position shift to lower energies with increasing oxidation. Samples consisting of PSII-enriched thylakoid-membrane particles derived from spinach were excited with a specified number (0–3) of laser flashes and probed by a single x-ray pulse soon after each final laser flash. As is the case with dispersive detection, the full emission spectrum was

recorded during each intense, polychromatic x-ray pulse. To match the microsecond kinetics of OEC activity, the researchers used multi-bunch x-ray exposures of 22–44-μs duration.

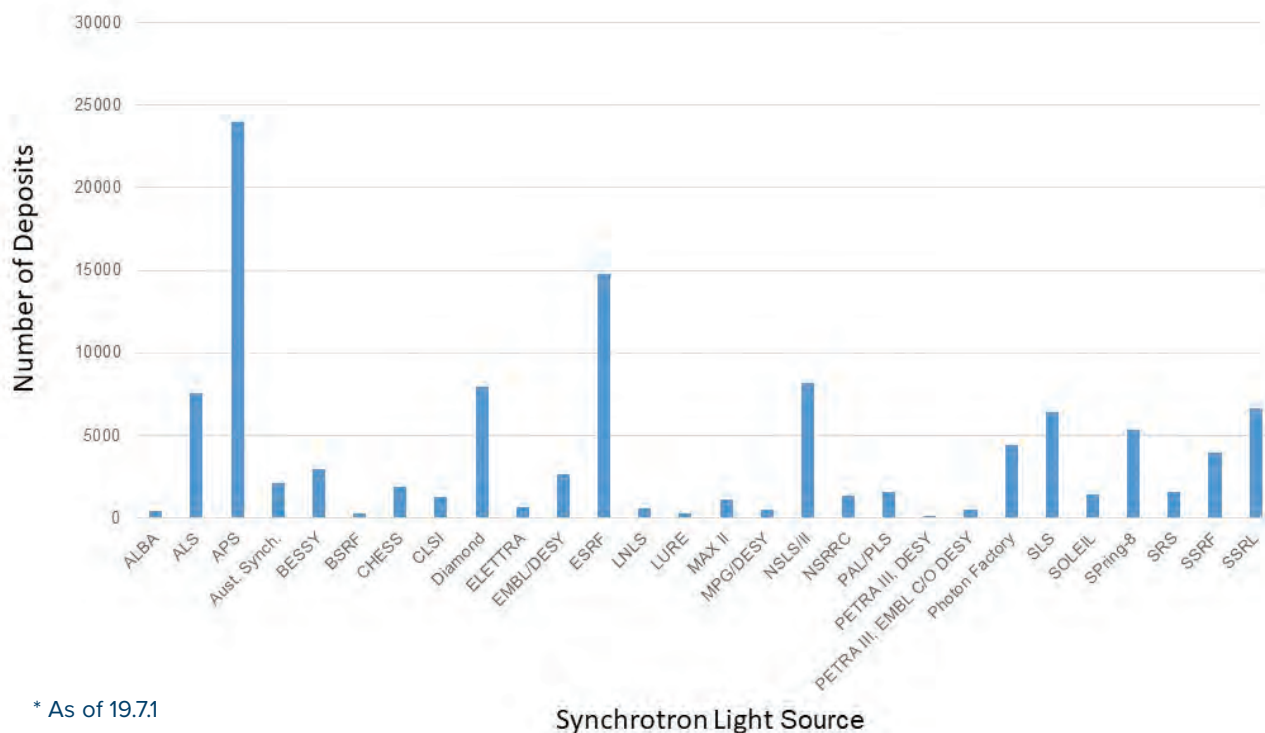
These experiments revealed that during the oxygen evolution step brought about by three laser flashes, the first moment of the Mn Kβ_{1,3} peak increases ~50 μs and ~200 μs after the last flash. This robust and statistically significant spectral shift suggests that the OEC undergoes a significant transformation at short timescales during the S₃-to-S₀ transition (Fig. 1). The researchers proposed that these changes correspond to the fast reduction of the Mn centers from the (Mn^{IV})₄ state following the creation of a short-lived isoform of the S₃ state, in which the O–O bond has formed. This result supports the researchers' earlier proposal that O–O bond formation occurs prior to the transfer of the final (fourth) electron from the Mn₄Ca cluster to an oxidized tyrosine Tyr_z residue. — Vic Comello

See: Katherine M. Davis^{†‡}, Brendan T. Sullivan^{†‡‡}, Mark C. Palenik^{†‡‡‡}, Lifen Yan[†], Vatsal Purohit^{†‡‡‡}, Gregory Robison^{†‡‡‡‡}, Irina Kosheleva², Robert W. Henning², Gerald T. Seidler³, and Yulia Pushkar^{*‡}, “Rapid Evolution of the Photosystem II Electronic Structure during Water Splitting,” *Phys. Rev. X* **8**, 041014 (2018). DOI: 10.1103/PhysRevX.8.041014

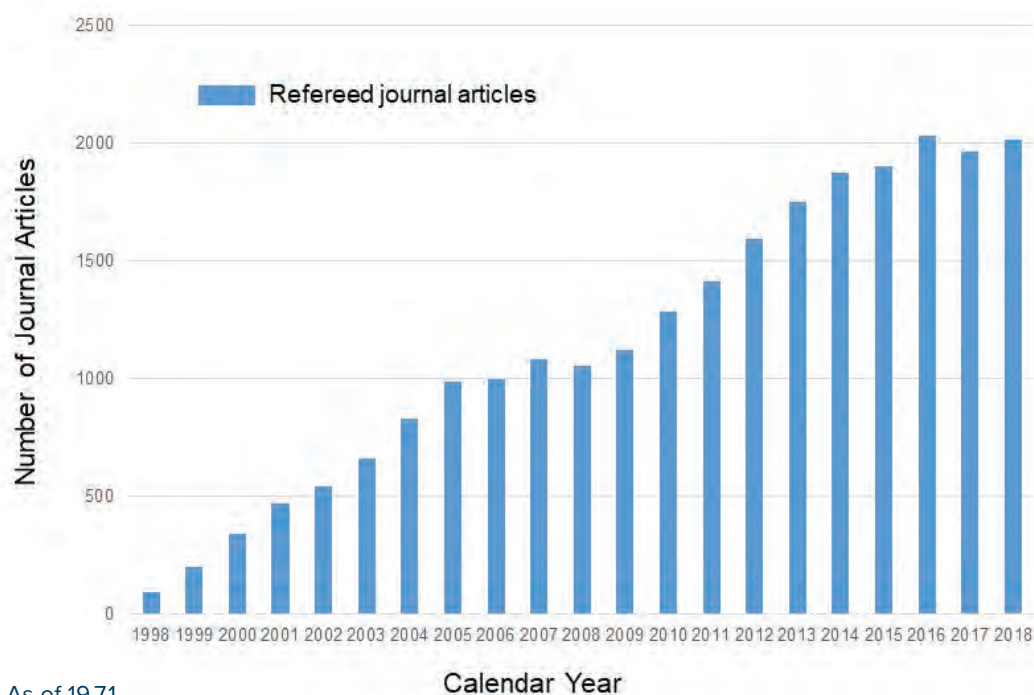
Author affiliations: ¹Purdue University, ²The University of Chicago, ³University of Washington Present addresses: [†]Princeton University, [‡]Oak Ridge National Laboratory, ^{‡‡}Naval Research Laboratory, ^{‡‡‡}Purdue University, ^{‡‡‡‡}Hanover College
Correspondence: * ypushkar@purdue.edu

This research was supported by the National Science Foundation (NSF) CHE-1350909 (Y.P.), and the NSF Graduate Research Fellowship under Grant No. DGE0833366 (K.D.). G.T.S. acknowledges support from the U.S. Department of Energy (DOE) Office of Science, under Grant No. DE-SC0002194. Use of the BioCARS beamline was supported by the National Institutes of Health, National Institute of General Medical Sciences Grant No. 1R24GM111072. The time-resolved setup at BioCARS was funded in part through a collaboration with Philip Anfinrud (NIH/ NIDDK). This research used resources of the Advanced Photon Source, a U.S. DOE Office of Science User Facility operated for the DOE Office of Science by Argonne National Laboratory under Contract DE-AC02-06CH11357.

Deposits in Protein Data Bank - Light Sources Worldwide*



Number of APS Journal Articles, Calendar Years 1998-2018*



To search lists of APS publications see https://beam.aps.anl.gov/pls/apsweb/pub_v2_0006.review_start_page



STRUCTURAL BIOLOGY

A New Molecule Could Help Put the STING on Cancer

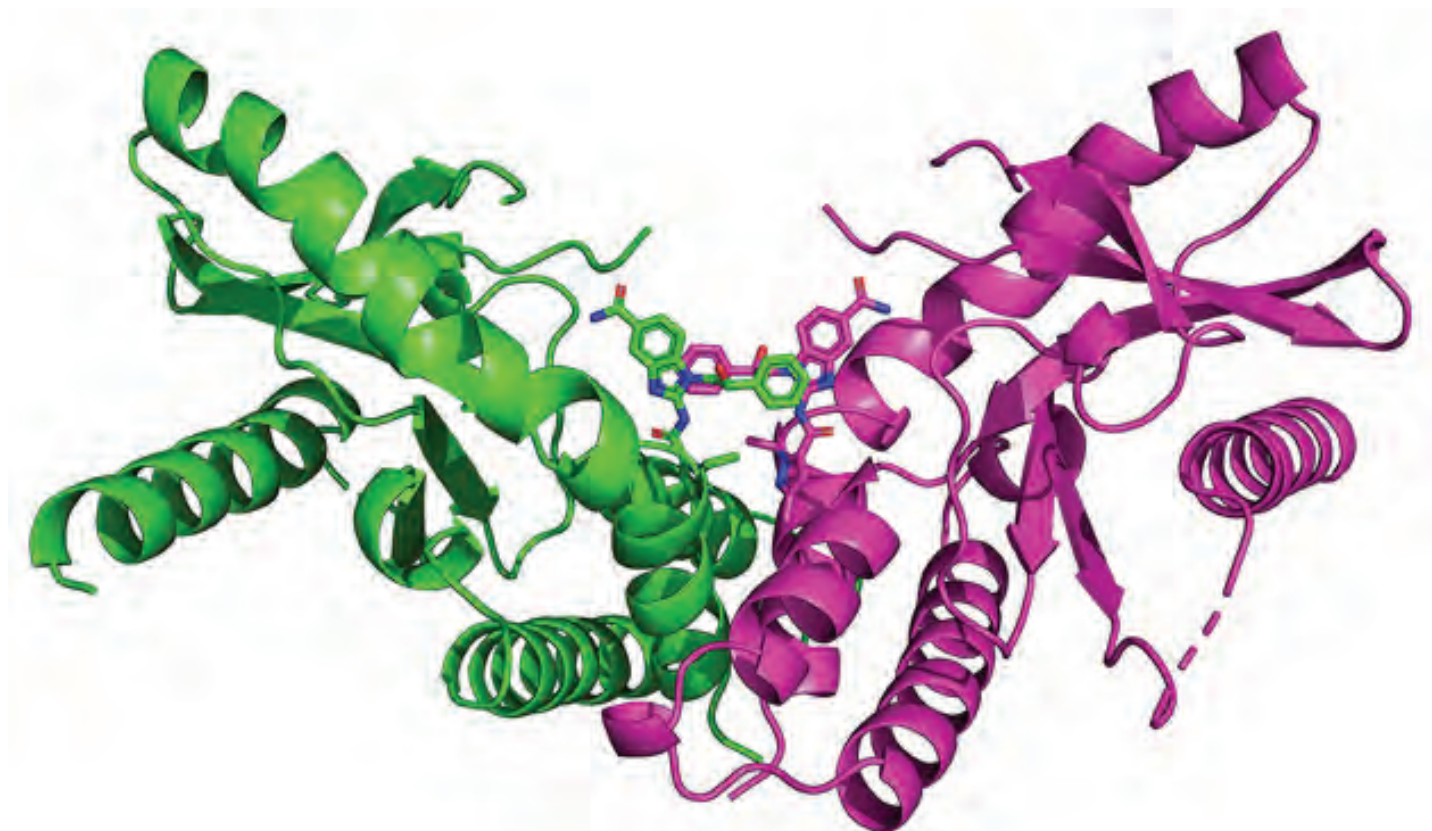


Fig. 1. X-ray crystal structure of the STING protein bound to one of the new molecules.

The protein STING (stimulator of interferon genes) is a component of the innate immune system. It plays a major role in the immune response to cancer, and abnormal STING signaling has been shown to be associated with certain cancers. Immunomodulatory approaches using agonists to target STING signaling are therefore being investigated as anticancer treatments. However, the compounds in clinical trials typically are injected intratumorally in patients with solid cancers. In this study, researchers discovered a novel STING agonist, known as an amidobenzimidazole (ABZI), which can be given by intravenous injection and could therefore potentially open up its evaluation as a treatment for hard-to-reach cancers. Using x-ray diffraction data collected at the APS, researchers investigated ABZI compounds and STING. Their results may have important implications for anticancer immunotherapy.

STING is a protein that mediates innate immunity, and one function of the STING signaling pathway is in mobilizing an immune response against tumors. STING proteins can be activated by cyclic dinucleotides, small molecules that are made by the cytosolic DNA sensor, cGAS, upon sensing of DNA leaking out of the nucleus as a result of DNA damage, including that which might be associated with cancer development.

As such, the potential use of activators of the STING pathway represents a growing area of interest in cancer immunotherapy that aims to stimulate a specific type of T-cell in the immune system that targets and destroys cancer cells. Development of synthetic cyclic dinucleotide molecules to target the STING pathway has become a particular focus in this area. To date, these synthetic molecules have been investigated in clinical trials, in which patients with accessible solid tumors receive injections of these compounds directly into their tumors. This treatment aims to activate the STING pathway and the immune system, and ultimately shrink the tumor.

However, this method of drug delivery is not only challenging to perform, but inevitably is only useful for patients who have solid accessible tumors. With this in mind, the researchers from GlaxoSmithKline developed a new small-molecule STING agonist that can be given by intravenous injection.

First, they used high-throughput screening as a technique to search among millions of small molecules, hoping to find some that bind to STING and regulate its activity. In this process, they found that the small molecule ABZI showed promise in this area.

Next, using diffraction data collected at the LS-CAT 21-ID-F beamline at the APS, the group determined the crystal structure of one ABZI compound in complex with STING (Fig. 1), which itself is a homodimer of two identical subunits. They showed that two molecules of the ABZI compound were in close proximity to each other when they bound to STING.

Based on this information, the researchers produced a diABZI compound by covalently linking together two of the ABZI compounds. The diABZI bound to STING ~1000-fold more tightly than did the original ABZI.

After further modifying the structure of the diABZI to make it even more potent, the group tested it in a mouse model of colorectal cancer, in which mice with colorectal tumors received either diABZI or vehicle by intravenous injection. Compared with the vehicle-treated animals, the diABZI-treated mice showed improved survival and tumor regression, with 8 out of 10 mice being tumor-free by day 43.

According to the researchers, diABZIs are novel compounds and are also the first potent, non-nucleotide STING agonists. The results of this study hold promise for a new therapeutic approach with potential to improve cancer treatment. — Nicola Parry

See: Joshi M. Ramanjulu*, G. Scott Pesiridis, Jingsong Yang, Nestor Concha, Robert Singhaus, Shu-Yun Zhang, Jean-Luc Tran, Patrick Moore, Stephanie Lehmann, H. Christian Eberl, Marcel Muelbaier, Jessica L. Schneck, Jim Clemens, Michael Adam, John Mehlmann, Joseph Romano, Angel Morales, James Kang, Lara Leister, Todd L. Graybill, Adam K. Charnley, Guosen Ye, Neysa Nevins, Kamelia Behnia, Amaya I. Wolf, Viera Kasparcova, Kelvin Nurse, Liping Wang, Yue Li, Michael Klein, Christopher B. Hopson, Jeffrey Guss, Marcus Bantscheff, Giovanna Bergamini, Michael A. Reilly, Yiqian Lian, Kevin J. Duffy, Jerry Adams, Kevin P. Foley, Peter J. Gough, Robert W. Marquis, James Smothers, Axel Hoos, and John Bertin, "Design of amidobenzimidazole STING receptor agonists with systemic activity," *Nature* **564**, 439 (20/27 December 2018).

DOI: 10.1038/s41586-018-0705-y

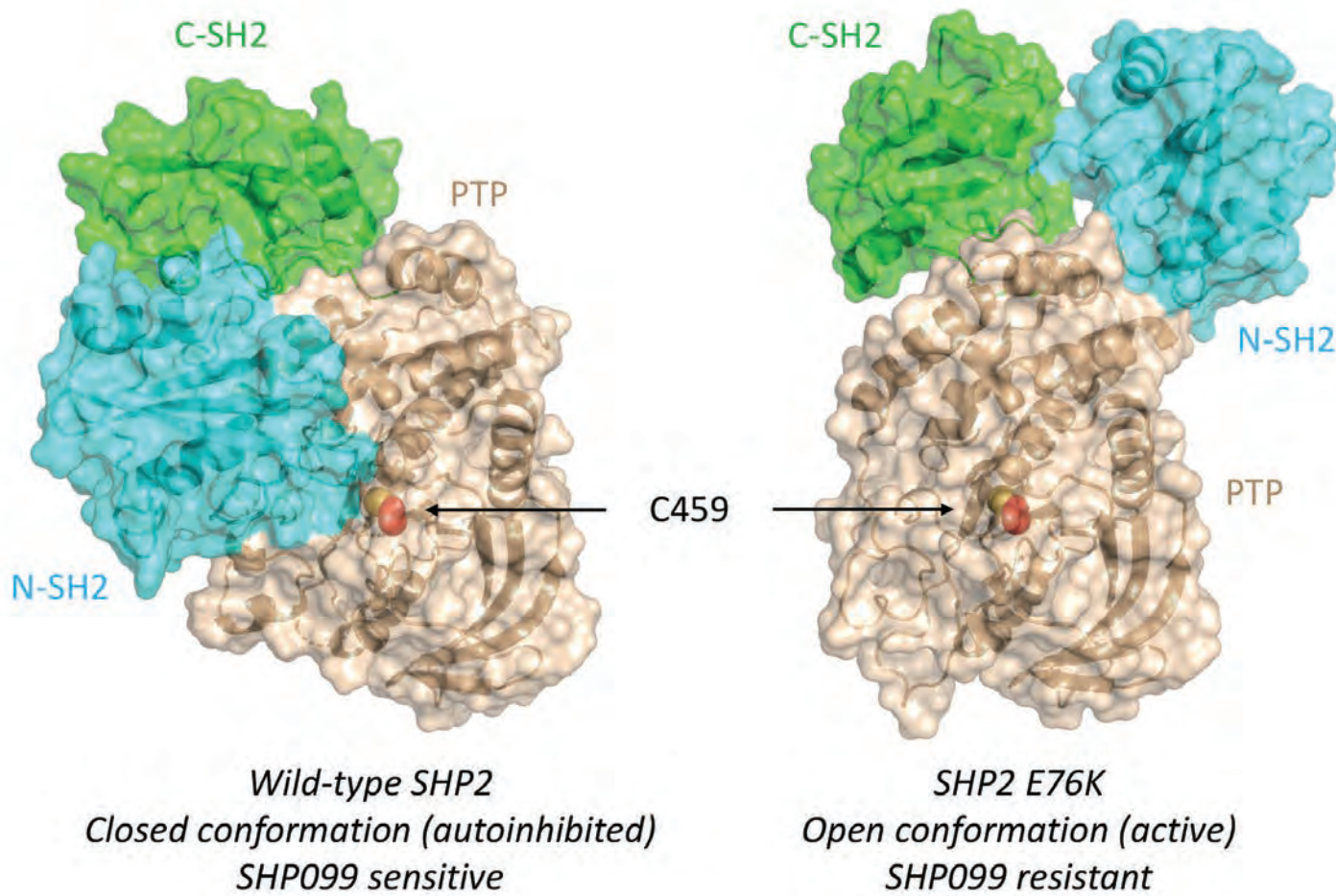
Author affiliation: GlaxoSmithKline

Correspondence: *joshi.m.ramanjulu@gsk.com

Use of the Life Sciences Collaborative Access Team beamline was supported by the Michigan Economic Development Corporation and the Michigan Technology Tri-Corridor (Grant 085P1000817). This research used resources of the Advanced Photon Source, a U.S. Department of Energy (DOE) Office of Science User Facility operated for the DOE Office of Science by Argonne National Laboratory under Contract No. DE-AC02-06CH11357.

A Target Mutation that Renders a Cancer Drug Ineffective

Mutations in the gene *PTPN11*, which encodes a common enzyme called SHP2, can result in developmental disorders, such as Noonan Syndrome, and act as oncogenic drivers in patients with certain blood cancers. Due to the well understood role of the enzyme SHP2 in Noonan Syndrome and in tumorigenesis, many companies are currently trying to develop drugs that inhibit the enzyme. However, it is unclear what impact mutations to SHP2 may have on the potential efficacy of drugs targeting this enzyme. Using the APS, researchers investigated the effect that the most frequently observed mutation of *PTPN11*, E76K, has on the structure of SHP2 and its allosteric inhibition by SHP099. They found that SHP2E76K adopts an open conformation, resulting in the elimination of the binding pocket for SHP099. Because the E76K mutation reduces the inhibitory potency of SHP099 for SHP2 by more than 100-fold, the researchers conclude that an effective allosteric inhibitor of SHP2E76K would need to exhibit at least two additional orders of magnitude greater potency than SHP099.



Encoded by the gene *PTPN11*, SHP2 is ubiquitously expressed in the cytoplasm of many cell types and plays a regulatory role in various cell signaling events that are important for a diversity of cell functions, such as mitogenic activation, metabolic control, transcription regulation, and cell migration.

SHP2 has a relatively conserved structure and function. SHP2 contains two tandem SH2 domains (N-SH2 and C-SH2), a catalytic protein tyrosine phosphatase (PTP) domain, and a C-terminal tail that has at least two phosphorylation sites. This protein adopts a closed autoinhibited conformation in which the N-SH2 domain engages the catalytic pocket of the PTP domain and physically occludes the active site. Upon stimulation of receptor tyrosine kinases or cytokine receptors by their ligands, the SH2 domains bind to induced phosphotyrosine sites to induce a conformational change that un-masks the PTP domain to permit full catalytic activity of the phosphatase. Normally, the binding of tyrosine-phosphorylated ligands to the SH2 domains is required to overcome autoinhibition, but oncogenic mutations of SHP2 destabilize the autoinhibited conformation and lead to enhanced activity. Thus, depending on the cellular context, the result is either physiologic activation of SHP2, or oncogenic signaling in tumors. As an oncogene, SHP2 regulates cancer cell survival and proliferation primarily by activating the RAS-ERK signaling pathway. Due to its role in tumor growth, as well as in T-cell inactivation, SHP2 has become one of the most important anti-cancer targets for the pharmaceutical industry.

Scientists have recently discovered allosteric modulators that stabilize the closed form of SHP2. One such compound, SHP099, acts as a molecular glue between the N-SH2 domain and the catalytic domain. SHP099 has been reported to exhibit antiproliferative activity in cancer cell lines that are dependent on SHP2. It remains an open question, however, whether common mutant forms of SHP2 can be allosterically inhibited by SHP099.

Researchers from the Harvard Medical School, the

< Fig. 1. The wild-type enzyme SHP2 contains a protein tyrosine phosphatase catalytic domain (PTP domain) and two SH2 domains (N-SH2 and C-SH2). This version of SHP2 assumes a closed conformation in which the enzyme is autoinhibited. An allosteric inhibitor called SHP099 stabilizes SHP2. A specific mutation (E76K) to the gene, *PTPN11*, that encodes SHP2, results in a 120° pivot of the C-SH2 domain and relocalization of the N-SH2 domain. In this more open conformation of SHP2, the binding pocket for SHP099 is eliminated, thereby making SHP2 100 times more resistant to the allosteric inhibitor.

Dana Farber Cancer Institute, and the Novartis Institutes for Biomedical Research investigated the impact of *PTPN11* mutations on the structure of SHP2 and on allosteric inhibition by SHP099. Using data obtained from macromolecular x-ray crystallography experiments performed at the IMCA-CAT beamline 17-ID-B at the APS, they found that the most frequently occurring SHP2 cancer mutation, a potent E76K substitution, results in a 120° pivot of the C-SH2 domain and relocalization of the N-SH2 domain to an alternative PTP domain interaction surface. This more open conformation of SHP2, confirmed using size-exclusion chromatography-small-angle x-ray scattering experiments performed at the Bio-CAT beamline 18-ID-D at the APS, results in the elimination of the binding pocket for SHP099 and, ultimately, a 100-fold decrease in the allosteric inhibitor's potency toward the E76K mutated enzyme (Fig. 1).

One conclusion to draw from these results is that because a significant number of patients with *PTPN11*-mutated cancers bear the E76 mutation, any potential allosteric inhibitor for these patients would need to exhibit at least two additional orders of magnitude greater potency than SHP099. An effective allosteric inhibitor would also require a longer target residence time to achieve successful suppression of SHP2's tumorigenesis activity. Alternatively, effective therapies employing multiple allosteric inhibitors to target more than one distinct pocket on SHP2 could halt or slow tumor growth associated with this protein. — Chris Palmer

See: Jonathan R. LaRochelle^{1,2}, Michelle Fodor³, Vidyasiri Vemulapalli^{1,2}, Morvarid Mohseni³, Ping Wang³, Travis Stams³, Matthew J. LaMarche³, Rajiv Chopra³, Michael G. Acker^{3*}, and Stephen C. Blacklow^{1,2**}, "Structural reorganization of SHP2 by oncogenic mutations and implications for oncoprotein resistance to allosteric inhibition," *Nat. Commun.* **9**, 4508 (2018). DOI: 10.1038/s41467-018-06823-9

Author affiliations: ¹Harvard Medical School, ²Dana-Farber Cancer Institute, ³Novartis Institutes for Biomedical Research

Correspondence: * Michael.Acker@novartis.com

** Stephen_Blacklow@hms.harvard.edu

This work was supported by the DFCI-Novartis Drug Discovery Program, National Institutes of Health award 1 R35 CA220340 (to S.C.B.), and a fellowship from the American Cancer Society (award number 128126 to J.R.L.) Use of the IMCA-CAT beamline at the Advanced Photon Source was supported by the companies of the Industrial Macromolecular Crystallography Association through a contract with Hauptman-Woodward Medical Research Institute. Bio-CAT is supported by grant P41 GM103622 from the National Institute of General Medical Sciences of the National Institutes of Health. This research used resources of the Advanced Photon Source, a U.S. Department of Energy (DOE) Office of Science User Facility operated for the DOE Office of Science by Argonne National Laboratory under contract no. DE-AC02-06CH11357.

A Compound that Exploits a Novel Binding Site on a Diabetes Target

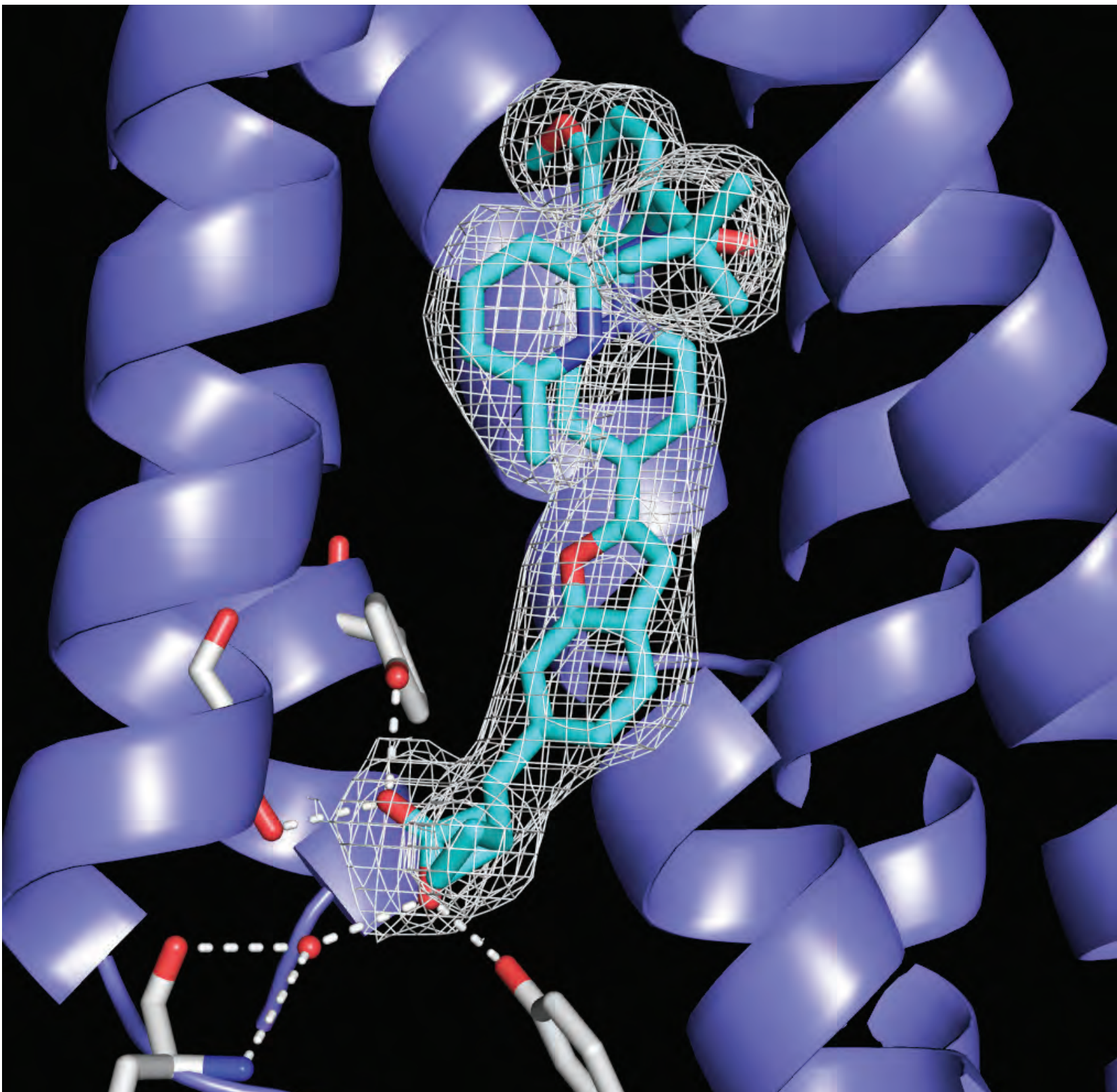


Fig. 1. Structure of GPR40 (purple) in complex with compound 1 (cyan).

Free fatty acid receptor 1 (FFAR1 or GPR40) has recently received significant interest as a diabetes therapeutic target. This G-protein-coupled receptor modulates FFA-stimulated insulin secretion in pancreatic β cells and incretin secretion in enteroendocrine cells in a glucose-dependent manner. Activation of GPR40 by synthetic partial and full agonists is known to occur via distinct allosteric sites. A previously obtained crystal structure of GPR40 in complex with a recently failed phase III drug candidate called “TAK-875” revealed the allosteric site for the partial agonist. Researchers have now performed x-ray crystallography at the APS to characterize the 2.76-Å crystal structure of human GPR40 in complex with a synthetic full agonist, “compound 1,” bound to a second allosteric site [1]. Compound 1 binds in the lipid-rich region of the receptor near intracellular loop 2 (ICL2). Upon binding, ICL2 becomes stabilized, which likely results in the enhanced GPR40 activity. Both the endogenous free fatty acid (FFA), γ -linolenic acid, and compound 1 exhibit positive cooperativity with TAK-875, suggesting that this second allosteric site could also serve as an FFA binding site. These findings point to the therapeutic potential of this new GPR40 agonist.

The World Health Organization reported in 2014 that diabetes afflicts an estimated 422 million adults globally. In the United States, about 1.7 million new cases of diabetes are reported each year — a rate that could result in 1 out of every 3 adults having diabetes by 2050. Type 2 diabetes mellitus (T2DM) accounts for about 90% of all diabetes. The conventional approach to treat T2DM is to improve glycemic control, but current clinical treatments of T2DM are associated with side effects such as hypoglycemia and weight gain, creating a significant demand for new anti-diabetic medicines with improved metabolic profiles.

In the last decade, FFAR1 or GPR40 has emerged as an attractive diabetes therapeutic target with glucose-lowering and weight loss potential. Upon binding by dietary long-chain free fatty acids (FFAs), it increases glucose-stimulated secretion of insulin in pancreatic β cells and the secretion of incretins (a group of metabolic hormones that augment insulin secretion) in enteroendocrine cells.

About five years ago, the clinically studied synthetic GPR40 agonist, TAK-875, advanced to a phase III clinical trial before its termination due to toxicity. While clinical

data demonstrated that TAK-875 had potent anti-diabetic effects with minimal side effects, such as hypoglycemia and weight gain, *in vitro* and *in vivo* studies showed that it functioned as a partial agonist and only minimally affected incretin release from enteroendocrine cells.

AM-1638 is part of a class of compounds that has been found to be a full agonist for GPR40 and also to robustly stimulate incretin secretion. This class of full agonists also acts allosterically with the endogenous FFAs but binds to a topographically distinct site from TAK-875. Moreover, unlike TAK-875, which activates only the $G\alpha_q/Ca^{2+}$ pathway, these full agonists increase intracellular Ca^{2+} and cAMP levels as a result of GPR40 coupling to both $G\alpha_q$ and $G\alpha_s$ subunits, potentially explaining their ability to elicit potent incretin secretion.

The disparate pharmacology of these compounds suggests the possibility that aside from the orthosteric site for engaging endogenous FFAs, GPR40 has an additional two distinct allosteric binding sites: A1 engages ligands such as TAK-875, and A2 engages ligands such as AM-1638. A previously obtained crystal structure of GPR40 bound to TAK-875 revealed the location of site A1.

Using macromolecular x-ray crystallography experiments performed at the LRL-CAT 31-ID x-ray beamline at the APS, researchers from the Lilly Biotechnology Center and the Lilly Research Laboratory, aided by LRL-CAT beamline personnel, characterized the 2.76-Å crystal structure of human GPR40 complexed with the proprietary compound 1 bound in site A2 (Fig. 1). Binding of compound 1, which belongs to the same family as AM-1638, stabilizes the intracellular loop 2 (ICL2) of GPR40 in a helical conformation. Mutagenesis studies demonstrate that this loop is important for $G\alpha_s$ coupling, which likely triggers increases in circulating levels of the insulin and the incretin hormone GLP-1. Furthermore, positive functional cooperativity is observed between TAK-875 and compound 1 and γ -linolenic acid (γ -LA), raising the possibility that A2 could also serve as an FFA binding site.

These findings, as well as other recently reported agonist-bound GPR40 structures (e.g., the GPR40 structure with the same A2 binding site determined at the IMCA-CAT beamline 17-ID at the APS [2]), provide structural evidence that agonists binding distinct allosteric sites of the same receptor modulate G-protein signaling. This allosteric mechanism expands the understanding of basic pharmacology, and could provide insight into the function of other members of the GPCR family. In addition, these results may be useful for the ra-

“Diabetes” cont’d. on page 73

The First-Ever Binding Trajectory of a Cancer Drug to its Target

The human protein Indoleamine 2,3-Dioxygenase 1 (hIDO1) is a key enzyme in the kynurenine metabolic pathway. This pathway is often active in tumor cells and has been linked to the way tumor cells escape from the immune system. Several hIDO1 inhibitors have been used in clinical trials, including BMS-986205 (BMS). BMS is a frontline cancer immunotherapeutic drug and a best-in-class hIDO1 inhibitor, highlighting the need to understand the precise mechanism by which it inhibits hIDO1. Researchers solved, for the first time, a full binding trajectory of a drug to its target using experimentally determined, atomic-resolution snapshots of hIDO1 as it is bound and inhibited by BMS. To build these atomic models, crystallographic data were collected at the APS. These structural data offer a molecular explanation for the remarkable efficacy and puzzling irreversible activity of the drug and suggest a novel strategy for drug development targeting hIDO1 and related enzymes.

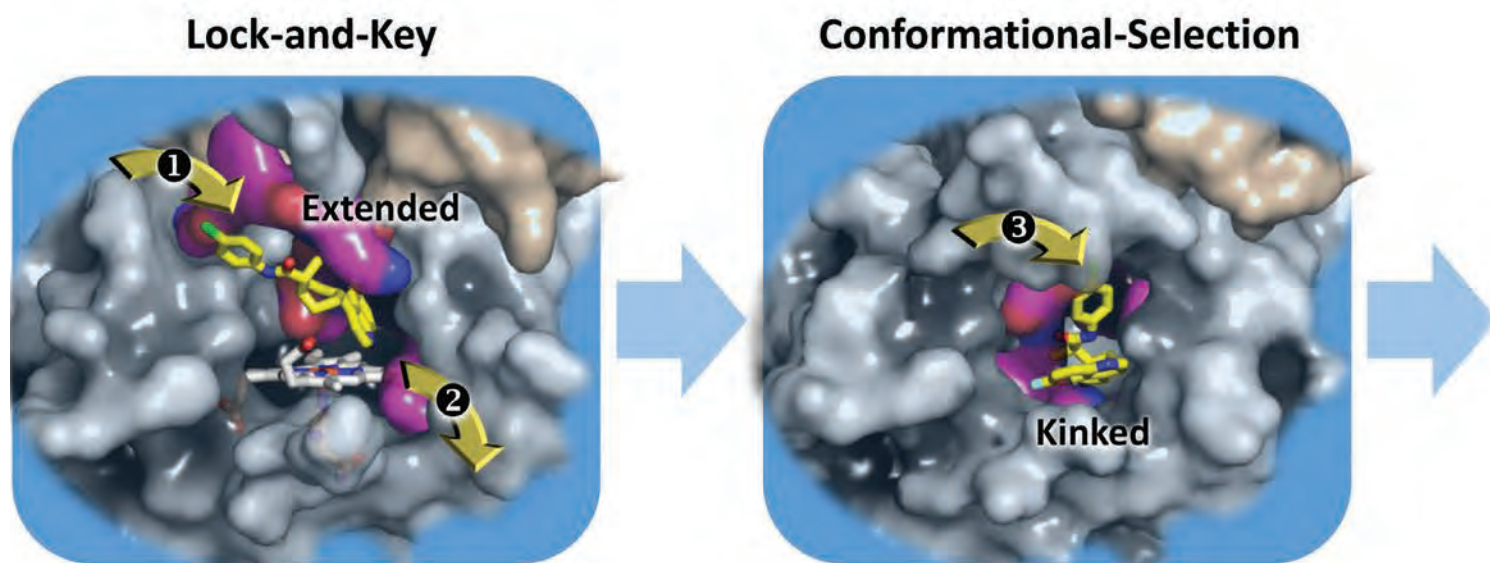


Fig. 1. Binding Trajectory of BMS-986205 (BMS) to human Indoleamine 2,3-Dioxygenase 1 (hIDO1) based on three snapshots captured by x-ray crystallography. The binding trajectory is illustrated by a sequential mechanism (steps 1-4). BMS and heme molecules are shown as yellow and grey sticks, respectively.

Pre-clinical efficacy of drugs is generally determined by measuring drug kinetics. The strength of the interaction between a drug and its target (binding affinity) is assessed through measures of how frequently a drug binds to (the association constant) or diffuses away from (the dissociation constant), the target protein in solution. Though these parameters provide valuable information

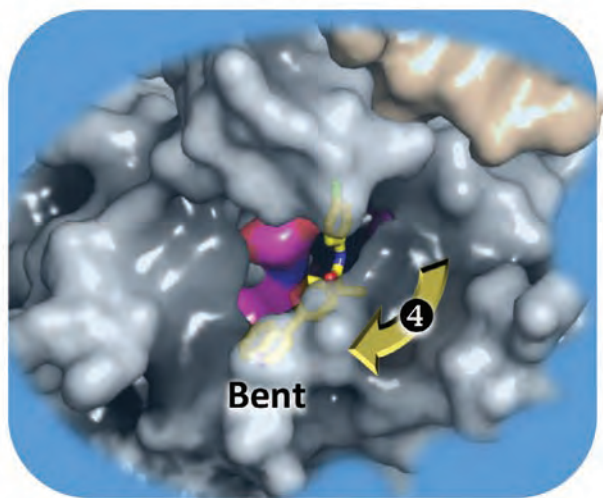
about the drug as it moves from the laboratory bench to clinical trials, drug efficacy is also tied to the pathway by which the drug finds its way to the final binding site within its protein target (i.e., the binding trajectory of the drug). Because proteins are dynamic, binding trajectories typically cannot be determined experimentally. Rather, they are most often attainable only through computational approaches, such as molecular dynamics simulations.

In the case of hIDO1 and BMS, however, researchers from the Albert Einstein College of Medicine were able to use x-ray crystallography data obtained by the LRL-CAT staff at beamline 31-ID-D of the APS to capture three high-resolution snapshots of hIDO1 during BMS binding.

First, BMS binds hIDO1 through a classic lock-and-key mechanism via interactions with a solvent-exposed surface cleft near the active site of the protein (step 1 in Fig. 1). This initial binding cracks open a central heme-binding pocket. Within this pocket lies a heme essential for enzyme activity that is released, leaving the enzyme non-functional (step 2). BMS then moves into the vacant heme binding site where it is driven to adopt a new high-energy kinked conformation, via a conformational-selection mechanism, that allows it to remain bound to the inside of the heme-binding pocket (step 3). Finally, BMS undergoes a large-scale rearrangement, adopting a bent conformation via an induced-fit mechanism (step 4). In this final state, the BMS-protein complex is in an energy-minimum state, which means that stable association of the drug with its target, rather than dissociation, is favored.

This mechanism explains why BMS is so effective and how it is able to irreversibly inhibit hIDO1 where other in-

Induced-Fit



hibitors cannot, a feature that makes it an appealing clinical therapy. This new understanding the BMS binding trajectory underscores the value of these types of data and also points to potential strategies for development of additional therapies for cancer and beyond.

— Emma Nichols

See: Khoa N. Pham and Syun-Ru Yeh*, “Mapping the Binding Trajectory of a Suicide Inhibitor in Human Indoleamine 2,3-Dioxygenase 1,” *J. Am. Chem. Soc.* **140**, 14538 (2018). DOI: 10.1021/jacs.8b07994

Author affiliation: Albert Einstein College of Medicine

Correspondence: * syun-ru.yeh@einstein.yu.edu

This work is supported by National Institute of Health Grant GM115773 and National Science Foundation Grant CHE-1404929 (to S.-R.Y.). Use of

LRL-CAT was provided by Eli Lilly Company, which operates the facility. This research used resources of the Advanced Photon Source, a U.S. Department of Energy (DOE) Office of Science User Facility, operated for the DOE Office of Science by Argonne National Laboratory under Contract No. DE-AC02-06CH11357.

“Diabetes” cont’d. from page 71

tional design of better GPR40 agonists with the potential to improve future therapies for T2DM. — Chris Palmer

See: [1] Joseph D. Ho^{1*}, Betty Chau¹, Logan Rodgers¹, Frances Lu¹, Kelly L. Wilbur², Keith A. Otto², Yanyun Chen², Min Song², Jonathan P. Riley², Hsiu-Chiung Yang², Nichole A. Reynolds², Steven D. Kahl², Anjana Patel Lewis², Christopher Groshong¹, Russell E. Madsen¹, Kris Conners¹, Jayana P. Lineswala², Tarun Gheyji¹, Melbert-Brian Decipulo Saflor¹, Matthew R. Lee¹, Jordi Benach³, Kenton A. Baker¹, Chahrazad Montrose-Rafizadeh², Michael J. Genin², Anne R. Miller², and Chafiq Hamdouchi^{2**}, “Structural basis for GPR40 allosteric agonism and incretin stimulation,” *Nat. Commun.* **9**, 1645 (2018). DOI: 10.1038/s41467-017-01240-w

Author affiliations: ¹Lilly Biotechnology Center San Diego, ²Lilly Research Laboratories, ³Lilly Research Laboratories Collaborative Access Team

Correspondence: * ho_joseph_d@lilly.com,

** hamdouchi_chafiq@lilly.com

Use of the Lilly Research Laboratories Collaborative Access Team was provided by Eli Lilly Company, which operates the facility. This research used resources of the Advanced Photon Source, a U.S. Department of Energy (DOE) Office of Science User Facility operated for the DOE Office of Science by Argonne National Laboratory under Contract No. DE-AC02-06CH11357.

[2] Jun Lu^{1*}, Noel Byrne¹, John Wang¹, Gerard Bricogne², Frank K. Brown¹, Harry R Chobanian¹, Steven L. Colletti¹, Jerry Di Salvo¹, Brande Thomas-Fowlkes¹, Yan Guo¹, Dawn L. Hall¹, Jennifer Hadix¹, Nicholas B. Hastings¹, Jeffrey D. Hermes¹, Thu Ho¹, Andrew D. Howard¹, Hubert Josien¹, Maria Kornienko¹, Kevin J. Lumb¹, Michael W. Miller¹, Sangita B. Patel¹, Barbara Pio¹, Christopher W. Plummer¹, Bradley S. Sherborne¹, Payal Sheth¹, Sarah Souza¹, Srivanya Tummala¹, Clemens Vornrhein¹, Maria Webb¹, Samantha J. Allen¹, Jennifer M. Johnston¹, Adam B. Weinglass¹, Sujata Sharma¹, and Stephen M. Soisson^{1**}, “Structural basis for the cooperative allosteric activation of the free fatty acid receptor GPR40,” *Nat. Struct. Mol. Biol.* **24** (7), 570 (2017). DOI: 10.1038/s41467-017-01240-w

Author affiliations: ¹Merck Research Laboratories, ²Global Phasing Limited

Correspondence: * jun_lu3@merck.com,

** stephen_soisson@merck.com

This research used resources at the IMCA-CAT beamline, supported by the companies of the Industrial Macromolecular Crystallography Association through a contract with Hauptman-Woodward Medical Research Institute. We thank K. Battaile and A.M. Mulichak for data collection assistance and L.J. Keefe for direction of IMCA-CAT operations. This research used resources of the Advanced Photon Source, a U.S. Department of Energy (DOE) Office of Science User Facility operated for the DOE Office of Science by Argonne National Laboratory under Contract No. DE-AC02-06CH11357.

A Small Molecule Plays a Big Role in HIV Infectivity

In a clear success of medical science, people with the human immunodeficiency virus (HIV) can now stay healthy for decades with daily oral medications. However, the burden of living with the disease remains high, and many are eager for less cumbersome treatments or, ideally, a cure. Scientists have been hampered by the incredible complexity and robustness of the HIV life cycle, but they continue to make progress in teasing out all of HIV's secrets in search of new weapons against the virus. Researchers used high-brightness x-rays from the APS to solve the structures of domains from HIV's Gag protein, the proteolytic cleavage (the process of breaking the peptide bonds between amino acids in proteins) of which triggers viral maturation. They focused in particular on discerning the role of inositol hexakisphosphate (IP6), a naturally-occurring, negatively-charged cofactor that associates with Gag. The researchers' structural and functional analyses suggests a model wherein IP6 is critical for two steps in the HIV life cycle: assembly and maturation. Their results are another, crucial step toward new treatments for HIV.

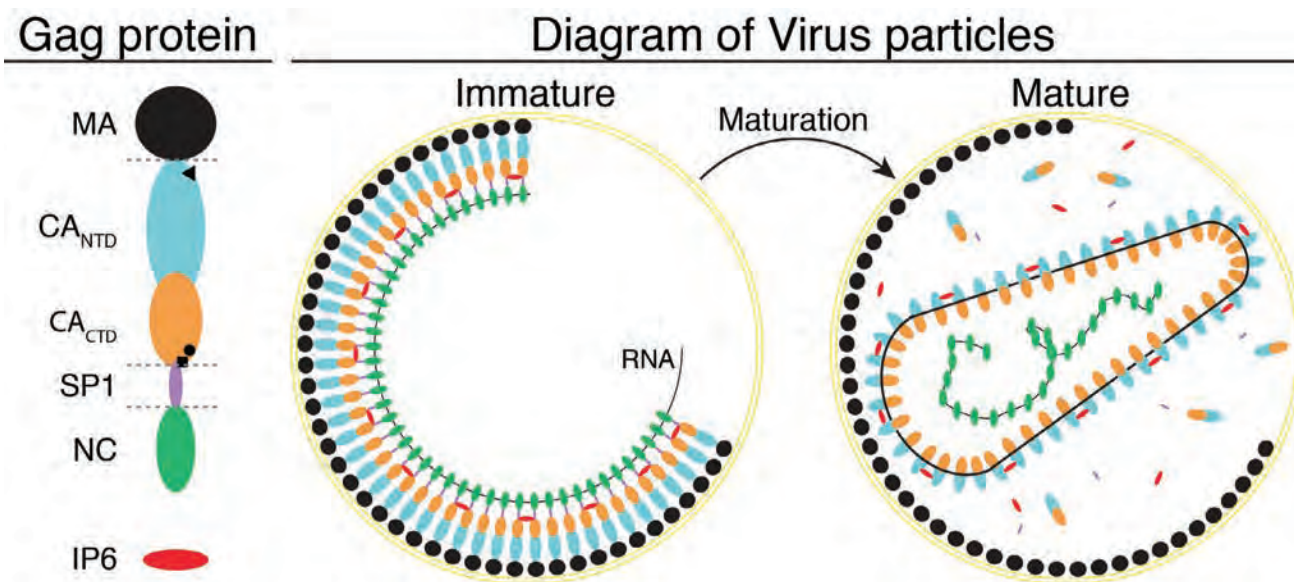


Fig. 1. Left: Diagram of HIV-1 Gag, with the indicated positions of the conserved arginine (triangle) and the conserved lysines (circle, square) involved in IP6 binding. Dotted lines indicate protease cleavage sites. Right: Diagram of Gag organization in immature virions. Following cleavage of Gag by protease (that is, maturation), CA re-organizes to form a mature core around viral RNA. From R.A. Dick et al., *Nature* **560**, 509 (3 August 2018). © 2018 Springer Nature Limited. All rights reserved.

Different HIV pharmaceutical treatments interrupt varying stages of the HIV life cycle, which has several parts: 1) binding to the host immune cell, 2) fusion with the host cell membrane; 3) release of the viral capsid into the cytoplasm and reverse transcription to turn the RNA genome into DN; 4) transport of the viral DNA into the nucleus and integration into the host genome; 5) transcription of the viral DNA into RNA and synthesis of viral proteins, including Gag, by the host's cellular machinery; 6) assembly of viral proteins into the immature virus at the cell surface; and 7) the budding of an immature virus from the host cell, triggering maturation, which is brought about by the proteolytic cleavage of Gag into its constitutive domains. Immature HIV is not infectious, and inhibitors of the viral protease have been a mainstay of pharmaceutical intervention in HIV replication, although eventually inhibitor resistant mutants emerge.

Previous work had suggested that IP6, which is present in all mammalian cells, interacts with Gag, which is a polyprotein, meaning a protein with multiple domains. These domains include matrix (MA), which interacts with the host's cellular membrane; capsid (CA), which forms the internal shell of the mature virus; nucleocapsid (NC), which binds to and compacts the genomic RNA; and SP1, a 14-residue spacer peptide that separates CA from NC. During virus assembly, Gag forms a hexamer that creates an immature lattice underneath the viral membrane. After virus budding, Gag is cleaved, breaking the immature lattice and triggering the reassembly of Gag's components into the various parts of the mature virus, with the liberated CA domain forming the mature capsid lattice. In vitro, IP6 stimulates the assembly of purified Gag protein into immature virus-like particles.

In this study, the researchers from Cornell University, the University of Virginia, the University of Delaware, EMBL (Germany), the Institute of Science and Technology Austria, and the University of Missouri removed the gene responsible for the synthesis of IP6 from a human cell line and found a 10-fold to 20-fold reduction of HIV particle production, underscoring the importance of IP6 in the viral life cycle.

As a next step, the researchers utilized the SER-CAT 22-ID beamline to collect x-ray diffraction data that provided the key to solving the structure of a hexamer consisting of a Gag construct in a pre-proteolytic cleavage state (immature), including parts of the CA domain, plus

SP1, in the presence of IP6 (Fig. 1). Indeed, the crystal structure showed IP6 bound to the hexamer, interacting with two conserved lysine side chains, supporting the idea that IP6 is an assembly cofactor. Mutating those lysine residues abolished HIV's infectivity, again suggestive of the importance of IP6. To examine how IP6 exerts its influence on the construct, the researchers performed a molecular dynamics simulation, with and without IP6. Without the cofactor, the hexamer's symmetry fell apart rapidly; however, when they ran the simulation again with IP6, the 6-fold symmetry was stabilized.

The influence of IP6 seemed to go beyond assembly assistance of full-length Gag; the team also explored the impact of IP6 on post-cleavage Gag. Proteolysis unmask a conserved arginine residue that is known to be essential for HIV infection. When the researchers mutated that arginine to an alanine residue in a post-cleavage Gag construct, IP6 no longer promoted assembly of the mature capsid lattice. When they solved the structure of this construct with IP6, the researchers found IP6 bound to the newly exposed arginine residue, promoting the formation of a hexamer of CA protein and thus the mature lattice that forms the viral capsid. The finding that a small molecule has such importance at two steps of the HIV life cycle may inspire the development of novel therapeutics.

— Erika Gebel Berg

See: Robert A. Dick^{1*}, Kaneil K. Zadrozny², Chaoyi Xu³, Florian K.M. Schur^{4,5}, Terri D. Lyddon⁶, Clifton L. Ricana⁶, Jonathan M. Wagner², Juan R. Perilla³, Barbie K. Ganser-Pornillos², Marc C. Johnson⁶, Owen Pornillos^{2**}, and Volker M. Vogt¹, "Inositol phosphates are assembly co-factors for HIV-1," *Nature* **560**, 509 (3 August 2018). DOI: 0.1038/s41586-018-0396-4

Author affiliations: ¹Cornell University, ²University of Virginia, ³University of Delaware, ⁴EMBL, ⁵Institute of Science and Technology Austria, ⁶University of Missouri

Correspondence: * rad82@cornell.edu, ** opornillos@virginia.edu

This work was supported by the National Institutes of Health (NIH) grants R01-GM107013 (V.M.V.), R01-GM105684 (G. W. Feigenson), P30-GM110758 and P50-GM082251 (J.R.P.), R01-AI129678 (O.P. and B.K.G.-P.), U54-GM103297 (O.P.), and R01-GM110776 (M.C.J.). F.K.M.S. was supported by Deutsche Forschungsgemeinschaft grant BR 3635/2-1 awarded to J.A.G. Briggs. J.M.W. was supported by NIH postdoctoral fellowship grant F32-GM115007. This research used resources of the Advanced Photon Source, a U.S. Department of Energy (DOE) Office of Science User Facility operated for the DOE Office of Science by Argonne National Laboratory under Contract No. DE-AC02-06CH11357.

Toward a Universal Therapy against Ebola Virus

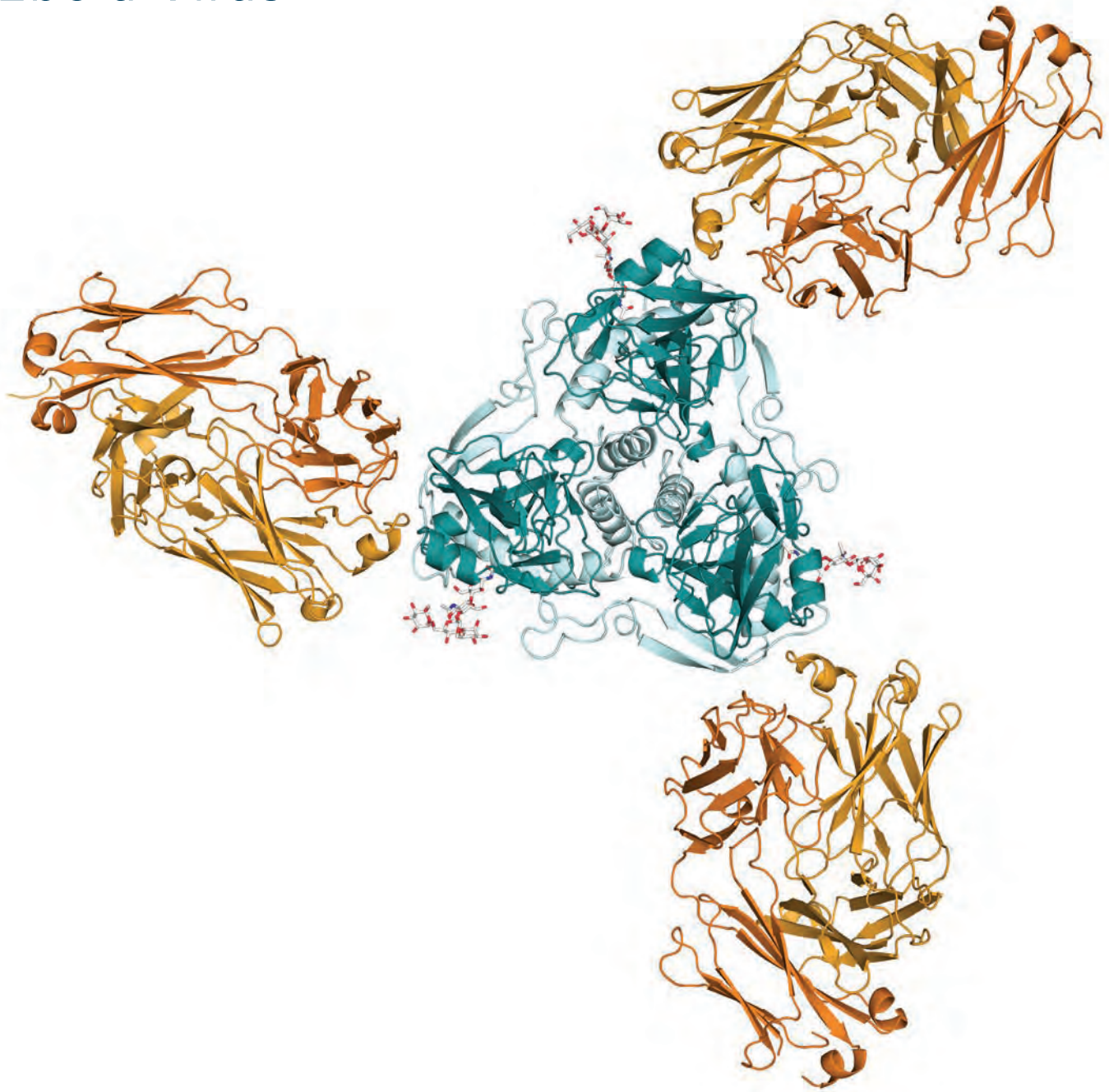


Fig. 1. Three antigen-binding fragments of ADI-15946 (orange) are shown bound to the surface glycoprotein of Ebola virus (teal).

Ebola virus is a member of the *Ebolavirus* genus, which also contains other pathogenic viruses such as Sudan virus and Bundibugyo virus. Ebola virus infection causes Ebola virus disease (EVD), a severe and frequently fatal hemorrhagic fever in humans and non-human primates that has implications for global biosecurity and public health. A major challenge in treating this disease lies in the fact that five different viruses in the *Ebolavirus* genus can cause it. In order to enter and infect the host animal, Ebola virus has to first attach to a host cell. A glycoprotein (GP) on the surface of the virus is critical for this attachment, and all five ebolaviruses have a single but different GP on each of their surfaces. Antibodies against these GPs are therefore attractive candidates for broadly reactive therapeutics that may be capable of treating EVD, regardless of the specific virus responsible for the disease outbreak. Understanding the molecular interactions between broadly neutralizing antibodies and the Ebola virus GP is therefore crucial to the design of next-generation immunotherapeutic cocktails. Scientists from The Scripps Research Institute have recently focused on understanding how antibodies directed against ebolavirus GPs can mount an effective neutralization response against multiple members of the *Ebolavirus* genus. Using x-ray crystallography, the team collected diffraction data at the APS in order to examine the three-dimensional molecular interaction between an antibody and its target, the ebolavirus GP. The results of this study will instruct vaccine design aimed at eliciting a broadly neutralizing humoral immune response against ebolaviruses.

The fight against this deadly illness cost the international community more than \$50 billion during the 2014–2016 West Africa outbreak alone. As of March 6, 2019, the ongoing EVD outbreak in the Democratic Republic of the Congo had infected nearly 10,000 people, with an approximately 57% fatality rate. Although these two most recent outbreaks were caused by Ebola virus itself, other viruses in the *Ebolavirus* genus have caused deadly outbreaks among humans, and likely will do so again in the future. However, because rapid identification of causative *Ebolavirus* species can be difficult, treatment strategies and therapeutics are needed that can combat multiple virus species in the *Ebolavirus* genus. Such antibodies that can neutralize all five viruses are exceedingly rare.

In this study, the researchers investigated how one broadly neutralizing antibody, ADI-15946, interacts with the viral glycoprotein. Working at the GM/CA-XSD structural biology facility x-ray beamline 23-ID-B at the APS, they evaluated a three-dimensional molecular model of the structure of both the viral GP epitope (the part that antibody binds to) and the antibody's paratope (the part that binds to the epitope) in complex with the viral GP cellular receptor (Fig. 1).

In particular, the model of the paratope enabled them to engineer the antibody to improve binding and neutralization of more distant members of the *Ebolavirus* genus. Functional insights provided by the study's accompanying biochemistry also confirmed the structural

observations of this interaction. Together, the data highlight an epitope on the various *Ebolavirus* GPs that is susceptible to broad neutralization by a single antibody.

Unexpectedly, the researchers also found that the antibody's binding site on the GP occupies a pocket on the GP surface that is usually closed off by a loop that descends from the glycan cap, or stalk region, of the GP. Future *Ebolavirus* vaccine design will need to take this observation into consideration in order to design an effective immunogen that is capable of eliciting broadly neutralizing antibodies that target the ADI-15946 paratope via a humoral immune response. — Nicola Parry

See: Brandyn R. West, Crystal L. Moyer, Liam B. King, Marnie L. Fusco, Jacob C. Milligan, Sean Hui, and Erica Ollmann Saphire*, "Structural Basis of Pan-Ebolavirus Neutralization by a Human Antibody against a Conserved, Yet Cryptic Epitope," *mBio* **9**(5), e01674-18 (September/October 2018). DOI: 10.1128/mBio.01674-18.

Author affiliation: Scripps Research

Correspondence: * erica@scripps.edu

The authors acknowledge a National Institutes of Health (NIH) NIAID Centers of Excellence in Translational Research award for the Viral Hemorrhagic Fever Immunotherapeutic Consortium (U19 AI109762) and NIH R01 AI132204 for support. GM/CA-XSD is funded in whole or in part with Federal funds from the National Cancer Institute (ACB-12002) and the National Institute of General Medical Sciences (AGM-12006). This research used resources of the Advanced Photon Source, a U.S. Department of Energy (DOE) Office of Science User Facility operated for the DOE Office of Science by Argonne National Laboratory under Contract No. DE-AC02-06CH11357.

The Power of Entropy: Solving the Allosteric Mystery of a Disordered Tail

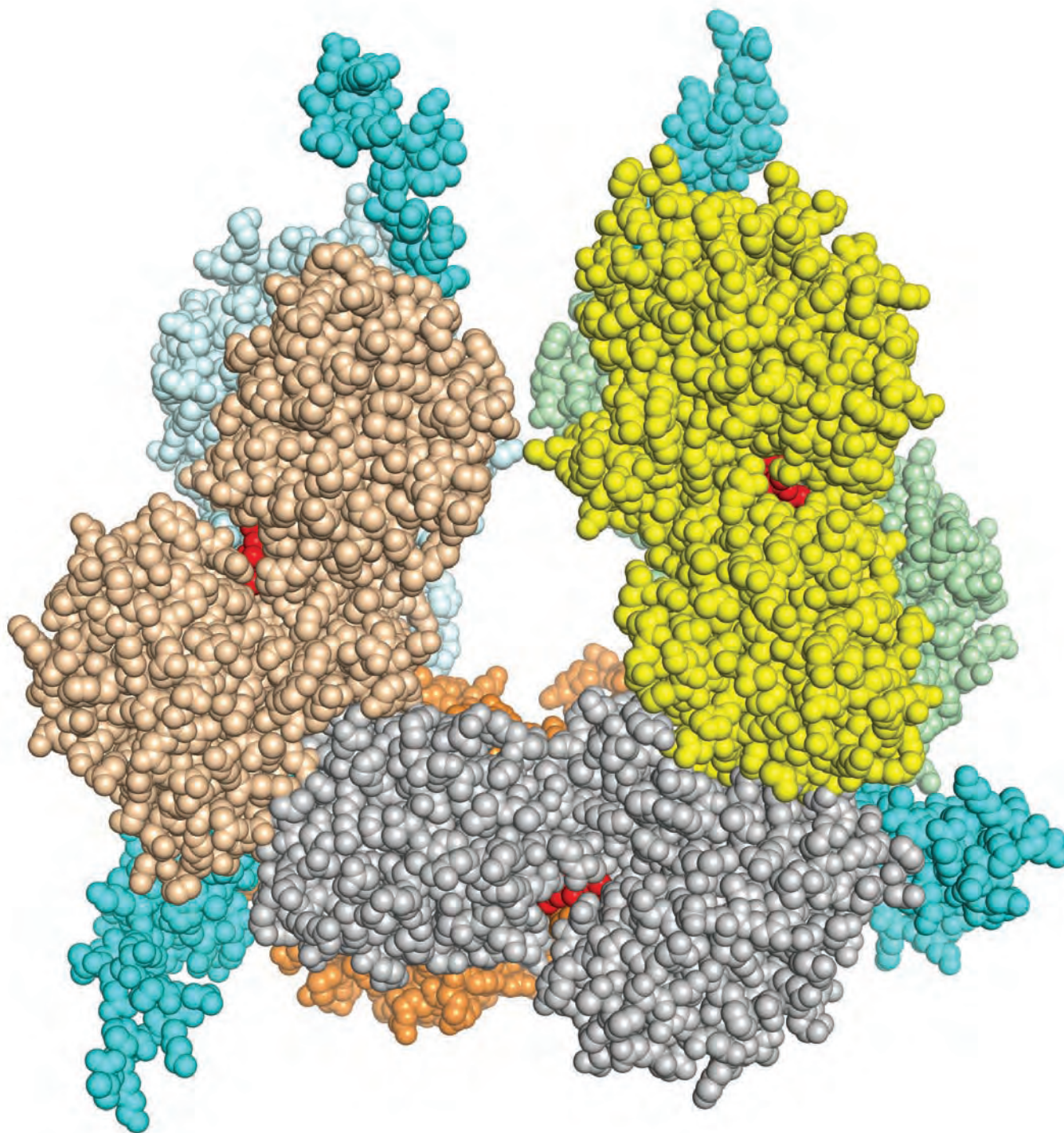


Fig. 1. The inactive form of the UGDH hexamer in sphere representation with UDP-Xylose shown in red. The cyan colored portion is an energy minimized structure of the ID-tail. It is never observed in crystal structures, so the researchers used MD simulations to minimize the energy and then simply attached it to the protein's x-ray crystal structure.

Almost half of the human proteome (the complete set of proteins expressed by an organism) contains bits that are intrinsically disordered, the purpose of which remain largely unknown. Researchers teased out the role of a disordered region (ID-tail) of UDP-glucose-6-dehydrogenase (UGDH), an enzyme involved in the biosynthesis of complex carbohydrates that help mediate cellular communications. The researchers, using the APS, solved the high-resolution structures of UGDH hexamers with and without the ID-tail and used the structural insights to decipher the ID-tail's job. The tail provides an entropic force that makes UGDH's active site more susceptible to allosteric inhibition, and is therefore key to cellular regulation of the protein. This study suggests that the intrinsically disordered parts of the enzyme offer a mechanism for tuning the protein energy landscape. This finding may offer a framework for understanding the role of disordered proteins and disordered protein segments in nature and explain their ubiquity.

Intrinsically disordered proteins don't have the relatively rigid three-dimensional structures of the other major classes of proteins, including globular and membrane proteins. This flexibility has upended the canonical structure-function relationship and has made it more difficult to draw connections between the shape of disordered proteins and their activity. The ID-tail of UGDH, as its name would suggest, is the disordered 30-residue C-terminus of the protein, wagging about without any discernable higher structure. The rest of the protein is globular, forming dimers that coalesce into an inactive hexamer of UGDH. Upon binding UDP-glucose, the UGDH hexamer undergoes an allosteric switch to its active state, catalyzing the conversion of UDP-glucose to UDP-glucuronate. UDP-xylose serves as an allosteric inhibitor of this reaction, binding to UGDH's active site in place of UDP-glucose and triggering an allosteric switch to an inactive state.

To examine the role of the ID-tail, the team from the University of Georgia, the University of Michigan, Washington University in St. Louis, and the University of Pennsylvania utilized the SER-CAT 22-ID x-ray beamline at the APS to obtain 2.6-Å data sets of two versions of UGDH: one with and one without the ID-tail (Fig. 1). Kinetic experiments showed that UGDH bound to and converted UDP-glucose with or without the tail, demonstrating that catalysis was tail agnostic. However, when the researchers looked at what happened when they added UDP-xylose in place of UDP-glucose, the ID-tail did make a difference.

A tail-less UGDH had a much lower affinity for UDP-xylose compared with UGDH with its ID-tail. By studying the thermodynamics of the system, the researchers concluded that the ID-tail was producing an entropic force that was pushing the protein toward a structural state that is more favorable to UDP-xylose binding.

To explore this concept further and look at what, if any, influence the sequence of the disordered region plays, the researchers swapped the ID-tail with a series of alternate tails; those with randomized sequences, those that swapped negative charges for positive charges, and polyserine, among other constructs. These substitute tails had little effect on the protein's affinity for UDP-xylose, suggesting that the entropic force is independent of sequence identity. Interestingly, the ID-tail sequence is conserved among proteins related to UGDH from other species, leading the authors to suggest the sequence may have an unrelated biological function that supplies the evolutionary pressure to maintain the sequence.

While the sequence didn't seem to matter, the team also looked at whether sequence length impacted UDP-xylose affinity. When the researchers compared UDP-xylose affinity of UGDH constructs with different length tails, they found that affinity increased with increasing length and then tapered off to a maximum affinity at around 30 residues. Tails as long as around 60 residues were associated with UGDH affinity for UDP-xylose similar to those with 30 residues. Monte Carlo simulations of the protein with varying tail lengths supported the relationship between the entropy of the tail and affinity to UDP-xylose, with tails shorter than 30 residues employing less entropic force and those with tails above 30 supplying maximum force. — Erika Gebel Berg

See: Nicholas D. Keul¹, Krishnadev Oruganty², Elizabeth T. Schaper Bergman³, Nathaniel R. Beattie¹, Weston E. McDonald¹, Renuka Kadirvelraj¹, Michael L. Gross³, Robert S. Phillips¹, Stephen C. Harvey⁴, and Zachary A. Wood^{1*}, "The entropic force generated by intrinsically disordered segments tunes protein function," *Nature* **563**, 584 (22 November 2018). DOI: 10.1038/s41586-018-0699-5

Author affiliations: ¹University of Georgia, ²University of Michigan, ³Washington University in St. Louis, ⁴University of Pennsylvania

Correspondence: * zaw@uga.edu

This work was supported by the National Institutes of Health (NIH) National Institute of General Medicine grants R01GM114298 awarded to Z.A.W. and P41GM103422 awarded to M.L.G. SER-CAT is supported by its member institutions (see www.ser-cat.org/members.html), and equipment grants (S10_RR25528 and S10_RR028976) from the NIH. This research used resources of the Advanced Photon Source, a U.S. Department of Energy (DOE) Office of Science User Facility operated for the DOE Office of Science by Argonne National Laboratory under Contract DE-AC02-06CH11357.

Structuring Hearing and Deafness

Hearing relies on sensory receptors in the inner ear that transform the mechanical forces from sound into electrical signals that can be interpreted by the brain. The receptors are called “hair cells” and these have small hair-like projections called “stereocilia” that are arranged from shortest to tallest. As sound moves in and is detected, the stereocilia lean into one another, like uneven dominos, and transmit the mechanical signal through linker proteins at the top of each stereocilia, the tip links. Although these tip link filaments are a small part of the overall structure of the hair cell, they are essential to hearing as they convey force to the inner-ear ion channels that mediate sensory perception. Over 100 mutations in one of the tip link proteins, an enormous structural protein called Cadherin-23 (CDH23), have been associated with inherited deafness. In order to understand the structural basis for the disruption of hearing associated with these mutations, a research group employed high-brightness x-rays from the APS to solve 13 structures of CDH23 fragments that show the location of 65% of the CDH23 deafness mutations. This work advances our understanding of both hearing and deafness.

The first task faced by the researchers from The Ohio State University was to choose which regions of the enormous CDH23 protein to study. In the tip link, CDH23, and another protein, proto-cadherin-15 (PCDH15), form the upper and lower ends, respectively, of the filament, tethering each hair cell stereocilium to the next in the bundle through transmembrane attachments. Both are very large structural proteins with multiple subunits that pack one after the other like beads on a necklace. These subunits are called “cadherin repeats,” although each repeat is truly unique. The repeats comprise 7 β -strands connected by 6 loop regions and connecting linkers between them, which contain up to 3 binding sites for calcium, an important regulator of cadherin function and mechanics. The CDH23 section has 27 repeats, making this protein one of the largest of the cadherin superfamily.

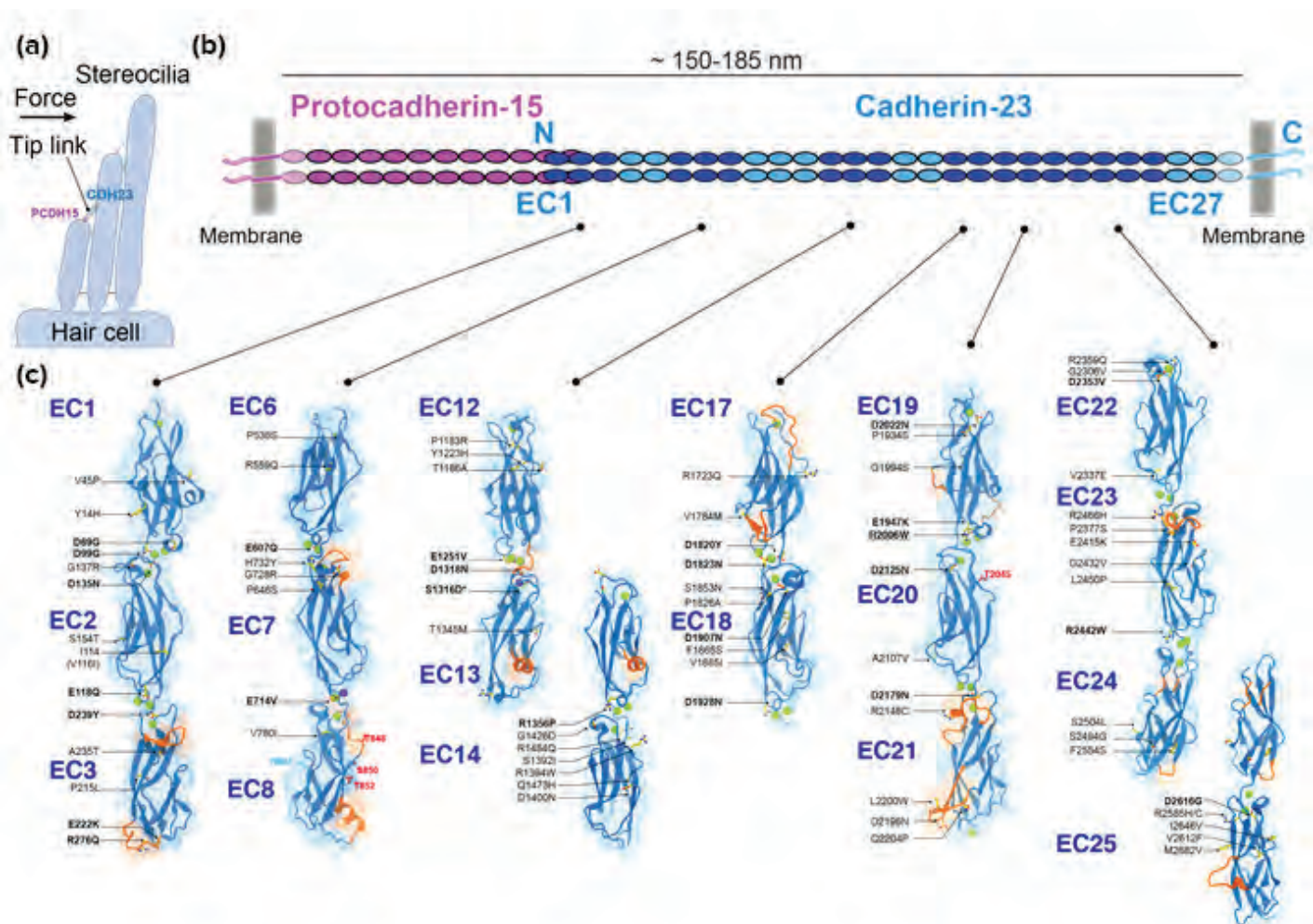
After studying the known sequences of CDH23 from a variety of species and testing many of the repeats to determine their suitability for structural studies, the team focused on 18 that included the most and least conserved versions over the length of the tip link and that covered about 2/3 of the CDH23 length. The structures for these repeats, solved with diffraction data from the NE-CAT 24-ID-C and 24-ID-E x-ray beamlines at the APS, showed for the first time multiple unique structural variations and deafness mutation sites along CDH23.

Among the 13 CDH23 structures depicting 18 of its repeats, the data allowed the researchers to visualize 76 out of 116 known deafness mutation sites. Careful analysis of the location of each of these mutations allowed the

group to classify them into categories based on their potential structural impact. The first category included amino acid changes that disrupted the hydrophobic core of the protein, potentially disrupting the structure of the β -strands. The second category included amino acid changes on the outer-facing surface of the protein that could affect the interface with PCDH15 and the function of the tip link. These mutations could, for example, affect the response of the tip link to loud sounds. The third group of mutations included those that affect calcium binding at the linkers between repeats. These are also implicated in disruption of the mechanical signal due to their potential effects on the rigidity of the tip link.

Structural insights for the mutations altering calcium-binding sites were further supported by thermal stability assays, which demonstrated that disruption of CDH23 calcium binding alters the stability of the protein in various ways. These data suggest that mutations to calcium-binding sites destabilize the way the CDH23 repeats interact with each other and reduce their ability to withstand force from large stimuli. These studies provide insight into the different ways that mutations in CDH23 can cause deafness, whether through disruption of protein stability, protein-protein interactions, or calcium binding, and also important information regarding the role of these structures in sensitively detecting and transmitting the mechanical signals from sounds that reach the inner ear.

The next challenge for the team is to build a complete structural model of CDH23 including all 27 of its re-



peats and to establish whether there is a clear correlation between the severity of the deafness phenotype caused by inherited mutations and their structural effects on the tip link. — Sandy Field

See: Avinash Jaiganesh, Pedro De-la-Torre, Aniket A. Patel, Domenic J. Termine, Florencia Velez-Cortes, Conghui Chen, and Marcos Sotomayor*, “Zooming in on Cadherin-23: Structural Diversity and Potential Mechanisms of Inherited Deafness,” *Structure* **26**, 1210 (September 4, 2018). DOI: 10.1016/j.str.2018.06.003
 Author affiliation: The Ohio State University
 Correspondence: *sotomayor.8@chemistry.ohio-state.edu

This work was supported by The Ohio State University and the National Institutes of Health National Institute on Deafness and Other Communication Disorders (NIH/NIDCD) grants K99/R00 DC012534 and R01 DC015271), and the Alfred P. Sloan Foundation (FR-2015-65794). P.D. is a Pelotonia fellow. This work is based upon research conducted at the NE-CAT beamlines, which are funded by the National Institute of General Medical Sciences from the National Institutes of Health (P30 GM124165). The Pilatus 6M detector on the 24-ID-C beamline is funded by a NIH-ORIP HEI grant (S10 RR029205). This research used resources of the Advanced Photon Source, a U.S. Department of Energy (DOE) Office of Science User Facility operated for the DOE Office of Science by Argonne National Laboratory under Contract No. DE-AC02-06CH11357.

Fig. 1. Zooming in on Cadherin-23, a protein essential for hearing. (a) Schematic representation of a cochlear hair-cell stereocilia bundle row highlighting the tip-link location. (b) The tip link, formed by the tip-to-tip interaction of Protocadherin-15 (purple) and Cadherin-23 (blue). Schematic representation of all Protocadherin-15 and Cadherin-23 extracellular cadherin (EC) repeats. Both proteins are products of deafness genes and are thought to form parallel dimers. Dark blue ovals indicate repeats for which the Ohio team solved x-ray crystallographic structures (PDB codes 5w4t, 5tfm, 5tfl, 5vh2, 5wj8, 5wjm, 5tfk, 5vvm, 5zu8, 5vt8, 5un2, 5ulu, 5i8d). (c) Ribbon diagram of Cadherin-23 structures (blue) with unusual features highlighted in orange and with transparent molecular surface representation. Deafness-related mutations are shown as yellow sticks and are listed (boldfaced residues are in conserved calcium-binding motifs). Calcium ions are shown in green. Adapted from A. Jaiganesh et al., *Structure* **26**, 1210 (2018). © 2018 Elsevier Ltd.

Peering Inside a Pathogen

Among bacteria, *Legionella pneumophila*, which is causing the severe pneumonia known as Legionnaires' disease in humans, translocates the largest known assortment of pathogenic factors, called "effectors," into host cells during infection. These more than 330 effectors allow the deadly microbe to successfully establish a home base from which to replicate inside evolutionarily disparate organisms such as drinking water-dwelling amoebas and human macrophages. Macromolecular x-ray crystallography performed at the APS has revealed that the *L. pneumophila* effectors MavC and MvcA are structural homologs of cycle inhibiting factor (Cif) effectors, which have been shown to induce mammalian cell growth arrest. However, in contrast to canonical Cifs, both MavC and MvcA deamidate the residue Gln40 of ubiquitin but not Gln40 of human ubiquitin homolog NEDD8. The researchers found MavC and MvcA to be functionally diverse, with MavC impairing the ability of the E2-conjugating enzyme UBE2N to form Lys63 ubiquitin chains. This disruption to Lys63 scaffolds ultimately impairs the signal transduction of NF- κ B, which normally plays a role in fighting infection. Combined, these results illuminate a molecular mechanism of host manipulation by pathogenic bacteria and highlight the complex regulatory mechanisms integral to *L. pneumophila*'s pathogenic strategy (Fig. 1).

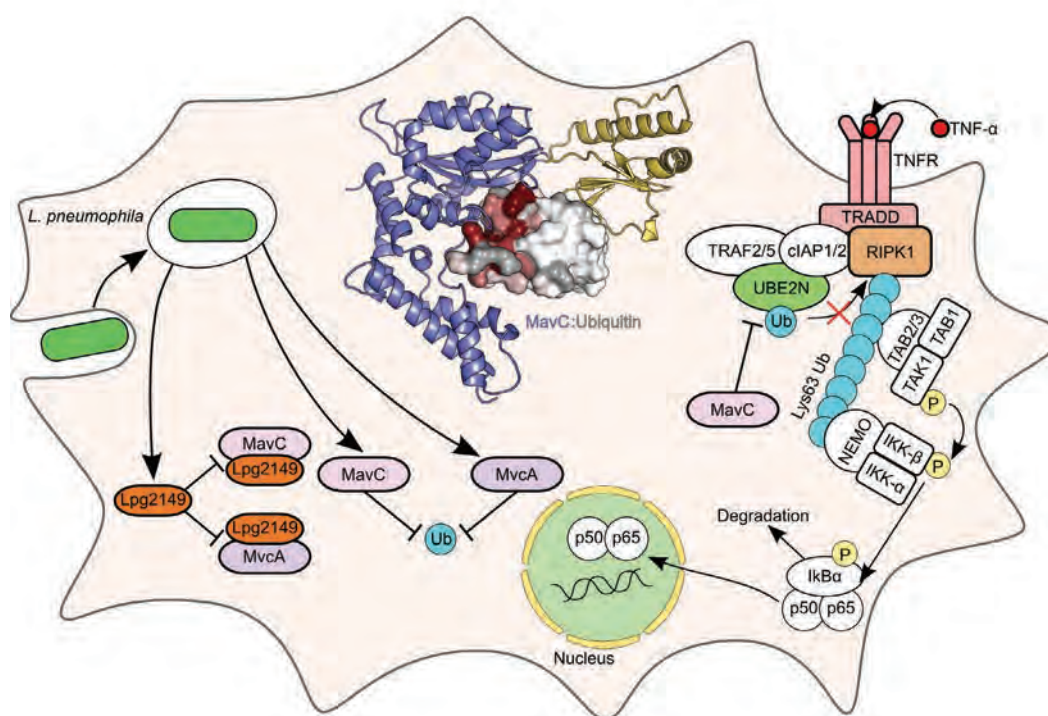


Fig. 1. Model of the secretion and regulation of MavC, MvcA, and Lpg2149 during *L. pneumophila* infection. In the absence of MavC, the enzyme UBE2N forms Lys63 ubiquitin chains on key components of NF- κ B signaling; namely, RIPK1 and RIPK2 (not pictured). These Lys63 chains act as scaffolds for downstream complexes to assemble, leading to NF- κ B signal transduction. Secretion of MavC impairs the ability of UBE2N to form Lys63 ubiquitin chains on these key components (red X). Because downstream complexes are not able to assemble on Lys63 scaffolds, NF- κ B is impaired in the presence of active MavC.

L. pneumophila causes Legionnaire's disease by infecting macrophages, a type of microbe-eating immune cell known as white blood cells, which are located in the alveolar sacs of the lungs. *L. pneumophila* is one of many Gram-negative pathogens using a common infection strategy of combining a complex protein secretion system with an impressive collection of over three hundred secreted effector proteins. These effectors interfere with signaling pathways of host cells to co-opt critical processes such as vesicle trafficking, ubiquitylation, gene expression, and lipid metabolism, all for the benefit of the bacteria's survival. *L. pneumophila* is unique in the size and complexity of this arsenal, using the conserved Dot/Icm type IV secretion system to translocate hundreds of effector proteins to human host cells.

A key target of many Gram-negative pathogens, including *L. pneumophila*, is the human ubiquitination system, which regulates a wide array of cellular functions via the attachment of one or multiple copies of a small protein called "ubiquitin" to a target protein, which leads to degradation or functional regulation of the target.

Many pathogens deploy effectors that hijack or impede ubiquitination. One such class of effectors is the Cif effector family, which has no known analogs in eukaryotes and is so far found exclusively in the effector arsenals of pathogens that use the system. Cif effectors interfere with host ubiquitination, modulate the eukaryotic cell cycle, and subsequently induce mammalian cell growth arrest. Cifs are specific enzymes that were shown to remove an amide group from the conserved glutamine residue Gln40 on NEDD8, the closest human homolog of ubiquitin. NEDD8 is a key regulator of the activity of Cullin-Ring E3 ligases, which regulate an extensive number of dynamic cellular processes, including multiple aspects of the cell cycle, transcription, signal transduction, and development. Although NEDD8 is the primary target of Cifs, some Cifs also deamidate ubiquitin.

Previous studies have identified several *L. pneumophila* effectors that interfere with host ubiquitination, but there are no known examples of Cif effectors in this or any other pathogen that use the type IV secretion system.

Researchers from the University of Toronto (Canada), the University of Calgary (Canada), and Argonne used macromolecular x-ray crystallography performed at the SBC-CAT and LS-CAT 19-ID-D and 21-ID (respectively) x-ray beamlines at the APS, to characterize the structure of two *L. pneumophila* effectors, MavC (also known as Lpg2147) and MvcA (MavC paralog A, or Lpg2148). The

crystal structures of MavC and MvcA suggest they are structural homologs of Cif effectors. However, additional structural and functional characterization indicated that, in contrast to previously characterized Cif effectors, MavC and MvcA, specifically, only deamidate ubiquitin and not human NEDD8. Furthermore, the researchers found that MavC and MvcA do not cause the cell cycle arrest that is a hallmark of all the previously characterized Cifs but, rather, modulate specific signaling pathways. For example, MavC was found to directly modulate the activity of the Lys63 linkage-specific E2-conjugating enzyme UBE2N. This leads to the disruption of ubiquitination in UBE2N-related pathways, such as NF- κ B signaling (Fig. 1), which normally helps regulate DNA transcription, cytokine production, cell survival, and the immune response to infection.

In addition, the researchers found that a protein encoded by the *lpg2149* gene, which is adjacent to the genes that encode MavC and MvcA, blocks the catalytic activity for both of these specialized ubiquitin deamidases, raising the possibility that this protein serves to regulate effector activity in *L. pneumophila*.

Together, this work reveals the complexity and diversity of the toolbox of molecular control techniques developed by pathogens such as *L. pneumophila*.

— Chris Palmer

See: Dylan Valleau¹, Andrew T. Quaille¹, Hong Cui¹, Xiaohui Xu¹, Elena Evdokimova¹, Changsoo Chang², Marianne E. Cuff², Malene L. Urbanus¹, Scott Houliston¹, Cheryl H. Arrowsmith¹, Alexander W. Ensminger¹, and Alexei Savchenko^{1,3*}, "Discovery of Ubiquitin Deamidases in the Pathogenic Arsenal of *Legionella pneumophila*," Cell Rep. **23**, 568, (April 10, 2018). DOI: 10.1016/j.celrep.2018.03.060

Author affiliations: ¹University of Toronto, ²Argonne National Laboratory, ³University of Calgary

Correspondence: * alexei.savchenko@ucalgary.ca

The Arrowsmith NMR facility is generously supported by funding from the Princess Margaret Cancer Centre of the University Health Network. This work was supported by National Institutes of Health grants GM074942 and GM094585 (to A.S. through the Midwest Center for Structural Genomics) and by the U.S. Department of Energy (DOE) Office of Biological and Environmental Research under contract DE-AC02-06CH11357. A.W.E. is supported by CIHR Operating Grant MOP-133406, the University of Toronto Department of Biochemistry, and infrastructure grant 30364 from the Canada Foundation for Innovation and the Ontario Research Fund. SBC-CAT is operated by UChicago Argonne, LLC, for the U.S. DOE Office of Biological and Environmental Research under contract DE-AC02-06CH11357. LS-CAT is supported by the Michigan Economic Development Corporation and the Michigan Technology Tri-Corridor (Grant 085P1000817). This research used resources of the Advanced Photon Source, a U.S. DOE Office of Science User Facility operated for the DOE Office of Science by Argonne National Laboratory under Contract DE-AC02-06CH11357.

Control Yourself!

Gene expression is one of the many wonders of biology. Our cells are able to pack 3 billion base pairs of DNA-encoded information into the tiny nucleus and then organize everything and selectively unpack only the genes needed for daily activities. This involves an orchestrated dance of gene expression, genome stability, and gene silencing – depending on the situation. Some aspects of this molecular dance are choreographed by histone methyltransferases (enzymes that transfer methyl groups from S-Adenosyl methionine onto the lysine or arginine residues of the H3 and H4 histones) that “tag” genes for silencing and maintain genomic stability. However, one outstanding question in this field concerns how these enzymes are regulated to avoid inappropriate gene silencing, an activity that has been implicated in a variety of diseases from cancer to metabolic disorders. Structural studies based on x-ray diffraction data collected at the APS have now provided important insight into this question.

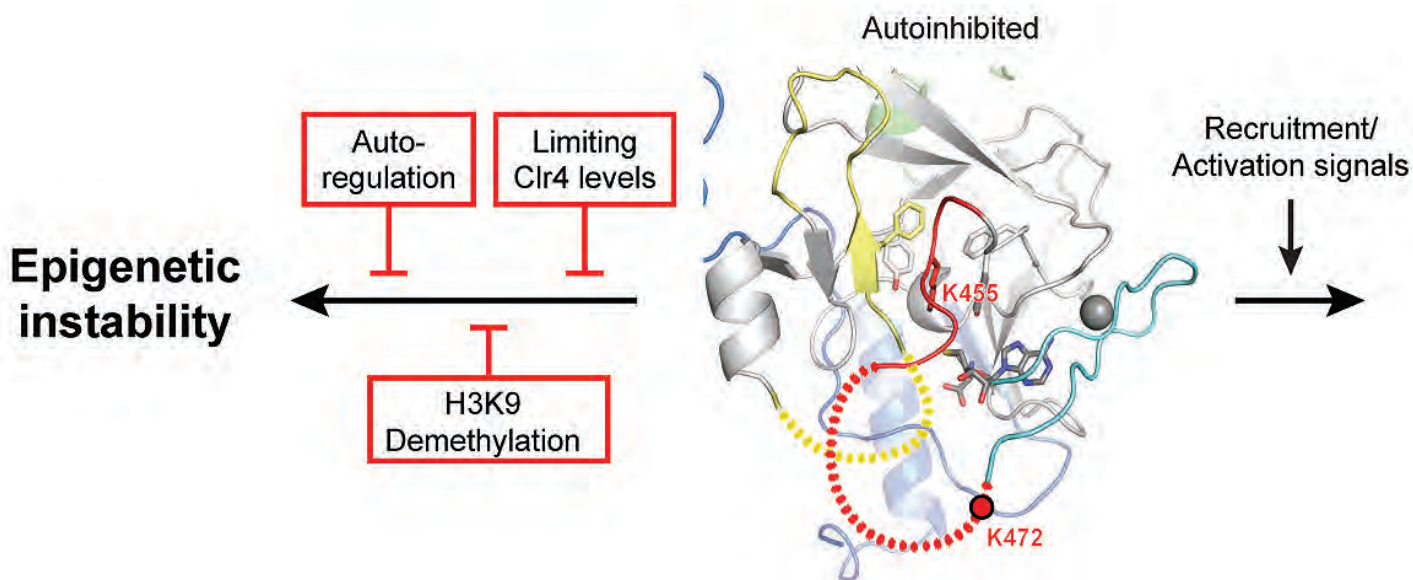


Fig. 1. Regulation of the fission yeast Clr4 methyltransferase by an autoregulatory loop allows for tight control of gene expression and silencing. The structure of Clr4 is shown as a ribbon diagram with the autoregulatory loop in red with key lysines in unmethylated (K455 and K472) and methylated forms (K455me and K472me) labeled and unstructured regions that change conformation between activated and autoinhibited states shown as red dots.

DNA is packed into a higher order structure, called “chromatin,” which involves wrapping it around histones, which are bundling proteins. Methyltransferases tag these histones at specific gene locations as a signal to other regulatory proteins that these genes should be unpacked (expressed) or not unpacked (silenced). For this research, the researchers from the Harvard Medical School, and the Howard Hughes Medical Institute were interested in the activity of the fission yeast methyltransferase, Clr4, a homolog of the human SUV39H enzymes. Clr4 tags the histone H3 protein by adding a methyl group to a specific lysine amino acid (H3K9) and promotes the formation of silent chromatin or heterochromatin. While studying the action of Clr4 on H3K9, the researchers noticed that the enzyme also appeared to

methylate itself; this unexpected finding led them down an interesting path.

First, the team conducted experiments to confirm that Clr4 added the methyl group to itself in the absence of H3K9 and showed that the activity appeared to be intramolecular, mediated by the enzyme itself, rather than a neighboring Clr4 molecule. Interestingly, the methylated form of Clr4 appeared to be more active than the non-methylated form. Next, they used liquid chromatography/mass spectrometry to identify the site of methylation and found that the enzyme was methylating its own lysine 455 (K455).

In order to understand this finding at the structural level, the researchers crystallized the non-methylated form of Clr4. The x-ray diffraction structural data obtained

The next step was to crystallize the methylated version of the enzyme. Solution of the structure, also determined at the NE-CAT beamline, revealed significant conformational changes compared to the non-methylated form. The autoregulatory loop containing K455 was now disordered and no longer occluded the catalytic site of Clr4. In addition, part of the autoregulatory loop that was disordered in the previous structure had now formed a helical structure that stabilized the active site. Further analysis of the structure and *in vitro* experiments revealed a second lysine, at position 472, that was also methylated for full activation of the enzyme.

Next, the team expressed their various Clr4 mutant enzymes in fission yeast and studied the effects on known pathways of heterochromatin formation and gene silencing. Their results showed that the hyperactive mutant Clr4 genes caused inappropriate silencing of genes important for cell growth and changes in the way the heterochromatin was organized, allowing it to spread beyond its normal boundaries. Additional experiments showed that Clr4 autoinhibition works in concert with other anti-silencing mechanisms in fission yeast to mediate appropriate control of gene expression and heterochromatin formation.

Comparison of these data to those of other labs suggests that this autoregulation may be a conserved mechanism in humans, too, with promising implications for basic research and drug design efforts. — Sandy Field

See: Nahid Iglesias^{1,2□}, Mark A. Currie^{1,2□}, Gloria Jih^{1,2}, Joao A. Paulo¹, Nertila Siuti^{1,2}, Marian Kalocsay¹, Steven P. Gygi¹, and Danesh Moazed^{1,2*}, “Automethylation-induced conformational switch in Clr4 (Suv39h) maintains epigenetic stability,” *Nature* **560**, 504 (23 August 2018). DOI: 10.1038/s41586-018-0398-2

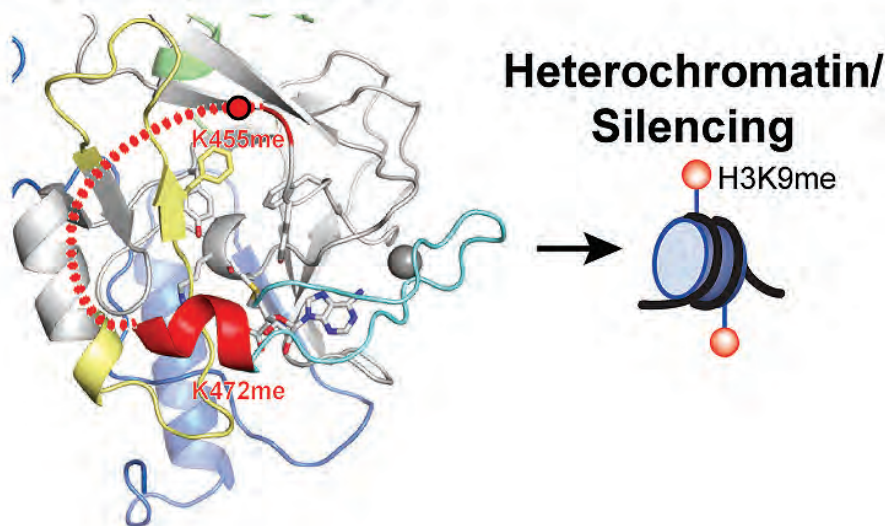
□Contributed equally to this work

Author affiliations: ¹Harvard Medical School, ²Howard Hughes Medical Institute

Correspondence: * danesh@hms.harvard.edu

We are grateful for assistance from the staff at NE-CAT. This work was supported by an EMBO long-term fellowship and a Swiss National Science Foundation postdoctoral fellowship (N.I.), K01 DK098285 (J.A.P.), National Institutes of Health (NIH) P50 GM107618 (M.K., S.P.G.) and NIH RO1 GM072805 (D.M.). D.M. is a Howard Hughes Medical Institute Investigator. This work is based upon research conducted at the NE-CAT-beamlines, which are funded by the National Institute of General Medical Sciences from the National Institutes of Health (P30 GM124165). This research used resources of the Advanced Photon Source, a U.S. Department of Energy (DOE) Office of Science User Facility operated for the DOE Office of Science by Argonne National Laboratory under Contract No. DE-AC02-06CH11357.

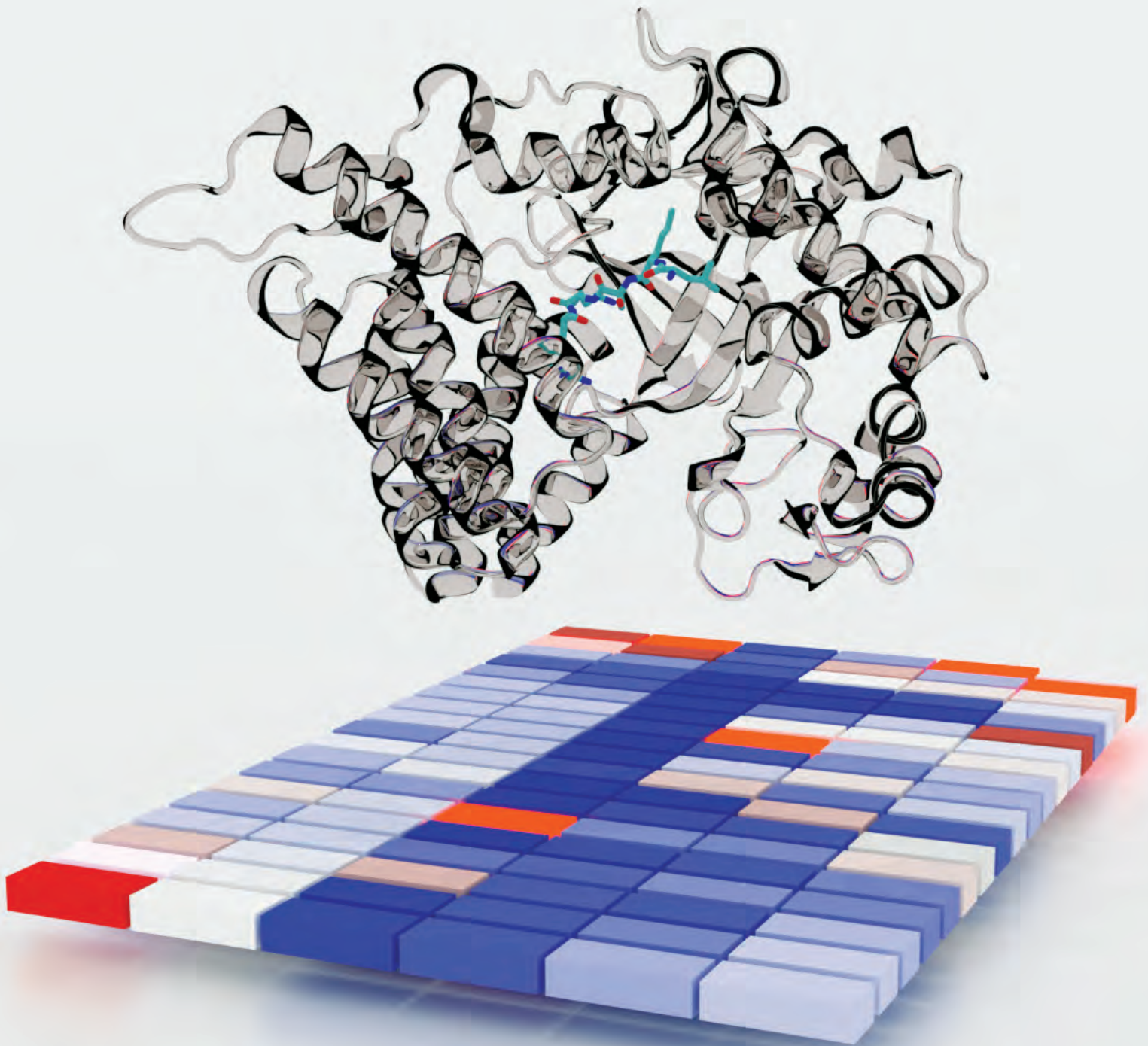
Automethylated/Activated



at the NE-CAT 24-ID-E x-ray beamline at the APS showed that K455 was part of an autoregulatory loop that occluded the histone binding site of the enzyme.

In fact, the alignment of K455 in the catalytic site showed that it was in the H3K9 binding site and in position to be methylated itself by the same mechanism. Mutation of K455 to an arginine amino acid that cannot be methylated (K455R), but which still favored inhibition by the autoregulatory loop, reduced the activity of the enzyme, while mutation to an alanine (K455A) increased enzyme activity by disrupting the positioning of the autoregulatory loop in the active site. These findings supported the group’s hypothesis that automethylation of K455 releases the loop’s inhibition of the active site, activating the enzyme.

Innovation Accelerates Our Understanding of Lysine Methylation Signaling



If you made it through elementary biology, you know that cells are the building blocks of life and the nucleus is the engine driving cell function. Housed inside the nucleus is the organism's genome, which comprises billions of DNA base pairs coiled around histone proteins to form nucleosomes. As histone proteins undergo changes, gene expression events are triggered. Lysine methylation is a histone modification process associated with functions like learning and memory. Although the last 20 years have been something of an enlightenment period for those studying lysine methylation, substantial gaps remain. One such gap involves a lack of understanding about lysine methyltransferases (KMTs), the family of enzymes responsible for catalyzing lysine methylation. Recently, a multi-institution team of scientists developed a functional proteomics platform that helps answer key questions about the connection between enzymes and their optimal, preferred substrates. This dynamic tool enables rapid KMT substrate selectivity mapping and can be employed to profile KMTs, identify new KMT substrates, and discover new KMT inhibitor scaffolds. To demonstrate and validate the platform, the researchers used the APS to collect x-ray diffraction (XRD) data and form important conclusions about the molecular basis for substrate selectivity. The debut of this platform shifts the proteomics field closer to fully grasping the biological role of lysine methylation.

Every human body contains about 6.5 ft of DNA per cell. This works out to several hundred trillion feet of DNA per person, which, when stretched out, would be enough to wrap around the Earth more than 2 million times. To compact this length of material into cells, proteins called "histones" bind to DNA and use electrostatic interactions to coil into units called nucleosomes, which then repeatedly fold onto one another to reduce to nanoscale chromatin fibers. The histone proteins responsible for this impressive coiling behavior are subject to various kinds of modifications, including acetylation, methylation, and ubiquitination. During histone methylation in particular, certain amino acids are modified via the addition of one or more methyl groups using covalent modifications on the histone tails. Methylation and demethylation, which are catalyzed by histone methyltransferase and demethylase enzymes, respectively, cause genes in DNA to turn on and off.

Lysine methylation is catalyzed by KMT enzymes, and although a great deal of progress has been made toward locating lysine methylation sites, only a handful of studies have been able to reliably link KMT enzymes with their preferred substrates. Scientists from the Van Andel Research Institute, the University of North Carolina at Chapel Hill, the Wayne State University School of Medicine, Michigan State University, and EpiCypher, Inc., de-

Fig. 1. Hybrid ribbon-surface representation of SMYD2 (white) bound to SAH and GWKLNleSKRG (Nle, norleucine) (blue sticks). Structure has been deposited in the Protein Data Bank (PDB) as PDB: 6MON.

veloped a substrate-selectivity screening platform that uses a lysine-oriented peptide library, or K-OPL, to map KMT substrate selectivity. To validate the platform's K-OPL approach, the researchers studied the structural and kinetic interactions between SMYD2 and a K-OPL-identified substrate. SMYD2 is a lysine methyltransferase capable of methylating both histone and non-histone proteins and can lead to repressed gene transcription. Various clinical research studies are currently exploring the biological connection between SMYD2 methylation of the tumor suppressor protein p53 and inhibition of the p53 function. SMYD2 has even been reported to suppress the transformation of cells into breast cancer tumor cells.

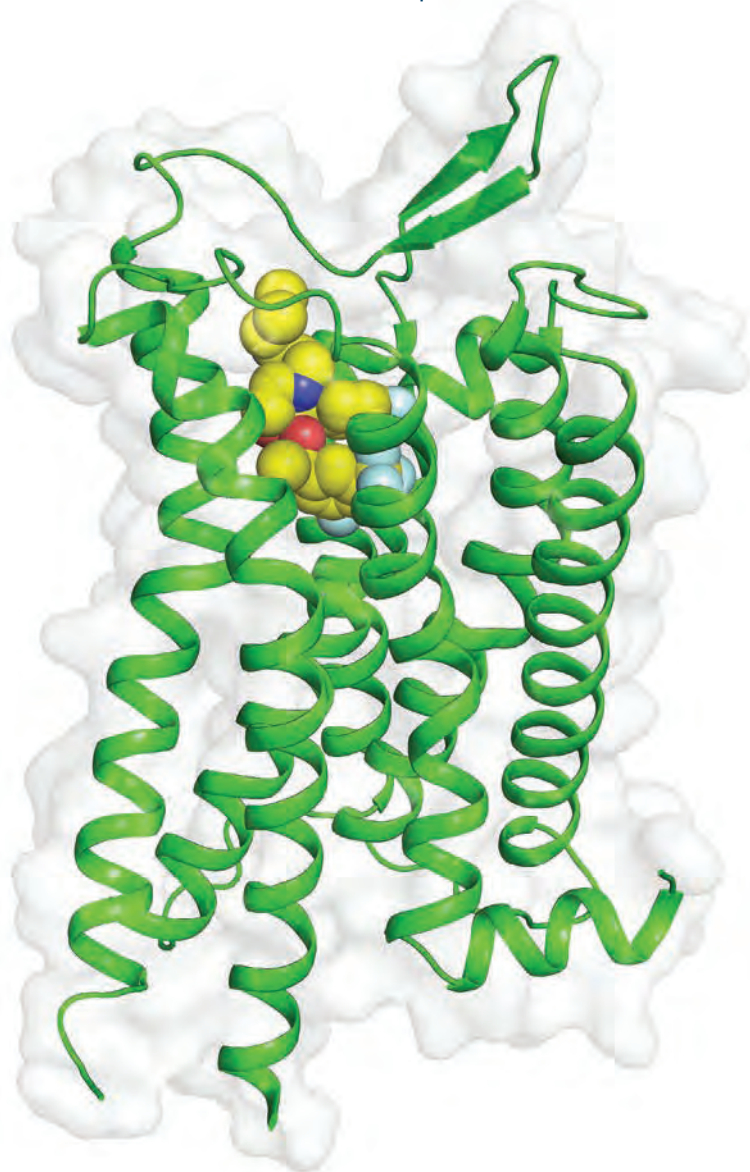
In order to identify the full range of SMYD2 targets, it was necessary to determine the molecular basis for SMYD2 substrate selectivity. To do this, the researchers, along with a colleague from the LS-CAT at the APS, used XRD data collected at the LS-CAT 21-D-F x-ray beamline to determine crystal structures. For this experiment, full-length human SMYD2 was expressed, purified, and crystallized. The crystals were then reacted with a peptide corresponding to the optimal K-OPL-derived SMYD2 substrate and analyzed by XRD. From the XRD data, the researchers observed that P-3 tryptophan was not resolved in the structure, which was puzzling since the peptide conformation was no different than previous SMYD2-SAH-peptide structures.

The researchers further investigated this result by performing molecular dynamic simulations to model the

"Lysine" cont'd. on page 89

How to Select a Selective Antagonist

Substance P was the first peptide neurotransmitter discovered and its importance has not waned in the intervening years. This small, 11-amino acid peptide plays a role in early responses to extreme physiological stressors with an emphasis on mediation of a wide array of functions including dilatation of blood vessels, inflammation, pain, vomiting, cell proliferation, and mood/anxiety/learning. It exerts its action through cellular receptors, called “tachykinin receptors,” that are present throughout the body and transmit the signal from substance P into cells through a G-protein-coupled signal transduction system. This receptor is the target of one approved drug, aprepitant (Merck brand name:EMEND®), for treatment of chemotherapy-induced nausea and vomiting. However, researchers hypothesize that a more complete understanding of tachykinin receptor signaling will yield key information important for the design of specific molecules to selectively target the other effects of substance P. Recent work at the APS probed the interactions of the NK1 tachykinin receptor (NK1R) with inhibitor molecules. The work provides important information that may aid in the design of new treatments for cancer, pain modulation, inflammation, and depression.



The main approach to understanding more about NK1R involved crystallizing the receptor in the presence of an inhibitor, L760735, which is a molecule with structural similarity to the approved drug aprepitant. The research team, from the University of Texas Southwestern Medical Center and the University of Pittsburgh, along with a colleague from the GM/CA-XSD macromolecular x-ray crystallography facility at the APS, collected diffraction data for the nearly full-length receptor/inhibitor complex at the GM/CA-XSD 23-ID-D x-ray beamline. Solution of the structure at 3.4-Å resolution was achieved using a protein engineering and lipid cubic phase crystallization strategy that the team had successfully employed in the past for another class of G-protein coupled receptors (Fig. 1).

The overall structure of NK1R bound to the inhibitor confirmed its similarity to the inactive state of other receptors in this class. For example, the intracellular conformation of NK1R was similar to that of other inactive G-protein coupled receptors, and the extracellular domain retained a loop that formed a conserved disulfide bond with transmembrane domain 3, a feature known to be important for substance P binding. This confirmed both that

< Fig. 1. The NK1 receptor is shown as a green cartoon inside a light gray molecular surface. The inhibitor ligand L760735 is shown in spheres.

the crystallized NK1R was in a biologically informative state and that the inhibitor behaved as expected.

Next, analysis of the binding site revealed that the inhibitor was lodged into a narrow pocket of the receptor, perpendicular to the membrane. The mouth of the pocket was lined with polar amino acids while deeper down, near the membrane, hydrophobic interactions were more prominent. Along the length of the pocket, interactions between the inhibitor and the receptor were consistent with previous mutational studies that identified certain amino acids as being important for either substance P or inhibitor binding. Interestingly, of the 12 amino acids lining the binding pocket, many had been identified by previous studies as being important for other nonpeptide inhibitors too. This suggests that the same binding pocket is used by molecules with diverse structures that modulate receptor activation, confirming the importance of understanding as much as possible about the binding pocket itself.

To learn more about the inhibitor binding site, the group conducted their own mutational analysis. The analysis revealed some residues that appear to be important for binding affinity and others that are more structural in nature. This allowed them to identify key interactions that might be exploitable for drug design.

Finally, molecular modeling of different scenarios for the binding interactions of L760735 and aprepitant with the binding pocket were used to determine which forms of the inhibitors had the strongest interactions. Binding of both L760735 and aprepitant was favored in their neutral, rather than charged, forms, providing additional information for inhibitor design. In the future, the team plans to study the activated form of the receptor in order to understand how the diverse signals of substance P are modulated and how these details might be teased apart to develop selective treatments for a wide array of important disease conditions. — [Sandy Field](#)

See: Jie Yin¹, Karen Chapman¹, Lindsay D. Clark¹, Zhenhua Shao¹, Dominika Borek¹, Qingping Xu², Junmei Wang³, and Daniel M. Rosenbaum^{1*}, “Crystal structure of the human NK1 tachykinin receptor,” *Proc. Natl. Acad. Sci. U.S.A.* **115**, 13264 (December 26, 2018). DOI: 10.1073/pnas.1812717115

Author affiliations: ¹The University of Texas Southwestern Medical Center, ²Argonne National Laboratory, ³University of Pittsburgh

Correspondence: * dan.rosenbaum@utsouthwestern.edu

This project was supported by an Edward Mallinckrodt, Jr., Foundation Scholar Award (to D.M.R.), the Welch Foundation (Grant I-1770 [to D.M.R.], and the National Institutes of Health [R01-GM117080 (to D.B.), R01-GM079383 and R21-GM097617 (to J.W.), and R01-NS103939 (to

D.M.R.). GM/CA-XSD has been funded in whole or in part with Federal funds from the National Cancer Institute (ACB-12002) and the National Institute of General Medical Sciences (AGM-12006). The Eiger 16M detector was funded by a National Institutes of Health–Office of Research Infrastructure Programs, High-End Instrumentation Grant (1S10OD 012289-01A1). This research used resources of the Advanced Photon Source, a U.S. Department of Energy (DOE) Office of Science User Facility operated for the DOE Office of Science by Argonne National Laboratory under Contract No. DE-AC02-06CH11357.

“Lysine” cont’d. from page 87

unresolved P-3 position. Figure 1 displays the hybrid ribbon-surface representation of SMYD2 bound to SAH and GWKLNleSKRG. When combined with the study’s other data, these experiments led the researchers to conclude that the optimal structure of a SMYD2 substrate would have neither tightly nor loosely coordinated peptides, but instead would be organized in a way that allows efficient catalysis without slowing the rate of turnover.

This study demonstrates the powerful ability of the platform to comprehensively map and screen KMT substrates. The K-OPL approach circumvents certain limitations of standard mass spectrometry-based analyses. In fact, the tool can be used to identify lysine methylation sites that MS proteomics datasets are unable to identify. The platform is also helping researchers explore important biochemical questions, including what impact missense mutations in human cancer have on lysine methylation signaling networks.

The researchers suggest that integrative K-OPL analyses like these will help move the field closer to understanding the role that lysine methylation plays in human disease. — [Alicia Surrao](#)

See: Evan M. Cornett¹, Bradley M. Dickson¹, Krzysztof Krajewski², Nicholas Spellmon³, Andrew Umstead⁴, Robert M. Vaughan¹, Kevin M. Shaw¹, Philip P. Versluis¹, Martis W. Cowles⁵, Joseph Brunzelle⁶, Zhe Yang³, Irving E. Vega⁴, Zu-Wen Sun⁵, and Scott B. Rothbart^{1*}, “A functional proteomics platform to reveal the sequence determinants of lysine methyltransferase substrate selectivity,” *Sci. Adv.* **4**, eaav2623 (28 November 2018). DOI: 10.1126/sciadv.aav2623

Author affiliations: ¹Van Andel Research Institute, ²University of North Carolina at Chapel Hill, ³Wayne State University School of Medicine, ⁴Michigan State University, ⁵EpiCypher, Inc., ⁶Northwestern University

Correspondence: * scott.rothbart@vai.org

This work was supported by the Van Andel Research Institute and grants from the National Institutes of Health to S.B.R. (R35GM124736) and Z.-W.S. (R43GM110869 and R44GM112234). This research used resources of the Advanced Photon Source, a U.S. Department of Energy (DOE) Office of Science User Facility operated for the DOE Office of Science by Argonne National Laboratory under Contract No. DE-AC02-06CH11357.

Protecting Cells against Reactive Oxygen Species

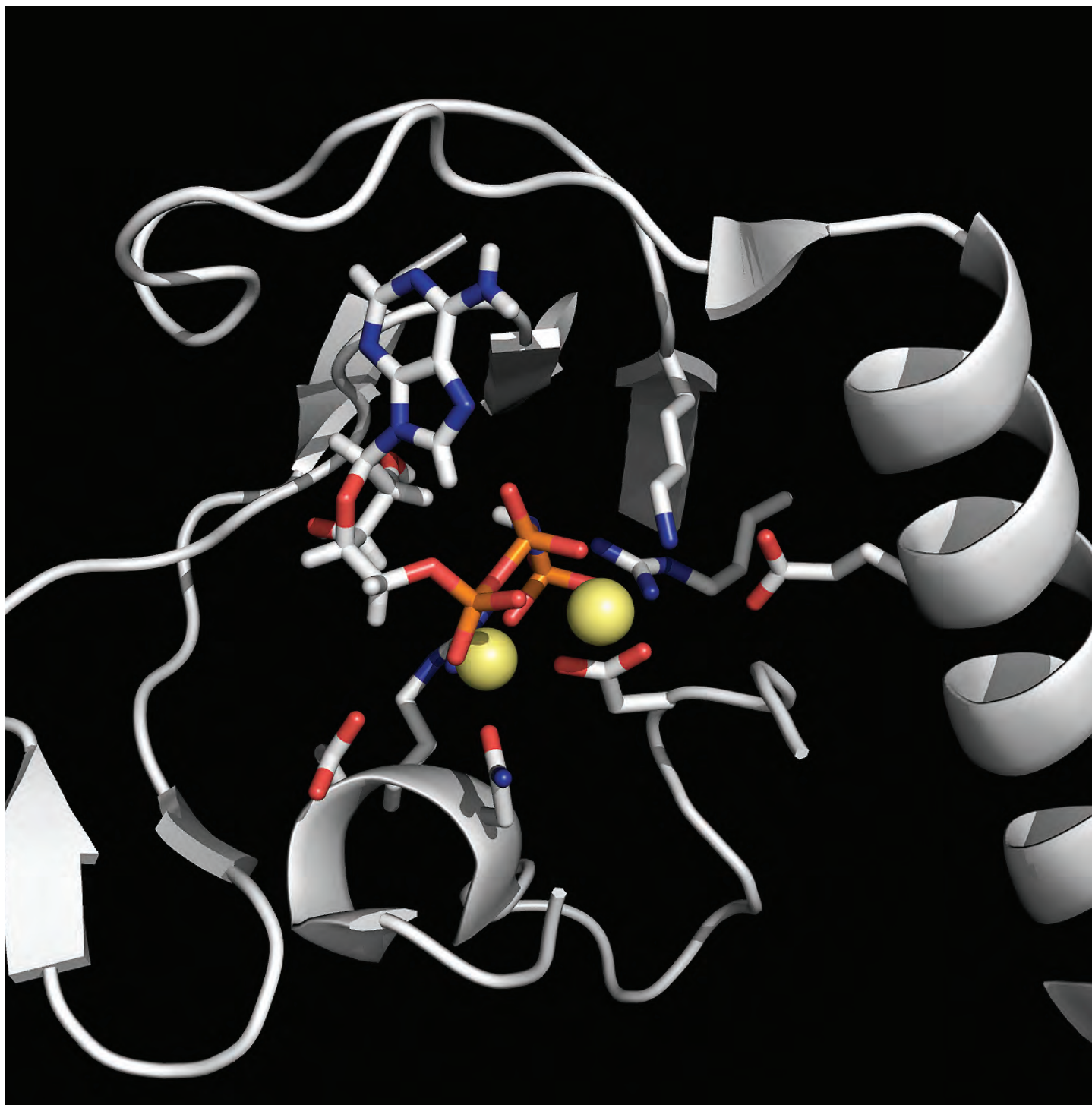


Fig. 1. Close-up view of the SeLO ATP binding pocket from data collected at SBC-CAT. The inverted nucleotide is shown as blue and white sticks, and the phosphates are shown in orange and red. Mg²⁺ and Ca²⁺ are shown as yellow spheres.

Virtually every cellular activity is regulated by protein kinases, a family of proteins that transfer the phosphate from the cellular energy source, adenosine triphosphate (ATP), to other proteins, a process (phosphorylation) that most often serves as an “on/off switch” for the target protein. About 10% of human protein kinases are classified as pseudokinases, meaning they are lacking the amino acids required to perform ATP binding and phosphate transfer. Though once believed to be inactive, one pseudokinase, Selenoprotein O (SelO), bears a molecular pattern indicating an important function: it is evolutionarily conserved across all kingdoms of life. To characterize SelO, researchers using the APS paired biochemical analysis with a high-resolution crystal structure of SelO. X-ray diffraction data collected at the APS revealed that SelO carries out a unique chemistry (AMPylation) that allows it to function in reducing reactive oxygen species (ROS) that damage the cell in diseases such as cancer and neurodegenerative diseases.

More than 500 protein kinases have been identified in the human genome. Protein kinases have important roles in a range of cellular functions, and many of these proteins are known to be dysregulated in disease. The most intense study has been applied to this subset of the protein kinase family, leaving more than 50% uncharacterized. While pseudokinases share similarities in both amino acid sequence and overall structure with protein kinases, they lack the catalytic active-site amino acids known to coordinate the phosphate groups. Though they do not carry out the traditional kinase function, pseudokinases that have been studied have a range of functions, including structural roles and allosteric regulation of other proteins. This variety makes pseudokinases attractive drug targets. Prior to the current study, one such pseudokinase, SelO, was believed to be inactive; however, the degree of SelO conservation in species ranging from bacteria to humans had been noted as a reason to believe that the function of SelO is important. In addition, SelO is one of only 25 selenoproteins in humans that contain the essential element selenium (in the form of an amino acid, selenocysteine, or Sec), a property that supported the hypothesis that SelO has a unique function.

To uncover the function of SelO, the researchers from the University of Texas Southwestern Medical Center, the Polish Academy of Sciences, the Warsaw University of Life Sciences (Poland), and the Howard Hughes Medical

Institute paired macromolecular x-ray crystallography structural data from studies carried out at the SBC-CAT 19-ID-D beamline at the APS with biochemical analysis. The data from SelO revealed a kinase-like structure (Fig. 1), but with the active site and resident ATP in an inverted orientation. Further biochemical analysis revealed that SelO transfers AMP (ATP stripped of the terminal and penultimate phosphate, the former of which is transferred by canonical kinases) rather than a phosphate. Identification of novel AMPylation activity for the protein kinase fold suggests that other pseudokinases may have alternative transferase activities and highlights a need for more investigation.

Further biochemical analysis revealed that SelO localized to the mitochondria where it AMPylates proteins involved in redox homeostasis, thereby acting as an antioxidant. Together, structural and biochemical analysis revealed that SelO defends against ROS, which can lead to cell death if left unchecked. This mode of response to oxidative stress was previously undocumented and serves to broaden our understanding of ROS signaling.

Future work will focus on studying the functional implications of SelO-mediated AMPylation in the physiology and pathophysiology of higher eukaryotes in order to contribute to the discovery of new therapeutics that combat the effects of ROS in a wide range of disorders, including neurodegeneration and cancer. — Emma Nichols

See: Anju Sreelatha¹, Samantha S. Yee^{1‡}, Victor A. Lopez¹, Brenden C. Park¹, Lisa N. Kinch⁴, Sylwia Pilch², Kelly A. Servage¹, Junmei Zhang^{1‡‡}, Jenny Jiou¹, Monika Karasiewicz-Urbańska³, Małgorzata Łobocka^{2,3}, Nick V. Grishin^{1,4}, Kim Orth^{1,4}, Roza Kucharczyk², Krzysztof Pawłowski³, Diana R. Tomchick¹, and Vincent S. Tagliabracci^{1*}, “Protein AMPylation by an Evolutionarily Conserved Pseudokinase,” *Cell* **175**, 809 (October 18, 2018). DOI: 10.1016/j.cell.2018.08.046

Author affiliations: ¹University of Texas Southwestern Medical Center, ²Polish Academy of Sciences, ³Warsaw University of Life Sciences, ⁴Howard Hughes Medical Institute Present addresses: [‡]The University of Texas Health Science Center at San Antonio, ^{‡‡}University of Pittsburgh

Correspondence: * vincent.tagliabracci@utsouthwestern.edu

This work was supported by National Institutes of Health grants R00DK099254 (V.S.T.), GM094575 and GM127390 (N.V.G.), GM115188 (K.O.), T32DK007257-37 (A.S.), and T32GM008203-29 (V.A.L.); Welch Foundation grants I-1911 (V.S.T.), I-1505 (N.V.G.), and I-1561 (K.O.); the Once upon a Time Foundation (K.O.); a CPRIT grant RP170674 (V.S.T.); and the Polish National Science Centre grant 2014/15/B/NZ1/03359 (K.P.). V.S.T. is the Michael L. Rosenberg Scholar in Medical Research, a Cancer Prevention Research Institute of Texas Scholar (RR150033), and a Searle Scholar (SSP-2018-2745). SBC-CAT is operated by UChicago Argonne, LLC, for the U.S. Department of Energy (DOE) Office of Biological and Environmental Research under Contract DE-AC02-06CH11357. This research used resources of the Advanced Photon Source, a U.S. DOE Office of Science User Facility operated for the DOE Office of Science by Argonne National Laboratory under Contract DE-AC02-06CH11357.

Small Molecules Show Therapeutic Potential for Alzheimer's Disease

One symptom of Alzheimer's disease is an increase in the brain's amount of amyloid beta, a peptide whose purpose within the human body is not well understood. Amyloid beta appears in people with Alzheimer's disease in two forms. The most well-known is dense plaques packed together on the brain. But soluble amyloid beta, according to one hypothesis for the mechanisms involved in the disease, can contribute to unregulated calcium transfer between cells, which disrupts the ability of communication cells used by the human nervous system to pass signals using their synapses. Biochemical experiments have shown that interactions involving the PDZ structural domain of the protein interacting with C kinase (abbreviated as PICK1) are necessary for amyloid beta to disrupt synapses. So inhibiting PICK1 could have an effect on the amount of soluble amyloid beta in the brain, and on the chemical reactions that negatively impact memory and learning in people with Alzheimer's. Research at the APS produced x-ray diffraction data of a PICK1 inhibitor molecule whose presence resulted in positive therapeutic chemical changes, including a decrease in soluble amyloid beta. Although the specific PICK1 inhibitor compounds that the team created and characterized had too large a molecular weight to cross into the brain easily, the team concluded, based on their potency and selectivity, that similar small-molecule inhibitors have great potential for future therapeutic applications to Alzheimer's disease.

PICK1 is found in dendritic spines, the portion of the communication cell, called a "neuron," which receives electrical impulses from synapses. The density of dendritic spines is related to synaptic plasticity and thus memory and learning. In people with Alzheimer's disease, a decrease in dendritic spine density correlates with an increase in soluble amyloid beta. The receptor GluA2, which mediates glutamate transmission to the central nervous system and binds with PICK1, is also influenced by the presence of soluble amyloid beta. By creating a molecule that inhibits the interaction between PICK1 and GluA2, the researchers determined how these interactions impact the amount of soluble amyloid beta.

The team chose to investigate small-molecule inhibitors rather than peptides because the former can be designed so that they degrade less and are more cell permeable than peptides. They began by creating a series of tests to assess the selectivity and potency — a

measure of how concentration affects the desired chemical response — of the new inhibitors. A high-throughput screen generated potential inhibitor compounds that would disrupt the interaction between PICK1 and GluA2; then the team narrowed the results to one non-peptide compound with a sufficiently low half-maximal inhibitory concentration. After synthesizing the compound, they made a number of changes to improve its potency.

Next, as a starting point for their structure-based design process, the team created a three-dimensional structure of the PICK1 PDZ domain with the inhibitor compound by collecting x-ray diffraction data at the LRL-CAT 31-ID x-ray beamline at the APS. They used the structure to create a second inhibitor compound with higher potency. Then they investigated the selectivity of the two compounds, specifically how efficiently they bound with domains similar to the PICK1 PDZ domain. In both cases, the team found the compounds more likely to bind with the correct site rather than similar ones.

When they explored the inhibitory effects of these compounds, using cultured hippocampal neurons, they found three main results: There was an increase in surface GluA2 in neurons; there was a decrease in the concentration of calcium within cells due to the presence of amyloid beta; and the reduction of neuronal activity, called "long-term depression," was suppressed. These results confirm that PICK1 is involved in transporting GluA2 receptors between cells, in mediating the effects of amyloid beta, and with synaptic plasticity. — Emma Nichols

See: Edward Y.S. Lin¹, Laura F. Silvian¹, Douglas J. Marcotte¹, Charles C. Banos¹, Flora Jow¹, Timothy R. Chan¹, Robert M. Arduini¹, Fang Qian¹, Darren P. Baker¹, Chris Bergeron¹, Catherine A. Hession¹, Richard L. Huganir², Cassandra F. Borenstein¹, Istvan Enyedy¹, Jinming Zou¹, Ellen Rohde¹, Marion Wittmann¹, Gnanasambandam Kumaravel¹, Kenneth J. Rhodes¹, Robert H. Scannevin¹, Anthonie W. Dunah¹, and Kevin M. Guckian^{1*}, "Potent PDZ-Domain PICK1 Inhibitors that Modulate Amyloid Beta-Mediated Synaptic Dysfunction," *Sci. Rep.* **8**, 13438 (2018). DOI: 10.1038/s41598-018-31680-3

Author affiliations: ¹Biogen, Inc., ²Johns Hopkins University School of Medicine

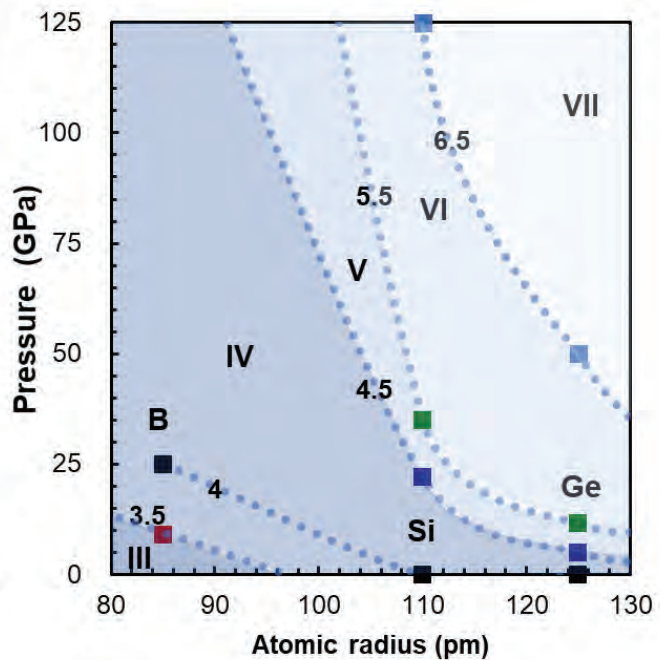
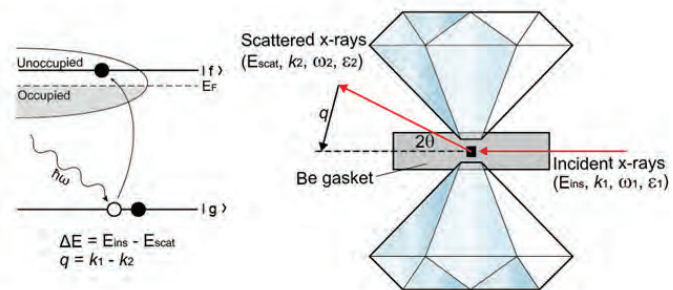
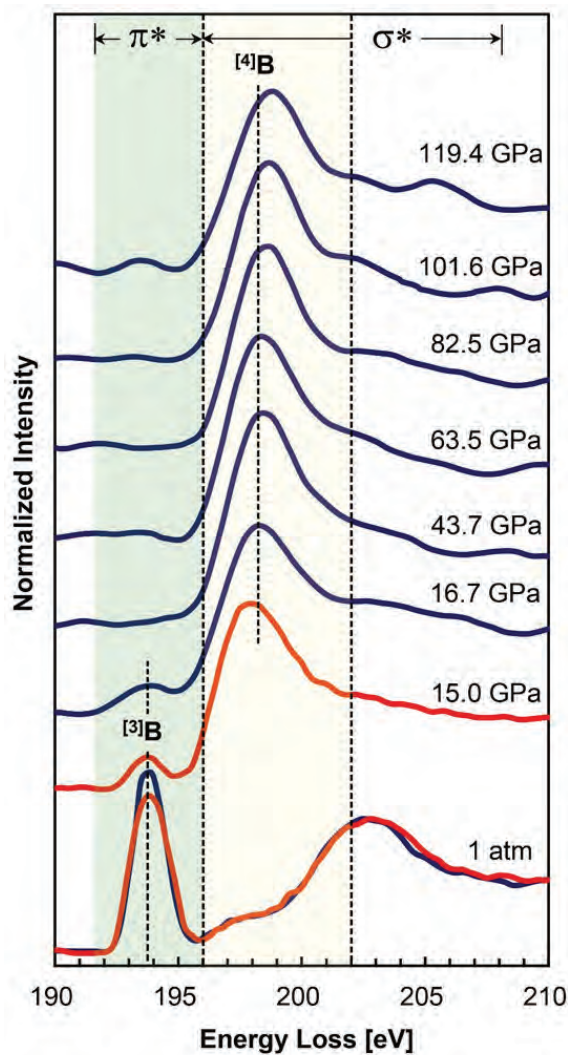
Correspondence: * kevin.guckian@biogen.com

Use of the LRL-CAT was provided by Eli Lilly Company, which operates the facility. This research used resources of the Advanced Photon Source, a U.S. Department of Energy (DOE) Office of Science User Facility, operated for the DOE Office of Science by Argonne National Laboratory under Contract No. DE-AC02-06CH11357.

ENVIRONMENTAL, GEOLOGICAL & PLANETARY SCIENCE

Amorphous Boron Oxide at Megabar Pressures

Materials at Earth's core-mantle boundary are exposed to extreme pressures that are very difficult to replicate in the laboratory. In this work, researchers developed a unique probe to reveal the electronic structures of amorphous glasses at above megabar pressures (> 1 million atmospheric pressure, >100 GPa). In boron oxide glasses, densification takes place as the oxygen-oxygen (O-O) bond distance is reduced and four-coordinated boron (⁴B) is prevalent. This work, carried out at the APS, presents a new opportunity to understand the evolution of atomic structures in melts at the core-mantle boundary.



Understanding the structures of oxide glasses at the extremely high-pressure (above megabar) conditions — which are relevant to Earth’s core-mantle boundary — is exceedingly difficult. Researchers know that the molecular networks of a material under extreme compression can be very different from those same networks at ambient pressure. In other words, what we know about materials at lower pressures is not necessarily representative of those same materials at extremely high pressures. However, no experimental probe has been able to depict the bonding environments of amorphous materials at lowermost mantle pressures (up to 134 GPa).

In this study, researchers from Seoul National University (Korea) and the Carnegie Institution of Washington carried out non-resonant inelastic x-ray scattering (NIXS) to probe core electron excitation from oxide glasses in a diamond anvil cell. The researchers collected boron and oxygen K-edge NIXS spectra for vitreous boron oxide ($v\text{-B}_2\text{O}_3$) at the HP-CAT beamline 16-ID-D at the APS. The IXS spectra revealed the unique densification paths of atomic configurations in oxide glasses under extreme compression. At pressures up to ~ 120 GPa, the packing density of B_2O_3 glasses increased as the O-O distance was reduced and smaller ring networks formed. The densification paths were characterized by the unexpected stability of four coordinated boron; indeed, at extremely high pressure, only four-coordinated boron ($^{4\text{B}}$) was prevalent.

The study revealed the effect of the atomic radius of framework cations on packing density; that is, the framework cation with the smaller atomic radius undergoes coordination transformation at higher pressure. Highly coordinated cations, such as $^{[4,5,6]\text{Si}}$ and $^{[4,5,6]\text{Ge}}$, form glasses at much lower pressure, than B. While more experimental

data to quantify the boundaries and additional theoretical confirmations of the proposed predominance are needed, this simple relationship in boron oxide glasses under extreme compression prevails for all oxide glasses, and thus provides a unique predictive tool to unveil the structural transformation in complex glasses and melts.

This densification model is useful for understanding the stability, oxygen configuration, and solubility of elements and isotopes as they transition into the dense melts at the core-mantle boundary. Dense oxide melts with ^{13}O can result in enhanced contraction at the base of the lower mantle, which increases melt density. This suggests that dense melts may be stable when they are in contact with crystalline Mg-silicate polymorphs. The abundant ^{14}B in the lowermost mantle may explain the enrichment of ^{10}B , instead of ^{11}B , in the region, as ^{10}B will preferentially partition into the highly coordinated boron in oxides.

This work reveals the evolution of boron coordination sites under extreme compression and becomes possible with the development of a new way to study the structure of oxide glass at extreme megabar pressure. The new capability allows researchers to detail the atomistic origins of melt densification in the extreme pressures found at the core-mantle boundary and gain new insights about the composition of our planet. — Dana Desonie

See: Sung Keun Lee^{1*}, Yong-Hyun Kim¹, Paul Chow², Yunming Xiao², Cheng Ji², and Guoyin Shen², “Amorphous boron oxide at megabar pressures via inelastic X-ray scattering,” *Proc. Natl. Acad. Sci. U.S.A.* **115**(23) 5855 (June 5, 2018).

DOI: 0.1073/pnas.1800777115

Author affiliations: ¹Seoul National University, ²Carnegie Institution of Washington

Correspondence: * sungklee@snu.ac.kr

< Fig. 1. Left: Boron K-edge IXS spectra for B_2O_3 glass at pressures above Megabar pressure conditions. Right-top: Inelastic x-ray Raman scattering processes in a diamond anvil cell. E_{ins} (E_{scat}), k_2 (k_1), ω_1 (ω_2), and ϵ_1 (ϵ_2) are energy, wave vector, frequency, and polarization vector of the incident (and scattered) photon, respectively. $|g\rangle$ and $|f\rangle$ are the initial and final electronic states. E_F is the Fermi energy. Right-bottom: Predominance diagram of distinct coordination states of B, Si, and Ge in diverse oxide glasses with varying pressure and atomic radius of each cation. Adapted from S.K. Lee et al., *Proc. Natl. Acad. Sci. U.S.A.* **115**(23) 5855 (June 5, 2018). Copyright © 2018 National Academy of Sciences. Online ISSN 1091-6490

This work was supported by Samsung Science and Technology Foundation Grant BA1401-07, National Research Foundation of Korea Grant 2017R1A2A1A17069511 (to S.K.L.), and Department of Energy (DOE)-Basic Energy Sciences, Division of Materials Sciences and Engineering Award DE-FG02-99ER45775 (to G.S.). HP-CAT operations are supported by the DOE-National Nuclear Security Administration under Award DE-NA0001974, with partial instrumentation funding by the National Science Foundation. This research used resources of the Advanced Photon Source, a U.S. DOE Office of Science User Facility operated for the DOE Office of Science by Argonne National Laboratory under Contract DE-AC02-06CH11357.

Cell Envelope Sulphydryl Sites Play a Key Role in Se(IV) Interactions With Microbes

Understanding how selenium (Se) cycles in the environment is important for addressing widespread selenium deficiency and for bioremediation of selenium pollution. This study solves a long-standing mystery of how negatively charged dissolved selenite anions overcome electrostatic repulsion to interact with negatively-charged bacterial cells. The results, obtained at the APS, reveal the key role of bacterial cell envelope sulphydryl binding sites in the adsorption of selenite anions to bacterial cells, and in the reduction of selenite to neutral organo-selenium species.

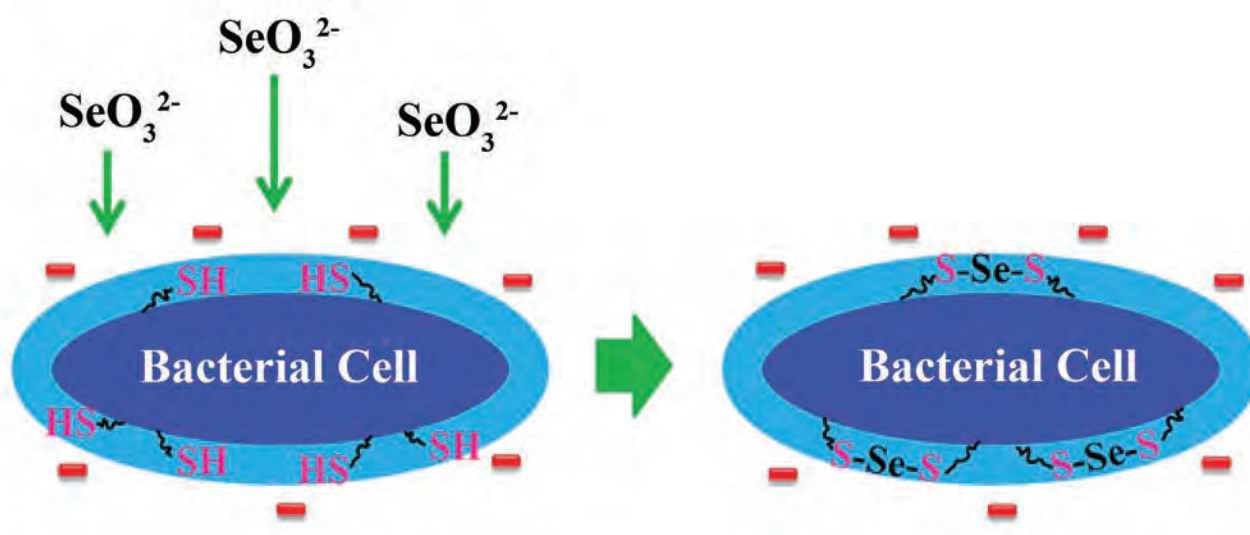


Fig. 1. Selenite adsorption is controlled by sulphydryl sites in the cell envelope of *Bacillus subtilis* cells where it is reduced to form organo-Se compounds. From Q. Yu et al., *Environ. Sci. Technol.* **52**, 10400 (2018). © 2018 American Chemical Society

Selenium is an essential micronutrient, but it can be toxic at high concentrations. Globally, between 0.5 to 1 billion people have a Se deficiency, whereas excess Se is a pollutant in high concentrations when it is a byproduct of mining, agricultural, petrochemical, and industrial manufacturing activities. To address these concerns, science must understand the factors that control the global cycling of selenium.

Microorganisms are important in the selenium cycle; they can oxidize, reduce, methylate, and assimilate Se in natural or contaminated settings and therefore significantly change the element's bioavailability and toxicity. Microbes reduce water-soluble selenate [Se(VI)] to insoluble elemental Se nanoparticles [Se(0)] in a two-step process: First, a limited range of microorganisms can reduce Se(VI) to selenite [Se(IV)] in anaerobic or microaerobic environments; then a wider range of microbes can reduce Se(IV) to Se(0) under anaerobic or aerobic conditions. This work focuses on the second step because it occurs in a wider range of geological settings.

For Se(IV) to be bioavailable to bacteria and undergo reduction to Se(0), it must adsorb onto cell surfaces. Bacterial cells are negatively charged under environmental pH conditions, leading to extensive adsorption of aqueous cations and minimal adsorption of aqueous anions. However, because some bacteria can adsorb and reduce Se(IV), selenite anions must bind onto the bacterial cells. In this study, the researchers from the University of Notre Dame, the Institute of Chemical Engineering (Bulgaria), Argonne, and the China University of Geoscience had as their objective determining if bacterial sulfhydryl sites, which create strong covalent bonds with chalcophile elements, such as mercury or Se, are responsible for the bioavailability of Se to bacterial cells (Fig. 1).

To determine the role of sulfhydryl sites in adsorption, the researchers measured selenite adsorption onto bacterial cells with and without the sulfhydryl sites blocked chemically. In unblocked sulfhydryl sites, a significant concentration of selenite adsorbed onto the cells. However, in blocked sulfhydryl sites, Se(IV) adsorption did not occur, indicating that selenite adsorption offsets the electrostatic repulsion between the dissolved Se(IV) anions and negatively charged cell surface. Unlike in cation ad-

sorption onto bacteria, Se(IV) adsorption is not reversible, suggesting that another process is also involved.

The researchers used Se K-edge (12 658 eV) x-ray absorption near edge structure spectroscopy, carried out at the MR-CAT 10-BM-A,B bending magnet beamline at the APS. They determined the speciation and valence state of Se in the biomass samples after Se(IV) adsorption. These analyses revealed that most of the adsorbed Se(IV) was reduced by the bacteria and bound to sulfhydryl sites to form reduced organo-Se compounds. During the experiment, selenite decreased from 100% to 17%; most Se converted to reduced organo-Se compounds (R₁S-Se-SR₂).

This study was the first to show that bacterial cell envelope sulfhydryl sites are responsible for the adsorption and bioavailability of Se(IV) anions and that, once adsorbed, the Se(IV) reduces to neutrally charged organo-Se compounds. Sulfhydryl binding sites are essential for the environmental cycling of Se, where bacteria facilitate the reduction of Se(IV) to elemental Se(0). This affects the mobility and behavior of Se in the environment.

To better understand the global cycling of Se, future studies must focus on the relationship between cell-envelope sulfhydryl sites and the microbial reduction and conversion of Se oxyanions to other Se species.

— Dana Desonie

See: Qiang Yu^{1*}, Maxim I. Boyanov^{2,3}, Jinling Liu^{1,4}, Kenneth M. Kemner³, and Jeremy B. Fein¹, “Adsorption of Selenite onto *Bacillus subtilis*: The Overlooked Role of Cell Envelope Sulfhydryl Sites in the Microbial Conversion of Se(IV),” *Environ. Sci. Technol.* **52**, 10400 (2018). DOI: 10.1021/acs.est.8b02280

Author affiliations: ¹University of Notre Dame, ²Institute of Chemical Engineering, ³Argonne National Laboratory, ⁴China University of Geoscience

Correspondence: * qyu@nd.edu

Funding for this project was provided in part by U.S. National Science Foundation grant EAR-1424950. M.I.B. and K.M.K. were supported in part by the Subsurface Science Scientific Focus Area (SFA) at Argonne National Laboratory funded by the Subsurface Biogeochemical Research Program, Office of the Biological and Environmental Research, U.S. Department of Energy (DOE) Office of Science, under contract DE-AC02-06CH11357. MR-CAT operations are supported by the U.S. DOE and the Materials Research Collaborative Access Team member institutions. This research used resources of the Advanced Photon Source, a U.S. DOE Office of Science User Facility operated for the DOE Office of Science by Argonne National Laboratory under Contract No. DE-AC02-06CH11357.

Shock-Compressed Forsterite Overturns Prior “Mixed Phase” Theories

To provide a better understanding of the interior structure and dynamics of the Earth’s mantle, it is imperative to know the equation of state and phase diagrams of MgO-MgSiO₃ thermodynamic systems. A more detailed understanding of partial melting and chemical stratification of the mantle is provided from extensive research focused on Mg₂SiO₄ at high pressures over a wide range of thermodynamic conditions. However, there is no stable compound of Mg₂SiO₄ in the Earth’s lower mantle. Thus, in order to get an equilibrium state of homogeneous forsterite, it must be decomposed into at least two compounds, periclase and bridgmanite. *In situ* powder x-ray diffraction observations of forsterite crystal structure samples shocked to 44(3) and 73(5) GPa done at the APS show chemical segregation of forsterite does not occur on dynamic timescales, but the nonequilibrium states persist to 73(5) GPa, where the shock temperature is predicted to be ~2500 K.

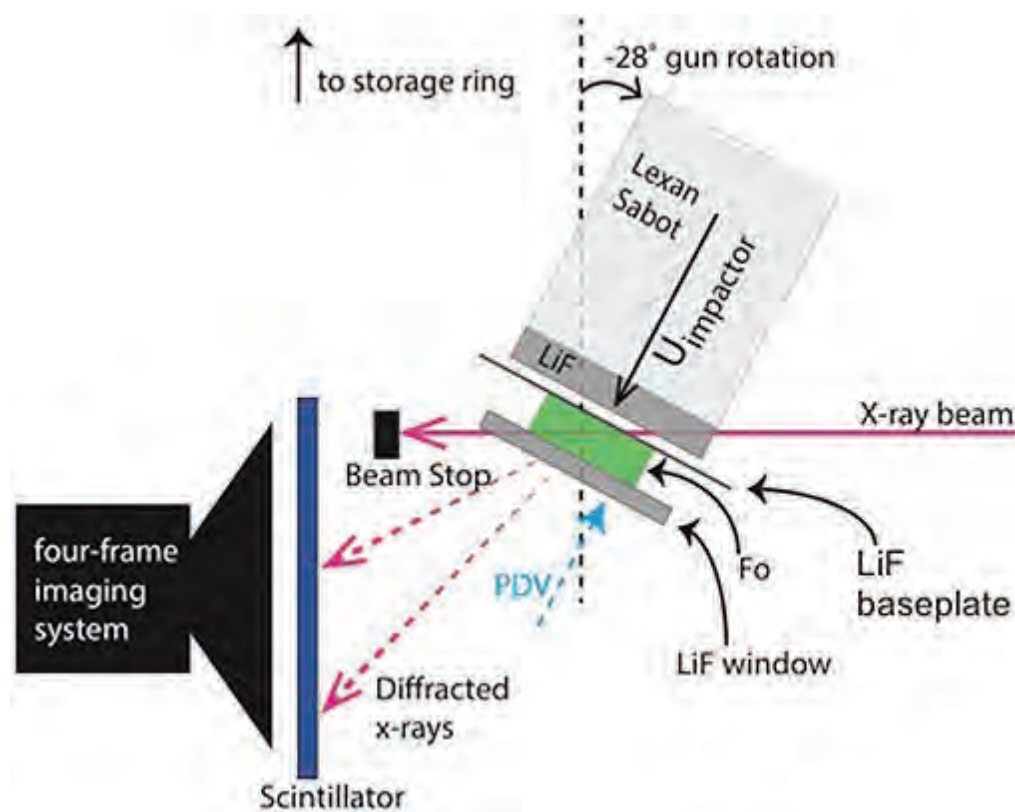


Fig. 1. The beam configuration for *in situ* x-ray diffraction measurements is shown in this schematic drawing. The cylindrical axis of the sample is 28° with respect to the beam direction so that the beam path does not probe laterally released states. The path of the beam penetrates the Lexan sabot, LiF impactor, LiF baseplate, forsterite sample, and LiF window. The driver and window materials are chosen to minimize x-ray attenuation. Diffracted x-rays are collected every 153.4 ns on an LSO scintillator coupled to a four-frame imaging system (Luo et al., 2012). From M.G. Newman et al, Geophys. Res. Lett. **45**, 8129 (11 July 2018). Copyright © 1999-2018 John Wiley & Sons, Inc. All rights reserved

Forsterite separates into periclase and bridgmanite by chemical segregation. Static compression experiments at high temperature have demonstrated that chemical segregation of Mg_2SiO_4 happens at pressures above 23 GPa. Under isothermal compression at 300 K, the composition has remained stable when it should have assembled into periclase and bridgmanite, suggesting kinetic effects may inhibit the decomposition process at low temperatures.

The temperatures and pressures of the Earth's lower mantle, below 136 GPa and 3600 K, may be achieved in uniaxial plate impact experiments. These experiments help in the study of the equation of state of geophysically important materials. Previous shockwave experiments on Mg_2SiO_4 have defined several phase transitions below 136 GPa based on density, sound-speed measurements, and shock-temperature measurements. *In situ* observations of these phases behind the shock front have not been performed; thus, the crystalline phases upon shock compression are unknown. Shock-recovery experiments have shown an absence of evidence of the chemical segregation of forsterite, and samples shocked to 78 GPa suggest that the nature of the "Mixed Phase" region between 50-120 GPa is not a complete transformation to periclase and bridgmanite.

Researchers from the California Institute of Technology, Lawrence Livermore National Laboratory, the University of Minnesota, the University of Nevada, Las Vegas, Cornell University, and Washington State University, working at the DCS 35-ID beamline, launched a Lexan Sabot using a two-stage light case gun (Fig. 1) — which is capable of generating projectile velocities up to ~ 5.7 km/s — at forsterite discs covered by a 1-mm LiF window. The forsterite samples were cut into 5, 2-mm-thick discs and polished flat. A disc was then covered by the LiF window and impacted by a 4-mm-thick LiF single-crystal flyer plate mounted on the sabot. Other studies were carried out at the GSECARS 13-ID beamline, also at the APS.

The forsterite was shock compressed at 44(3) and 73(5) GPa. The peaks in two diffraction images taken prior to release of 44(3)-GPa ambient pressure were consistent with forsterite compressed to the Hugoniot density. The lattice parameters of the structures were further refined using the difference between the observed and theoretical d-spacing for two forsterite structure. Although the

two forsterite structures were consistent with the Hugoniot density, the fit to the periclase structure did not correspond well with the equation of state in both of these shots, suggesting periclase is not present when forsterite is shocked to the Hugoniot at pressures up to 73(5) GPa.

The results of the forsterite lattice compression correspond with a previously described low-pressure Hugoniot regime, showing that the density collapse at 50 GPa is a deformational change to a metastable structure. Consistent with shock-recovery results, there was no observance of assemblage of periclase and bridgmanite in the diffraction pattern. Significant crystallization of periclase was not observed at microsecond timescales, thus bounding the ionic diffusivities in forsterite to below $1 \text{ nm}^2/\mu\text{s}$ at elevated pressures and temps. Metastable forsterite persists even at elevated Hugoniot pressures and temperatures. With the lack of periclase, this suggests that chemical segregation does not occur in the shocked solid materials on the sub-microsecond timescale.

These results illustrate that kinetic, and not equilibrium, states can dictate equation-of-state measurements on dynamic compression experiments.

— Gwenevier Johnson

See: M.G. Newman¹, R.G. Kraus², M.C. Akin², J.V. Bernier², A.M. Dillman³, M.A. Homel², S. Lee⁴, J. Lind², J.L. Mosenfelder³, D.C. Pagan⁵, N.W. Sinclair⁶, and P. D. Asimow¹, "In Situ Observations of Phase Changes in Shock Compressed Forsterite," *Geophys. Res. Lett.*, **45**, 8129 (11 July 2018). DOI: 10.1029/2018GL077996
Author affiliations: ¹California Institute of Technology, ²Lawrence Livermore National Laboratory, ³University of Minnesota, ⁴University of Nevada, Las Vegas, ⁵Cornell University, ⁶Washington State University
Correspondence: * matthew.g.newman@gmail.com

This work was performed under the auspices of the U.S. Department of Energy (DOE) by Lawrence Livermore National Laboratory under Contract DE-AC52-07NA27344. M.G.N., M.C.A., and R.G.K. acknowledge support under grant number 15-ERD-012. M.C.A., J.V. B., D.C.P., J.L., and M.A.H. acknowledge support under LLNL LDRD 16-ERD-010. J. L.M. acknowledges support from National Science Foundation EAR1161023. GSECARS is supported by the National Science Foundation-Earth Sciences (EAR-1634415). This publication is based upon work performed at the DCS, which is operated by Washington State University under the U.S. DOE-National Nuclear Security Administration award DE-NA0002442. This research used resources of the Advanced Photon Source, a U.S. DOE Office of Science User Facility operated for the DOE Office of Science by Argonne National Laboratory under contract DE-AC02-06CH11357.

Constraining Partial Melt Fractions in Upper Mantle Low-Velocity Zones

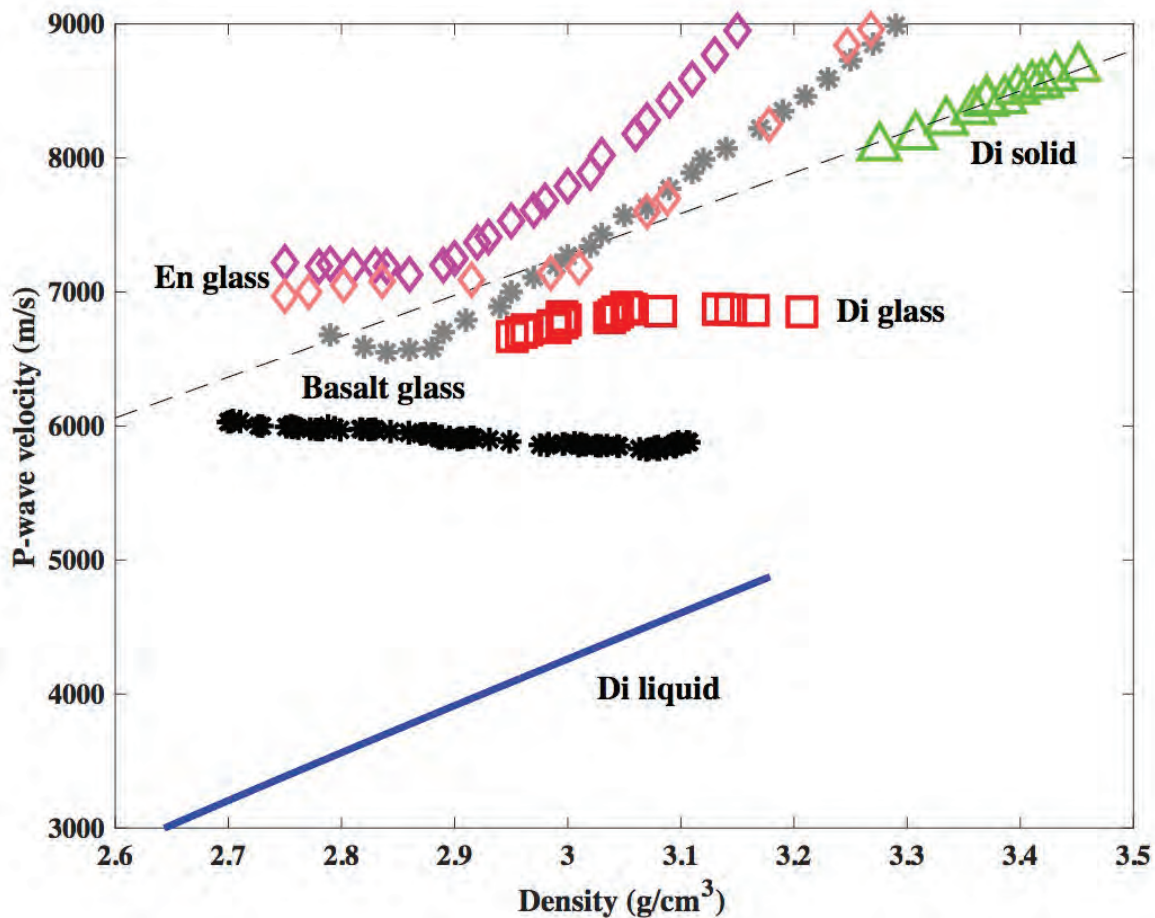


Fig. 1. P-wave velocity and density systematics for Di liquid (blue curve this study), Di glass (red squares, from Sakamaki et al., 2014), Di solid (green triangles, from Li and Neuvill, 2010), basalt glass (stars, black from Clark et al., 2016, and gray from Liu and Lin, 2014) and En glass (diamonds, orange from Sanchez-Valle and Bass, 2010, and magenta from Liu and Lin, 2014). The dashed line corresponds to the behavior of solids. This figure shows that silicate liquids behave completely different from silicate glasses and solids in their high-pressure acoustic properties. From M. Xu et al., *J. Geophys. Res.-Sol. Ea*, **123**, 8676 (29 October 2018). ©2018. American Geophysical Union. All Rights Reserved.

A commonality between the Earth and other terrestrial planets in our solar system is the presence of partially molten silicate rocks in mantles or crusts. Depending on the density contrast between the melts and surrounding materials, the melts will transfer chemical species to either the surface or the deep mantle, resulting in different geochemical evolution scenarios. Thus, the equation of state (EOS) for silicate liquids is required for modeling the processes related to mantle melting, magma differentiation and solidification, etc. In addition, the seismic detection of the presence of silicate melts requires knowledge of the sound velocity of melts at relevant mantle conditions, which has not been directly measured. A team of researchers working at the APS performed the first high-pressure and high-temperature ultrasonic sound velocity measurements on liquid diopside ($\text{CaMgSi}_2\text{O}_6$), a composition that is representative of the melt produced in the Earth's mantle, and tightly constrained its EOS using the high-pressure sound velocity data. They found that the fractions of melts present in the mantle low-velocity zones may be significantly underestimated in previous studies, thus broadening our understanding of the Earth's interior.

The equations of state for silicate liquids, prior to the research done at the APS, were mainly obtained by performing density measurements on melts at high pressures. Because of the strong correlation between the two fitted EOS parameters — bulk modulus and the pressure dependence of bulk modulus — density data obtained over a limited pressure range do not provide robust constraint on bulk modulus, which is proportional to the pressure derivative of density. Sound velocity, directly related to both density and bulk modulus, can tightly constrain the EOS by giving direct information on the two parameters.

Sound velocities are also highly important for interpreting seismic data to show the existence of melts in the mantle. Generally, global seismic velocities increase with depth, but in some areas (Hawaii, the Japan arc, and the top of the core-mantle boundary) the velocities are slower than the global average. Partial melts are one potential explanation. Prior to this study, there have been no known reported high-pressure experimental data on the sound velocity of silicate liquids. Instead, silicate glasses have been frequently used as analogs to infer the acoustic properties of liquids at high pressures.

The researchers in this study, from Case Western Reserve University, Southern University of Science and Technology (China), Université de Lille (France), and The University of Chicago, performed sound-velocity measurements on diopside liquid in a 10-MN multi-anvil press at the GSECARS beamline 13-ID-D of APS under conditions from ~0.5 GPa to 4 GPa, and 2010 K to 2375 K. They used the ultrasonic technique to measure the velocity of a liquid sample, with the help of synchrotron x-ray imag-

ing for sample-length determination. Their measured sound velocities of liquid diopside are much lower than those of glasses, and show a monotonic increase with pressure in contrast to glasses, suggesting that silicate glasses may not be good analogs to study the acoustic and compressional properties of silicate liquids, and that larger melt fractions than previously thought are required to explain the low-velocity anomalies (Fig. 1). The velocity data were also used to place tight constraints on the EOS of diopside liquid. Their EOS is consistent with prior dynamic compression data at much higher pressures, validating its accuracy, at least to pressures at the bottom of the upper mantle. The calculated density of diopside liquid based on this EOS suggests that it is unlikely for diopside liquid to become denser than the solid upper mantle; so the diopside melt would migrate upward if it were generated in the upper mantle. — [Gwenevier Johnson](#)

See: Man Xu¹, Zhicheng Jing^{1,2*}, Julien Chantel^{1,3}, Peixiu Jiang¹, Tony Yu⁴, and Yanbin Wang⁴, “Ultrasonic Velocity of Diopside Liquid at High Pressure and Temperature: Constraints on Velocity Reduction in the Upper Mantle Due to Partial Melts,” *J. Geophys. Res.-Sol. Ea.* **123**, 8676 (29 October 2018).

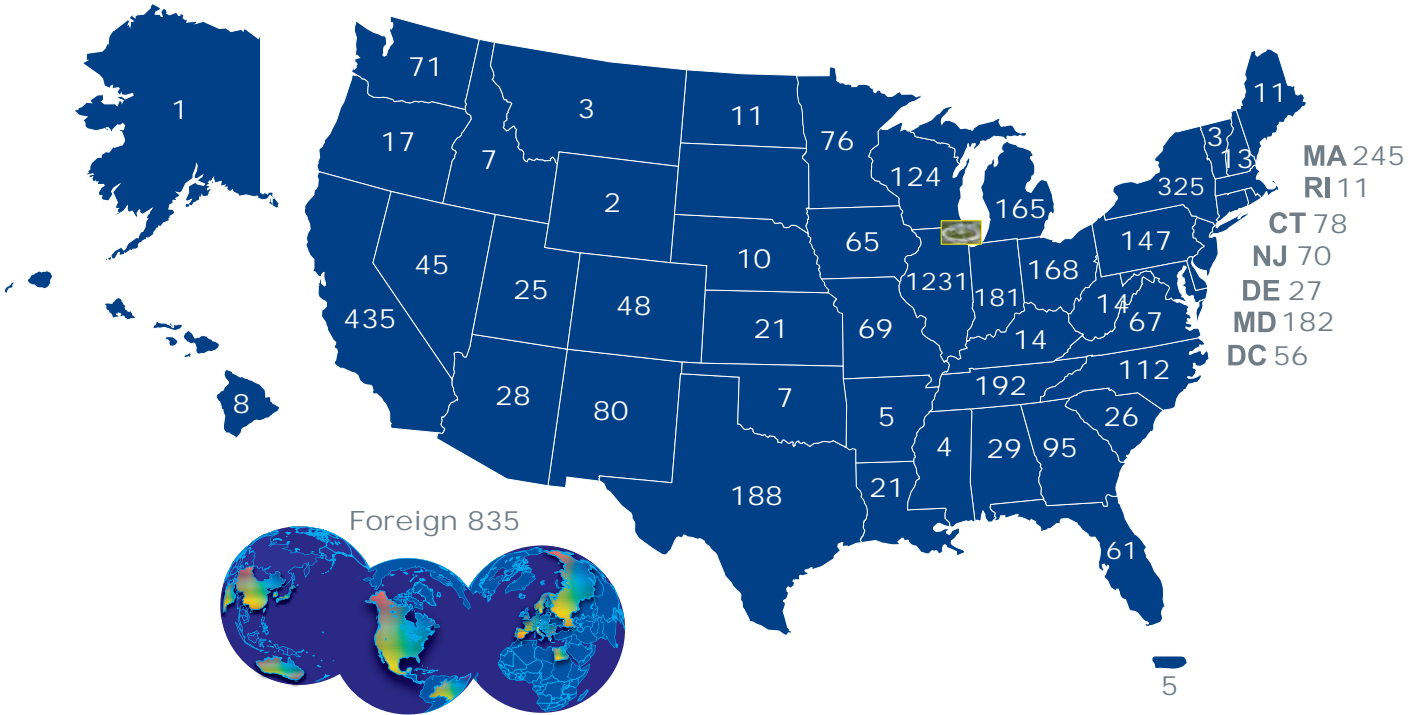
DOI: 10.1029/2018JB016187

Author affiliations: ¹Case Western Reserve University, ²Southern University of Science and Technology, ³Université de Lille, ⁴The University of Chicago

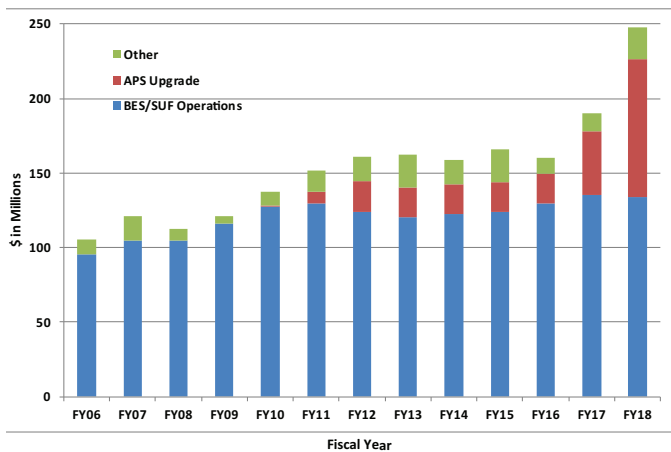
Correspondence: * jingzc@sustc.edu.cn

This research was supported by the National Science Foundation (EAR-1619964) to Z. J. and Y. W. GSECARS is supported by the National Science Foundation-Earth Sciences (EAR-1634415) and U.S. Department of Energy- (DOE) GeoSciences (DE-FG02-94ER14466). This research used resources of the Advanced Photon Source, a U.S. DOE Office of Science User Facility operated for the DOE Office of Science by Argonne National Laboratory under contract DE-AC02-06CH11357.

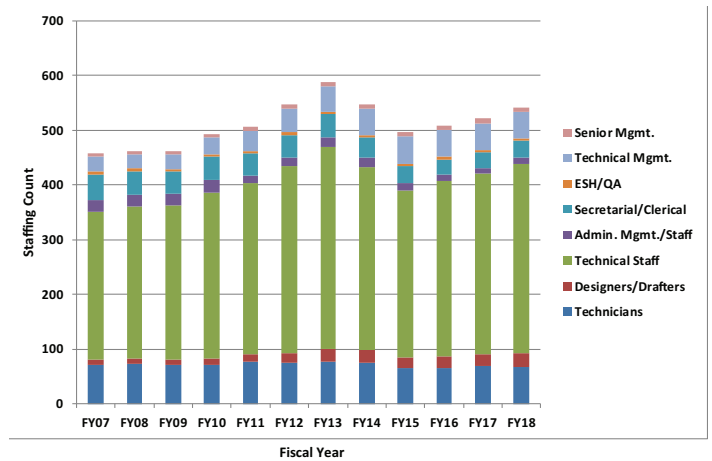
APS users by institutional geographic distribution (FY 2018)



APS Funding (FY 2006 - FY 2018)



APS Staffing (FY 2007- FY 2018)

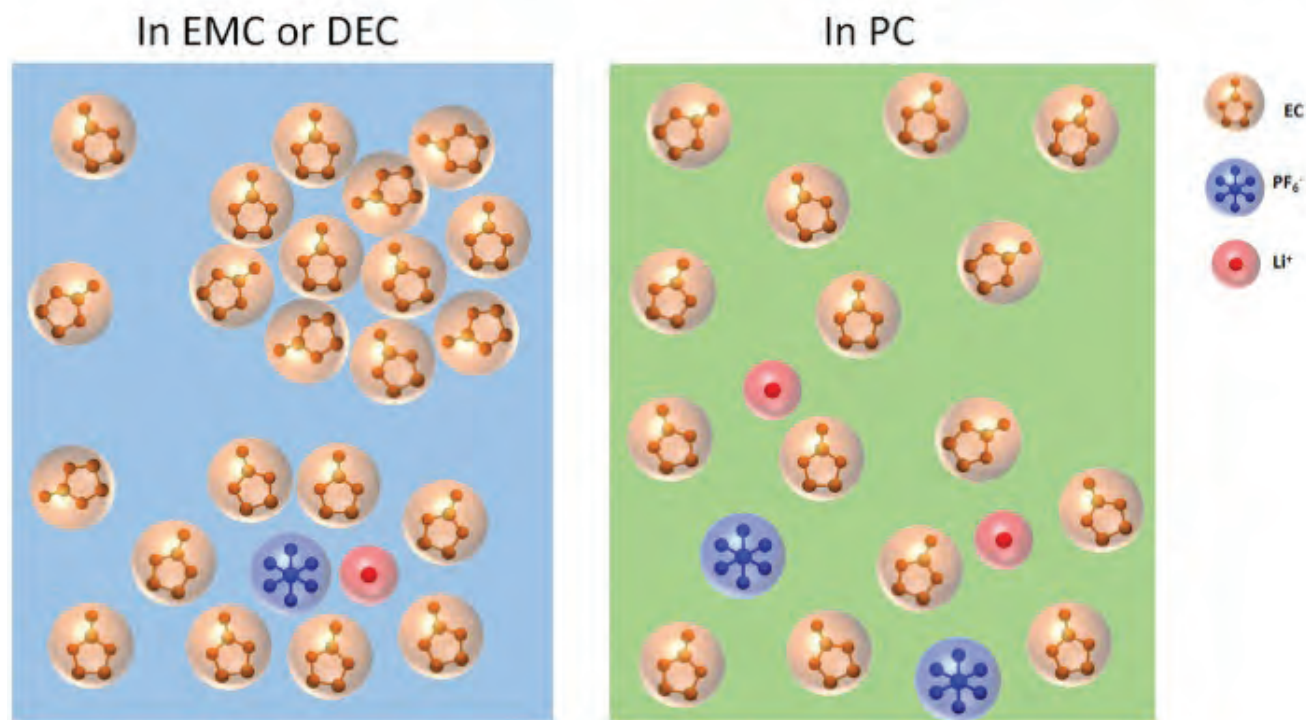




NANOSCIENCE

Unexpected Nanoclusters in Lithium-Ion Battery Electrolytes

Commercially available since the 1970s, the lithium-ion (Li-ion) battery is the workhorse power source for a variety of applications, including cell phones, laptops, and electric vehicles. However, the basic science underlying how these batteries work at the atomic and molecular levels remains incompletely understood, preventing the technology from reaching its full potential. Lithium-ion batteries are comprised of positive electrodes (anodes), negative electrodes (cathodes), and an electrolyte. The electrolyte's main role is to act as a conductive pathway for the movement of electricity (in the form of lithium ions, in this case) passing from the anode to the cathode during discharge, allowing the battery to operate. Researchers using the APS made a surprising discovery about the complexity of the interactions between different components of the electrolyte, one of the challenges that is set out to be studied in the DOE-funded, Argonne-led Joint Center for Energy Storage Research program over the next five years. The fundamental understanding gained from such a study may one day help enhance battery performance.



In a typical commercial lithium rechargeable battery, lithium ions dissolved in electrolytes move from the positive to the negative pole of the battery when it is charging. The ions then move in the opposite way when the battery is in use. Lithium ions, however, do not migrate alone; they are surrounded by electrolytes that facilitate the trip from one pole to the other. Effective electrolytes must have a handful of specific characteristics. While they are in contact with both the anode and the cathode, they must not react with either. They must allow a high degree of mobility of lithium ions between the two electrodes. And they must be inexpensive if the price of batteries is to continue to fall. The typical electrolyte in reasonably priced lithium-ion batteries is a lithium salt (usually lithium hexafluorophosphate, or LiPF_6) mixed into an organic solvent. That solvent is often a mix of ethylene carbonate (EC), diethyl carbonate (DEC), ethyl methyl carbonate (EMC), and propylene carbonate (PC). Lithium ions are thought to associate mainly with EC, forming so-called “solvation shells,” while DEC, EMC, and PC merely smooth the way for these shells to move between the batteries’ poles, like “lubricants.”

The performance, safety, and charge/discharge rate of lithium-ion batteries are determined by a variety of electrolyte physiochemical characteristics, including chemical stability and transport properties. Much research has been done to understand the impact that microscopic structures have on these properties for battery electrolytes such as $\text{LiPF}_6/\text{EC}/\text{EMC}$ and $\text{LiPF}_6/\text{EC}/\text{DEC}$. Although traditional spectroscopy techniques such as nuclear magnetic resonance, Fourier-transform infrared spectroscopy, and Raman are commonly used to provide tantalizing hints about the binding of solvent molecules, they cannot detect solvent aggregate formation.

-angle x-ray scattering (SAXS), a technique for ana-

< Fig 1. Typical lithium-ion battery electrolytes include a lithium salt (usually LiPF_6) mixed into an organic solvent consisting of ethylene carbonate (EC, orange) with some combination of diethyl carbonate (DEC), ethyl methyl carbonate (EMC), or propylene carbonate (PC). Using SAXS, researchers found that EC forms 1-nm-sized clusters when mixed with LiPF_6 and either DEC or EMC, while EC fully dissolves in PC. Also, LiPF_6 formed ion pairs (Li^+ , red, and PF_6^- , blue) in the presence of EC/DEC and EC/EMC mixtures, but not in an EC/PC mixture. Image courtesy of Zhou Yu.

lyzing the elastic scattering behaviors of x-rays when traveling through a material, has proven to be a very powerful technique for providing direct size information of nanometer-scale structures such as colloids, porous materials, biomolecules, and proteins.

A team of researchers, from Northern Illinois University and Argonne, used SAXS experiments at the XSD 12-ID-B and -C beamlines of the APS to study different varieties of lithium-ion battery electrolytes. Surprisingly, the researchers found that the cyclic carbonate, EC, formed 1-nm-sized clusters when mixed with a linear carbonate, either EMC or DEC, while no such clusters were found when EC was mixed with another cyclic carbonate, PC, likely due to differences in dielectric constant between the linear and cyclic carbonates. Adding LiPF_6 to either the EC/EMC mixture or the EC/DEC mixture resulted in the formation of a LiPF_6 structure roughly 0.6 nm in size, corresponding to the previously reported size of LiPF_6 contact ion pairs. Surprisingly, LiPF_6 contact ion pairs were absent in EC/PC electrolyte (Fig. 1). The presence of EC nanoclusters and LiPF_6 ion pairs in linear carbonate is thought to decrease battery performance by reducing electrolyte viscosity and conductivity, respectively. Unfortunately, even though neither EC nanoclusters nor LiPF_6 ion pairs are present in the $\text{LiPF}_6/\text{EC}/\text{PC}$ electrolyte, the defoliation of graphite by PC hinders the application of PC in commercial lithium-ion batteries consisting of graphite anodes.

These findings increase our knowledge of the behaviors of lithium-ion battery electrolytes and could inspire improvements to the design of the macroscopic properties of these important electrolytes. — Chris Palmer

See: Zhang Feng¹, Erik Sarnello², Tao Li^{1,2*}, and Lei Cheng^{1,**}, “Microscopic View of the Ethylene Carbonate Based Lithium-Ion Battery Electrolyte by X-ray Scattering,” *J. Electrochem. Soc.* **166**(2), 47 (January 4, 2019). DOI: 10.1149/2.0971816jes

Author affiliations: ¹Argonne National Laboratory, ²Northern Illinois University

Correspondence: * tli4@niu.edu, ** leicheng@anl.gov

This research was supported by the Joint Center for Energy Storage Research (JCESR), a U.S. Department of Energy (DOE) Energy Innovation Hub. This research used resources of the Advanced Photon Source, a U.S. DOE Office of Science User Facility operated for the DOE Office of Science by Argonne National Laboratory under Contract No. DE-AC02-06CH11357.

Transforming Hydrogels May Improve Sustained Drug Delivery

Almost every drug has unintended side effects, which can range from minor inconveniences like drowsiness to severe toxicity that limits how much can be administered or even prevent drugs from being approved for use. The field of drug delivery has thus emerged with the objective of finding innovative ways of directing drugs to their specific disease targets within the body while avoiding off-target effects in unrelated tissues. When successful, drug efficacy can be improved and required dosages can be lowered, all while avoiding troublesome side effects. Nanotechnology has proven to be a key tool in this process, resulting in nanoscale drug vehicles (nanocarriers) for a variety of clinical applications such as cancer chemotherapy, treatment of bacterial infections, and avoiding liver disease. In work conducted at the APS, researchers investigated the potential of designing hydrogel nanocarriers, which may provide new avenues for investigation in long-term drug delivery in a variety of diseases.



To date, nanocarrier administration has been limited to short-term bolus injections or IV infusions. However, for some applications, sustained drug delivery via targeted nanocarriers may be desirable. For example, in long-term processes, such as wound healing, hormone therapy, and transplantation, it may be desirable to expose the patient to controlled, long-term delivery of the drug. For these applications, researchers have developed implantable hydrogels and scaffolds composed of synthetic or natural biopolymer networks that trap the nanocarriers for slow release, much like a tiny, fine-mesh strainer. However, because these scaffolds play only a structural role and are not involved in drug delivery itself, current versions may elicit a foreign body response, causing the polymer networks to be walled off by the immune system in stiff fibrous capsules that can cause pain for the patient and reduce the efficiency of drug release.

In experimentation at the APS, researchers from Northwestern University and the University of Illinois at Chicago carried out studies that supported their hypothesis: It might be possible to design a hydrogel that could transform into the nanocarriers, avoiding this unwanted immune response. In this plan, the entire implanted hydrogel itself breaks down into the drug-delivery vehicle, resulting in sustained nanocarrier release with no leftover or unused polymer network remaining to elicit an unwanted immune response.

The first step for the research team was to develop and characterize the nanocarriers. They hypothesized that they could take advantage of the properties of block copolymers (BCPs), mixtures of polymers that can assemble into stable structures under controlled conditions, to build their transforming hydrogel. In this case, the BCPs self-assemble into polymer networks composed of cylindrical filaments (filomicelles) that can transform into nanoscale spherical vehicles (micelles). This transition from cylinders to spheres was shown to be dependent on surface tension, and the released micelles were found to be excellent vehicles for diagnostic and therapeutic

< Fig. 1. Transmission electron microscopy micrograph (false-colored) of a mixed population of spherical micelles and worm-like filomicelles. Filomicelles were self-assembled from poly (ethylene glycol)-block-poly (propylene sulfide) polymer via thin-film rehydration. Upon oxidation, filomicelles undergo an inducible cylinder-to-sphere transition into micelles. The researchers' laboratory has recently engineered filomicelles as vehicles for sustained drug delivery.

agents. When loaded with drugs, these hydrogels serve as depots that undergo cylinder-to-sphere transitions, where the released spheres transport drugs in a targeted fashion for months at a time.

Using both small-angle x-ray scattering experiments conducted at the DND-CAT beamline at the APS and cryogenic transmission electron microscopy, the team verified that they could build cylindrical filomicelles of stable and consistent length and width, and that these filomicelles transition to spheres at the cylinder ends through a budding process (Fig. 1). These experimental data were supported by thermodynamic modeling of the transition that suggested the process could be triggered by oxidation, which resulted in changes in surface tension at the interface between the polymer network and the surrounding solution (e.g., water or blood), triggering the cylinder-to-sphere transition.

The next step was to verify that the filomicelles could still undergo the spherical transformation after they were crosslinked into a stable hydrogel network. After optimizing the crosslinking of the filaments into hydrogels of desired viscosity, the team loaded a light-inducible photo-oxidizer into the filaments to precisely trigger and control the transition to micelles. Incredibly, highly uniform monodisperse micelles were found to form regardless of the time of oxidation or the density of the crosslinkers. Best of all, the size of the nanoscale spheres was optimal for delivery to their chosen physiological target, lymphatic tissues where cells of the immune system reside.

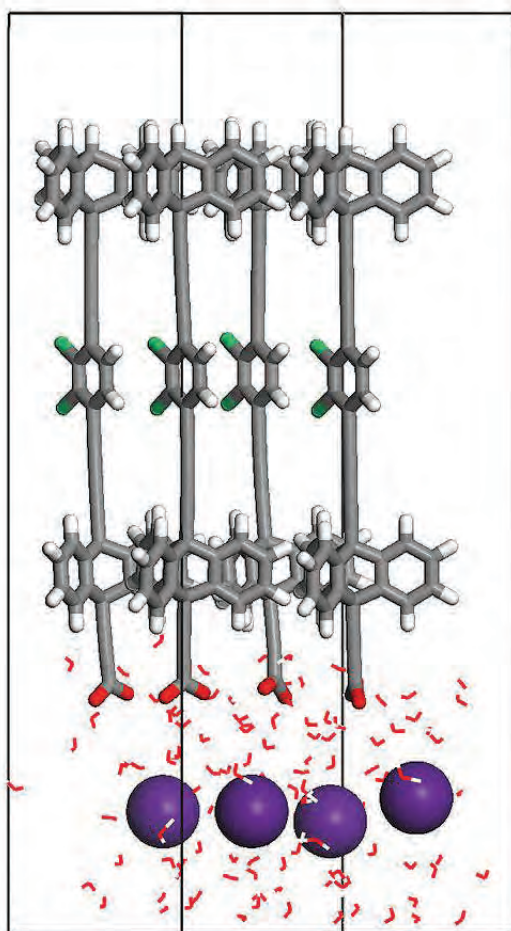
Finally, it was time to test the new transforming hydrogel in an animal model. Injection of a dye-tagged version of the filaments mixed with the crosslinker allowed *in situ* formation of the hydrogels under the skin of mice within seconds to minutes. As hoped, the team found the injectable hydrogel transformed into micelles due to physiological levels of oxidation. A second dye, serving as a mock drug molecule, was loaded within the filaments and was found to stably transfer to the released micelles. By employing two separate dyes, both the polymer and the mock drug payload could be traced and colocalized within the desired target immune cells in lymph nodes of the mice. No sign of infiltrating inflammatory cells or fibrous capsule formation was observed at the implant site over the course of a month of sustained micelle release.

Together, these results quantitatively demonstrated that the transforming hydrogels could continuously re-

“Hydrogels” cont'd. on page 109

Novel Molecular Rotors that Meet Theoretical Requirements for Nano-Electronics

Regular arrays of dipolar molecular rotors promise a variety of applications, in particular, miniaturization of analog electronics and production of nano-electronics. To be used for this purpose, the arrays should exhibit ferroelectric collective behavior, with all dipoles spontaneously pointing in the same direction. Theory suggests that to achieve this, the arrays should ideally be triangular, with all rotational axes parallel. In the current study, researchers utilized the APS to explore the ability of specifically designed and synthesized molecular rotors assembled on an aqueous surface to form such a tight trigonal lattice, with the rotor axes standing perpendicular to the surface. This desired arrangement was actually found, and the theoretical ideal for generating a two-dimensional (2-D) ferroelectric phase has been reached. The next step will be to transfer the monolayer to an electrically insulating solid substrate. If it can be accomplished without ruining the ideal structure achieved on the aqueous subphase, the transferred monolayer is expected to be ferroelectric and it will thus become possible to make any water-resistant surface ferroelectric. If the structure does not survive, the way will have been paved for further modification of the molecular structure of the rotors to make the array transferable to solid substrates without damage. This advance has both theoretical and practical applications in nano-electronics.



With the long-term goal of producing a 2-D sheet of molecular rotors on a flat, solid surface for use in both fundamental research and applications in nanoscience, the researchers, from the University of Colorado Boulder, the Academy of Sciences of the Czech Republic, and Lawrence Berkeley National Laboratory, first investigated a 2-D phase of molecular rotors organized on the surface of a liquid-air interface, or aqueous phase (Fig. 1). The rotors were made from a rod with a terminal carboxylic acid group and a dipolar rotor (2,3-dichloro-1,4-phenylene) that contained two Y-shaped triptycenes designed to form two interlocking decks. Together, these chemical structures were designed to organize into a sheet of rotors that stood perpendicular to a surface, with all dipoles parallel. This feature also maximized the number of rotors in a given surface area and allowed unhindered dipole rotation, a motion required for ferroelectric activity. Furthermore, the rotors were designed to pack together in a trigonal formation, an organization in agreement with theoretical requirements for ferroelectricity.

In order to confirm that the designed qualities of the rotors led to the expected packing and orientation in a 2-D phase, the researchers used the grazing-incidence x-ray diffraction technique at the ChemMatCARS 15-ID x-ray beamline at the APS to measure the structure of the monolayer. Analysis of the diffraction pattern confirmed that each vertically oriented rotor occupies a space (also called a “cell”) that is 8.13 Å by 8.40 Å in a trigonal lattice formation (Fig. 1). Thus, the rotors on the aqueous surface were indeed in exactly the configuration desired for ferroelectricity and are a promising first step. This discovery paves the way for additional research aimed at producing next-generation molecular rotors that can be transferred to a solid substrate without ruining the ideal structure achieved at the aqueous surface. Future work will be aimed at modifying the rotor structure so that they can withstand the transfer process. The transfer would then allow the generation of a 2-D phase of ferroelectric rotors that can be applied to any water-resistant surface. — Emma Nichols

See: Jirí Kaleta^{1,2}, Jin Wen¹, Thomas F. Magnera², Paul I. Dron², Chenhui Zhu³, and Josef Michl^{1,2*}, “X-ray diffraction structure of a monolayer of molecular rotors on aqueous subphase from grazing-incidence X-ray diffraction,” *Proc. Natl. Acad. Sci. U.S.A.*

< Fig. 1. Side view of PM6-optimized structure of the major phase of Cs salt of the rod-shaped molecular rotor on water.

115(38), 9373 (2018). DOI: 10.1073/pnas.1712789115

Author affiliations: ¹Academy of Sciences of the Czech Republic, ²University of Colorado Boulder, ³Lawrence Berkeley National Laboratory

Correspondence: * josef.michl@colorado.edu

We thank Dr. Binhua Lin, Dr. Mati Meron, and Dr. Wei Bu of the ChemMatCARS facility of the University of Chicago for helpful discussions and assistance with the measurements. Work in Prague was supported by the European Research Council (ERC) under the European Community’s Framework Programme (FP7/2007-2013) ERC Grant 227756 and by the Institute of Organic Chemistry and Biochemistry, Academy of Sciences of the Czech Republic (RVO: 61388963). Work in Boulder was supported by U.S. National Science Foundation (NSF) Grant DMR 1608424. ChemMatCARS Sector 15 is principally supported by the Divisions of Chemistry (CHE) and Materials Research (DMR), NSF, under Grant NSF/CHE-1346572. This research used resources of the Advanced Photon Source, a U.S. Department of Energy (DOE) Office of Science User Facility operated for the DOE Office of Science by Argonne National Laboratory under Contract No. DE-AC02-06CH11357.

“Hydrogels” cont’d. from page 107

lease micelles that transported payloads to target tissues and cells without inducing inflammation.

The experiments performed at the APS were critical for the fundamental characterization and understanding of these novel hydrogels, which may have a wide range of applications in the treatment of chronic pathologies, including cardiovascular disease, cancer, and diabetes.

Immediate next steps for these transforming injectable hydrogels are focusing on low-dosage cancer immunotherapy and novel platforms for vaccination against infectious diseases.

— Sandy Field & Evan A. Scott

See: Nicholas B. Karabin¹, Sean Allen¹, Ha-Kyung Kwon¹, Sharan Bobbala¹, Emre Firlar², Tolou Shokuhfar², Kenneth R. Shull¹, and Evan A. Scott^{1*}, “Sustained micellar delivery via inducible transitions in nanostructure morphology,” *Nat. Commun.* **9**, 624 (2018). DOI: 10.1038/s41467-018-03001-9

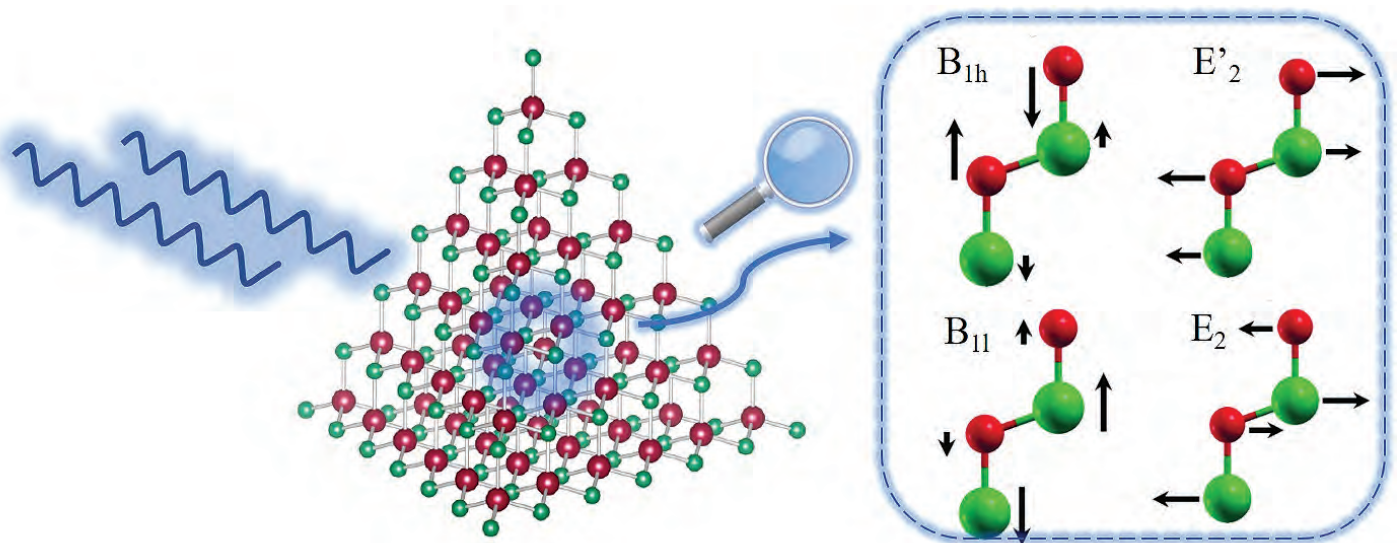
Author affiliations: ¹Northwestern University, ²University of Illinois at Chicago

Correspondence: * evan.scott@northwestern.edu

This research was supported by the National Science Foundation (NSF) CAREER award CBET-1453576, the National Institutes of Health Director’s New Innovator Award no. 1DP2HL132390-01, and the 2014 McCormick Catalyst Award. N.B.K. was supported in part by the Northwestern University Graduate School Cluster in Biotechnology, Systems, and Synthetic Biology, which is affiliated with the Biotechnology Training Program. T.S. and E.F. are grateful to the NSF CAREER award DMR-1564950 for providing partial financial support. H.K.K. was funded by the Center for Hierarchical Materials Design (ChiMaD). DND-CAT is supported by Northwestern University, E.I. DuPont de Nemours & Co., and The Dow Chemical Company (the latter both part of DowDuPont.) This research used resources of the Advanced Photon Source, a U.S. Department of Energy (DOE) Office of Science User Facility operated for the DOE Office of Science by Argonne National Laboratory under Contract No. DE-AC02-06CH11357.

How Surface Ligands Influence the Lattice Dynamics of Cadmium Selenide Quantum Dot Nanoparticles

These days, when one has an epiphany, it's a figurative solid-state light bulb that lights up over one's head. Those energy-conscious, white-light spectrum bulbs could benefit from the characteristics of semiconducting quantum dot nanoparticles – an alternative to the currently-used solid phosphors. In order to leverage these nanoparticles' valuable properties, materials scientists need a thorough understanding of their lattice structure and energy dynamics and how those characteristics differ between a bulk sample of the crystal and the nano-sized one. Unfortunately, the most widely-used materials characterization methods are tailored to bulk crystals. However, recent research efforts carried out at the APS and at the National Synchrotron Light Source II (NSLS-II) at Brookhaven National Laboratory have yielded new structural and energetic insights into quantum dot nanoparticles. This has been achieved by pairing a new technique for precisely generating cadmium selenide quantum dots and x-ray scattering techniques. In addition to demonstrating the advantages of this combination, the researchers concluded that the nanoparticle material could be intentionally manipulated to select for certain desired electronic behaviors.



Quantum-dot nanoparticles are of interest in applications ranging from electronics to biology because of their optoelectronic properties. These include their size-tunable band gaps, high efficiency at producing light, and long-term stability. The key challenges in utilizing a specific nanoparticle are two-fold: determining its structure with atomic precision, and detailing the energy dynamics of its lattice. When characterizing the lattice, scientists are most interested in atomic bonding and the behavior of atomic collective excitations (phonons). Phonons are quantum atomic vibrations generated in the lattice; from the phonon density of states, scientists can calculate many thermodynamic properties relevant in optoelectronic applications.

The research team in this study, comprising members from Columbia University, Miami University, Argonne, Brookhaven National Laboratory, and the American Physical Society, began by generating gram quantities of identical cadmium selenide quantum-dot nanoparticles. These quantum dots are important and novel because they are atomically precise. This atomical precision allowed the team to determine the dots' structure by applying pair distribution function analysis to powder x-ray scattering diffraction data taken of the nanoparticles at beamline 28-ID-2 at the NSLS-II.

The combination of atomical precision and a structure solution allowed the team to use density functional theory to derive theoretical values for the phonon density of states, which they then measured using the HERIX spectrometer at XSD Sector 30, beamline 30-ID-B,C, at the APS. The team subjected bulk and nanoparticle samples (of three different sizes) to applied high-energy-resolution inelastic x-ray scattering with an overall energy resolution of 1.5 MeV. Figure 1 shows a depiction of this scattering and vibrational states in the nanoparticle the team was hoping to find. They reduced this scattering data and from it, calculated measured values for the phonon density of states for all samples.

When the team compared the phonon density of states – both the theoretical values and the measured ones – for the nanoparticles and the bulk sample, they

< Fig. 1. Depiction of the x-ray scattering from cadmium selenide quantum dot nanoparticles that, when combined with theory, results in an understanding of the energies of vibrational states (shown on the right).

found that the peaks for the nanoparticles were blue-shifted with respect to the bulk sample. They also found that the peaks that appeared in the bulk sample were significantly broader and less distinct in the nanoparticles' phonon density of states.

Because of the small size of the nanoparticles, the team had expected their features in the phonon density of states to be sharper than the bulk sample rather than flattened. Since each sample was atomically precise, they concluded that this flattening occurred because the lengths of the atomic bonds varied across an individual quantum-dot sample.

The team was surprised to discover the theoretical calculations predicted a red-shift rather than the blue-shift that was observed. The team found that by adding heavy surface ligands to the calculations, they could replicate the blue-shift observed in their measurements. The team concluded that it should be possible to vary the surface ligand's mass to manipulate the phonon density of states, and thus manipulate the phonon frequencies, which is a result worthy of a very bright lightbulb indeed.

– Mary Alexandra Agner

See: Chenyang Shi^{1*}, Alexander N. Beecher¹, Yan Li², Jonathan S. Owen¹, Bogdan M. Leu^{3,4}, Ayman H. Said³, Michael Y. Hu³, and Simon J.L. Billinge^{1,5**}, “Size-Dependent Lattice Dynamics of Atomically Precise Cadmium Selenide Quantum Dots,” *Phys. Rev. Lett.* **122**, 026101 (2019).

DOI: 10.1103/PhysRevLett.122.026101

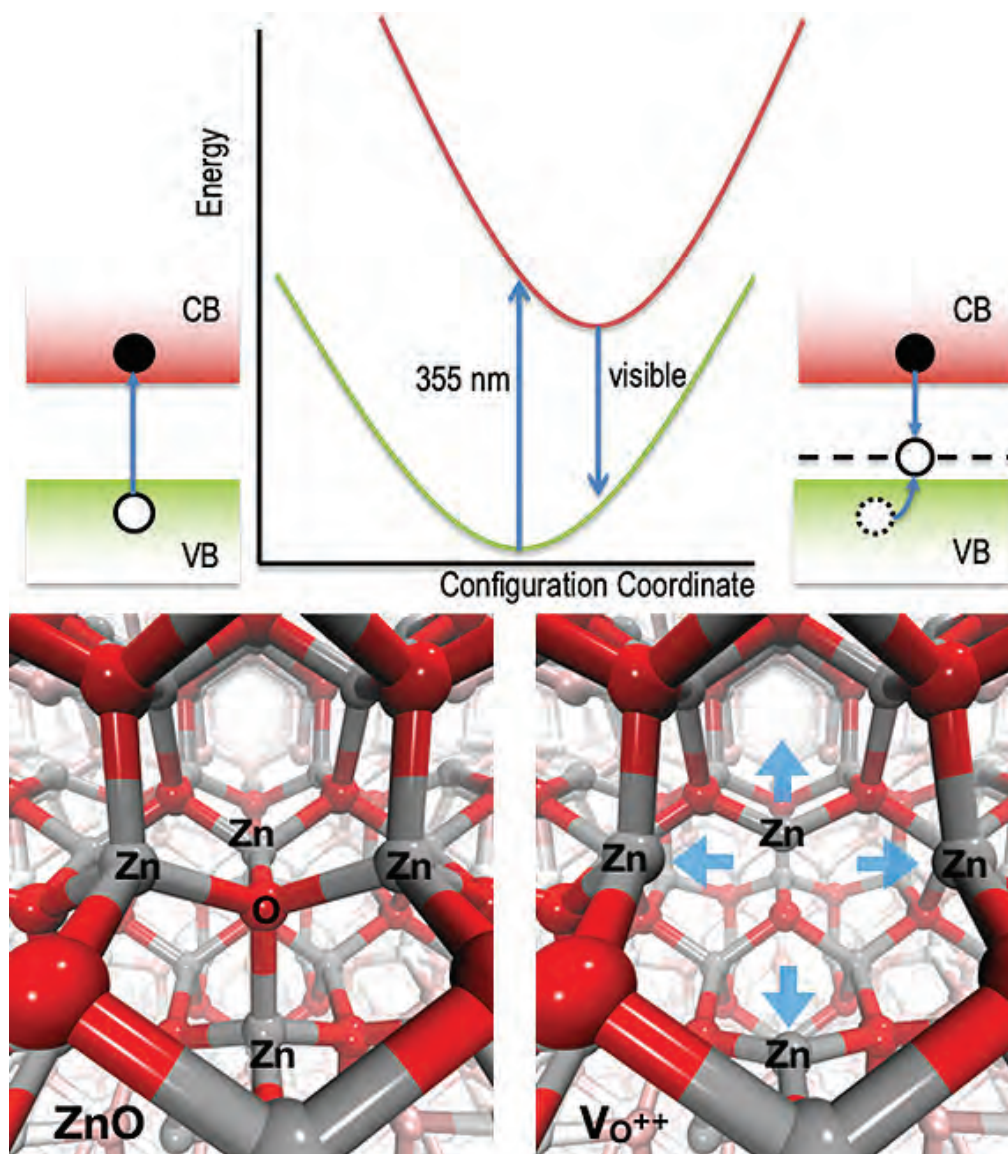
Author affiliations: ¹Columbia University, ²American Physical Society, ³Argonne National Laboratory, ⁴Miami University, ⁵Brookhaven National Laboratory

Correspondence: * cs3000@columbia.edu, ** sb2896@columbia.edu

Work in the Billinge group was supported by the U.S. Department of Energy (DOE) Office of Science-Basic Energy Sciences under Contract No. DE-SC0012704. Work on the nanoparticle synthesis and characterization was supported by the National Science Foundation through Contract No. NSF-CHF-1151172. The NSLS II is a U.S. DOE Office of Science User Facility operated for the DOE Office of Science by Brookhaven National Laboratory under Contract No. DE-SC0012704. Computations made use of resources of the National Energy Research Scientific Computing Center, a U.S. DOE Office of Science User Facility supported by the Office of Science of the U.S. Department of Energy under Contract No. DE-AC02-05CH11231. This research used resources of the Advanced Photon Source, a U.S. DOE Office of Science User Facility operated for the DOE Office of Science by Argonne National Laboratory under Contract No. DE-AC02-06CH11357.

Revealing the Hole Story for ZnO Nanoparticles

Transition metal oxide (TMO) nanoparticles have attracted an increasing amount of attention from researchers due to their potential for use in solar-energy conversion and photocatalysts, devices that can help to alleviate escalating worldwide energy demands. These devices use sunlight to generate charge carriers: negatively charged electrons and equivalent positive charges called “holes.” Thus, to effectively design these devices, it’s crucial to understand how these charge carriers are created, move around, and are trapped within the crystal lattice of these nanomaterials at room temperature, and at different time and length scales. Researchers using the APS have gained insights that could eventually be used to better design materials to optimize device performance.



Although most studies have focused on titanium dioxide (TiO₂) nanostructures, those made of zinc oxide (ZnO) are promising contenders, with an electron mobility two orders of magnitude larger than TiO₂. The properties of ZnO are also more customizable due to its ability to be easily synthesized in a variety of nanoparticle sizes and shapes. Yet, ZnO's applications have been limited due to its photocorrosion under ultraviolet radiation and its rapid recombination of electrons and holes, which limits device efficiency. Both of these limitations are linked to the nature of defect sites in this material, which are thought to act as charge traps.

Researchers have taken advantage of several techniques to try to shed light on the structure and energetics of these defects, including time-resolved x-ray absorption spectroscopy (XAS), which provides information on the local geometric and electronic structure of matter after photoexcitation of the material. But although this technique is ideal for investigating electrons, it doesn't reveal much information about holes.

To resolve this discrepancy, an international team of researchers came to the XSD 7-ID-D beamline at the APS where they combined XAS with resonant x-ray emission spectroscopy (RXES), which provides complementary information on electronic structure.

Their results show that holes created by light are trapped in pre-existing, singly charged oxygen vacancies in the ZnO crystal structure, converting the vacancy to doubly charged and displacing the surrounding four Zn atoms away (Fig. 1).

Using an aqueous colloidal suspension of ZnO nanoparticles 32 nm in diameter, the researchers illuminated samples with pulses of laser light, causing the samples to glow. They concurrently collected XAS and RXES data, providing detailed information on the charge carrier dynamics in the nanostructures.

Their data suggest that electrons in the ZnO nanoparticles remain largely delocalized at an energy level known as the "conduction band." However, within 80 ps

< Fig 1. Energy landscape showing configuration coordinate and creation of the electron-hole pair in the conduction and valence bands, respectively (top). ZnO crystal structure showing intact lattice (bottom left) and oxygen vacancy with corresponding Zn atom motion away from the vacancy upon hole trapping.

of illumination, the photoexcited holes became trapped in positive, singly charged defects within the crystal lattice where oxygen atoms were missing. These holes changed the level of charge from single to double, a difference that affected the placement of the Zn atoms. To accommodate the charge change, the four Zn atoms that surround the O vacancy moved outward, away from the vacancy by about 15%. Theoretical simulations support these results.

The authors suggest that these findings could help researchers find ZnO materials that minimize electron-hole recombination to improve device performance. For example, ZnO nanorods have fewer oxygen vacancies, making them candidates for a type of material that should exhibit less hole trapping and, therefore, reduced recombination events, a boon for developing potentially more efficient photovoltaic devices. — [Christen Brownlee](#)

See: Thomas J. Penfold¹, Jakub Szlachetko^{2,3}, Fabio G. Santomauro⁴, Alexander Britz^{5,6}, Wojciech Gawelda^{5,7}, Gilles Doumy⁸, Anne Marie March⁸, Stephen H. Southworth⁸, Jochen Rittmann⁴, Rafael Abela², Majed Chergui⁴, and Christopher J. Milne², "Revealing hole trapping in zinc oxide nanoparticles by time-resolved X-ray spectroscopy," *Nat. Commun.* **9**, 478 (2018). DOI: 10.1038/s41467-018-02870-4

Author affiliations: ¹Newcastle University, ²Paul Scherrer Institut, ³Polish Academy of Sciences, ⁴FSB and Lausanne Centre for Ultrafast Science (LACUS), ⁵European XFEL, ⁶The Hamburg Centre for Ultrafast Imaging, ⁷Adam Mickiewicz University, ⁸Argonne National Laboratory

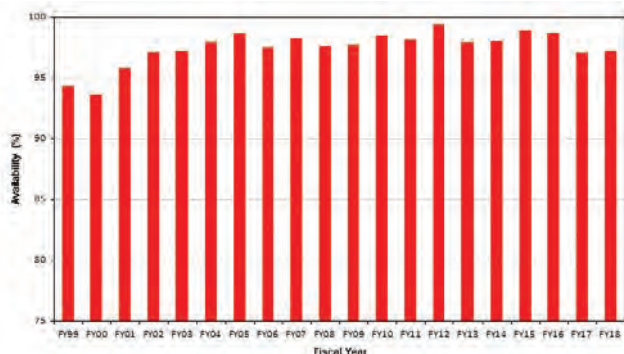
Correspondence: * chris.milne@psi.ch

G.D., A.M.M. and S.H.S. were supported by the U.S. Department of Energy (DOE) Office of Science-Basic Energy Sciences, Chemical Sciences, Geosciences, and Biosciences Division under Contract No. DE-AC02-06CH11357. M.C. acknowledges support by the Swiss National Science Foundation (NSF) through the NCCR-MUST, by COST programs PER-SPECTH2O (CM0702) and XLIC (CM1204), and the European Research Council Advanced Grant H2020 ERCEA 695197 DYNAMOX. A.B. and W.G. acknowledge financial support from the Hamburg Center for Ultrafast Imaging (University of Hamburg), Deutsche Forschungsgemeinschaft (via SFB925, TPA4), and the European XFEL GmbH. W.G. further acknowledges support from the National Science Centre Poland (NCN) under SONATA BIS 6 grant No. 2016/22/E/ST4/00543. C.J.M. acknowledges support by the Swiss NSF through the NCCR-MUST. T.J.P. acknowledges support from the Leverhulme Trust, grant number RPG-2016-103. J.S. acknowledges National Science Centre, Poland (NCN) for support under grant no. 2015/18/E/ST3/00444. This research used resources of the Advanced Photon Source, a U.S. Department of Energy (DOE) Office of Science User Facility operated for the DOE Office of Science by Argonne National Laboratory under Contract No. DE-AC02-06CH11357.

X-ray Availability and Reliability

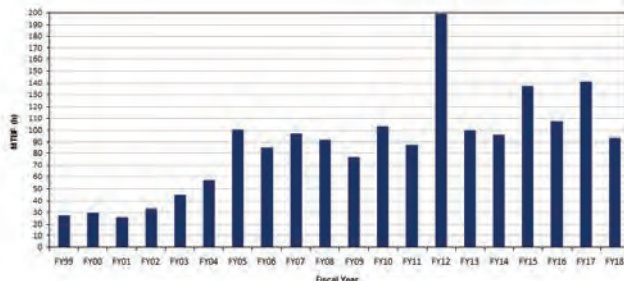
In fiscal year 2018*, the APS x-ray source continued to function as a highly reliable delivery system for synchrotron x-ray beams for research. Several factors support the overall growth in both the APS user community and the number of experiments carried out by that community. But there is a direct correlation between the number of x-ray hours available to users; the success of the APS experiment program; and the physicists, engineers, and technicians responsible for achieving and maintaining optimum x-ray source performance. Below are definitions of important measures for the delivery of x-ray beam to users (latest data shown graphically).

X-ray Availability FY99-FY18



X-ray Availability: The number of hours that beam is available to users divided by the number of hours of scheduled beam delivery prior to the beginning of a run. The specific definition of available beam is that the APS main control room has granted permission to users to open shutters, and there is more than 50-mA stored beam in the storage ring.

MTBF FY99-FY18



Storage Ring Reliability: A measure of the mean time between beam losses (faults), or MTBF, calculated by taking the delivered beam and dividing by the total number of faults. The APS targets, and routinely exceeds, 70 h MTBF. A fault is defined as complete unavailability of beam either via beam loss or removal of shutter permit not related to weather. A fault also occurs when beam has decayed to the point where stability and orbit can no longer be considered reliable (50 mA).

* While the highlights in, and title of, this report cover calendar year 2018, data on accelerator performance and user statistics are measured on the basis of fiscal years.

Typical APS Machine Parameters

LINAC

Output energy	425 MeV
Maximum energy	500 MeV
Output beam charge	0.3–3 nC
Normalized emittance	5–20 mm-mrad
Frequency	2.856 GHz
Modulator pulse rep rate	30 Hz
Gun rep rate	2–12 Hz
(1–6 pulses, 33.3 ms apart every 0.5 s)	
Beam pulse length	8–15 ns
Bunch length	1–10 ps FWHM

PARTICLE ACCUMULATOR RING

Nominal energy	425 MeV
Maximum energy	450 MeV
Circumference	30.66 m
Cycle time	500 ms or 1000 ms
Fundamental radio frequency (RF1)	9.77 MHz
12th harmonic RF frequency (RF12)	117.3 MHz
RMS bunch length	0.34 ns
(after compression)	

INJECTOR SYNCHROTRON (BOOSTER)

Nominal extraction energy	7.0 GeV
Injection energy	425 MeV
Circumference	368.0 m
Lattice structure	10 FODO cells/ quadrant
Ramping rep rate	2 Hz or 1 Hz
Natural emittance	69 nm-rad (actual) 92 nm-rad (nominal)
Radio frequency	351.930 MHz

STORAGE RING SYSTEM

Nominal energy	7.0 GeV
Circumference	1104 m
Number of sectors	40
Length available for insertion device	5.0 m
Nominal circulating current, multibunch	100 mA
Natural emittance	2.5 nm-rad
RMS momentum spread	0.096%
Effective emittance	3.1 nm-rad
Vertical emittance	0.040 nm-rad
Coupling (operating)	1.5%
Revolution frequency	271.555 kHz
Radio frequency	351.935 MHz
Operating number of bunches	24 to 324
RMS bunch lengths	33 ps to 25 ps
RMS bunch length of 16 mA in hybrid mode	50 ps

NOVEL ACCELERATOR & X-RAY TECHNIQUES & INSTRUMENTATION

Production of Vacuum Chambers for the Linac Coherent Light Source II

The Linac Coherent Light Source (LCLS) at the SLAC National Accelerator Laboratory was the world's first x-ray free-electron laser when it became operational in 2009. The APS contributed to the project by designing and building the undulator line, including 41 undulator vacuum chambers [1]. The chambers' thin wall, small aperture, and aperture surface finish presented new production challenges. Although the aperture surface finish met requirements, schedule constraints at that time prevented further improvement of the polishing method beyond what was needed for the project. When presented with the opportunity to build vacuum chambers for the new undulator lines of the LCLS-II upgrade, the members of the AES Mechanical Engineering and Design Group project core team were eager to improve the process wherever possible, as well as meet the new technical needs of the LCLS-II free-electron laser.



Members of the AES LCLS-II vacuum chamber core team with the last crate of LCLS-II vacuum chambers ready to ship to SLAC.

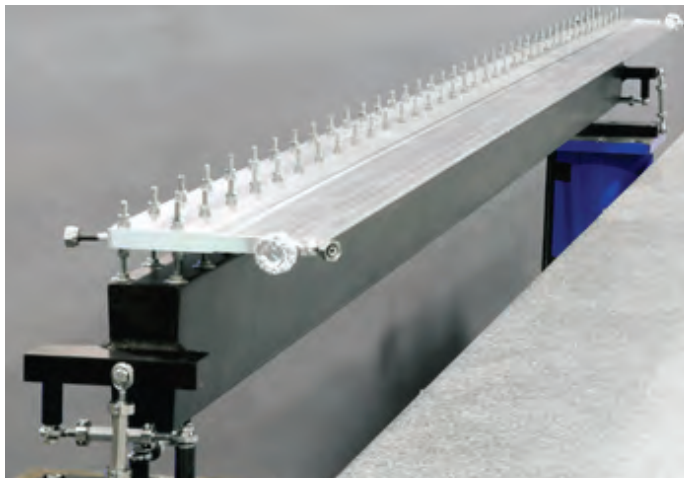


Fig. 1. A SXR chamber on an alignment beam before installation of Earth-field coils.

Because of an extremely short electron-bunch length, one of the key requirements of the LCLS-II physics specification was to achieve the best possible surface finish within the chamber aperture. The highly polished aperture was achieved through a renewed collaboration with Engineered Finishing, Inc., the abrasive-flow machining vendor that polished the chambers for the original LCLS.

Normally, the maximum aspect ratio for this process is 8/1, depth/aperture. In this case, the process was modified to enable polishing of a small, oval-aperture extrusion (5 mm x 11 mm) with an aspect ratio $\sim 700/1$. The improved process permitted simultaneous polishing of two 4-m-long extrusions to meet the critical surface roughness finish defined by the radio-frequency impedance requirements — and with more consistent polishing results than before. The surface finish was improved from an average of 812-nm rms to an average surface finish of 238-nm rms. More importantly for the success of the project, the average longitudinal rms surface roughness slope of all chambers was to be less than 20 mrad; in fact, an average longitudinal surface roughness slope of 8.50 mrad was achieved, with no chamber exceeding 20 mrad.

For the LCLS-II upgrade, two slightly different variations of chambers were required: one version for a soft x-ray (SXR, Fig. 1) undulator line, and one for a hard x-ray

(HXR, Fig. 2) undulator line. The HXR chambers are mounted and aligned in a vertical orientation because the HXR undulators are a special type: horizontal-gap, vertically-polarized undulators.

Among the many requirements were that all chambers would be fabricated from an aluminum extrusion, maintain a finished nominal wall thickness of 0.5 mm, maintain a vacuum of less than 1×10^{-6} Torr, and a maximum outgassing rate after bake-out of less than 2×10^{-10} Torr*L/sec/cm². Chambers for both undulator lines are capable of being aligned to within ± 100 - μ m straightness along their entire length. For this upgrade, all chambers are water cooled so that an operating temperature of 20° C, $\pm 1^\circ$ C can be maintained. All chambers have coils installed within the surface of the chamber to allow cor-



Fig. 2. Five HXR chambers assembled in alignment fixtures, with water fittings and Earth-field coils. Photo by Dave Boughton

recting for the Earth's magnetic field (without violating the space constraints; that is, the chamber thickness could not exceed 6 mm $\pm 0.15/-0.05$ mm).

Upon completion, 64 chambers (26 SXR chambers and 38 HXR chambers, and their alignment systems) were delivered to SLAC for the LCLS-II upgrade. By meeting or exceeding the challenging requirements of the LCLS-II free-electron laser upgrade, these undulator vacuum chamber systems helped enable the next generation of free-electron lasers.

Contact: Greg E. Wiemerslage (wiemer@anl.gov)

REFERENCE

- [1] E. Trakhtenberg, G. Wiemerslage, M. Erdmann, P. Den Hartog, "LCLS Extruded Aluminum Vacuum Chamber - New Approaches," MEDSI/Pan-American SRI 2008 Meeting, Canadian Light Source (2009).

EPICS @ 30: EPICS 7 Advances the Capabilities of the APS Controls Network

Almost 30 years ago, the Los Alamos and Argonne national laboratories agreed to share software development work for machine control systems and called the result EPICS, the Experimental Physics and Industrial Control System. That collaboration continues today with EPICS 7, which remains at the forefront for large distributed control systems.



Attendees at the 2018 EPICS Collaboration Meeting, held at the APS on June 11-15, 2018.

The APS has always used the EPICS control system toolkit to build and run its real-time accelerator control system. Personnel from what is now the AES Controls Group, together with their colleagues at Los Alamos, were largely instrumental in forming the EPICS Collaboration, an informal group that now spans 5 continents and over 25 countries, with more projects and users of the software than can be counted; the main mailing list now has over 900 subscribers. Among other things, EPICS provides the communications software that allows operators in the APS Main Control Room to observe and adjust settings on most of the technical equipment spread around the APS storage ring.

In the early years of EPICS at the APS, information sent over the network between that equipment and its clients tended to be readings from individual sensors, or scalar values to set the current in a magnet or the target position of a motor. In some cases, it included arrays of those kinds of values, but the complexity of the data was limited and the values sent were homogeneous. The EPICS Channel Access network protocol was designed in 1989 to quickly and efficiently transfer these kinds of data, and while the networks it now runs on are up to 10,000 times faster than back then, the kinds of data the protocol can send over the wire are still essentially the same as when it was first released.

30 years later, the devices that EPICS connects to are much more complex, with many related parameters or sets of attributes that must be attached to the raw data. A data structure designed to hold information for one device is unlikely to be quite the same as that needed for others. Thus, for the last ten years, members of the EPICS community have been developing a new flexible network protocol to augment and eventually replace Channel Access. The code implementing this was first included in the EPICS 7 software package released in December 2017.

The new network protocol is called “PV Access,” and it can transport any data that can be encoded using the associated PV Data software library. Like Channel Access, the network protocol implements a client/server model, where any number of servers listen to clients asking for objects by name; the appropriate server replies, and the client sends it requests to read, monitor, and/or write data from/to that object. New in this protocol are features allowing a client to ask the server to execute a specific operation and return a result once finished.

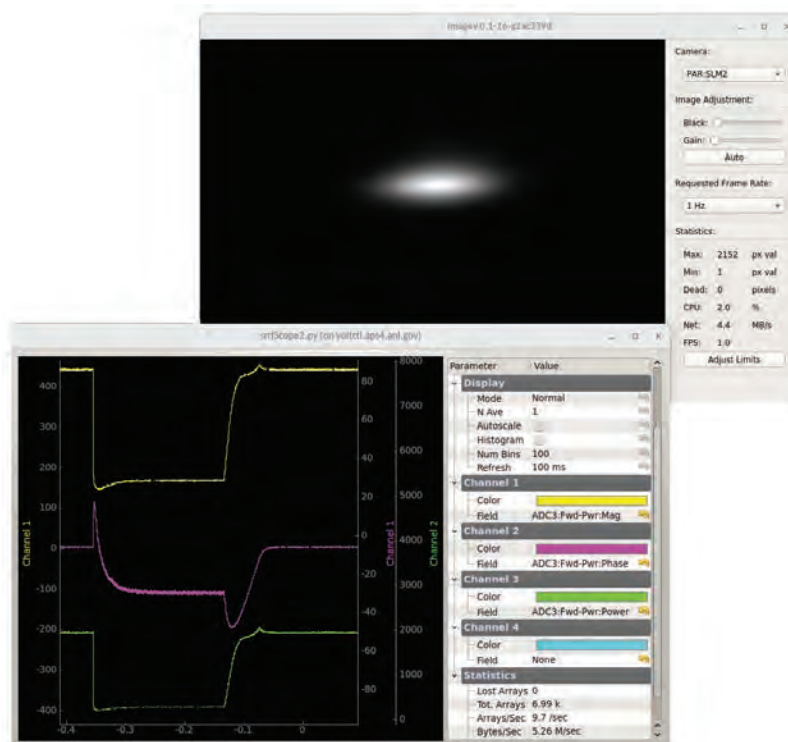


Fig. 1. Components of the “C2 Data Viewer” application, being developed for the APS Upgrade, to display control system data obtained in real-time using the PV Access network protocol.

Many APS beamlines (and other x-ray light sources around the world) already rely on Mark Rivers’ (GSE-CARS) AreaDetector package, which can collect and process multi-dimensional data such as video streams. These complex streams of scientific data can be more efficiently encoded by PV Data and transported using the PV Access protocol — earlier versions of AreaDetector could only use Channel Access for data transport, which doesn’t achieve frame rates that are as high.

The APS Controls Group has been using PV Access to prototype APS Upgrade projects for several years. The new high-speed data acquisition (DAQ) system will depend upon it to achieve the performance required to commission and run the new multi-bend achromat electron accelerator that is at the heart of the APS Upgrade. As part of its Upgrade work, the Group is developing a PV Access client program called the “C2 Data Viewer” (Fig. 1) to display camera images and other complex data structures from the DAQ.

Contact: Andrew N. Johnson (anj@anl.gov)

This research used resources of the Advanced Photon Source, a U.S. Department of Energy (DOE) Office of Science User Facility operated for the DOE Office of Science by Argonne National Laboratory under Contract DE-AC02-06CH11357.

Making Fine Pictures from Coarse Data

Next-generation synchrotrons will be able to produce useful x-ray fluxes at energies greater than 50 keV. Coherent diffraction imaging using such x-rays can penetrate dense materials to probe lattice distortions and defects of embedded grains and nanoparticles. But the downside is that the short wavelength of these x-rays results in diffraction patterns that are spatially compressed, compared to current measurements, and harder to resolve. Researchers have devised a mathematical treatment that can take data from high-energy diffraction studies to yield information on fringes that can be analyzed in the usual way. A computer simulation demonstrates the validity of the method. Going from x-rays with energies of around 10 keV, typical of coherent diffraction measurements today, up to 50 keV compresses the spatial extent of diffraction patterns by the same factor. In principle, moving the detectors five times further away from the scattering site would allow the same resolution to be achieved, but such an adjustment is impractical in environments with limited space. A team of researchers, with an assist from the APS, developed a practical method for analyzing diffraction fringes produced by high-energy x-rays such as those produced by the APS. The team accomplished this through a combination of carefully controlled detector movements and the mathematical optimization of the output from the detector utilized at an x-ray beamline to collect data from the interaction of x-ray beam and the sample being studied.

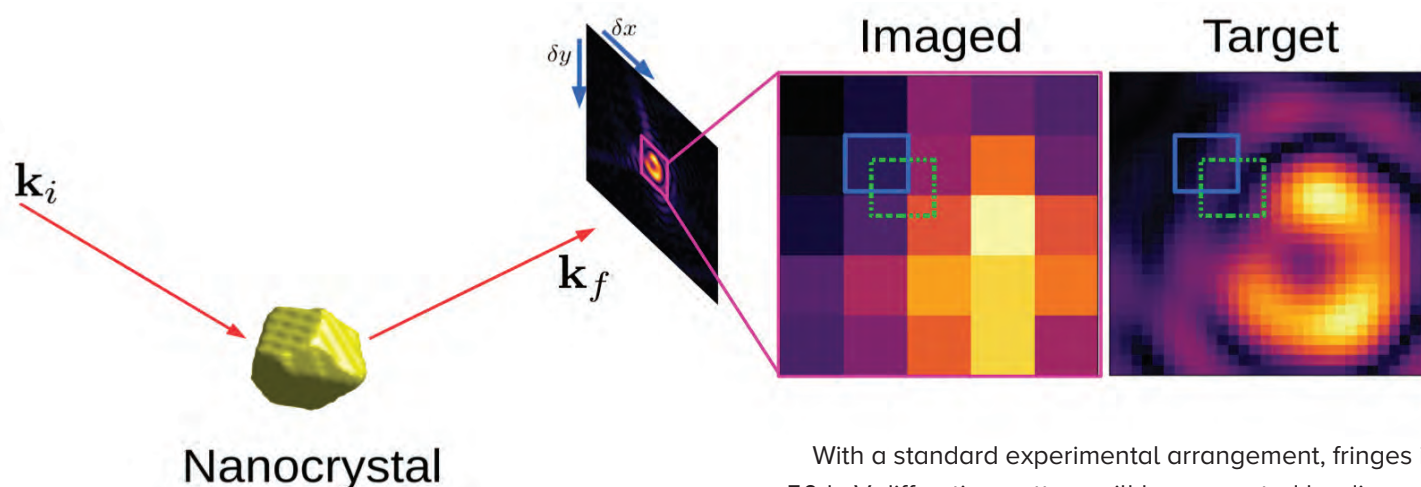


Fig. 1. The x-ray diffraction pattern from a nanocrystal is poorly captured when the pixel size is large compared to the scale of fringes in the pattern (“Imaged”). By shifting the detector through sub-pixel increments, indicated by the blue (solid line) and green (dashed line) squares, the pixels aggregate different parts of the diffraction pattern. Suitable processing of the data can then yield a pattern with greatly improved resolution (“Target”). Figures from S. Maddali et al., *Sci. Rep.* **8**, 4959 (2018).

With a standard experimental arrangement, fringes in a 50-keV diffraction pattern will be separated by distances smaller than the pixel size of the detector. Each data point will be intensity-averaged over some patch of the diffraction pattern. The researchers, from Northwestern University and Argonne, note that it is possible to get around this difficulty by repeatedly moving the detector through a distance smaller than the pixel size, so that each data point samples a distinct patch of the pattern (Fig. 1). However, this method alone does not provide enough information to fully recreate the diffraction pattern that would have been recorded by a detector with spatial resolution equal to the sub-pixel increment of the detector movements — there are more unknown pixel val-

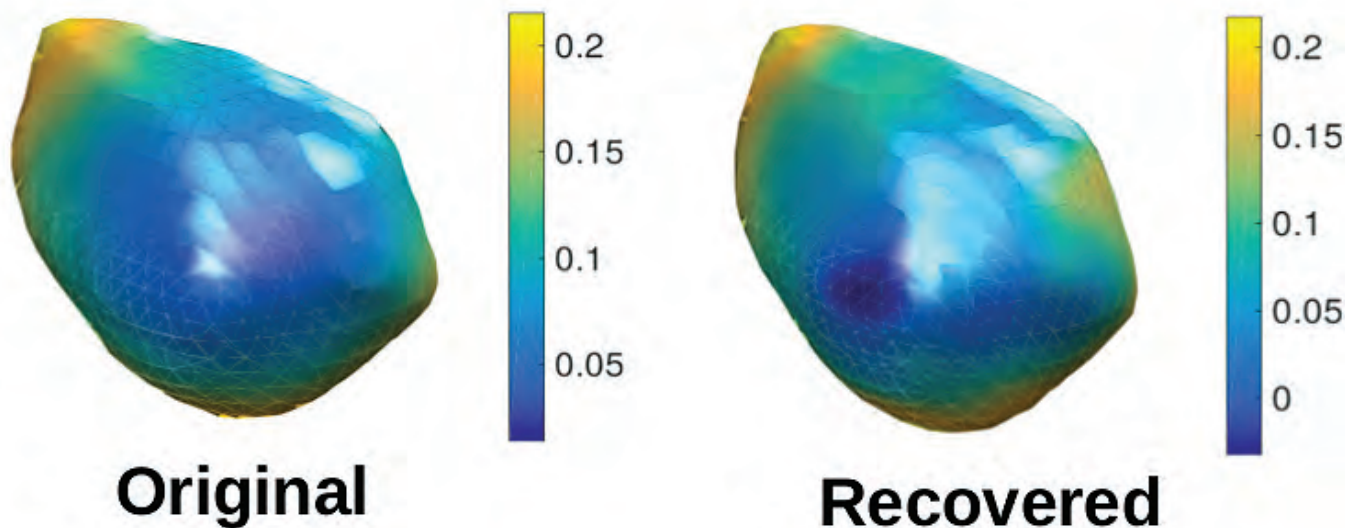


Fig. 2. An algorithm for treating sparsely sampled data, subject to an optimization constraint that embodied the limited bandwidth of the diffraction pattern, produced an image of a simulated nanoparticle very close to the original.

ues at the higher resolution than there are data points to solve for them.

To simplify the technique and make it practical, the researchers exploit an additional property of such experiments: When the object of interest is a sample of limited size, the detector output is bandwidth-limited. To put that another way, a Fourier transform of the data will be sparse, in the sense that the desired information is contained in a limited number of Fourier components, the uninteresting ones being zero. As a result, it is possible to capture data from a relatively small number of detector positions and analyze it with standard algorithms for processing sparse data, with the additional constraint that the number of null Fourier components should be maximized.

As a demonstration, the team carried out a simulation to generate and detect a diffraction pattern from a small, irregularly shaped particle in empty space. For a certain pixel size, the simulation represented scattering of 9-keV x-rays and yielded data comparable to a real experiment. By combining the same signals in bins of six times the size, the simulation instead represented scattering of 54-keV x-rays. Similarly, combining different sets of adjacent data bins was equivalent to shifting the detector through a sub-pixel distance (Fig. 2).

The researchers showed that a judicious choice of detector positions yielded a collection of signals that could be processed by an off-the-shelf algorithm for dealing with sparse data. With the solution constrained to have as few non-zero Fourier components as possible,

the method gave a picture of the simulated particle that was very close to the original (see illustration). A good result was obtained from measurements at as few as seven distinct detector positions.

A crucial element of the simulation was that, because the size of the target was known, an optimized set of detector positions could be set in advance. In a real experiment, the researchers imagine that their technique would be combined with other kinds of observation to approximately describe the object of interest so an appropriate, sparse sampling strategy could be designed. Use of this method, in effect, takes away the need for a large experimental space and places the burden of obtaining high-quality results on computational techniques in conjunction with a customized data-sampling procedure.

— David Lindley

See: S. Maddali¹, I. Calvo-Almazan¹, J. Almer¹, P. Kenesei¹, J.-S. Park¹, R. Harder¹, Y. Nashed^{1,2}, and S.O. Hruszkewycz¹, “Sparse recovery of undersampled intensity patterns for coherent diffraction imaging at high X-ray energies,” *Sci. Rep.* **8**, 4959 (2018). DOI: 10.1038/s41598-018-23040-y

Author affiliations: ¹Argonne National Laboratory, ²Northwestern University

Correspondence: * smaddali@anl.gov

Design, simulation, and demonstration of the in-plane detector translation up-sampling framework for high-energy coherent x-ray diffraction was supported by Laboratory Directed Research and Development funding from Argonne National Laboratory, provided by the Director, Office of Science, of the U.S. Department of Energy (DOE) under Contract No. DE-AC02-06CH11357. Adaptation of sparsity-based signal processing methods to coherent diffraction patterns up-sampled via detector translation was supported by the U.S. DOE Office of Science-Basic Energy Sciences, Materials Science and Engineering Division. Phase retrieval of the up-sampled patterns and feasibility estimates were supported by the Advanced Photon Source, a U.S. DOE Office of Science User Facility operated for the DOE Office of Science by Argonne National Laboratory under Contract No. DE-AC02-06CH11357.

How Convolutional Neural Networks Greatly Enhance Low-Dose X-ray Tomography

Transmission x-ray microscopy (TXM) provides highly-detailed three-dimensional (3-D) images of samples at the nanoscale level. Generally speaking, high-resolution images require longer x-ray exposures. However, the structures of some materials are especially vulnerable to x-ray damage. For such radiation-sensitive materials, researchers face the challenge of achieving high-resolution images while preserving sample integrity. One solution is to utilize image-processing techniques that glean more information from short-duration exposures. In this study, researchers applied a deep convolutional neural network (CNN) approach to short-duration (low-dose) tomographic scans for imaging dose-sensitive brain tissue at the nanoscale. CNN is one of the most popular deep-learning techniques because it aims to mimic the feature analysis of the neural networks within animal brains. The researchers applied CNN to both simulated and actual TXM scans. The actual scans were performed on a complex biological sample at the APS. The tests demonstrated a 10-fold improvement in x-ray signal quality as compared to conventional image-processing methods. The resulting signal improvement should enable scientists to obtain images from short-duration tomographic scans that are comparable to those of long-duration scans. Other types of x-ray imaging techniques should also benefit from the CNN processing technique.

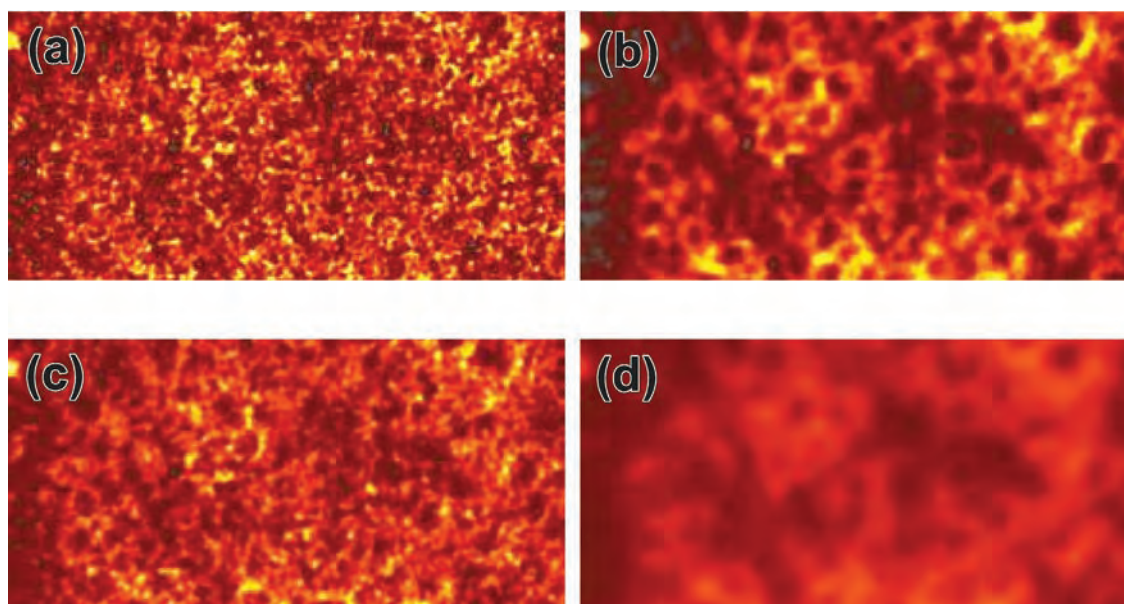


Fig. 1. Images derived from x-ray projections through a small region of mouse brain at 30-nm pixel resolution. All four panels depict the same brain region and utilize low-dose x-ray scanning (2 sec per scan). The image in (a) was reconstructed from low-dose projections without any enhancement, and where it is difficult to discern individual brain structures. In contrast, the CNN-enhanced image in (b) clearly shows individual axon (nerve fiber) cross-sections, and achieves a clarity rivaling images derived from high-dose, 30-sec scans. The bottom two images, (c) and (d), were enhanced using conventional methods. Panel (c) contains lots of noise (artifacts), while (d) is severely blurred. Figures adapted from X. Yang et al., *Sci. Rep.* **8**, 2575 (2018).

Computed tomography (CT) has become a familiar medical imaging technology that is also used to image materials in laboratories and synchrotron facilities. As scientists push for ever-higher CT resolutions, the absorbed radiation dose increases dramatically. These high radiation doses can structurally damage samples, which limits follow-up testing and restricts studies of dynamic processes, such as cell metabolism or battery cycling.

Both hardware and software solutions have been devised to ameliorate radiation damage. The hardware approach involves hardening the sample to reduce x-ray damage from high-dose scans. The most popular hardening method is cryogenic freezing (vitrification), which locks the sample's structure into place. Unfortunately, vitrification prevents observation of dynamic processes, complicates the scanning setup, and severely limits the range of experimental pressures and temperatures.

By contrast, the software approach utilizes low-dose scans to reduce damage. To counteract the poorer images resulting from low-dose scans, scientists attempt to pull more information with an advanced, machine learning-based denoising method from the x-ray projections, which are two-dimensional patterns formed when an x-ray beam passes through a sample. Hundreds of two-dimensional projections, taken from different angles, are typically required for a 3-D tomographic image. A neural network learns through repetition and high-quality datasets that are difficult to obtain at the nanoscale, especially on materials that cannot sustain a high x-ray dose. To circumvent this physical limitation, researchers from Argonne, the Georgia Institute of Technology, The University of Chicago, and Northwestern University utilized a deep CNN on projections rather than full 3-D volumes, since low-noise projections can be recorded with a low dose (~10-sec exposure) whereas low-noise 3-D volumes would necessitate exposing a sample to a much



Fig. 2. An image showing individual myelin sheaths, highlighted with different colors, surrounding mouse-brain axons revealed by the experimental nano-CT scans. The image is derived from the same CNN enhancements of the low-dose x-ray projections that were used to produce the image in Fig. 1b.

higher dose (~10-min exposure). With this approach, it becomes possible to use CNN to produce a map between the image features of a few low-dose and high-dose x-ray projections. Using this map, CNN could then enhance the remaining low-dose projections.

CNN was first applied to purely synthetic (computer-generated) data. The simulation randomly distributed nanoscale-sized balls throughout a microscopic cube. Hundreds of simulated high-dose x-ray projections were then computed. Subsequently, hundreds of low-dose projections were produced by introducing noise into the high-dose projections. Once CNN learned the differences between a few low-dose/high-dose pairs, it was used to

“Neural” cont’d. on page 127

The APS Data Management System

Data are essential to the scientific discoveries enabled by experiments performed at the APS. At present, the APS generates an estimated 10 PB of raw experimental data per year. Data volumes and rates continue to quickly increase due to beamline advances such as improved detectors, high-throughput instrumentation, and multi-modal instruments that can acquire several measurements in a single experiment. This trend is expected to continue in the future and will be accelerated by the improved source and instruments that are part of the APS Upgrade Project. Successful management of data is of particular importance to the current and future scientific productivity of the APS.

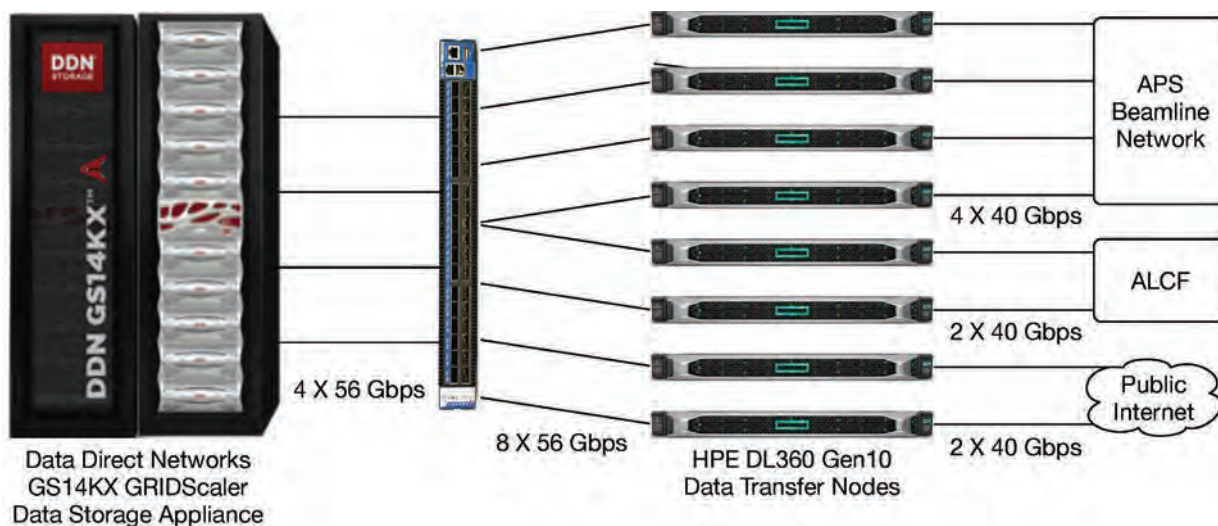


Fig. 1. Pictorial diagram of APS Data Management System logical connections. A storage system in the APS computer room provides 3.6 PB of storage space for the APS. APS Data Management System tools are currently deployed on 27 APS beamlines to automate the transfer, organization, and distribution of data on this system. APS users and collaborators can access data from off-site using Globus Online.

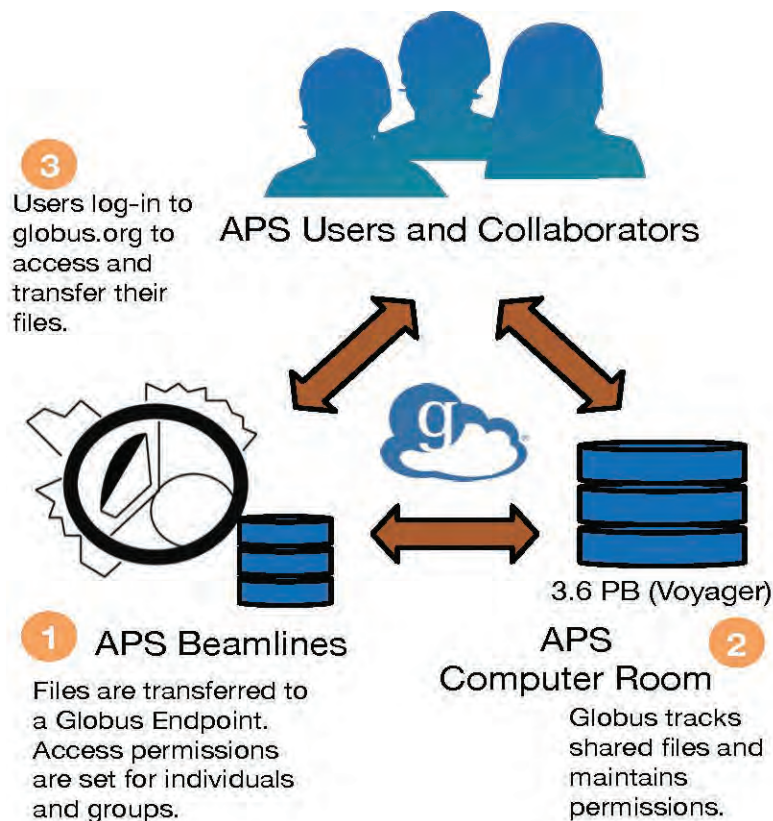


Fig. 2. The APS Data Management System storage infrastructure. A Data Direct Networks storage appliance with 3.6 PB of usable storage connects to an InfiniBand switch. Four data transfer nodes link the storage to the beamline network, two data transfer nodes connect the storage to the Argonne Leadership Computing Facility, and two data transfer nodes provide links to the public Internet.

The APS is adopting more automated and consistent approaches to managing data across its wide array of beamlines. The APS Data Management System (Fig. 1) is a set of software and hardware infrastructure that automates the organization, transfer, storage, and distribution of data collected at the APS.

- Beamline data-acquisition systems are monitored for the generation of new files that feed the data workflow.
- Data files are automatically copied from acquisition systems to a central storage system.
- A metadata catalog tracks user and experiment information along with information such as file checksums.
- Access permissions are set based on user information from the APS proposal and safety databases.
- A processing service supports user-defined data workflows and automated data processing tasks.

Experimenters and staff at the APS may interact with the system via a web portal, graphical user interface,

command line tools, or an application programming interface. Users can download data at their home institutions using the Globus Online data transfer tool.

To date, this system has been successfully integrated at 27 APS beamlines.

These capabilities are backed by a new, high-performance data storage infrastructure shown in Fig. 2. The APS installed a Data Direct Networks GS14KX GRIDScaler appliance in its main computer room. Its current configuration, consisting of 1 controller unit and 5 drawers of 450 disks, provides approximately 3.6 PB of usable storage. When fully populated with 20 drawers of 1800 disks, the system will host approximately 15 PB of usable storage. Additional controllers and disks may be added to further expand capacity.

An InfiniBand switch connects the storage system to a cluster of eight high-speed data transfer nodes that provides access to the storage appliance. The Data Direct

“Data” cont’d. on page 127

Variable X-ray Focal Spot Sizes for Kirkpatrick-Baez Mirrors Using Compound Refractive Lenses

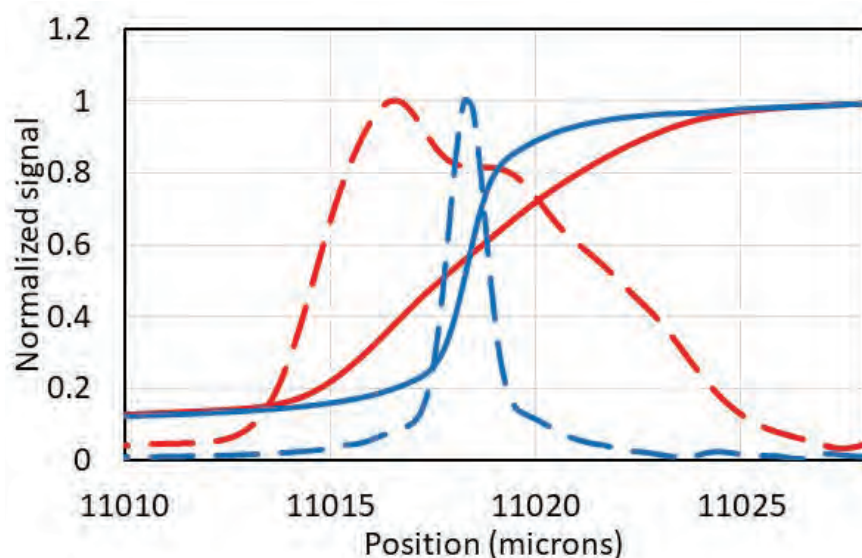


Fig. 1. The solid lines are knife-edge scans across the K-B-focused beam with (red) and without (blue) the CRL. The dashed lines are derivative curves showing more directly the beam size.

Kirkpatrick-Baez (K-B) mirrors are popular optics for focusing x-rays to micron-level spots. These small beams can be used to image complex samples in scanning fluorescence microprobes. Since the optics are achromatic, research with the micro-x-ray absorption near-edge structure and micro-x-ray absorption fine structure synchrotron research techniques can then be carried out on interesting regions by scanning the incident energy. If the interesting regions are few and far between it can be necessary to scan large areas of a sample. This can be time consuming with a micron-sized beam. Therefore, users often request a zoom capability or variable focus for the microprobe. There are several methods for reproducibly expanding the beam size. The sample can be moved upstream or downstream, but this would require moving detectors that are focused on the sample. The mirror angle or bending can be changed, but this can also move the focus on the sample. A common approach is to have an intermediate focus as the source point for the K-B mirrors; then the K-B focus can be changed by using slits to change the intermediate focus. However, with the advent of brighter sources such as the APS Upgrade, this can be inefficient. For such sources it is possible to focus the entire beam to sub-micron spots. Thus, using slits to control the size would result in beam loss for larger sizes.

This work demonstrated that compound refractive

lenses (CRLs) can be used to reproducibly change the beam size on the sample without moving the center of the beam. The CRL creates a new effective source point for the K-B mirror, expanding the focus. Figure 1 shows an example for a CRL placed close to the standard K-B mirrors at APS beamline 20-ID. In this case, the nominal 1- μm focus is expanded to approximately 9 μm with the insertion of the lens. The amount of expansion can be easily estimated and selected by knowing the x-ray energy and number of lenses.

A downside of the CRL is their energy dependent properties. However, most experiments would only use the expanded beam in survey mode and switch back to the small achromatic beam for spectroscopy. This switch can be made in a few seconds.

Contact Steve M. Heald (heald@anl.gov)

See: Steve M. Heald* and Eric M. Dufresne, "Using refractive lenses to provide a variable spot size for Kirkpatrick-Baez mirrors," *J. Synchrotron Rad.* **25**(5), 1514 (2018).

DOI: 10.1107/S1600577518010603

Author affiliation: Argonne National Laboratory

Correspondence: * heald@aps.anl.gov

This research used resources of the Advanced Photon Source, an Office of Science User Facility operated for the U.S. Department of Energy (DOE) Office of Science by Argonne National Laboratory, and was supported by the U.S. DOE under Contract No. DE-AC02-06CH11357.

“Neural” cont’d. from page 123

enhance all the remaining low-dose projections. Even for the low-dose projections with the highest noise level (30%), CNN improved their resolution to nearly that of the high-dose projections.

Nano-CT experiments were performed with the TXM at XSD beamline 32-ID of the APS to further confirm the efficacy of CNN enhancement. The sample was a portion of mouse brain, radiation-hardened with plastic. Several high-dose x-ray projections, each formed from a 30-sec exposure, were taken from various angles. Afterward, 361 low-dose projections (lasting 2 sec each) were recorded.

The computations were carried out on Cooley, a GPU cluster at the Argonne Leadership Computing Facility. With 48-T K80 dual-GPU nodes, the computing time of the data enhancement procedure can be reduced to less than 10 min for most of the tomographic scanning with full-size resolution data. After training with a few pairs of low-dose/high-dose projections, CNN enhanced the resolution of several hundred low-dose projections to nearly that of the high-dose projections. Figure 1 compares tomographic images derived from the raw low-dose projections to images derived from enhanced low-dose projections using two conventional methods and CNN. The CNN-enhanced image is by the far the best, and was used to reconstruct the myelinated mouse brain axons in Fig. 2.

This study demonstrated that CNN can produce high-quality CT images from low-dose scans. Moreover, since a low-dose scan is simply a short-duration scan, CNN processing should enable improved 3-D imaging of dynamic (quickly-occurring) processes. CNN should also benefit other types of x-ray imaging, such as x-ray fluorescence and ptychography. — Philip Koth

See: Xiaogang Yang^{1*}, Vincent De Andrade¹, William Scullin¹, Eva L. Dyer², Narayanan Kasthuri^{1,3}, Francesco De Carlo¹, Doga Gürsoy^{1,4}, “Low-dose x-ray tomography through a deep convolutional neural network,” *Sci. Rep.* **8**, 2575 (2018). DOI: 10.1038/s41598-018-19426-7

Author affiliations: ¹Argonne National Laboratory, ²Georgia Institute of Technology, ³The University of Chicago, ⁴Northwestern University

Correspondence: * dgursoy@anl.gov

This research used resources of the Argonne Leadership Computing Facility, which is a U.S. Department of Energy (DOE) Office of Science User Facility supported under Contract DE-AC02-06CH11357. This research used resources of the Advanced Photon Source, a U.S. DOE Office of Science User Facility operated for the DOE Office of Science by Argonne National Laboratory under Contract No. DE-AC02-06CH11357.

“Data” cont’d. from page 125

Networks controller connects to the switch via four 56-Gbps InfiniBand links. Each data transfer node connects to the switch via its own 56-Gbps InfiniBand link, and to the larger facility network via its own 40-Gbps Ethernet link. Four data transfer nodes connect to the internal beamline network and are dedicated for fast data transfers from beamline data acquisition devices. Two data transfer nodes are reserved for data transfer between the APS and the Argonne Leadership Computing Facility over a dedicated network path. The other two data transfer nodes are dedicated for data transfers over the public Internet.

The maximum performance of the system is approximately 30 GB/s of aggregate file I/O. The General Parallel File System provides a robust POSIX-compliant file system. It maintains the high-performance characteristics of the underlying hardware needed to accommodate the wide variety of data access patterns that experiments perform and that the many APS beamlines demand.

The APS Data Management System will continue to be deployed at more beamlines in the coming years. Based on feedback, these resources will be improved with new features and capabilities. The APS is now better equipped to realize the data management tasks critically needed to deal with the deluge of data the APS Upgrade will produce.

Contact: Sinisa Veseli (sveseli@anl.gov),
Dariusz Jarosz (djarosz@anl.gov),
Roger Sersted (rs1@anl.gov),
Dave Wallis (wallis@anl.gov), and
Nicholas Schwarz (nschwarz@anl.gov)

Many helped to make this work possible: William Allcock (Argonne Leadership Computing Facility); Jonathan Almer, Francesco De Carlo, Ian Foster, Barbara Frosik, Arthur Glowacki, Doga Gürsoy, Chris Jacobsen, Peter Kenesei, Faisal Khan, Dave Leibfritz, Wenjun Liu, Suresh Narayanan, Michael Papka, Jun-Sang Park, Brian Pruitt, Brian Robinson, Ken Sidorowicz, Jonathan Tischler, Brian Toby, Stefan Vogt, and Ruqing Xu (all APS); Rachana Ananthakrishnan (Argonne/The University of Chicago), Connor Horn and Prithvi Ramanathan (APS summer students), and Collin Schmitz (APS co-op student).

Funding for this work is supported by the U.S. Department of Energy Office of Science-Basic Energy Sciences, Contract No. DE-AC02-06CH11357.

Development of a Kappa Diffractometer for Intermediate X-ray Energies at APS Beamline 29-ID

An ultra-high vacuum, non-magnetic kappa geometry diffractometer has been designed and commissioned for the resonant soft x-ray scattering (RSXS) branch of the XSD Intermediate Energy X-ray (IEX) beamline 29-ID at the APS. There were three main design goals for this diffractometer: kappa geometry, non-magnetic, and high-precision. The kappa geometry was chosen to allow for a large q-range and space for a sample environment (electric or magnetic fields). Non-magnetic components were used for all the components above and including the κ -arm to avoid disturbing magnetic or electric fields during experiments. Lastly, the diffractometer precision requirement of a sphere of confusion (SOC) of less than $50\ \mu\text{m}$ was a key driving factor for this instrument in terms of rotation stages and machining precision.

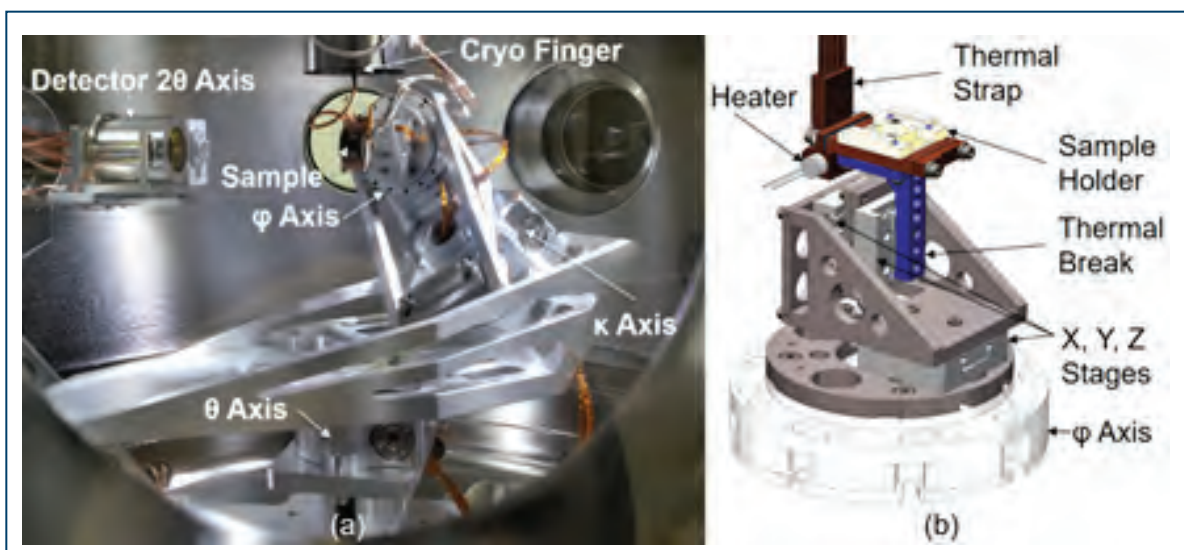


Fig. 1. (a) Image of the commissioned kappa diffractometer inside the RSXS vacuum chamber on the APS 29-ID beamline with the main components identified. (b) A close up model of the components above the ϕ axis. The model also shows the new thermal break and thermal strap.

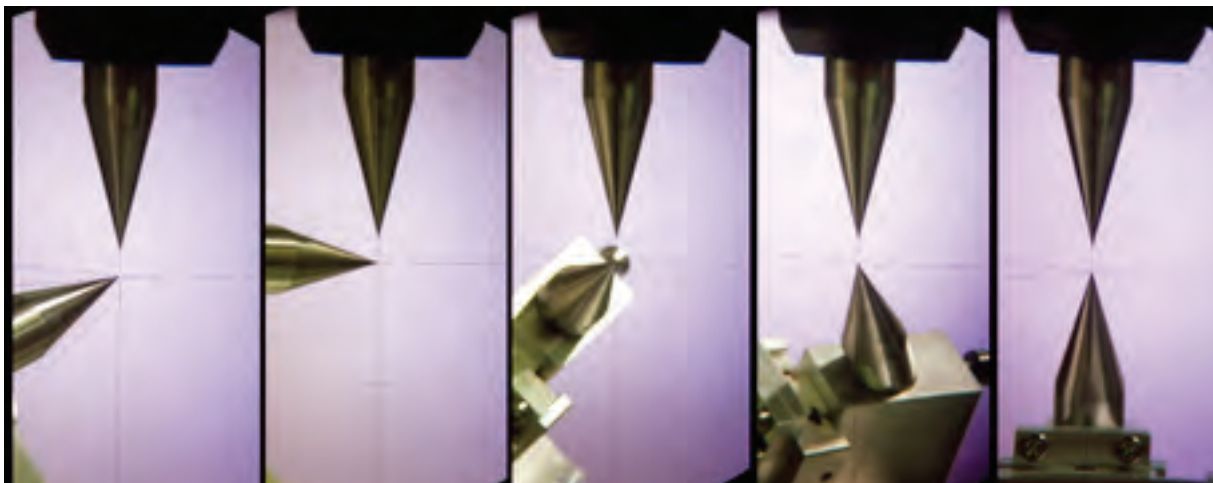


Fig. 2. Images through the alignment telescope during simultaneous rotation of the θ axis through 120° and 360° rotation of both κ and ϕ axes. The bottom pin represents the sample position and the top pin the 2θ axis, which supports the detector.

The complete diffractometer can be seen in Fig. 19(a), shown installed into the RSXS UHV vacuum chamber at 29-ID. The precise SOC ($< 50 \mu\text{m}$) requirement drove the design method. In order to reach this goal, it was decided that a combination of precision machining, Finite element analysis, and stage precision would be used instead of calibrating an error-correction table. This has the advantage that the upper bound of the SOC requirement can be achieved without any control hardware, making the device more robust.

The main arms of the θ and κ axes were machined from a single solid block of 6061 aluminum, which was then hardened to 6061-T6 to further add dimensional stability. Machining was performed on a high-precision, 5-axis milling machine with subsequent measurement in a coordinate measurement machine to ensure that the critical mounting planes were within $1 \mu\text{m}$ of the convergence point of the axes. Even with the high-precision machining, distortion from gravity had to be accounted for once the arms were loaded. Iterative finite-element analysis and balancing resulted in the complex shape shown for the arms. The side braces counteracted the loading distortion and kept the accuracy of the mounting planes. Lastly, the rotation stages for axes θ and κ (PRS-110, Physik Instrumente GmbH & Co.), and ϕ (SR-7021, SmarAct GmbH) were chosen based on their wobble, flatness, and runout precision.

Commissioning of the diffractometer was conducted in several phases: assembly and alignment in a clean room, followed by installation into the vacuum chamber, a second alignment to confirm the SOC was maintained,

and cryogenic cooling of a test sample to 27 K. Alignment was performed using optical alignment telescopes and precision pins located at the convergence of axes. The final alignment accuracy can be seen in Fig. 2, which shows images of various rotation positions. The resolution of the alignment scope was $25 \mu\text{m}$; therefore, the SOC achieved was less than $25 \mu\text{m}$, a factor of 2 better than the design requirement.

Currently, the diffractometer is going through a slight upgrade of the cryogenic and thermal components. The new components can be seen Fig 1(b); these include a thicker thermal strap to reach sample temperatures of $\leq 20 \text{ K}$, a new thermal break made from Vespel® SP-1, and a redesigned cooling finger extension for better conductance and temperature measurement. Compared to the previous MACOR® thermal break, the new thermal break has a lower thermal conductivity above 1 K and is safer to use near x-rays in terms of maintaining the vacuum environment due to the release of fluorocarbons. Future plans also include pushing the SOC down to $5 \mu\text{m}$ by way of laser alignment or calibration of error correction tables.

Contact: Steven P. Kearney (skearney@aps.anl.gov)

See: Steven P. Kearney, Deming Shu, Fanny Rodolakis, Dohn Arms, Pete Jemian, and Jessica McChesney, "Mechanical design of a UHC non-magnetic kappa diffractometer," AIP Conf. Proc. **2054**, 060039. (2019). DOI: 10.1063/1.5084670

Author affiliation: Argonne National Laboratory

The authors would like to acknowledge Michael McDowell, Keenan Lang, and Joerg Stremper of XSD for their help in commissioning this instrument, and the team at A.J.R. Industries, Inc., for the manufacturing effort. This work was supported by the U.S. Department of Energy Office of Science-Basic Energy Sciences, under Contract No. DE-AC02-06CH11357.

The Mechanism of Hemoglobin-ligand Allostery is Not a Closed Case

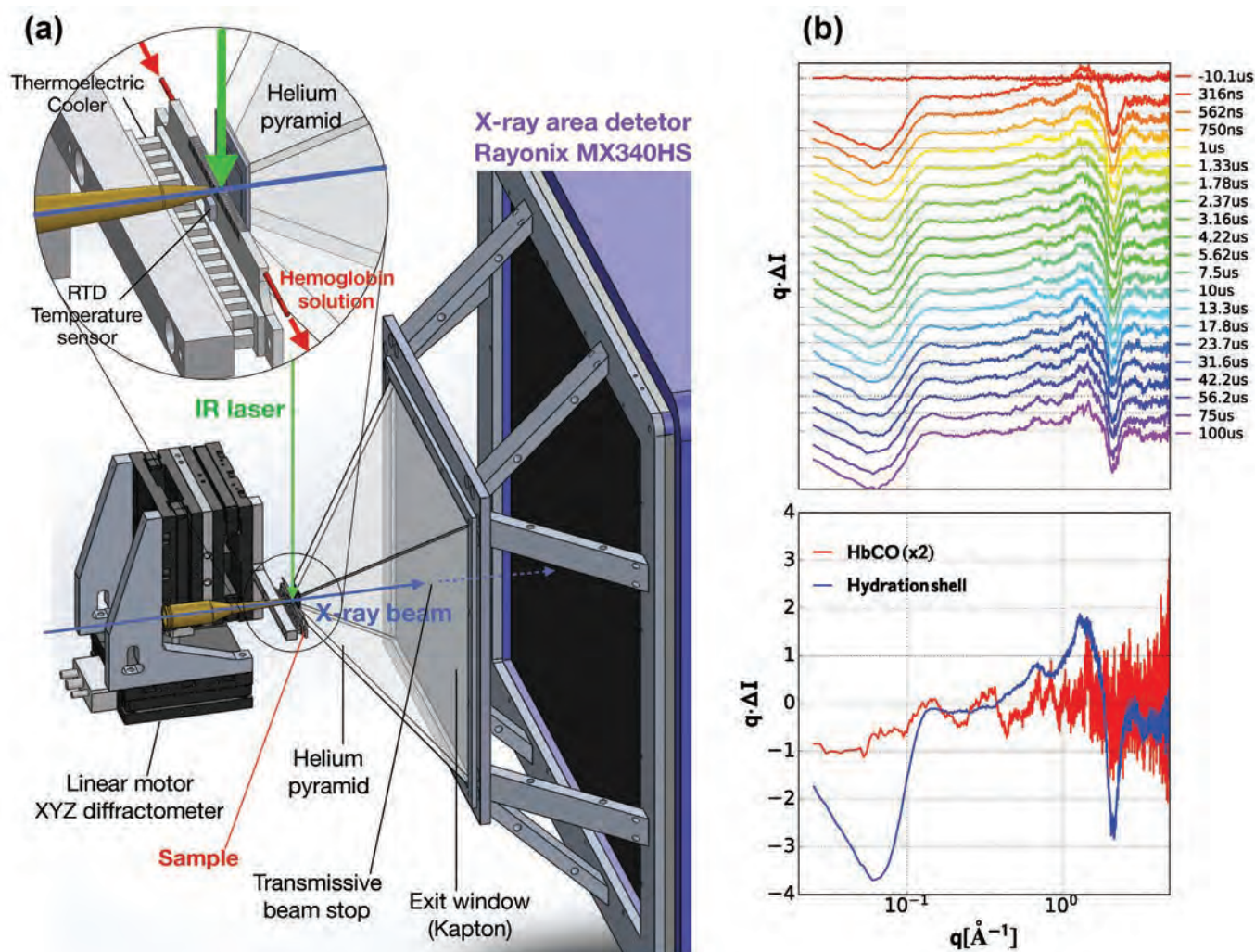


Fig. 1. Time-resolved SAXS/WAXS infrastructure used to track x-ray scattering of hemoglobin following a T-jump. (a) The sample capillary is held in a temperature-controlled, slotted beryllium-oxide ceramic support that is positioned with a high-speed linear motor XYZ diffractometer. A downward directed infrared laser pulse (<10 ns) is focused on the sample capillary and triggers a sudden T-jump. A suitably-delayed, short-duration burst of x-rays pass through the heated sample with its scattered photons traversing a helium-purged pyramid before impinging on an x-ray detector. (b) The time-resolved scattering patterns (upper panel) can be decomposed (lower panel) into contributions that reflect temperature-dependent scattering changes arising from the HbCO and its hydration shell. The time-dependent changes observed from the HbCO contribution arise from changes in the relative populations of at least two different R quaternary structures, and unveil for the first time the time scale for this quaternary conformational transition.

Hemoglobin is one of the most well-known and studied proteins in the human body and is responsible for transporting oxygen from the lungs to the rest of the body as part of a process called aerobic respiration. It is also capable of binding and transporting carbon monoxide and nitrous oxide. The mechanism by which hemoglobin binds these target molecules and the protein's resulting structural changes has been studied since the mid-1800s and is used as a model for studying other proteins that exhibit a similar structure-function relationship. Recently, scientists built new infrastructure that helped reveal the underlying complexities of the hemoglobin-ligand binding model. Using the APS, the researchers were able to observe a change in x-ray scattering following a temperature jump for carbon monoxide-bound hemoglobin vs. non-bound hemoglobin. These results, which give scientists a deeper mechanistic understanding of the hemoglobin model, will help inform future discoveries about how other important allosteric proteins work in the body as well.

At a simplistic level, the current conformational model for hemoglobin assumes two different states: "Tense" or "T-State," referring to the conformation of the non-bound hemoglobin protein; and "Relaxed" or "R-State," referring to the conformation where the target molecule is bound to the iron atoms in the hemoglobin structure. Binding or release of the target molecules results in a cooperative transition between the two different conformational states (i.e., $R \leftrightarrow T$), which significantly alters its ligand-binding affinity. However, recent time-resolved spectroscopic studies provided an indication that the kinetics did not follow a clean $R \leftrightarrow T$ transition, but instead indicates some amount of R-State heterogeneity due to an allosteric intermediate that is not accounted for in the traditional model. Furthermore, no structurally equivalent study is available to properly interpret the complex kinetics uncovered in the time-resolved spectroscopic study.

To address this issue, a team of researchers, from the National Institutes of Health, Argonne, and The University of Chicago, developed the capabilities required to pursue time-resolved small- and wide-angle x-ray scattering (SAXS/WAXS) studies of proteins following a temperature jump (Fig. 1). These experiments were conducted at the BioCARS 14-ID beamline at the APS, which, after infrastructure improvements, has the capability to investigate structural dynamics in proteins on time scales as fast as 100 psec. The temperature jump is a critical aspect to the experimental design because the scattering pattern of a protein in solution is very sensitive to changes in the protein's size and shape. Since increasing the temperature alters the relative population of different protein conformations, time-resolved SAXS/WAXS following a temperature jump provides the researchers with the ability to probe the dynamics of these structural changes in hemoglobin.

The researchers provide proof-of-concept for this new approach for studying allosteric proteins. Using carbon monoxide bound hemoglobin (carbonmonoxyhemoglobin,

HbCO) for the study, the researchers evaluated the kinetics of a quaternary structure transition. The change in x-ray scattering observed following the temperature jump for the carbon monoxide bound hemoglobin vs. non-bound hemoglobin provided unambiguous evidence for more than one R-State in HbCO, but only one T-State in the non-bound hemoglobin state.

According to the researchers, this new approach to understanding allosteric proteins presents a crucial opportunity to reinterpret the complex kinetics of the $R \leftrightarrow T$ transition with a model that accounts for R-State heterogeneity. Additionally, correlating structural signatures from this study with those of known crystal structures for HbCO can provide a better understanding of the structural identity of these R-States. But most importantly, improving our understanding of the allostery mechanism for hemoglobin will improve our understanding of all allosteric proteins and, by relation, our understanding of the mechanism for some of our most fundamental biological pathways. — Alicia Surrao

See: Hyun Sun Cho¹, Friedrich Schotte¹, Valentyn Stadnytskyi¹, Anthony DiChiara², Robert Henning³, and Philip Anfinrud^{1*}, "Dynamics of Quaternary Structure Transitions in R-State Carbonmonoxyhemoglobin Unveiled in Time-Resolved X-ray Scattering Patterns Following a Temperature Jump," *J. Phys. Chem. B* **122**, 11488 (October 4, 2018). DOI: 10.1021/acs.jpcc.8b07414

Author affiliations: ¹National Institutes of Health, ²Argonne National Laboratory, ³The University of Chicago

Correspondence: * anfinrud@nih.gov

This research was supported by the Intramural Research Program of the National Institute of Diabetes and Digestive and Kidney Diseases, National Institutes of Health. Use of BioCARS was supported by the National Institutes of Health, National Institute of General Medical Sciences Grant R24GM111072. The time-resolved setup at Sector 14 was funded in part through a collaboration with Philip Anfinrud (NIH/NIDDK). This research used resources of the Advanced Photon Source, a U.S. Department of Energy (DOE) Office of Science User Facility operated for the DOE Office of Science by Argonne National Laboratory under Contract DE-AC02-06CH11357.

Bringing Hybrid MBE Thin-Film Growth and Characterization to the APS

Researchers recently designed, constructed, installed, and tested a portable metalorganic gas delivery system intended to interface with an existing molecular beam epitaxy (MBE) chamber at the APS, thus upgrading the MBE chamber to a hybrid molecular beam epitaxy (HMBE) system. HMBE is a powerful thin-film growth technique capable of accessing a wider variety of metal cations than conventional MBE while facilitating more rapid synthesis of complex oxide films, often with fewer compositional defects. The HMBE instrument is connected directly to a 6-circle surface x-ray diffractometer to permit the *in situ* application of several surface x-ray diffraction (SXRD) techniques in order to achieve a deep understanding of the atomic-scale mechanisms that take place during oxide crystal growth. These techniques include grazing incidence x-ray scattering and spectroscopy, measurement of crystal truncation rods and fractional-order peaks, and diffuse scattering, all of which can be applied to films consisting of only a few atomic layers. Exploiting these techniques can determine crystal structure on multiple length scales to reveal defects, surface reconstructions, island sizes, and domains, while the *in situ* capabilities allow these features to be observed as they evolve.

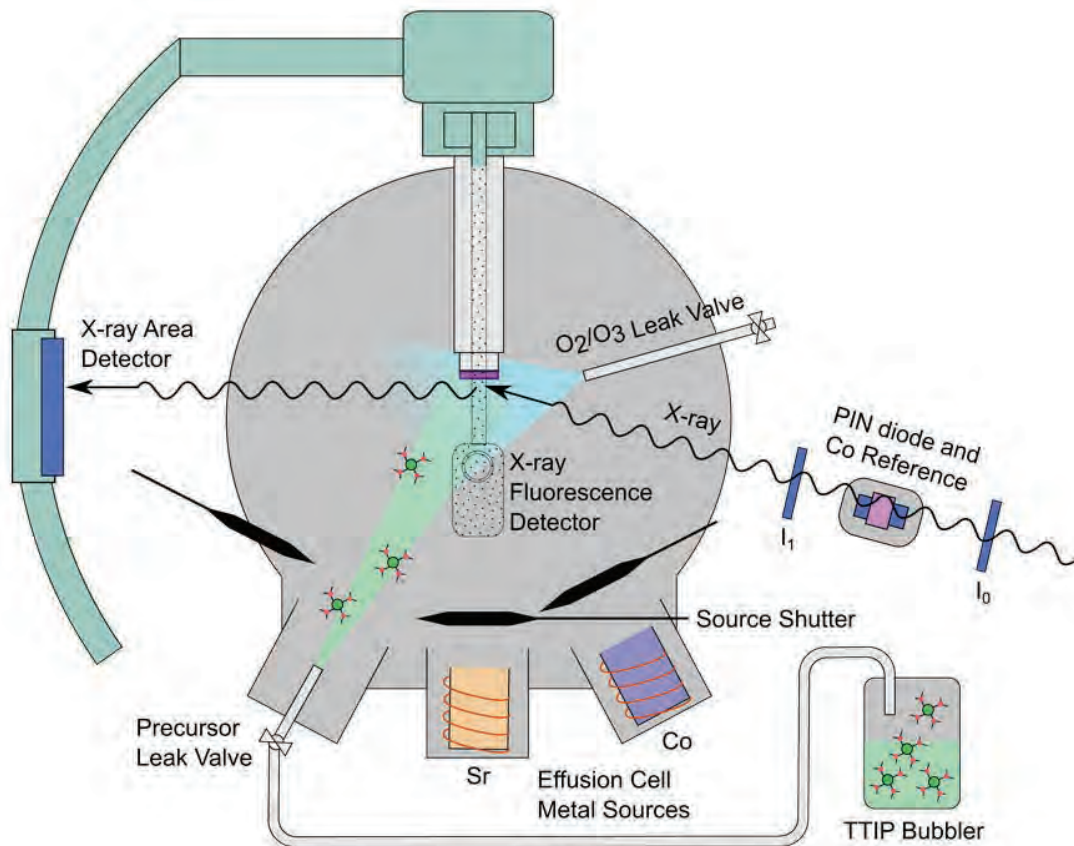


Fig. 1. Schematic of HMBE gas delivery system interfaced with the Sector 33-ID-E MBE system as configured for growth of oxide films containing Sr, Ti, Co, and O and *in situ* x-ray diffraction as well as x-ray fluorescence of the Co K edge.

Thin films of oxide materials are being used increasingly in diverse applications such as gas sensing, solid oxide fuel cells, electrochemical supercapacitors, solar cells, catalysis, and resistive switching, thus prompting the development of HMBE, which uses both gas metalorganic precursors and solid metal sources in the form of traditional effusion cells. HMBE has multiple advantages over conventional MBE for oxide synthesis. The high volatility of the metalorganic precursors allows for high growth rates, improved flux stability, and adsorption-controlled growth, which lead to unprecedented stoichiometry control. Additionally, HMBE avoids reliance on the extreme deposition conditions created by the introduction of ozone or an oxygen plasma to maintain stoichiometry, as many metalorganic compounds contain the necessary oxygen as ligands. This is particularly valuable in the deposition of ternary oxides such as perovskite oxides (ABO_3) when the elementary metals (A and B) differ significantly in oxidation potential.

The combined HMBE system (Fig. 1) at XSD x-ray beamline 33-ID-E at the APS was first tested using the metalorganic precursor titanium isopropoxide (TTIP) to grow thin films of TiO_2 , which were characterized *in situ* using SXRD techniques. Testing then continued with the growth and *in situ* characterization of $SrTiO_3$ films (again at 33-ID-E), which were grown using TTIP and strontium (Sr) from an effusion cell. Figure 2 shows specular CTR differences after growth of $SrTiO_3$ films using two different Sr fluxes. These experiments showed that the HMBE chamber works well with the instrument's *in situ* SXRD capabilities in investigating a variety of processes that occur during oxide thin-film growth.

This unique instrument supports the use of a wide range of metalorganic precursors and solid metal sources, permitting *in situ* studies of many different complex oxides. It is also possible to monitor specific diffraction conditions with high precision that are challenging or impossible to track with reflection high-energy electron diffraction (RHEED). Planned studies exploiting the unique capabilities of this system will focus on understanding oxide thin-film growth dynamics. Data from these experiments will be compared to those from *in situ* RHEED measurements, ultimately providing a more complete picture of thin-film synthesis and interfacial evolution. These studies will also be used to investigate the potential of HMBE as a method for producing high-quality films for next-generation oxide devices. As this hybrid system was designed with portability in mind, it also can be coupled to other existing (and future) film growth setups, such as a

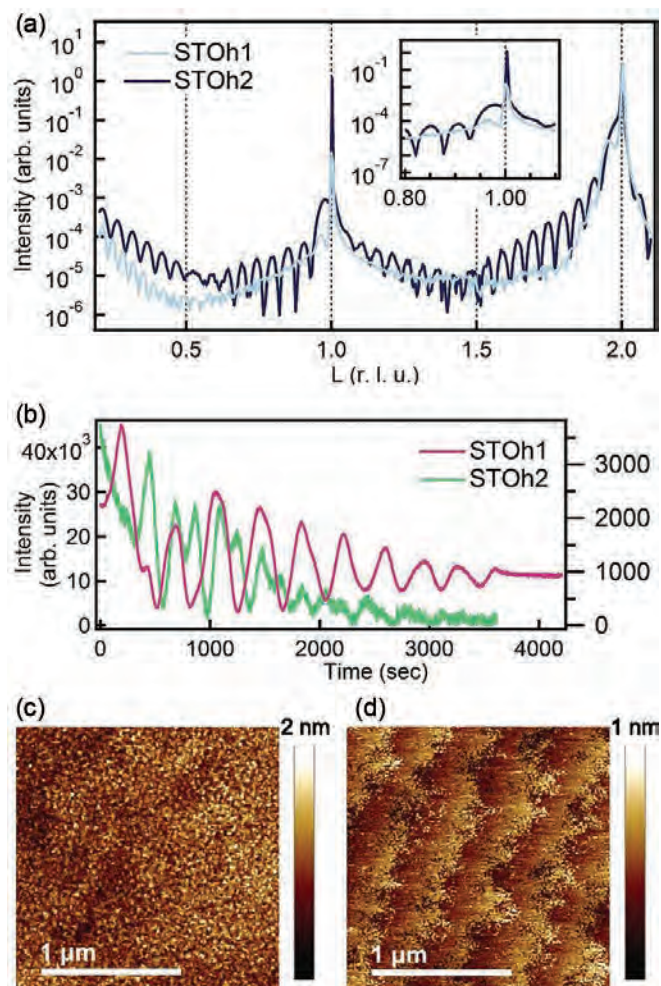


Fig. 2. Room-temperature results for two $SrTiO_3$ films grown at $750^\circ C$ with 110 mTorr TTIP under Sr fluxes of 2.35×10^{12} atoms/cm² sec (STOh1) and 2.67×10^{12} atoms/cm² sec (STOh2). (a) X-ray scattering along the specular $0\ 0\ L$ direction at room temperature. (b) Scattered x-ray intensities measured during growth at $750^\circ C$ at the reciprocal lattice position $H\ K\ L = 0\ 0\ \frac{1}{2}$ r.l.u. (c) (d) Room-temperature $2\ \mu m \times 2\ \mu m$ atomic force microscopy micrographs of the films (c) STOh1 and (d) STOh2.

pulsed laser deposition system, to provide an alternative-source capability. — Vic Comello

See: Tassie K. Andersen^{1,2*}, Seyoung Cook^{1,2}, Erika Benda¹, Ha-woong Hong¹, Laurence D. Marks², and Dillon D. Fong¹, "Development of a hybrid molecular beam epitaxy deposition system for *in situ* surface x-ray studies," Rev. Sci. Instrum. **89**, 033905 (2018). DOI: 10.1063/1.5008369

Author Affiliations: ¹Argonne National Laboratory, ²Northwestern University

Correspondence: * Tassie_Andersen@amat.com

T.K.A., S.C., and D.D.F. were supported by the U.S. Department of Energy (DOE) Office of Science-Basic Energy Sciences. This research used resources of the Advanced Photon Source, a U.S. DOE Office of Science user facility operated for the DOE Office of Science by Argonne National Laboratory under Contract No. DE-AC02-06CH11357.

Extending Multispeckle X-Ray Photon Correlation Spectroscopy to Sub-Microsecond Timescales

X-ray photon correlation spectroscopy (XPCS) measures spontaneous thermal and quantum fluctuations at the nanoscale in condensed matter. As such, it is a probe of the complex energy landscape of emergent functional materials, providing knowledge about their potential applications. Keys to performing such measurements are a partially coherent x-ray beam and a high-frame-rate area detector with spatial resolution sufficient to resolve the finely-featured interference pattern that is obtained when making such measurements. The upcoming APS Upgrade (APS-U) makes the need for high-frame-rate detectors especially acute because the tremendous gains in coherent flux will, in principle, increase the best time resolution of XPCS by 4 orders of magnitude, allowing measurements of nanoscale fluctuations in aqueous environments such as those relevant to biochemical function [1]. To achieve such gains in practice, however, requires detectors with frame rates far higher than those available from commercially available pixel-array-detectors (PADs), which are currently limited to 9 kHz or slower.

With this goal in mind, scientists in the XSD Time Resolved Research Group at beamline 8-ID-I of the APS established a collaboration with colleagues at the AGH University of Science and Technology (Poland) to apply the ultrafast x-ray camera (UFXC) to XPCS measurements. In 2016, the team demonstrated the applicability of this detector to XPCS with 11-kHz frame rates [2] and subsequently demonstrated 50-kHz frame rates in 2017 [3]. For 11-kHz and 50-kHz measurements, as illustrated by the schematic timing diagram in Fig. 1(a), there is no acquisition dead time during a measurement sequence; the two-counters-per-pixel alternate between accumulating counts and being read out.

The team's most recent achievement was the demonstration of a "burst mode" where 12 frames were acquired at frame rates of either 390-kHz or 1.2-MHz and saved to the two counters associated with each pixel before a longer pause was used to read out each pair of counters. Following these two events, the cycle repeated itself. The timing for this mode is illustrated schematically in Fig. 1(b).

By merging otherwise identical measurements made at 50 kHz, 390 kHz, and 1.2 MHz, the team demonstrated time sensitivity to nanoscale fluctuations extending continuously from 826 ns to 60 s, or nearly 8 decades in time. Particularly noteworthy is that the 1.2-MHz frame rate corresponds to an exposure time of less than the

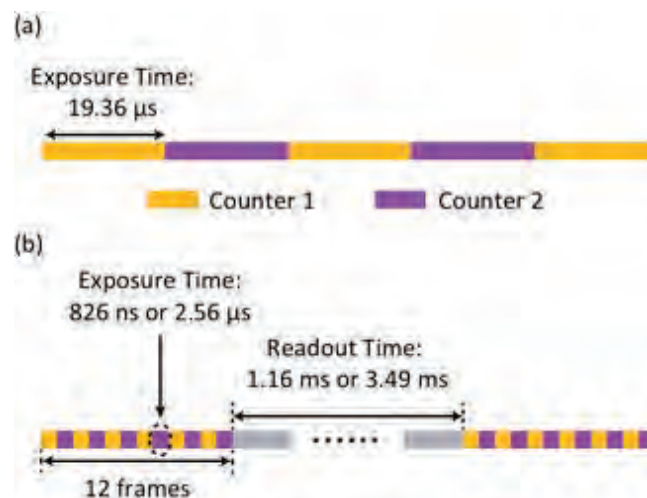


Fig. 1. Illustration of UFXC operation modes: (a) continuous mode and (b) burst mode. In continuous mode, the two counters per pixel alternate between accumulating events and being read out while in burst mode, the counts in 12 short exposures are stored in pixel-local counters before a longer interval is used to read out the stored data.

transit time of an electron bunch around the APS storage ring, which is a significant advance toward the goal of resolving the scattering signal from individual electron bunches in the storage ring that are currently spaced 153 ns apart.

As a demonstration of burst-mode operation, the

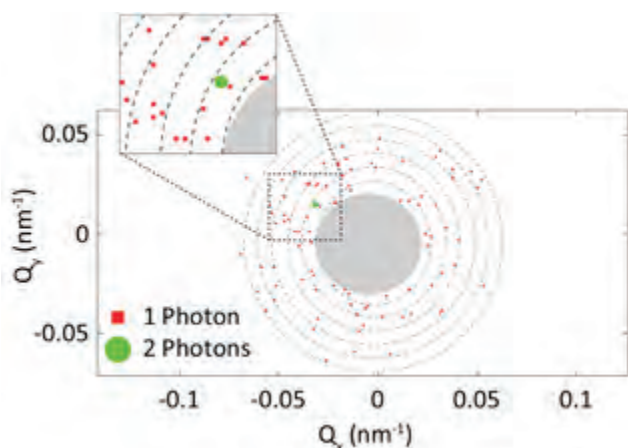


Fig. 2. 1.2-MHz burst-mode data acquired from the 57-nm-radius silica suspension. A single frame showing the sparsity of the signal. The grey circle is the masked-out shadow of the direct-beam stop and the dashed circles delineate annuli with equivalent length-scale sensitivity.

team made measurements of the fluctuating interference pattern resulting from the Brownian motion of 57-nm-radius silica nanoparticles in water. Figure 2 shows the coherent x-ray scattering intensity in a single 826-ns exposure (1.2 MHz), demonstrating how sparse the data is from the APS today; the signal will improve by 2-to-3 orders of magnitude with the APS-U. Despite the sparse data, a high-quality correlation function can be calculated and is shown in Fig. 3, which presents results obtained by combining correlation decays measured in 1.2-MHz and 390-kHz burst modes with that obtained in 50-kHz continuous mode. The accuracy of the measurements on this model system was checked by fitting the time scale of the exponential decays as a function of inverse length-scale sensitivity that is referred to as the wave vector transfer, or Q . The results, as shown in the inset of Fig. 3, agree well with the anticipated inverse-length-scale-squared scaling, as first derived by Einstein.

Despite the impressive achievement demonstrated with what is now the fastest XPCS area detector in the world, the sparse signal level illustrated in Fig. 2 makes the practical application of this detector to many systems today a significant challenge. The APS-U and the XPCS feature beamline will address this shortcoming, allowing studies of dynamics that evolve with time and that are critical to understanding the physics of aging and phase transitions in many topical systems such as colloidal gels, metallic glasses, and spin and charge ordered structures.

Contact Qingteng Zhang (qzhang234@anl.gov)

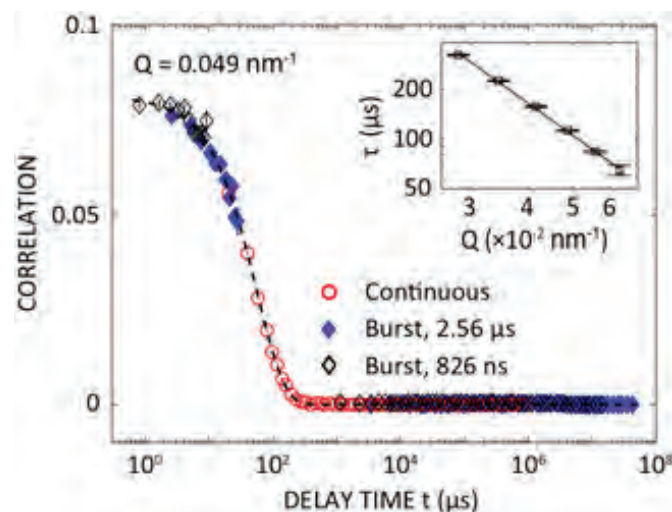


Fig. 3. Correlation decay obtained from silica nanoparticles suspended in water. The dashed line is a fit to a single exponential decay. The inset shows the time scale of the correlation decay versus wave vector transfer or Q (open squares) and the solid line is a fit with the slope set to -2.

REFERENCES

- [1] P. Chung et al., “ α -Synuclein Sterically Stabilizes Spherical Nanoparticle-Supported Lipid Bilayers,” *ACS Appl. Bio. Mater.* **2**, 1413 (2019). DOI: 10.1021/acsabm.8b00774.
- [2] Q. Zhang et al., “Submillisecond x-ray photon correlation spectroscopy from a pixel array detector with fast dual gating and no readout dead-time,” *J. Synchrotron Rad.* **23**, 679 (2016). DOI: 10.1107/S1600577516005166.
- [3] Q. Zhang et al., “Dynamic scaling of colloidal gel formation at intermediate concentrations,” *Phys. Rev. Lett.* **119**, 178006 (2017). DOI: 10.1103/PhysRevLett.119.178006.

See: Qingteng Zhang¹, Eric M. Dufresne¹, Suresh Narayanan¹, Piotr Maj², Anna Kozioł², Robert Szczygiel², Pawel Grybos², Mark Sutton³, and Alec R. Sandy^{1*}, “Sub-microsecond-resolved multi-speckle X-ray photon correlation spectroscopy with a pixel array detector,” *J. Synchrotron Rad.* **25**, 1408 (2018). DOI: 10.1107/S1600577518009074

Author affiliations: ¹Argonne National Laboratory, ²AGH University of Science and Technology, ³McGill University

Correspondence: * asandy@anl.gov

This material is based upon work supported by Laboratory Directed Research and Development (LDRD) funding from Argonne National Laboratory, provided by the Director, Office of Science, of the U.S. Department of Energy (DOE) under Contract No. DE-AC02-06CH11357. AGH University of Science and Technology was supported by the National Center for Research and Development, Poland, PBS1/A3/12/2012. This research used resources of the Advanced Photon Source, a U.S. DOE Office of Science User Facility operated for the DOE Office of Science by Argonne National Laboratory under contract No. DE-AC02-06CH11357.



Christine Dunham (Emory University) was awarded the "2018 Cozzarelli Prize" for best Biological paper published in Proc. Natl. Acad. Sci. U.S.A. in 2018. Commentary by J.F. Atkins: "Culmination of a half-century quest reveals insight into mutant tRNA-mediated frameshifting after tRNA departure from the decoding site." **Dunham** was also named a 2018 American Society of Biochemistry and Molecular Biology (ASBMB) Young Investigator.



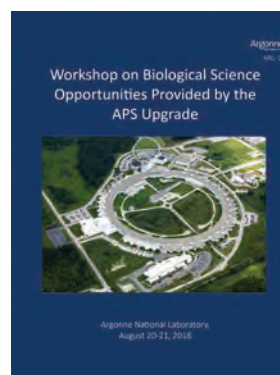
Bi-Cheng Wang (University of Georgia and SER-CAT Director) was awarded the iHuman "Structure of Life Award," which is presented to worldwide scientists who have made outstanding contributions to structural biology community in 2018.



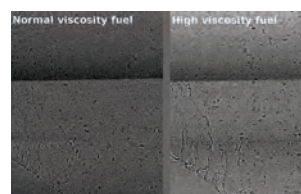
Mikhail Solovjev (Rutgers University) earned a U.S. Department of Energy Science Graduate Student Research award to work at the APS on first-of-its-kind materials analysis.



The 2018 Gopal K. Shenoy Excellence in Beamline Science Award, awarded by the APS Users Organization Steering Committee, was presented to **Hua Zhou** (XSD) at the annual APS/CNM Users Meeting. The award recognizes Zhou's pioneering work in the field of synchrotron radiation studies of complex oxide heterostructures, using various sectors of the APS.

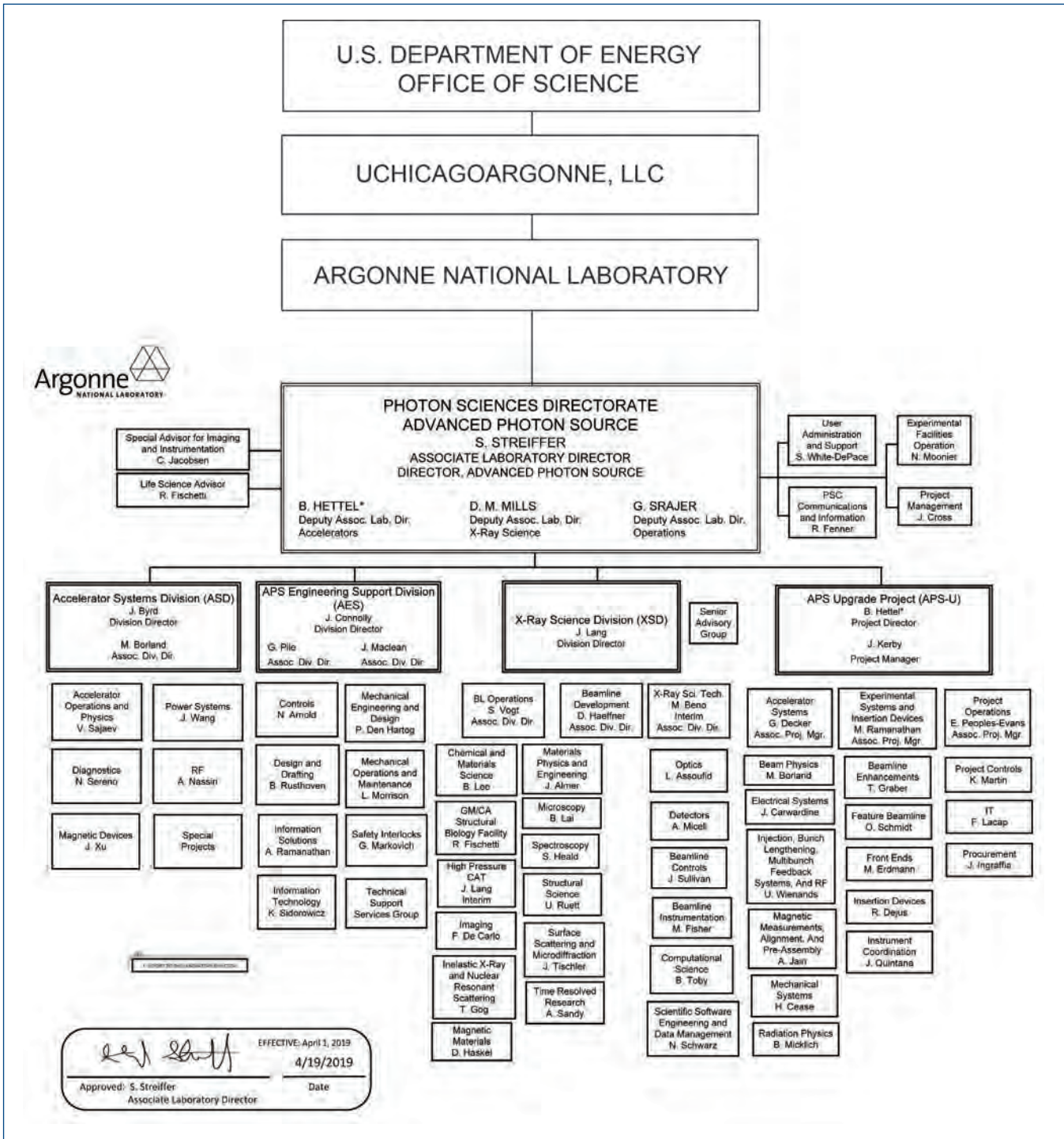



The report on the "**Workshop on Biological Science Opportunities Provided by the APS Upgrade**" held at Argonne on August 20-21, 2018, is now available. This workshop was organized "...to discuss the biological science opportunities offered by the unique new capabilities of the [APS Upgrade, APS-U] and how the broad structural biology community could best exploit them." The 24-page report (ANL-19/04) is available as a pdf download from: <https://bit.ly/2xcYUrF>



Imaging and measuring the atomization process in a gas turbine combustor using XSD beamline 7-BM at the APS was chosen by **RDECOM Research Laboratory**, the Army's corporate research laboratory under the Army Research Laboratory (ARL), as one of the 2018 top 10 "coolest" advances, showcasing what Army scientists and engineers are doing to support the soldier of the future. The RDECOM Research Laboratory's chief scientist, Dr. Alexander Kott, handpicked these ARL initiatives.

APS Organization Chart




 EFFECTIVE: April 1, 2019
 4/19/2019
 Approved: S. Streiffer
 Associate Laboratory Director

APS Source Parameters

UNDULATOR A (31 INSERTION DEVICES [IDs] IN 25 SECTORS)

Period: 3.30 cm
Length: 2.1 m in sectors 16, 21, 23, 24, 28, 34; 2.3 m in Sector 6;
2.4 m in sectors 1, 2, 5, 7, 8, 9, 10, 11, 15, 17, 18, 19, 20, 22, 26, 28,
31, 32, 33
Minimum gap: 10.5 mm
 B_{\max}/K_{\max} : 0.892 T/2.75 (effective; at minimum gap)
Tuning range: 3.0–13.0 keV (1st harmonic)
3.0–45.0 keV (1st–5th harmonic)
On-axis brilliance at 7 keV (ph/s/mrad²/mm²/0.1%bw):
4.1 x 10¹⁹ (2.4 m), 4.0 x 10¹⁹ (2.3 m), 3.3 x 10¹⁹ (2.1 m)
Source size and divergence at 8 keV:
 Σ_x : 276 μm Σ_y : 11 μm
 Σ_x : 12.7 μrad (2.4 m), 12.8 μrad (2.3 m), 12.9 μrad (2.1 m)
 Σ_y : 6.7 μrad (2.4 m), 6.8 μrad (2.3 m), 7.1 μrad (2.1 m)

2.30-CM UNDULATOR (2 IDs IN SECTORS 11, 14)

Period: 2.30 cm Length: 2.4 m
Minimum gap: 10.5 mm
 B_{\max}/K_{\max} : 0.558 T/1.20 (effective; at minimum gap)
Tuning range: 11.8–20.0 keV (1st harmonic)
11.8–70.0 keV (1st–5th harmonic, non-contiguous)
On-axis brilliance at 12 keV (ph/s/mrad²/mm²/0.1%bw): 6.9 x 10¹⁹
Source size and divergence at 12 keV:
 Σ_x : 276 μm Σ_y : 11 μm
 Σ_x : 12.3 μrad Σ_y : 5.9 μrad

2.70-CM UNDULATOR (5 IDs IN SECTORS 3, 12, 14, 35)

Period: 2.70 cm
Length: 2.1 m in Sector 12; 2.4 m in sectors 3, 14, and 35
Minimum gap: 10.5 mm
 B_{\max}/K_{\max} : 0.698 T/1.76 (effective; at minimum gap)
Tuning range: 6.7–16.0 keV (1st harmonic)
6.7–60.0 keV (1st–5th harmonic, non-contiguous)
On-axis brilliance at 8.5 keV (ph/s/mrad²/mm²/0.1%bw):
5.7 x 10¹⁹ (2.4 m), 4.7 x 10¹⁹ (2.1 m)
Source size and divergence at 8 keV:
 Σ_x : 276 μm Σ_y : 11 μm
 Σ_x : 12.7 μrad (2.4 m), 12.9 μrad (2.1 m)
 Σ_y : 6.7 μrad (2.4 m), 7.1 μrad (2.1 m)

3.00-CM UNDULATOR (8 IDs IN SECTORS 12, 13, 16, 21, 23, 27, 34)

Period: 3.00 cm
Length: 2.1 m in sectors 12, 13, 16, 21, 23, 34; 2.4 m in Sector 27
Minimum gap: 10.5 mm
 B_{\max}/K_{\max} : 0.787 T/2.20 (effective; at minimum gap)
Tuning range: 4.6–14.5 keV (1st harmonic)
4.6–50.0 keV (1st–5th harmonic)
On-axis brilliance at 8 keV (ph/s/mrad²/mm²/0.1%bw):
4.8 x 10¹⁹ (2.4 m), 3.9 x 10¹⁹ (2.1 m)
Source size and divergence at 8 keV:
 Σ_x : 276 μm Σ_y : 11 μm
 Σ_x : 12.7 μrad (2.4 m), 12.9 μrad (2.1 m)
 Σ_y : 6.7 μrad (2.4 m), 7.1 μrad (2.1 m)

3.50-CM SMCO UNDULATOR (SECTOR 4)

Period: 3.50 cm Length: 2.4 m
Minimum gap: 9.75 mm
 B_{\max}/K_{\max} : 0.918 T/3.00 (effective; at minimum gap)
Tuning range: 2.4–12.5 keV (1st harmonic)
2.4–42.0 keV (1st–5th harmonic)
On-axis brilliance at 7 keV (ph/s/mrad²/mm²/0.1%bw): 3.7 x 10¹⁹
Source size and divergence at 8 keV:
 Σ_x : 276 μm Σ_y : 11 μm
 Σ_x : 12.7 μrad Σ_y : 6.7 μrad

3.60-CM UNDULATOR (SECTOR 13)

Period: 3.60 cm
Length: 2.1 m
Minimum gap: 11.0 mm
 B_{\max}/K_{\max} : 0.936 T/3.15 (effective; at minimum gap)
Tuning range: 2.2–11.8 keV (1st harmonic)
2.2–40.0 keV (1st–5th harmonic)
On-axis brilliance at 6.5 keV (ph/s/mrad²/mm²/0.1%bw): 2.8 x 10¹⁹
Source size and divergence at 8 keV:
 Σ_x : 276 μm Σ_y : 11 μm
 Σ_x : 12.9 μrad Σ_y : 7.1 μrad

1.72-CM UNDULATOR (3 IDs IN SECTORS 30, 35)

Period: 1.72 cm
Length: 4.8 m (2 x 2.4 m) in Sector 30; 2.4 m in Sector 35
Minimum gap: 10.6 mm
 B_{\max}/K_{\max} : 0.330 T/0.53 (effective; at minimum gap)
Tuning range: 23.7–26.3 keV (1st harmonic)
On-axis brilliance at 23.7 keV (ph/s/mrad²/mm²/0.1%bw):
1.0 x 10²⁰ (4.8 m), 4.4 x 10¹⁹ (2.4 m)
Source size and divergence at 23.7 keV:
 Σ_x : 276 μm Σ_y : 11 μm
 Σ_x : 11.6 μrad (4.8 m) 11.9 μrad (2.4 m)
 Σ_y : 4.3 μrad (4.8 m), 4.9 μrad (2.4 m)

1.80-CM UNDULATOR (SECTOR 32)

Period: 1.80 cm
Length: 2.4 m
Minimum gap: 11.0 mm
 B_{\max}/K_{\max} : 0.244 T/0.41 (effective; at minimum gap)
Tuning range: 23.8 - 25.3 keV (1st harmonic)
71.4 - 75.9 keV (3rd harmonic)
On-axis brilliance at 23.8 keV (ph/s/mrad²/mm²/0.1%bw): 2.8 x 10¹⁹
Source size and divergence at 23.8 keV:
 Σ_x : 276 μm Σ_y : 11 μm
 Σ_x : 11.9 μrad Σ_y : 4.9 μrad

IEX 12.5-CM QUASI-PERIODIC POLARIZING UNDULATOR (SECTOR 29)

Period: 12.5 cm
Length: 4.8 m
Circular polarization mode:
Max. currents: horizontal coils 34.4 A, vertical coils 20.7 A
 K_{\max} : 2.73 (effective; at max. currents)
 B_{\max} : 0.27 T (peak; at max. currents)
Tuning range: 0.44–3.5 keV (1st harmonic)
On-axis brilliance at 1.8 keV (ph/s/mrad²/mm²/0.1%bw): 1.4 x 10¹⁹
Linear horizontal polarization mode:
Max. current: vertical coils 47.6 A
 K_{\max} : 5.39 (effective; at max. current)
 B_{\max} : 0.54 T (peak; at max. current)
Tuning range: 0.24–3.5 keV (1st harmonic)
0.24–11.0 keV (1st–5th harmonic)
On-axis brilliance at 2.1 keV (ph/s/mrad²/mm²/0.1%bw): 1.1 x 10¹⁹
Linear vertical polarization mode:
Max. current: horizontal coils 50.3 A
 K_{\max} : 3.86 (effective; at max. current)
 B_{\max} : 0.37 T (peak; at max. current)
Tuning range: 0.44–3.5 keV (1st harmonic)
0.44–11.0 keV (1st–5th harmonic)
On-axis brilliance at 2.1 keV (ph/s/mrad²/mm²/0.1%bw): 1.1 x 10¹⁹
Fast polarization switching not required
Source size and divergence at 2 keV:
 Σ_x : 276 μm Σ_y : 13 μm
 Σ_x : 13.9 μrad Σ_y : 8.8 μrad

12.8-CM CIRCULARLY POLARIZING UNDULATOR (SECTOR 4)

Period: 12.8 cm

Length: 2.1 m

Circular polarization mode:

Max. currents: horizontal coils 1.34 kA, vertical coils 0.40 kA

K_{\max} : 2.85 (effective; at max. currents)

B_{\max} : 0.30 T (peak; at max. currents)

Tuning range: 0.4–3.0 keV (1st harmonic)

On-axis brilliance at 1.8 keV (ph/s/mrad²/mm²/0.1%bw): 3.1×10^{18}

Linear horizontal polarization mode:

Max. current: vertical coils 0.40 kA

K_{\max} : 2.85 (effective; at max. current)

B_{\max} : 0.30 T (peak; at max. current)

Tuning range: 0.72–3.0 keV (1st harmonic)

0.72–10.0 keV (1st–5th harmonic)

On-axis brilliance at 2.1 keV (ph/s/mrad²/mm²/0.1%bw): 2.3×10^{18}

Linear vertical polarization mode:

Max. current: horizontal coils 1.60 kA

K_{\max} : 3.23 (effective; at max. current)

B_{\max} : 0.34 T (peak; at max. current)

Tuning range: 0.58–3.0 keV (1st harmonic)

0.58–10.0 keV (1st–5th harmonic)

On-axis brilliance at 2.1 keV (ph/s/mrad²/mm²/0.1%bw): 2.3×10^{18}

Switching frequency (limited by storage ring operation): 0–0.5 Hz

Switching rise time: 50 ms

Source size and divergence at 2 keV:

Σ_x : 276 μm Σ_y : 12 μm

Σ_x : 16.7 μrad Σ_y : 12.7 μrad

1.80-CM SUPERCONDUCTING UNDULATOR (2 IDs IN SECTORS 1, 6)

Period: 1.80 cm

Length: 1.1 m

Gap: 9.5 mm (fixed)

Max. current: 450 A

B_{\max}/K_{\max} : 0.962 T/1.61 (effective; at maximum current)

Tuning range: 11.2–24.7 keV (1st harmonic)

11.2–150.0 keV (1st–13th harmonic, non-contiguous)

On-axis brilliance at 13 keV (ph/s/mrad²/mm²/0.1%bw): 3.2×10^{19}

Source size and divergence at 13 keV:

Σ_x : 276 μm Σ_y : 11 μm

Σ_x : 13.2 μrad Σ_y : 7.5 μrad

3.15-CM HELICAL SUPERCONDUCTING UNDULATOR (SECTOR 7)

Period: 3.15 cm

Length: 1.2 m

Coil winding diameter: 31.0 mm

Max. current: 450 A

B_{\max}/K_{\max} : 0.413 T/1.213 ($B_x=B_y$ effective; at maximum current)

Tuning range: 6.0–13.0 keV (1st harmonic)

On-axis brilliance at 6.0 keV (ph/s/mrad²/mm²/0.1%bw): 2.2×10^{19}

Source size and divergence at 6 keV:

Σ_x : 276 μm Σ_y : 11 μm

Σ_x : 14.7 μrad Σ_y : 10.0 μrad

APS BENDING MAGNET

Critical energy: 19.51 keV

Energy range: 1–100 keV

On-axis brilliance at 16 keV (ph/s/mrad²/mm²/0.1%bw): 5.4×10^{15}

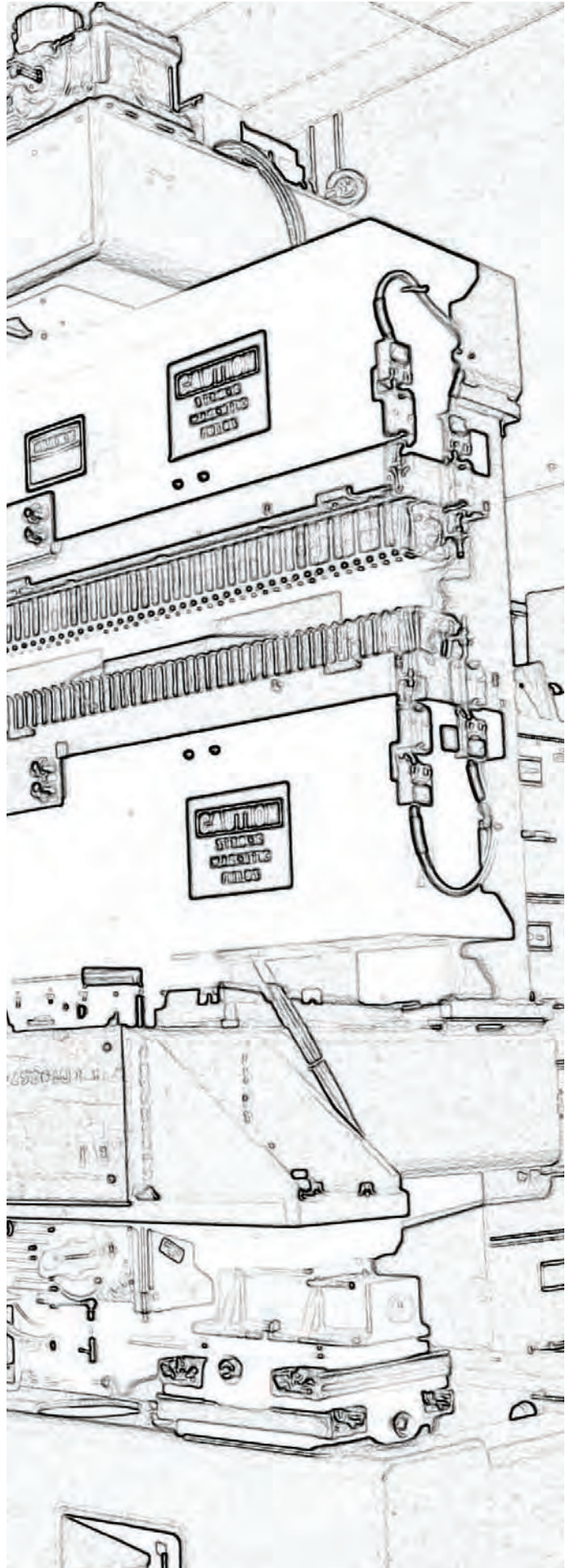
On-axis angular flux density at 16 keV (ph/s/mrad²/0.1%bw): 9.6×10^{13}

Horizontal angular flux density at 6 keV (ph/s/mradh/0.1%bw): 1.6×10^{13}

Source size and divergence at the critical energy:

Σ_x : 92 μm Σ_y : 31 μm

Σ_x : 6 mrad Σ_y : 47 μrad



Acknowledgments

APS Science 2018 Editorial Board:

Mark A. Beno (ANL-PSC), John Byrd (ANL-ASD), John P. Connolly (ANL-AES), Robert F. Fischetti (ANL-PSC), Robert O. Hettel (ANL-PSC), Jim Kerby (ANL-PSC), Jonathan C. Lang (ANL-XSD), Dennis M. Mills, (ANL-PSC), George Srajer (ANL-PSC), Stephen K. Streiffer (ANL-PSC), Stefan Vogt (ANL-XSD)

Reviewers:

Jonathan Almer, Francesco De Carlo, Thomas Gog, Daniel Haskel, Steve Heald, Barry Lai, Uta Ruett, Jon Tischler, Brian Toby, Alec Sandy, Randy Winans (all XSD); Jim Kerby (APS-U); Denis Keane (DND-CAT); Brue Bunker & Carlo Segre (MR-CAT); Mark Rivers, Vitali Prakapenka, Steve Sutton & Yanbin Wang (GSE-CARS); Vukica Srajer (BioCARS); Binhau Lin (ChemMatCARS); Lisa Keefe (IMCA-CAT); Thomas Irving (Bio-CAT); Andrzej Joachimiak (SBC-CAT); Keith Brister (LS-CAT); John Rose & Bi-Cheng Wang (SER-CAT); Michael Becker, Bob Fischetti & Janet Smith (GMCA-XSD); Kay Perry (NE-CAT); Jordi Benach (LRL-CAT); Yogendra Gupta & Paulo Rigg (DCS)

Unless otherwise noted, the research highlights in this report were written by:

Mary Alexandra Agner (marymary@alum.mit.edu)
William Arthur Atkins (waarc@grics.net)
Christen Brownlee (christenbrownlee@gmail.com)
Erika Gebel Berg (erikagebel@gmail.com)
David Bradley (david@sciencebase.com)
Vic Comello ANL-CPA - retired (vcomello@anl.gov)
Dana Desonie (desonie@cox.net)
Sandy Field (sfield@fieldscientific.com)
Joseph E. Harmon ANL-CPA (harmon@anl.gov)
Emma Nichols (emma@nascentmc.com)
Philip Koth (philkoth@comcast.net)
Kim Krieger (mskrieger@gmail.com)
David Lindley (dxlindley@gmail.com)
Chris Palmer (crpalmer2009@gmail.com)
Nicola Parry (nicola@parrymedicalwriting.com)
Neil Savage (neil@stefan.com)
Alicia Surrao (alicia@untoldcontent.com)
Mark Wolverton (exetermw@earthlink.net)

Photography: Wes P. Agresta, Mark L. Lopez (both ANL-CPA)

Aerial photograph of the APS: John Hill (Tigerhill Studio, <http://www.tigerhillstudio.com>)

Publications, contracts, rights and permissions, circulation: Jessie L. Skwarek (ANL-PSC)

Printing oversight: Gary R. Weidner (ANL-CPA)

Editorial, project coordination, design, photography: Richard B. Fenner (ANL-PSC)

Our thanks to the corresponding authors and others who assisted in the preparation of the research highlights, to the users and APS personnel who wrote articles for the report, and our apologies to anyone inadvertently left off this list. To all: your contributions are appreciated.



Office of Science

**Advanced Photon Source
Argonne National Laboratory
9700 S. Cass Ave.
Argonne, IL 60439 USA
www.anl.gov • www.aps.anl.gov**